

Dissertation

Third dredge-up in cluster AGB stars: observational constraints and improved opacity data for models

Dissertation zur Erlangung des akademischen Grades

Doktor der Naturwissenschaften (Dr. rer. nat.)

Verfasser: Michael T. Lederer

Matrikel-Nummer: 9725760

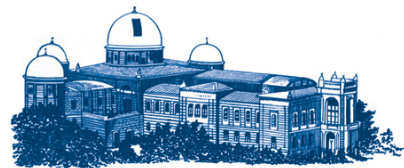
Dissertationsgebiet (lt. Studienblatt): A 091 413 Astronomie

Betreuer: Doz. Dr. Thomas Lebzelter

Wien, am 10. März 2009



universität
wien



Für Tamara

Abstract

The extant stellar evolution models largely agree on the theoretical picture of a low- or intermediate-mass star that has evolved towards the end of the asymptotic giant branch (AGB). During this evolutionary phase, chemical elements (mainly carbon, helium and products of the *s*-process) are synthesised in a series of recurring shell burning episodes. The burning products are then transported to the outer layers of the star by convective mixing events. This mechanism is usually condensed in the term *third dredge-up* (TDU). Subsequently, the chemically enriched matter is ejected into the interstellar medium by means of strong stellar winds that develop in the late stages of stellar evolution. As low- and intermediate-mass stars appear in a large number, it is crucial to assess their role within the cosmic matter cycle which requires detailed knowledge of the TDU onset and efficiency as a function of the stellar mass and metallicity.

The material presented in this thesis intends to contribute to the improvement of AGB star models in two ways. The first approach is to constrain the models with results from observations. I present high-resolution near-infrared spectra of AGB stars that belong to intermediate-age globular clusters (GC) in the Large Magellanic Cloud (LMC). A sample of GC stars has the advantage that fundamental stellar parameters like mass, metallicity, and age are usually well-defined and that the sample is—more or less—homogeneous in this respect, contrary to the situation that we find for a sample of field stars. The analysis of the observed spectra is done by a comparison with synthetic spectra based on hydrostatic atmosphere models computed with the MARCS code. We use features of the molecules CO and OH comprised in our observed wavelength range to derive the number ratio of carbon to oxygen atoms (C/O) and the carbon isotopic ratio $^{12}\text{C}/^{13}\text{C}$ together with the stellar parameters of each target. Eventually, we confront the outcomes of stellar evolution calculations with our findings.

The second part of the thesis deals with a new set of low-temperature mean opacity coefficients. Until recently, the change in chemistry due to the TDU in the cool layers of the star, where molecules are the dominant opacity source, has been neglected in almost all stellar evolution models. I show that already within a certain chemistry regime (i. e. an oxygen-rich or carbon-rich metal mixture) an alteration of the carbon abundance causes, due to the special role of the CO molecule, considerable changes in the Rosseland opacity which has distinct consequences for the stellar structure and evolution. In the stellar evolution models, the most pronounced effect can be expected when the TDU turns the initially oxygen-rich object into a carbon star. The new opacity database contains (beside a variation of the ^{12}C mass fraction) also tables with a varied abundance of ^{14}N . After describing the database as well as the tools and the data used for its computation, I point out the implications of the new opacity data for stellar evolution models.

Zusammenfassung

Aktuelle Sternentwicklungsmodelle zeichnen ein weitgehend einheitliches Bild von der Entwicklung eines Sterns aus dem unteren und mittleren Massenbereich (d.h. etwa 1–4 bzw. 4–8 Sonnenmassen), wenn diese bis zum Ende des Asymptotischen Riesenastes (engl. *asymptotic giant branch*, AGB) im Hertzsprung-Russell-Diagramm fortgeschritten ist. In dieser Entwicklungsphase entstehen im Sterninneren chemische Elemente (hauptsächlich Kohlenstoff, Helium und Produkte aus langsam ablaufenden Neutroneneinfangprozessen) in einer Abfolge von Brennphasen, welche in dünnen Massenschalen um einen inerten Kern ablaufen. Die neu entstandenen Elemente werden durch konvektive Mischprozesse, welche man als *third dredge-up* (TDU) bezeichnet, in die äußeren Schichten des Sterns transportiert. Von dort aus kann das chemisch angereicherte Material durch starke Sternwinde in das interstellare Medium gelangen. Diese Winde bilden sich in der Spätphase der Sternentwicklung. Da Sterne aus dem unteren und mittleren Massenbereich in großer Zahl vorkommen, ist es wichtig, ihre Rolle im kosmischen Materiekreislauf genau zu verstehen. Das wiederum erfordert detailliertes Wissen über die Bedingungen für das Auftreten von TDU und dessen Effizienz in Abhängigkeit von der Sternmasse und des Metallgehalts des Sterns. (Im astrophysikalischen Sprachgebrauch werden alle Elemente, die schwerer als Helium sind, als "Metalle" bezeichnet werden.)

Die vorliegende Arbeit zielt auf eine Verbesserung der AGB-Sternentwicklungsmodelle in zweierlei Hinsicht ab. Der erste Zugang ist derart, dass aus Beobachtungsergebnissen Schranken für die Modelle abgeleitet werden. Dies geschieht mithilfe von hochaufgelösten Nahinfrarotspektren von AGB-Sternen, die sich in Kugelsternhaufen der Großen Magellanschen Wolke befinden. Ein Stichprobe von AGB-Sternen in Kugelsternhaufen bietet den Vorteil, dass grundlegende Sternparameter wie die Masse, der Metallgehalt (oder auch "Metallizität") und das Alter relativ genau bekannt sind. Überdies ist eine solche Stichprobe in Bezug auf die genannten Parameter verhältnismäßig homogen. Diese Voraussetzungen sind bei Feldsternen in der Milchstraße üblicherweise nicht erfüllt. Die Analyse der beobachteten Spektren basiert auf einem Vergleich mit synthetisch erzeugten Spektren, die auf hydrostatischen Modellatmosphären beruhen, welche mit dem MARCS-Code berechnet werden. Wir benutzen Spektrallinien der Moleküle CO und OH, die in unseren beobachteten Spektralbereichen zu identifizieren sind, um das Zahlenverhältnis von Kohlenstoff- zu Sauerstoffatomen (C/O), das Verhältnis der beiden stabilen Kohlenstoffisotope ($^{12}\text{C}/^{13}\text{C}$) sowie die stellaren Parameter unserer Beobachtungsziele abzuleiten. Diese Größen vergleichen wir schlussendlich mit Ergebnissen von Sternentwicklungsrechnungen.

Der zweite Teil dieser Arbeit befasst sich mit neu berechneten Opazitätskoeffizienten für den Bereich niedriger Temperaturen, in dem Moleküle die Hauptopazitätsquellen

sind. Bis vor kurzem wurden die Auswirkungen einer sich ändernden chemischen Zusammensetzung der kühlen Atmosphärenschichten als Folge des TDU in fast allen Sternentwicklungsmodellen vernachlässigt. Bereits innerhalb eines bestimmten Chemieregimes — bedingt durch die spezielle Rolle des CO-Moleküls unterscheidet man zwischen sauerstoffreichen ($C/O < 1$) und kohlenstoffreichen Chemien ($C/O > 1$) — führt eine Änderung der Kohlenstoffhäufigkeit zu beträchtlichen Veränderungen des Rosseland-Opazitätsmittles. Dies hat wiederum deutliche Auswirkungen auf die Entwicklung des Sterns. Die größten Effekte sind dort zu erwarten, wo der TDU ein ursprünglich sauerstoffreiches Objekt in einen Kohlenstoffstern verwandelt. Die neue Opazitätsdatenbank enthält Tabellen, in denen der Anteil von ^{12}C (und auch ^{14}N) in mehreren Schritten variiert wird. Nach einer Beschreibung der Opazitäten sowie der zur Erstellung verwendeten Werkzeuge und Daten, werden die Auswirkungen der Daten auf Ergebnisse von Sternentwicklungsrechnungen erläutert.

Publications

The following publications were published or prepared during the term of the author's candidature.

Refereed journal papers

- Aringer, B., Girardi, L., Nowotny, W., Marigo, P. and Lederer, M. T. 2009. Synthetic photometry for carbon-rich giants. I. Hydrostatic dust-free models. *A&A*, accepted.
- Cristallo, S., Straniero, O., Gallino, R., Piersanti, L., Dominguez, I. and Lederer, M. T. 2009, ArXiv e-prints 0902.0243 ApJ, accepted
- Cristallo, S., Straniero, O., Lederer, M. T. and Aringer, B. 2007, *ApJ*, 667, 489-496
- Frémat, Y., Antonova, A., Damerджи, Y., Hansen, C. J., Lederer, M. T., Tüysüz, M., Lampens, P. and van Cauteren, P. 2006, *Communications in Asteroseismology*, 148, 77-81
- Lebzelter, T., Lederer, M. T., Cristallo, S., Hinkle, K. H., Straniero, O. and Aringer, B. 2008a, *A&A*, 486, 511-521
- Lederer, M. T. and Aringer, B. 2009, *A&A*, 494, 403-416
- Lederer, M. T., Lebzelter, T., Cristallo, S., Straniero, O., Hinkle, K. H. and Aringer, B. 2009. The puzzling dredge-up pattern in NGC 1978. *A&A*, submitted.
- Utenthaler, S., Lebzelter, T., Palmerini, S., Busso, M., Aringer, B. and Lederer, M. T. 2007, *A&A*, 471, L41-L45

Conference proceedings

- Cristallo, S., Straniero, O., Gallino, R., Lederer, M. T., Piersanti, L. and Domínguez, I. 2008. Progresses in AGB Modelling. In *Evolution and Nucleosynthesis in AGB Stars*, number 1001 in American Institute of Physics Conference Series, pages 3-10.
- Cristallo, S., Straniero, O., Gallino, R., Piersanti, L., Domínguez, I. and Lederer, M. T. 2008a. Why galaxies care about asymptotic giant branch stars. To appear in the *MemSAIt*, Vol. 80.
- Cristallo, S., Straniero, O. and Lederer, M. T. 2008b. Evolution and Nucleosynthesis of Low-Mass Metal-Poor AGB Models with C- and N-Enhanced Molecular Opacities. In O'Shea, B. W. and Heger, A., editors, *First Stars III*, number 990 in American Institute of Physics Conference Series, pages 320-324.
- Hron, J., Aringer, B., Kerschbaum, F., Lebzelter, T., Nowotny, W., Posch, T., Lederer, M., Richter, H., Galsterer, W., Höfner, S., Gautschy-Loidl, R. and Verhoelst, T. 2006. The Many Faces of Red Giants. In Coudé Du Foresto, V., Rouan, D. and Rousset, G., editors, *Visions for Infrared Astronomy, Instrumentation, Mesure, Métrologie*, pages 107-110.

- Lebzelter, T., Hinkle, K., Lederer, M. T., Posch, T. and Wood, P. 2007. AGB Stars in Globular Clusters. In Kerschbaum, F., Charbonnel, C. and Wing, R. F., editors, *Why Galaxies Care About AGB Stars: Their Importance as Actors and Probes*, number 378 in Astronomical Society of the Pacific Conference Series, pages 105-110.
- Lebzelter, T., Hinkle, K. H., Lederer, M. T., Cristallo, S., Straniero, O., Nowotny, W. and Wood, P. 2008. Observing Third Dredge Up in NGC 1846. In Guandalini, R., Palmerini, S. and Busso, M., editors, *Evolution and Nucleosynthesis in AGB Stars*, number 1001 in American Institute of Physics Conference Series, pages 56-62.
- Lebzelter, T., Lederer, M. T., Cristallo, S., Straniero, O. and Hinkle, K. H. 2008d. A study of AGB stars in LMC clusters. To appear in the proceedings of the IAU Symposium No. 256.
- Lederer, M. T. and Aringer, B. 2008a. Low Temperature Mean Opacities for the Carbon-rich Regime. In Guandalini, R., Palmerini, S. and Busso, M., editors, *Evolution and Nucleosynthesis in AGB Stars*, number 1001 in American Institute of Physics Conference Series, pages 11-18.
- Lederer, M. T., Aringer, B., Höfner, S. and Kerschbaum, F. 2007. Water Opacity in M Stars. In Kerschbaum, F., Charbonnel, C. and Wing, R. F., editors, *Why Galaxies Care About AGB Stars: Their Importance as Actors and Probes*, number 378 in Astronomical Society of the Pacific Conference Series, pages 127-128.
- Lederer, M. T., Lebzelter, T., Aringer, B., Nowotny, W., Hron, J., Uttenthaler, S. and Höfner, S. 2006, *Memorie della Societa Astronomica Italiana*, 77, 1008-1013
- Lederer, M. T., Lebzelter, T., Cristallo, S., Straniero, O., Aringer, B. and Hinkle, K. 2007. Third Dredge-up in Globular Cluster AGB Stars: Observation Versus Theory. In *American Institute of Physics Conference Series*, number 948 in American Institute of Physics Conference Series, pages 43-50.
- Uttenthaler, S., Lebzelter, T., Hron, J., Aringer, B., Lederer, M. T., Palmerini, S., Busso, M. and Käufl, H. U. 2008. Testing Evolutionary Models with Observations of Galactic Bulge AGB Stars. In Guandalini, R., Palmerini, S. and Busso, M., editors, *Evolution and Nucleosynthesis in AGB Stars*, number 1001 in American Institute of Physics Conference Series, pages 313-320.

Contents

Abstract	I
Zusammenfassung	III
Publications	V
Refereed journal papers	V
Conference proceedings	V
Contents	VII
1 Asymptotic giant branch stars	1
1.1 AGB stars in context	1
1.1.1 Which stars become AGB stars?	1
1.1.2 Motivation	3
1.2 Stellar evolution	5
1.2.1 The way to the AGB	5
1.2.2 Evolution on the AGB	7
1.2.2.1 Early AGB phase	7
1.2.2.2 Thermally pulsing AGB phase	8
1.2.3 Beyond the AGB	8
1.3 Nucleosynthesis	8
1.3.1 Triple-alpha process	9
1.3.2 Slow neutron capture process	10
1.3.3 Fluorine production	11
1.4 Mixing phenomena	12
1.4.1 Third dredge-up	12
1.4.2 Extra-mixing	14
1.5 The atmosphere	16
1.5.1 Molecules	16
1.5.2 Dynamical phenomena and dust	17
1.5.3 Beyond the atmosphere	19
1.6 Thesis outline	19
2 Third dredge-up in LMC cluster stars	21
2.1 Introduction	21
2.2 Observations	22
2.2.1 Targets	22
2.2.1.1 NGC 1846	23
2.2.1.2 NGC 1978	23
2.2.2 Spectroscopy	25

Contents

2.2.2.1	NGC 1846	25
2.2.2.2	NGC 1978	25
2.2.3	Data reduction	28
2.3	Data analysis	28
2.3.1	Contents of the observed wavelength ranges	28
2.3.2	Synthetic spectra	29
2.3.3	Determination of abundance ratios	33
2.3.4	Stellar evolutionary models	38
2.4	Results	40
2.4.1	NGC 1846	40
2.4.1.1	Cluster membership	40
2.4.1.2	Stellar parameters and abundance ratios	42
2.4.2	NGC 1978	45
2.4.2.1	Cluster membership	45
2.4.2.2	Stellar parameters and abundance ratios	45
2.5	Discussion	50
2.5.1	NGC 1846	50
2.5.1.1	Dredge-up along the AGB	50
2.5.1.2	The S-type stars	55
2.5.1.3	The carbon stars	57
2.5.2	NGC 1978	58
2.5.2.1	Toy models	60
2.5.2.2	Stellar evolutionary models	63
2.5.2.3	Alternative scenarios	67
2.6	Conclusions	70
3	Low-temperature Rosseland opacities	73
3.1	Introduction	73
3.2	Tool and method	76
3.3	Data sources	77
3.3.1	Continuous opacity	78
3.3.2	Atomic lines	79
3.3.3	Molecular data	79
3.4	Table design	81
3.5	Results and discussion	83
3.5.1	Comparison with other data	88
3.5.2	Interpolation	96
3.5.3	Sources of uncertainties	97
3.5.3.1	Adopting different solar element abundances	97
3.5.3.2	Uncertainties in molecular data	100
3.5.3.3	Numerics and parameters	102

3.5.3.4	Application of the Rosseland opacity data	102
3.6	Conclusions	103
4	Summary and future directions	105
4.1	Third dredge-up and extra-mixing in cluster stars	105
4.2	Low-temperature opacities	106
4.2.1	FRANEC	107
4.2.2	MONSTAR	109
4.2.3	MESA	110
4.2.4	Outlook	110
A	The Hardy interpolation method	113
A.1	Problem description	113
A.2	Interpolation on arbitrary grids	113
A.3	Opacity interpolation	115
B	The Rosseland mean	117
B.1	Radiative transfer in the stellar interior	117
B.2	Derivation of the Rosseland mean	118
C	Element abundances	121
C.1	Spectroscopic notation	121
C.1.1	Preferred definition	121
C.1.2	Literature tour (de force)	123
C.2	Formulae	125
C.2.1	Conversion from A values to isotopic mass fractions	125
C.2.2	Conversion from isotopic mass fractions to A values	127
C.2.3	Setting the mass fraction of ^{12}C to match a certain C/O ratio	127
	References	129
	Figures	143
	Tables	145
	Showcases	147
	Acronyms	149
	Danksagungen/Acknowledgements	151

Contents

Curriculum vitae 153

1 Asymptotic giant branch stars

Asymptotic giant branch (AGB) stars are named according to their position in the fundamental diagram of astrophysics, the Hertzsprung-Russell diagram (HRD). Stars that possess a low or intermediate mass enter the AGB phase in the late stages of their evolution. In the centre of an AGB resides an inert core, mainly consisting of carbon and oxygen. An unstable, nuclear active double-shell configuration is located outside this core. The internal structure is coated by an extended convective mantle, which is completed by the stellar atmosphere. Even further out, the so-called circumstellar envelope (CSE) follows, which is the terminal structural element of an AGB star and the interface to the interstellar medium (ISM). Recurring mixing events that bring nuclear processed material to the stellar surface are characteristic for this evolutionary stage. An intense, pulsation-enhanced dust-driven stellar wind carries the chemically enriched element mixture into the ISM.

This brief description comprises the basic characteristics of AGB stars and contains some directions about what makes it worthwhile to study them. First, the complex nature of the stellar structure and evolution renders them interesting research objects as such. Additionally, low-mass stars are numerous and thus represent the relevant building blocks of large stellar systems. Moreover, they are element factories that efficiently release their products. Therefore, they significantly contribute to the cosmic matter cycle. Last but not least, the sun as a low-mass star will eventually become an AGB star, and it is natural to ponder about its future.

In the following, I will elaborate most of what was said in the first paragraph. Topics that are particularly relevant for this thesis are emphasised, while complementary information is given in a compact form to complete the overall picture. The structure of the introductory chapter was to a large extent influenced by the numerous reviews on AGB stars (and also their progenitors and progeny), but in particular by the comprehensive book of Habing and Olofsson (2003).

1.1 AGB stars in context

1.1.1 Which stars become AGB stars?

The Vogt-Russell theorem (Vogt, 1926 and Russell et al., 1926) states that for every combination of mass and chemical composition of a star there exists a unique equilibrium configuration. In other words, the structure of a star is fully determined by its mass and composition. Since the publication of this conjecture, many counter-examples have been found, and it became evident that it is by no means a theorem in the mathematical sense (e. g. Kaehler, 1978). However, when applied to the evolution of a single star (i. e. a star

that does not reside in a binary system), it turns out to be a useful working hypothesis, given that rotation and magnetic fields play only a minor role.

Out of the two parameters mass and metallicity¹, it is basically the mass that determines whether a star runs through an AGB phase or not. Thus, the question in the section title is often answered by the phrase *low- and intermediate-mass stars*, and by common agreement this depicts the mass range between 0.8 and $8 M_{\odot}$. It also follows immediately that there must be a division between low-mass stars and intermediate-mass stars, which is of course a matter of definition. The mass limits quoted in the following depend on the metallicity of the star, but also on the (details in the implementation of the) code that was used to infer these quantities.

Iben and Renzini (1983) defined low-mass stars to be those that develop an electron-degenerate helium core after the main sequence phase. Following this notion, stars with initial masses of up to $2.5 M_{\odot}$ fall into the low-mass range. Accordingly, more massive objects are intermediate-mass stars. In terms of stellar evolution, this definition separates low-mass stars that ignite helium burning abruptly in a so-called *helium flash* from more massive stars that pass into the phase of helium burning smoothly. Herwig (2005) suggested a different criterion to distinguish between low- and intermediate-mass stars and adopts the following definition. Low-mass AGB stars do not experience hot bottom burning (HBB), while intermediate-mass stars do. HBB is the name for hydrogen burning occurring at the base of the convective mantle. This process causes an enhanced abundance of helium and nitrogen in the mantle and atmosphere, and influences the isotopic ratios of other elements such as carbon, aluminium, or magnesium, for instance. McSaveney et al. (2007) confirmed the theoretically well-established scenario of HBB with observations, which supports the argument of Herwig (2005) that his classification of low- and intermediate-mass stars is more meaningful from the observational point of view. The mass limit for the occurrence of HBB is about $4 M_{\odot}$.

What happens to stars that fall below the mass range quoted above? The lower limit of $0.8 M_{\odot}$ originates from the fact that stars less massive have not yet had time to evolve beyond the main sequence and to the AGB. Theoretical considerations imply that even objects with masses down to about $0.5 M_{\odot}$ might eventually evolve to the AGB phase. Objects that possess a mass below about one tenth of the solar mass ($\sim 0.08 M_{\odot}$) are not at all capable of burning hydrogen quiescently (Chabrier and Baraffe, 2000). This mass limit marks the division between stars and brown dwarfs. The region in-between, i. e. from 0.08 to $0.5 M_{\odot}$, roughly, is occupied by red dwarfs. Those objects are fully convective, and their central temperature is high enough to burn hydrogen. Due to the convective interior, the nuclear active regions are constantly supplied with fresh fuel. The star can thus consume a larger fraction of hydrogen compared with more massive

¹ We use the *metallicity* henceforth in our argumentation instead of the term *chemical composition*, although one has to bear in mind that also the helium abundance plays an important role for stellar evolution.

stars, and its evolution takes place on a time scale of trillions of years. Such objects do not undergo giant phases towards the end of their life (Adams et al., 2004).

Beyond a critical initial mass $M_{\text{up}} \simeq 8M_{\odot}$, a star on the AGB does not sustain its electron-degenerate carbon-oxygen core (see Sect. 1.2.2). At some point in the evolution, the conditions in the stellar core become suitable for the ignition of carbon burning. The final fate of such a *Super-AGB star* is either a neon-oxygen white dwarf, or the evolution ends in an electron-capture supernova. In that case, the remnant will be a neutron star. For an overview of the active field of Super-AGB star research see Siess (2007) and references therein. Entering the stage of carbon burning does not necessarily mean that the star runs through all burning phases. For this scenario, a minimum mass $M_{\text{mas}} \simeq 11M_{\odot}$ exists (Woosley et al., 2002). Such stars explode as supernovae and eventually leave behind either a neutron star or a black hole.

1.1.2 Motivation

The reasons to study AGB stars are manifold. The complex structure of an AGB star certainly provides an incentive by itself. A great number of physical processes take place on vastly different size, density, and temperature scales (i. e. spanning a range of 10, 30, and 7 order of magnitudes, respectively, according to Habing and Olofsson, 2003), as is illustrated in Fig. 1.1. The modelling of AGB stars requires the consistent application of concepts stemming from various physical disciplines, such as nuclear physics, atomic physics, molecular physics, hydrodynamics, radiation transport (electromagnetism in general), thermodynamics, or solid state physics. This complexity prohibits to model such a system as a whole and over extended time intervals. Still, the investigation of subsystems (e. g. the stellar interior or the atmosphere) that are simplified by approximations allow to deduce substantial information about the entire object and its evolution.

The atmospheres of AGB stars are extended (and thus exceedingly luminous), cool, and they pulsate.² With these characteristics AGB stars are valuable tools for the study of galaxies. Foremost, in remote systems they evince the presence of intermediate-age stellar populations and thus provide information about the star-formation history in galaxies. A comprehensive summary about this topic was given by Grebel (2007) who addressed also what makes AGB stars important to galaxies in general. That paper also contains many references supplementary to the ones presented in the remaining paragraph. AGB stars account for a substantial fraction of the luminosity of unresolved systems (e. g. Maraston, 1998) and leave their signatures in the spectral energy distributions

² AGB stars fill a radius of a few $100R_{\odot}$ and have typical effective temperatures around 3000 K. In combination ($L = 4\pi R^2 \sigma T_{\text{eff}}^4$) this may result in luminosities higher than $10^4 L_{\odot}$. AGB stars belong to the class of *long period variables* (LPVs) with periods ranging from 100 to below 1000 d, and with variations in the bolometric magnitude of up to 1^m. See also Fig. 1.1.

1 Asymptotic giant branch stars

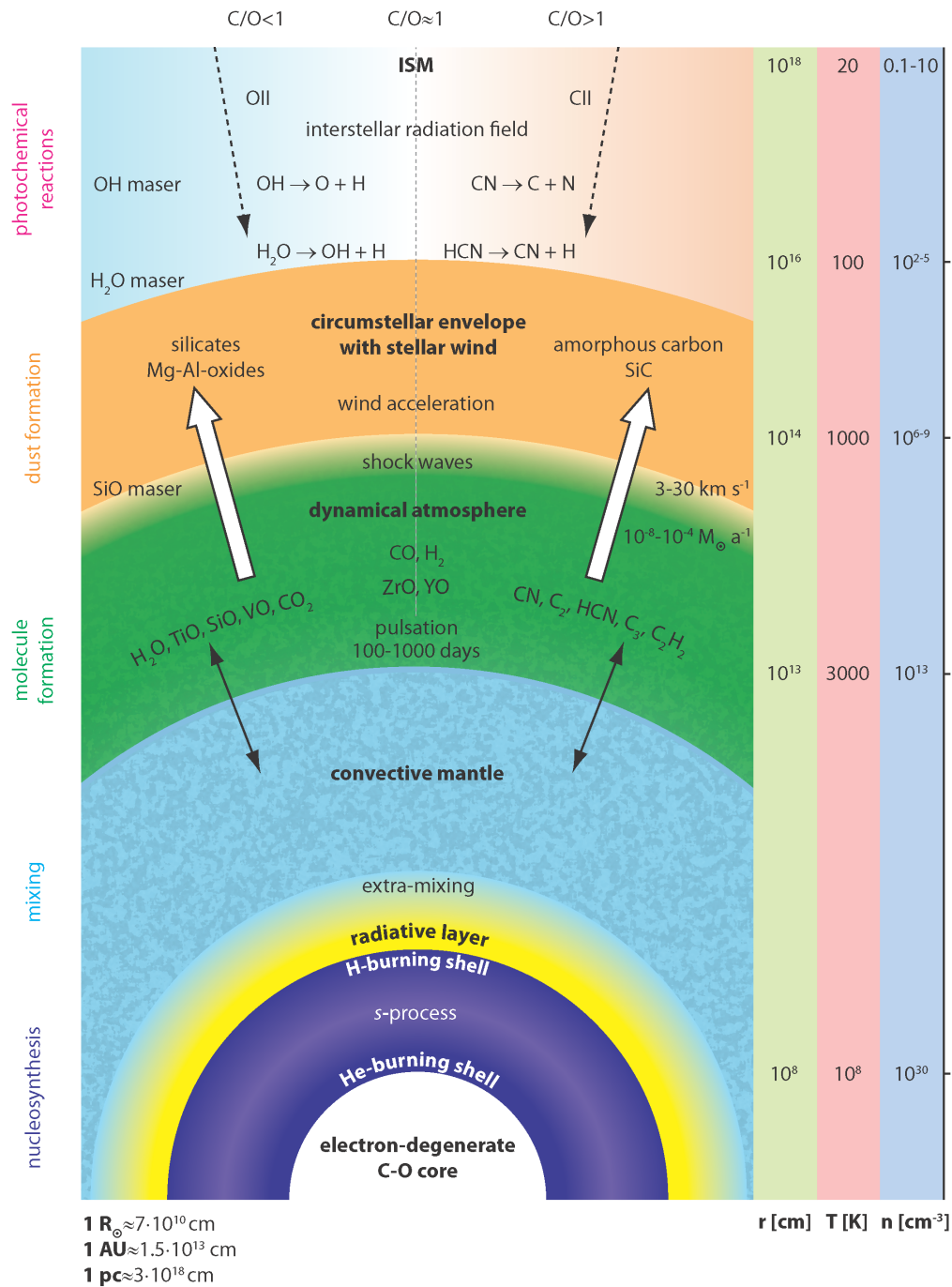


Figure 1.1 Schematic view of an AGB star (not to scale). This figure illustrates the complex structure of such an object. Various interrelated physical processes take place on different size, density, and temperature scales. Figure adapted from Josef Hron, after an idea from Thibaut Le Bertre.

of those (e. g. Maraston, 2005). Therefore, a concise picture of AGB stars is crucial for population synthesis models (see Marigo, 2007 for a recent overview). The low temperatures in AGB star atmospheres favour the formation of molecules (see also Sect. 1.5). In resolved systems the bright AGB stars can be used as tracers for the kinematics of the system (e. g. Dejonghe and van Caelenberg, 1999).

Low-mass stars in the late stages of their evolution eject large amounts of nuclear processed material. Since they are large in number, they are significant players in the cosmic matter cycle³ and severely influence the chemical evolution of their host galaxies. Tosi (2007) gave an overview about the role of AGB stars for chemical evolution models and motivated the improve of theoretical yields, such as completed for example by Cristallo et al. (2009).

This excursion about the role of AGB stars for galaxies shall be completed with a note on the well-defined relation between the luminosity and the pulsation period of Mira stars, which allows to utilise AGB stars as distance indicators (Feast, 2004).

The giant branch phases in stellar evolution are of importance for considerations about the future of sun and earth, too. However, details of the AGB phase of the sun will not matter to life on earth anymore, since our planet will have shifted out of the habitable zone long before, according to calculations from Schröder and Connors Smith (2008).

1.2 Stellar evolution

From the beginning to the final stages of the stellar life, the evolution of a low-mass star is significantly driven by the physical processes deep in the stellar interior. In this section I sketch the evolution of a single (i. e. not part of a binary system) low-mass star. It would be a futile attempt to go into details, therefore I refer to some of the numerous reviews and books on this subject, namely Iben and Renzini (1983), Busso et al. (1999), Habing and Olofsson (2003), Herwig (2005) and Catelan (2007).

To illustrate the content of the following sections, I show a colour-magnitude diagram (CMD) and its theoretical counterpart, the Hertzsprung-Russell diagram (HRD) in Fig. 1.2. These shall provide visual guidance to the evolutionary stages addressed below on the basis of tracks for an individual object (HRD) and within a sample of stars with different initial masses (CMD).

1.2.1 The way to the AGB

A star is born out of a molecular cloud that becomes unstable according to the Jeans criterion (Jeans, 1928). The cloud fragments into smaller entities, most of which will

³ Figure 20 in Busso et al. (1999) contains a nice illustration of the cosmic matter cycle.

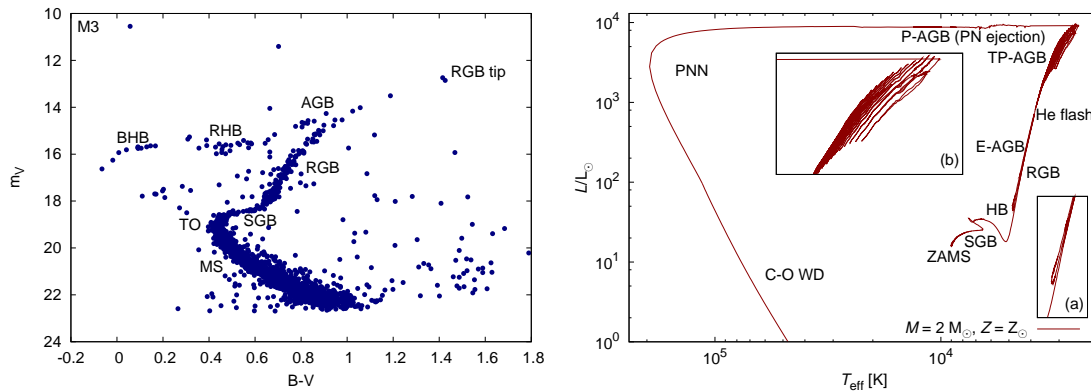


Figure 1.2 Example colour-magnitude diagram and Hertzsprung-Russell diagram. The left panel shows observational data for the cluster M3, each dot in the CMD corresponds to a star. In the right panel a theoretical evolution track for a star with $M = 2 M_{\odot}$ and solar metallicity in the HRD is plotted. Inset (a) zooms in to the horizontal branch phase, whereas inset (b) shows the track on the upper AGB where thermal pulses occur in greater detail. Abbreviations are referred to in the text. Data from Rey et al. (2001, CMD) and Herwig (2005, HRD).

give rise to low-mass stars (e. g. Chabrier, 2005). Grossly simplified, the object contracts and heats up until the temperature in the interior is high enough to ignite hydrogen burning. The star has then entered a state of hydrostatic and thermal equilibrium. At the beginning of its life, the star is located at the zero-age main sequence (ZAMS) in the HRD.

The following phase is the longest in the course of stellar evolution. The star fuses hydrogen to helium in its centre via the proton-proton (pp) chain on a time scale of 10^{10} a. During the core hydrogen burning phase, the star resides at the main sequence (MS). By the time the nuclear reactions have consumed all the hydrogen in the stellar core, the fusion of hydrogen advances in a shell around the centre and the star slowly leaves the MS. The star has reached the *turn-off point* (TO) in the stellar evolution track, and evolves to the sub-giant branch (SGB).

When the helium core (formed out of the ashes of hydrogen burning) exceeds the Schönberg-Chandrasekhar mass limit (Schönberg and Chandrasekhar, 1942), it starts to collapse on a thermal time scale. As a consequence, it heats up and releases energy. At the base of the hydrogen burning shell, the temperature increases and the CNO cycle becomes the main burning process. The energy provided by the nuclear reactions drives the expansion of the mantle, which cools down and becomes convective. In the HRD the star moves to higher luminosities and lower temperatures and ascends the red giant branch (RGB). An alternative name for the RGB used by theorists is *first giant branch*, because later in the evolution the star follows a similar track in the L - T_{eff} plane. During

the RGB phase, the surface convection zone reaches down to where partial hydrogen burning has taken place. The products of this process (mainly ${}^4\text{He}$, ${}^{13}\text{C}$, and ${}^{14}\text{N}$) are mixed throughout the outer layers of the star. This phenomenon is called the *first dredge-up*.

The continuing contraction and heating of the core leads eventually to the ignition of helium burning. The degenerate conditions in the core of low-mass stars lead to a positive feedback between the local temperature and the nuclear reaction rate, which is usually depicted as *thermonuclear runaway*. This *helium flash* at the RGB tip marks the end of the first ascent on the giant branch.

From the RGB tip the star evolves rapidly to the horizontal branch (HB, see also inset (a) of Fig. 1.2). Depending on the metallicity and on the details of the RGB phase, particularly in terms of mass loss, the stars either fall on the blue horizontal branch (BHB) or the red horizontal branch (RHB). The HB is the phase of core helium burning, the products of which are mainly ${}^{12}\text{C}$ and ${}^{16}\text{O}$ (see also Sect. 1.3.1). Hydrogen burning continues in a shell around the helium core. These ashes of helium burning form an inert C–O core as soon as the helium in the centre is exhausted. The star enters a stage of double-shell burning, and the same physical mechanisms as in the pre-RGB phase cause an expansion of the mantle. At this time, the star moves to the upper right in the HRD for the second time, and the track it follows during this period is the asymptotic giant branch.

1.2.2 Evolution on the AGB

1.2.2.1 Early AGB phase

At the beginning of the early AGB phase, the He-burning shell provides the major fraction of the luminosity. A part of the energy comes from the gravitationally contracting, electron-degenerate C–O core, while the hydrogen-burning shell contributes only marginally to the energy output.⁴ The He-burning shell becomes gradually thinner and declines in luminosity. This thin-shell configuration is thermally unstable and begins to oscillate (Schwarzschild and Härm, 1965 and Weigert, 1966). By this time, most of the luminosity originates from the hydrogen burning shell, whose energy output also starts to vary periodically.

⁴ In massive stars, the H-burning shell can even be extinguished by the large expansion of the mantle, which gives rise to the occurrence of the *second dredge-up*. The convection zone reaches down below the hydrogen-helium discontinuity and enriches the mantle with hydrogen-burning ashes (mainly ${}^4\text{He}$ and ${}^{14}\text{N}$). See Habing and Olofsson (2003).

1.2.2.2 Thermally pulsing AGB phase

The energy production rate in the helium burning shell is extremely sensitive to temperature perturbations. The shell itself is thin compared with the radius at which it is located. In combination, these two facts cause a recurrent activation of the helium burning shell, where the individual events are referred to as *He-shell flash* or *thermal pulse* (TP). During a thermal pulse, the He-shell provides almost the entire luminosity of the star, while the H-burning dies down intermittently and releases little energy. This leads to typical variations in the stellar luminosity of a factor three (compare inset (b) of Fig. 1.2). The TP-AGB phase lasts some 10^6 a, whereby the number of thermal pulses depends on the stellar parameters. The time between two consecutive TPs is long compared with the duration of a pulse itself (see Sect. 1.4.1 and Fig. 1.4), therefore the probability of observing an AGB star during a TP is low. Two important characteristics of the TP-AGB phase, namely the nucleosynthesis in and in-between the burning shells and the mixing mechanisms that disperse the newly formed elements, are treated in more detail in Sects. 1.3 and 1.4, respectively.

1.2.3 Beyond the AGB

Strong mass loss terminates the AGB phase. A slow (typically $10\text{--}20\text{ km s}^{-1}$) but efficient (up to $\dot{M} = 10^{-4} M_{\odot} \text{ a}^{-1}$) stellar wind erodes the hydrogen-rich mantle to a large extent. During this fast transition from the AGB to the planetary nebula (PN) phase, the object is usually dubbed *Post-AGB* (P-AGB) star. See the review from van Winckel (2003) for details about this evolutionary stage. The core is basically unaffected by the mantle ejection and the nuclear reactions continue. The star moves to higher temperatures in the HRD at a constant luminosity. The UV radiation may at some point ionise the expanding ejecta which results in the formation of planetary nebulae, which are discussed at length in Kwok (2000) and Balick and Frank (2002), for instance. When the nuclear activity in the planetary nebula nucleus (PNN) ceases, the ultimate episode in the life of the star commences. The remaining white dwarf (WD) becomes cooler and fainter by radiating away its thermal energy on a time scale of gigayears.

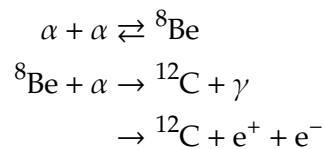
1.3 Nucleosynthesis

The double-shell structure in AGB stars (see Fig. 1.1) brings about a complex interplay of different nucleosynthesis processes. Due to the inherent instability of this configuration, the elements are mixed throughout the nuclear active regions and are (alternatively) exposed to hydrogen burning (mainly by means of the CNO cycle), helium burning (triple-alpha process, see Sect. 1.3.1), and the *s*-process (Sect. 1.3.2). An important feature of

AGB nucleosynthesis is that it forms many light nuclei from hydrogen and helium only,⁵ and heavier elements in neutron capture events on seed nuclei. While hydrogen and helium burning account for the luminosity of the star, other reactions (such as neutron capture reactions, for instance) do not contribute to the energy budget significantly and influence the element abundances only. The main burning products during the AGB phase are ${}^4\text{He}$, ${}^{12}\text{C}$, ${}^{14}\text{N}$, but also ${}^{16}\text{O}$, ${}^{19}\text{F}$, ${}^{22}\text{Ne}$, ${}^{23}\text{Na}$, ${}^{25}\text{Mg}$, ${}^{26}\text{Al}$, and ${}^{27}\text{Al}$ (Habing and Olofsson, 2003). The sophisticated nucleosynthesis models suffer in particular from uncertain reaction rates that can often not be measured in the laboratory for the relevant energy ranges (cf. e. g. the review by Catelan, 2007). In the following, I introduce some relevant nucleosynthesis processes. This topic is treated in way more detail in the reviews from Busso et al. (1999), Habing and Olofsson (2003) and Herwig (2005), although this list is not exhaustive.

1.3.1 Triple-alpha process

Out of the numerous nuclear reactions, the production of carbon is probably the most prominent nucleosynthesis process in TP-AGB stars. The carbon isotope ${}^{12}\text{C}$ is produced during helium burning by means of the so-called *triple-alpha* or Salpeter process (Salpeter, 1952). As indicated by the name of the process, three helium nuclei fuse to yield the main carbon isotope in the chain of reactions shown below and illustrated in Fig. 1.3.



The fuel for this reaction is brought to the burning regions as a consequence of the thermal instability of the helium burning shell, which gives rise to an inter-shell convection zone (see below) that mixes ${}^4\text{He}$ down and freshly synthesised ${}^{12}\text{C}$ outward.

A remarkable detail in the triple-alpha process is the eminently short half-life of the ${}^8\text{Be}$ isotope, which decays after approximately 10^{-16} seconds. An efficient production of carbon is only possible due to the fact that the reaction ${}^8\text{Be}(\alpha, \gamma){}^{12}\text{C}$ possesses a pronounced resonance (predicted by Hoyle et al., 1953 and experimentally confirmed by Cook et al., 1957) at the energies prevailing during the helium burning phases on the AGB. The short half-life of ${}^8\text{Be}$ is thus still long enough so that another alpha particle can react with the beryllium nucleus. In this way it is possible to bridge the instability gap at a mass number of $A = 8$. In turn, the reaction rate for a further alpha capture on a ${}^{12}\text{C}$ nucleus to produce ${}^{16}\text{O}$ is moderate, and a substantial amount of carbon "survives" the helium burning, while still some oxygen is produced.

⁵ This mode of element formation is called *primary*.

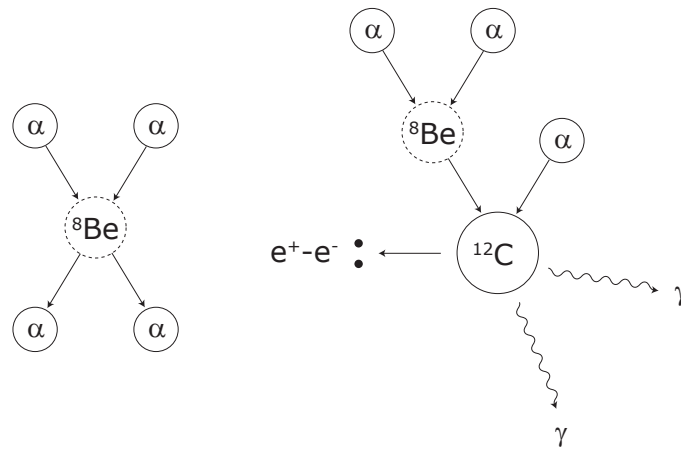


Figure 1.3 Reactions of the triple-alpha process. In a first step, two alpha particles (i. e. He nuclei) react to form the instable isotope ${}^8\text{Be}$. Only a resonance in the cross section of the subsequent reaction ${}^8\text{Be}(\alpha, \gamma){}^{12}\text{C}$ allows the production of the ${}^{12}\text{C}$ isotope before the beryllium nucleus decays back into two alpha particles. Figure adapted from Oberhummer (1993).

The production of carbon does not only affect the structure and evolution of an AGB star, it has also consequences for the chemical evolution of galaxies, since the chemically enriched matter is ejected from the star. Supernovae and Wolf-Rayet stars also contribute to the carbon content of the Milky Way, but according to Dray et al. (2003) the carbon yield of AGB stars is equally important.

1.3.2 Slow neutron capture process

Although this thesis is not primarily concerned with the *s*-process (first suggested by Burbidge et al., 1957), it shall nevertheless be mentioned briefly. This is because this process contributes significantly to the production of elements heavier than iron (i. e. mass numbers $A \geq 56$, see e. g. Arlandini et al., 1999), and the interior of an AGB star is a typical site for the occurrence of slow neutron capture reactions (e. g. Straniero et al., 2006). The term *slow* refers to the rate of neutron captures compared with the time scale of the beta decay. The counterpart for high neutron fluxes is the *r*-process (for *rapid neutron capture process*) occurring in novae, supernovae, and X-ray binaries. The mass number of an isotope increases by 1 in a neutron capture process, while the consecutive beta decay leaves the mass number unchanged, which leads to the formation of increasingly heavier elements.

The *s*-process takes place in the inter-shell region, where free neutrons are abundant. Two possible neutron sources are the reactions ${}^{13}\text{C}(\alpha, n){}^{16}\text{O}$ and ${}^{22}\text{Ne}(\alpha, n){}^{25}\text{Mg}$, whereby

the latter requires higher temperatures and thus contributes significantly to the neutron flux in intermediate-mass stars only. The former neutron source is related to the formation of the so-called ^{13}C pocket in the inter-shell region, which requires the ingestion of protons from the hydrogen-rich mantle. It is beyond the scope of this section to elaborate on the important issue of the ^{13}C pocket. I refer to the work of Cristallo et al. (2009, and references therein), who addressed the problem of the s -process and its strong metallicity dependence by means of a stellar evolution code that incorporates a full nuclear network from hydrogen to bismuth.

The s -process alters the abundances of elements from Sr to Pb to a different extent. Especially in the comparison of theoretical results with observations, it has become common to distinguish between *light* s -process (ls), *heavy* s -process (hs), and lead peak elements (Luck and Bond, 1991). A prominent observational signature of the s -process is the ^{99}Tc isotope in AGB star atmospheres. It has a half-life of the order of 10^5 a, and therefore, since other technetium isotopes have either a shorter half-life or are exceptionally rare in the universe (^{100}Tc which is only created by the r -process), the detection of this element coercively leads to the conclusion that it must have been created in the stellar interior and then mixed up to the atmosphere (see Sect. 1.4). Otherwise, if it was present at the time of the star formation, it would have had decayed already. This argument was first presented by Merrill (1952), see Lebzelter and Hron (2003) and Uttenthaler et al. (2007) for more recent investigations. Another approach to obtain information about the s -process from observations is the measurement of abundance ratios of elements that are influenced by so-called branching points. These are isotopes encountered in the path of the s -process that have a half-life comparable to the average time until the subsequent neutron capture event. As an example, Lambert et al. (1995) measured the Rb/Sr abundance ratio which is controlled by the branching point at ^{85}Kr and in this way inferred the neutron density at the site of the s -process.

1.3.3 Fluorine production

Jorissen et al. (1992) found a correlation of the C/O ratio with the fluorine abundance in AGB stars. In this way it was shown that fluorine is produced in low-mass stars during their AGB phase. To bring nucleosynthesis models in concordance with observational results is complicated by the fact that the reaction network determining the production and destruction of ^{19}F consists of many paths, which are strongly temperature-dependent and also rely on numerous other aspects (see Habing and Olofsson, 2003 for details). The problem of reproducing the large fluorine over-abundances found by Jorissen et al. (1992) within stellar evolution calculations lead also to assumptions about non-standard mixing processes (see Sect. 1.4.2) that presumably account for an enhanced fluorine production (Busso et al., 2007). The problem was alleviated by Abia et al. (2008) who found fluorine abundances in carbon stars that are by approximately 0.8 dex lower with respect

to earlier results. However, still no quantitative agreement between models and observations has been achieved. Moreover, it has to be emphasised that major depletion reaction rates of ^{19}F , for instance, still undergo distinct revisions (e.g. Ugalde et al., 2008). In this thesis, the question of fluorine production during the AGB phase is addressed in Sect. 2.5.1.1.

1.4 Mixing phenomena

Our knowledge about the ongoings in the stellar interior would be less detailed and the universe would bring forth much less complex entities if there were not physical mechanisms that transport the burning products to the atmosphere of the AGB star where they can be observed. Most of the time, the nuclear active regions are separated from the convective mantle by a radiative layer, i. e. a region where no convective motions take place. During a thermal pulse, this region disappears and the convective mantle reaches down to regions where the freshly synthesised elements reside. But even at times when the radiative layer prevails (during the interpulse phases), there appears to exist a mechanism that is able to cause the exchange of material between the hydrogen-burning shell and the mantle. The respective phenomena are explicated in the following.

1.4.1 Third dredge-up

Herwig (2005) explains dredge-up to be the convective mixing process that brings material processed by nucleosynthesis to the surface. Generally speaking, dredge-up occurs for the third time⁶ during stellar evolution when the star evolves on the TP-AGB (cf. Sects. 1.2.1 and 1.2.2.1). The thermal pulses (Sect. 1.2.2.2) are necessary but not sufficient to cause TDU. Its onset and efficiency are linked to the metallicity and also the mass of the stellar core and mantle (see Straniero et al., 2006 for a summary).

A thermal pulse sequence is best illustrated with a Kippenhahn diagram (Fig. 1.4). Before a TP commences, the hydrogen-burning shell provides almost the entire stellar luminosity, while the helium-burning shell is dormant. The H-shell deposits its ashes on the He-shell which grows in mass and heats up. This eventually triggers triple-alpha reactions which release energy, and the He-shell cannot reconfigure fast enough to compensate for the rise in temperature. Therefore a thermonuclear runaway sets in (*He-shell flash*), and radiation is not sufficient to fully account for the energy transport outwards. A convection zone develops (also called *pulse-driven convection zone*, PDCZ) that mixes the products of He-burning—carbon constitutes about 25 per cent of the mass in this

⁶ Depending on the stellar mass, a star may not encounter the second dredge-up (Sect. 1.2.2.1). Nevertheless, the convective mixing of nuclear processed material to the surface during the TP-AGB phase is always depicted *third* dredge-up.

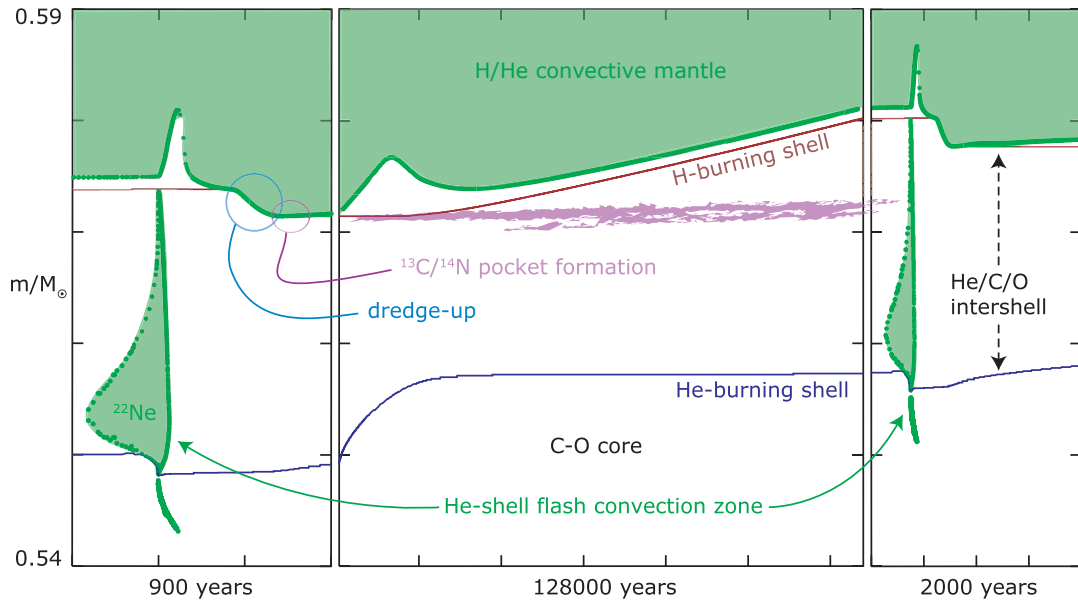


Figure 1.4 Thermal pulses (or *He-shell flashes*) and third dredge-up in a Kippenhahn diagram. This figure shows the time evolution of the mass coordinates of the burning shells. The nuclear active region is confined within a narrow mass range. Convective regions (the mantle and the pulse-driven convection zone) are shaded. A relevant feature in the plot is the penetration of the convective mantle to regions where nuclear processed material resides (labelled with "dredge-up"). Also note the different time scales of the thermal pulses and the interpulse phase. A detailed description is given in the text. The figure has been adapted from Herwig (2005), the data for a $M = 2 M_{\odot}$ and $Z = 0.01$ model come from Herwig and Austin (2004).

region—throughout the inter-shell. The expansion of the inter-shell after the ceasing activity of the He-shell and the retreat of the PDCZ extinguishes the hydrogen-burning shell. This is the point at which the convective mantle extends inwards to regions that are enriched in nuclear processed material. At the same time, the convection carries protons to this region that give rise to the formation of the ^{13}C pocket, which leads to the release of neutrons during the following interpulse phase. The re-establishment of the H-burning shell and the radiative layer below the convective mantle marks the end of the TDU episode.

The series of thermal pulses stops when mass loss has eroded the mantle. Together with other parameters (see above), details of the mass-loss process influence the strength and the number of thermal pulses and the efficiency of the TDU (Straniero et al., 2006). In the modelling of the TDU, also the numerical implementation of the various stellar

evolution codes matters (see Lugaro et al., 2003, Stancliffe et al., 2005 and Stancliffe, 2006).

The chemical composition of the stellar atmosphere changes as a consequence of TDU. This is a stepwise process since during the interpulse phases, which last roughly 100 times longer than a single TP, the nuclear active region is disconnected from the mantle and thus the abundances of the elements remain unaffected there. The repeated addition of carbon and *s*-process elements to the outer stellar layers permits to interpret the spectral types of low-mass giants as a sequence. An initially oxygen-rich low-mass star has the spectral type M on the AGB. When signatures of *s*-process elements are found in the atmosphere of the star, but the C/O ratio is still lower than 1, it is classified as MS. S stars have a C/O ratio close to 1 (although there are exceptions to this rule, see Lebzelter et al., 2008a and references therein). As soon as the abundance of carbon exceeds the one of oxygen, we call the star a carbon-star which corresponds to spectral type C, or SC if we still detect *s*-process elements. A star does not necessarily run through all this stages. For example, at very low metallicities the atmosphere can become carbon-rich right after the first TDU episode (Herwig et al., 2000).

1.4.2 Extra-mixing

From observations of element and isotope abundances in red giant stars and from measurements of isotopic ratios in pre-solar grains it became evident that an additional mixing process (other than a convective one such as TDU) must be at work in the stellar interior (see Busso, 2007 and references therein). This additional process is supposed to transport matter from the convective mantle through the region that, according to the Schwarzschild criterion (Schwarzschild, 1958), is stable against convection (the *radiative layer*) to the top of the hydrogen-burning shell and back. The configuration of the corresponding zones is illustrated in Fig. 1.5. Since this mechanism cannot be described by standard convective motions, it is frequently referred to as *extra-mixing*, although several other names can be found in the literature, e. g. deep mixing, slow mixing, or cool bottom processing (Wasserburg et al., 1995).

Nollett et al. (2003) considered the effects of extra-mixing on the abundance ratios C/O and N/O, and on the isotopic ratios $^{18}\text{O}/^{16}\text{O}$, $^{17}\text{O}/^{16}\text{O}$, $^{14}\text{N}/^{15}\text{N}$, $^{26}\text{Al}/^{27}\text{Al}$, but also the $^{12}\text{C}/^{13}\text{C}$ ratio is influenced (e. g. Busso, 2007). The authors argued that two parameters are sufficient to model the mixing process. These are the mass circulation rate \dot{M} at which the matter is transported between the convective mantle and the radiative layer, and the maximum temperature T_{max} to which the circulating material is exposed. These quantities determine the amount of material being processed by partial hydrogen burning. With this parametrisation a large number of plausible $(\dot{M}, T_{\text{max}})$ combinations can be examined rapidly, which allows to explore the consequences of extra-mixing on the element abundances. Since the abundance changes due to extra-mixing do not cause significant changes in the stellar structure and evolution, a post-processing approach to

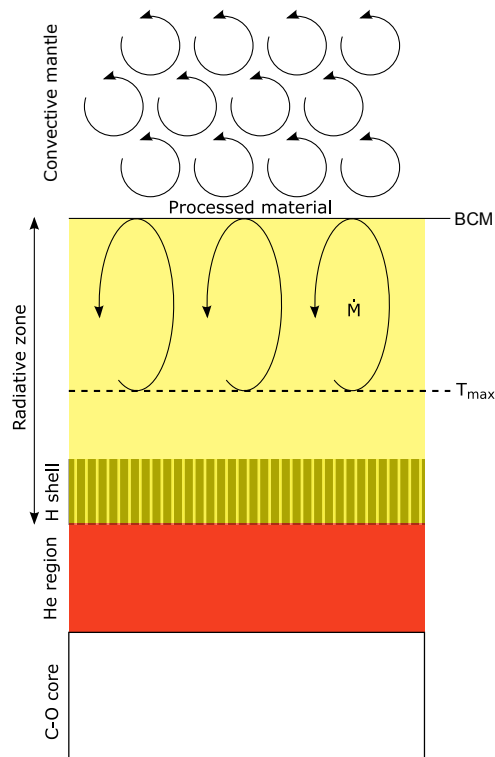


Figure 1.5 Schematic illustration of extra-mixing. The energy transport between the H-burning shell and the convective mantle takes place by means of radiation. Observations appear to imply that material from the bottom of the convective mantle (BCM) is transported to regions with a higher temperature by a non-convective mixing process. \dot{M} and T_{\max} are the decisive quantities in a parametrised approach. The physical origin of the mixing process (especially on the AGB) is still subject to discussions. Layer dimensions are not to scale. Following an idea from Nollett et al. (2003), see text for details.

assess the consequences of extra-mixing is justified (Nollett et al., 2003). The identification of the physical background of extra-mixing may lead over the depth and rate set by an individual mechanism, while the details thereof should be secondary (Nollett et al., 2003). Candidate scenarios could be put to test by means of their characteristic parameters and the (\dot{M}, T_{\max}) pairs singled out by a comparison of model calculations to observations.

To date, the occurrence of an additional mixing process is widely accepted, but the actual physical cause for extra-mixing, particularly on the AGB, is still not known. Sweigart

and Mengel (1979) were one of the first to address the question of CNO abundance anomalies in connection with meridional circulation. Shear instabilities in differentially rotating stars were considered as an option e. g. by Zahn (1992) and Maeder and Zahn (1998). However, it was shown by Palacios et al. (2006) that rotationally induced extra-mixing is not efficient enough to explain the abundance anomalies observed both in field and globular clusters stars. Eggleton et al. (2008) identified a mixing mechanism by studying three-dimensional RGB star models and emphasised that this type of mixing induced by an inversion of the mean molecular weight ($\delta\mu$ -mixing) appears compulsorily. The mechanism is mass and metallicity dependent and is a kind of thermohaline mixing (or double-diffusive mixing) that was also investigated by Stancliffe and Glebbeek (2008) and Cantiello et al. (2007) who concluded that is important throughout the whole AGB phase. Other groups invoked magnetic buoyancy to explain the occurrence of extra-mixing (Busso et al., 2007 and Nordhaus et al., 2008), while Denissenkov et al. (2008) even investigated the effects of magnetic fields in combination with thermohaline mixing. Two further examples are convective overshooting (Herwig, 2000) and internal gravity waves that besides an angular momentum transport could also account for extra-mixing in low-mass stars (Talon and Charbonnel, 2008).

The growing evidence of extra-mixing on the AGB together with the great variety of potential causes for its occurrence will drive further research on this topic.

1.5 The atmosphere

An inexact, anthropocentric definition of the atmosphere might be that it is what we see of the star. More sophisticated definitions such as the one in Habing and Olofsson (2003) include a number of restricting qualifiers and are rather lengthy. This is because the atmosphere as the blurred and dynamic interface between the stellar interior and the ISM does exhibit well-defined boundaries. The main characteristics of an AGB star atmosphere are low temperatures, densities, and gravities, the large extension, and dynamic processes such as pulsation, shock waves, dust formation, and mass loss. These properties make the modelling of cool star atmospheres a challenging task. However, the light originating from the atmosphere is our powerful diagnostic tool to study AGB stars, and therefore it is crucial to gain a thorough understanding of the physical processes in such a system. The problems related to that and possible ways to overcome them were discussed by Gustafsson (2007). Below I present some key issues of AGB star atmospheres briefly, for an extensive summary see the respective chapter in Habing and Olofsson (2003).

1.5.1 Molecules

The low temperatures in the atmosphere favour the formation of molecules, and this has important consequences for the atmospheric structure and the photometric and spectral

appearance of AGB stars (e. g. Tsuji, 1966). Compared with a single atom, a molecule possesses more internal degrees of freedom, since it can rotate and its building blocks can move relative to each other (vibration). Thus the electronic energy levels split into vibrational states and rotational states, with decreasing energy differences in the given order (see e. g. Herzberg, 1950 and Bernath, 2005 for the theory of molecular spectra). This gives rise to a huge number of transitions⁷, and the resulting large overall opacity influences the temperature–pressure structure of the atmosphere (e. g. Gustafsson et al., 2008).

The chemical composition of the medium determines which molecules are likely to form. Hereby the CO molecule with its high bond energy plays a key role. The less abundant species out of carbon and oxygen is almost completely locked up in CO molecules, while the remaining atoms of the more abundant element form other molecules (see also Sect. 3.1). This is the reason for the importance of the C/O ratio in the context of AGB stars. In an oxygen-rich regime ($C/O < 1$) molecules such as H₂O, TiO, SiO, OH, or VO have the highest partial pressures. In a carbon-rich environment ($C/O > 1$) the most abundant species are CN, CH, C₂, C₃, HCN, C₂H₂. CO is present in both cases. An overview about molecules in stellar environments was for example given by Jørgensen (1994, 1995).

The intricate energy level structure leads to a plethora of absorption lines which is typical for the spectra of late-type stars. Each molecule leaves its characteristic imprint in the spectral energy distribution due to a combination of rotation, vibration, and electronic transitions. The set of possible rotation transitions for a given vibration transition causes the occurrence of so-called *rotation–vibration bands* in the spectra of cool stars. Figure 1.6 shows three rotation–vibration bands resulting from second overtone transitions of the CO molecule at different resolutions. While the band structure is easy to spot in theoretical calculations that solely take into account data for CO, synthetic spectra based on a full data set illustrate the difficulties that may arise in the determination of element abundances from real spectra (cf. Gray, 1992 for a general introduction). In general, the many overlapping lines hamper a sound analysis. Beside the difficulty of dealing with line blends, especially the many weak lines of polyatomic molecules such as H₂O, HCN, C₂H₂, and C₃ make it difficult to identify the level of continuum absorption in observed spectra, even in those with a comparably high-resolution ($R \geq 50,000$). I will come back to these problems in Sect. 2.3.3.

1.5.2 Dynamical phenomena and dust

Depending on their evolutionary stage, low-mass giants exhibit various degrees of variability. AGB stars belong to the class of long period variables (LPV). Based on the periodicity and amplitude of the light curve, LPV are subdivided into Mira stars, semi-regular

⁷ For example, the line list of the water molecule from Barber et al. (2006) comprises over 500 million transitions.

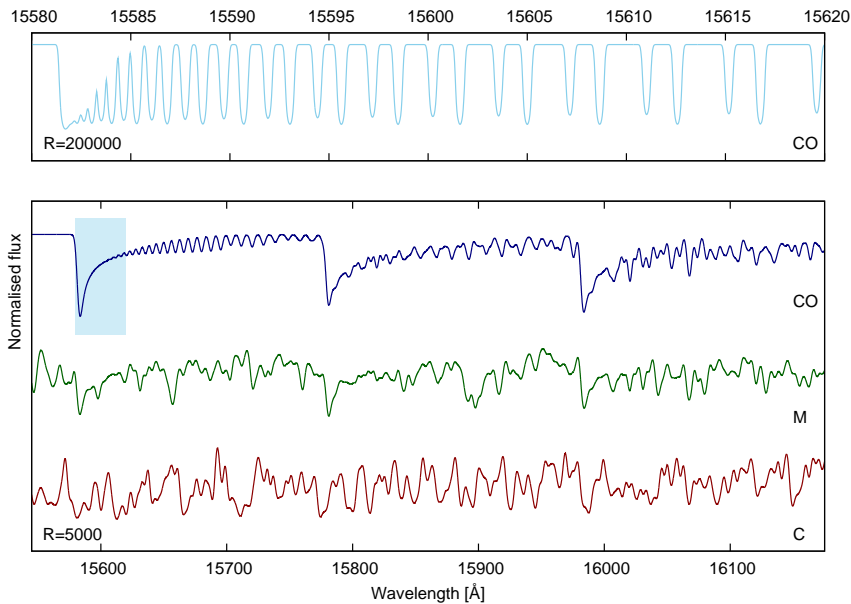


Figure 1.6 Sample spectra showing molecular bands of CO. See text for details. Top panel: High-resolution spectrum ($R = 200,000$) of the CO 3-0 band (no other line sources were included in the calculation). Bottom panel: A wider wavelength region at lower resolution ($R = 5000$) covering the CO 3-0, 4-1, and 5-2 second overtone transitions ($\Delta\nu = 3$) is shown. The shaded area indicates the wavelength range shown in the top panel. The topmost spectrum in the bottom panels again shows lines from CO only. Below spectra with a full line data set are displayed for both an oxygen-rich ($C/O = 0.48$) and a carbon-rich ($C/O = 1.40$) chemistry. The remaining model parameters are $T_{\text{eff}} = 2800$ K, $\log(g[\text{cm s}^{-2}]) = 0.0$, $M = 1 M_{\odot}$, $\xi = 2.5 \text{ km s}^{-1}$, and $Z = Z_{\odot}$.

variables (SRV), and irregular variables (Lb). The distinction between the classes SRV and Lb is purely phenomenological and may be due to sparse light-curve data (Lebzelter and Obbrugger, 2009).

Hydrostatic models calculated for example with the MARCS code (Gustafsson et al., 2008, the models are explicated in Sect. 2.3.2) are appropriate to describe the atmospheres of AGB stars only before they undergo large amplitude radial pulsations. These are excited by means of the so-called κ -mechanism resulting from a recurring ionisation and recombination of H and He atoms in the lowest atmospheric layers and in the convective mantle (Fox and Wood, 1982 and Gautschy and Saio, 1995). In this situation the atmosphere becomes a highly dynamic system. The pulsations levitate the atmospheric layers and generate shock waves that run outwards through the atmosphere. These locally heat and compress the gas, causing the formation of emission line spectra. The high densities and low temperatures in the medium behind a shock wave allow for the formation of dust grains. The dust species formed depend on the chemistry. In the oxygen-rich case,

mostly silicates and aluminium-rich oxides are created, while around a carbon star the dust consists of silicon carbide (SiC) and amorphous carbon. The dust grains interact with the radiation field from the star and are in this way accelerated, dragging along the gas through dynamic coupling. What has been described here in a nutshell is the scenario of a pulsation-enhanced dust-driven wind introduced by Höfner et al. (2003) and Höfner (2008). The mass loss induced by such a stellar wind with terminal velocities of about $10\text{-}20\text{ km s}^{-1}$ amounts to $10^{-7}\text{-}10^{-4}\dot{M}_{\odot}\text{ a}^{-1}$, which efficiently depletes the total mass of the star and thus eventually terminates the AGB phase.

1.5.3 Beyond the atmosphere

The matter transported away from the AGB star, i. e. the gas and the dust particles in the stellar wind, forms the circumstellar envelope (CSE). The ejecta are diluted and at large distances from the star both the density and the temperature decrease to the levels that prevail in the ISM. Thermal emission from CO, SiO, and other molecules (e. g. Olofsson et al., 1998) as well as maser emission mostly from SiO, H₂O, and OH (e. g. Soria-Ruiz et al., 2007) are diagnostic tools for the investigation of the CSE. After a *superwind* phase (see e. g. Lagadec and Zijlstra, 2008) the CSE can become optically thick. In this case one can detect the enshrouded objects in the infrared wavelength region only. Such objects are called either *OH/IR stars* since they often show OH maser emission, too (e. g. Habing, 1993), or obscured carbon stars when the envelope is carbon-rich (e. g. Menut et al., 2007).

1.6 Thesis outline

With the help of a homogeneous sample of stars, e. g. assembled from objects within the same globular cluster, it is possible to derive constraints for AGB star models, in particular with respect to the onset and efficiency of the TDU and the occurrence of extra-mixing. This can be achieved by measuring abundances and isotopic ratios in the atmosphere and setting the outcomes in relation to the evolutionary stage of the star. An advantage of the cluster-star approach is that the mass dependence of the phenomena of interest can be investigated accurately, since this stellar parameter is well-defined for those targets. The methods and results of this approach are presented in Chap. 2. Chapter 3 deals with a new set of low-temperature Rosseland opacity coefficients. These are an important ingredient for evolution models of low-mass stars, and they lead to quantitative changes of the model predictions, which are then in better agreement with observations. In Chap. 4 I summarise the work, give a few application examples for the Rosseland opacities, and try to motivate future research on the basis of the results of this thesis.

2 Third dredge-up in LMC cluster stars

This chapter is based on the following publications.

- Lebzelter, T., Lederer, M. T., Cristallo, S., Hinkle, K. H., Straniero, O. and Aringer, B. 2008a, *A&A*, 486, 511-521
- Lederer, M. T., Lebzelter, T., Cristallo, S., Straniero, O., Hinkle, K. H. and Aringer, B. 2009. The puzzling dredge-up pattern in NGC 1978. *A&A*, submitted.

2.1 Introduction

Modelling the final phases in the evolution of a low-mass star is a demanding task. The stellar interior is a site of rich nucleosynthesis (see Sect. 1.3 for a discussion of hydrogen burning, helium burning, and the *s*-process), particularly when the star evolves on the AGB. The freshly synthesised elements are carried to the outer layers of the star by means of the third dredge-up (TDU, see Sect. 1.4.1). The onset and efficiency of this mixing mechanism depends on the mass and the metallicity of the star (e. g. Iben and Renzini, 1983 and Straniero et al., 2003). Various stellar evolution models developed in the recent past (e. g. Straniero et al., 1997b, 2006, Herwig, 2000, Stancliffe et al., 2004 and Karakas and Lattanzio, 2007) agree on the theoretical picture of the TDU, but details are still subject to discussions. It is thus important to test the models against observations and to derive constraints to improve our understanding of the involved phenomena and related problems. Quantitative checks of the model predictions for third dredge-up efficiency have been so far restricted to AGB stars in the solar neighbourhood (e. g. Busso et al., 2001 and Lebzelter and Hron, 2003) or to indirect methods like the study of the progeny of AGB stars or synthetic stellar evolution (e. g. Marigo et al., 1999 and Van Eck et al., 2001). However, for studying ongoing nucleosynthesis and the third dredge-up itself, observations of AGB stars are needed. AGB stars are tracers of intermediate-age stellar populations, which can only be modelled accurately when the evolution of the constituents is known. Moreover, evolved low-mass stars undergo strong mass loss in the late stages of their evolution. They enrich the interstellar medium (ISM) with the products of nuclear burning and thus, as they are large in number, play a significant role in the cosmic matter cycle.

The primary indicator of TDU is a carbon surface enhancement. An originally oxygen-rich star can be transformed into a carbon star by an efficient dredge-up of ^{12}C to the surface. The criterion to distinguish between an oxygen-rich and a carbon-rich chemistry is the number ratio of carbon to oxygen atoms, C/O . During the thermally pulsing (TP) AGB phase, while the C/O ratio is constantly rising as a consequence of the TDU, there are mechanisms that may counteract the increase in the carbon isotopic ratio $^{12}\text{C}/^{13}\text{C}$.

It is suspected that the radiative gap between the convective envelope and the hydrogen burning shell can be bridged by a slow mixing mechanism (see Sect. 1.4.2). In this way, ^{12}C and isotopes of other elements are fed back to nuclear processing. The physical origin of this phenomenon is still not known, which is another argument to establish observational data in order to benchmark theoretical predictions.

Measurements of the carbon abundance and the carbon isotopic ratio have been done for a few bright field AGB stars (Lambert et al., 1986, Harris et al., 1987 and Smith and Lambert, 1990). The direct comparison of the values inferred from field star observations (the values for C/O range between 0.25 and 1.6, see Fig. 9 of Smith and Lambert, 1990) to evolutionary models is complicated by the fact that luminosity and mass of those targets can be determined only inaccurately, while both quantities are crucial input parameters for the models. A strategy to circumvent this problem is to observe AGB stars in globular clusters. They provide a rather homogeneous sample with respect to distance, age, mass, and metallicity. Admittedly, this simplistic picture is slowly disintegrating. There is evidence that globular clusters often harbour more than one population with abundance variations among the constituents (Mackey and Broby Nielsen, 2007, Piotto et al., 2007 and Renzini, 2008). The parameters like mass and metallicity are, however, still much better constrained than for field stars, thus it is possible to determine their evolutionary status and the mass of cluster AGB stars more accurately. This provides an important advantage for the comparison of observations with models of stellar atmospheres and evolution. For our purpose, i. e. investigating the abundance variations due to the TDU, the old Milky Way clusters are not well suited. The AGB stars of the current generation have an envelope mass too low for TDU to occur, while more massive stars have evolved beyond the AGB phase. The intermediate-age globular clusters in the LMC with stars in the mass range from 1.5 to $2 M_{\odot}$ (e. g. Girardi et al., 1995) serve our needs better.

In this chapter, we pursue this idea and study the AGB stars in the LMC globular clusters NGC 1846 and NGC 1978, and derive C/O and $^{12}\text{C}/^{13}\text{C}$ ratios. We give an overview of previous studies of these clusters and our observations in Sect. 2.2. Details about the data analysis are given in Sect. 2.3. The results follow in Sect. 2.4. We discuss our findings in Sect. 2.5, giving scenarios on how to interpret the measurements in NGC 1846 and, particularly, the puzzling case of NGC 1978 before we conclude in Sect. 2.6.

2.2 Observations

2.2.1 Targets

The target clusters NGC 1846 and NGC 1978 are both members of the intermediate-age ($\tau = 1 - 3$ Gyr) cluster population (Girardi et al., 1995) in the LMC. The following sections summarise studies of these clusters found in the literature.

2.2.1.1 NGC 1846

According to a recent investigation carried out by Grocholski et al. (2006), the cluster NGC 1846 has a metallicity of $[\text{Fe}/\text{H}] = -0.49 \pm 0.03$. Values given in older papers considerably disagree. Lebzelter and Wood (2007) summarised the literature and report a grouping around two different values of $[\text{Fe}/\text{H}]$. Some authors specified a metallicity around -1.5 (Dottori et al., 1983 and Leonardi and Rose, 2003), while others quoted values of about -0.7 (Bessell et al., 1983, Bica et al., 1986, Olszewski et al., 1991 and Beasley et al., 2002). The earliest determination of the metallicity of NGC 1846 was done by Cohen (1982), she derived a value of $[\text{Fe}/\text{H}] = -1.1$, which lies in-between the two groups outlined above.

Lebzelter and Wood (2007) performed a variability analysis of stars on the AGB in NGC 1846 and determined their mass to be close to $1.8 M_{\odot}$ resulting in a cluster age of 1.4×10^9 years. These values are about consistent with the results from Mackey and Broby Nielsen (2007) who presented a range of possible cluster ages from 1.5 to 2.5×10^9 years and masses on the AGB between 1.3 and $1.8 M_{\odot}$. Other age determinations for NGC 1846 have been done by Frantsman (1988, 1.0×10^9 a) and Bica et al. (1986, 4.3×10^9 a). The distance modulus of NGC 1846 is $(m - M)_0 = 18.13$ (Grocholski et al., 2007), and van den Bergh (2008) lists a cluster ellipticity of $\epsilon = 0.24^8$.

A number of AGB stars have been identified by Lloyd Evans (1980), and we use his naming convention (i. e. stars from this work are tagged LE) throughout this chapter. Near-infrared measurements and estimates of the bolometric magnitudes of the AGB stars have been presented by Frogel et al. (1990) and references therein. The carbon stars in the cluster indicate the possible occurrence of TDU in these objects. No stars with a high mid-infrared excess, an indicator of a very high mass loss rate, have been found (Tanabé et al., 1998 and Lebzelter and Wood, 2007).

The cluster velocity has been determined by various authors in the past. Schommer et al. (1992) reported a cluster velocity of $\langle v_r \rangle = +240 \text{ km s}^{-1}$ derived from measurements of two individual stars ($+231$ and $+248 \text{ km s}^{-1}$, respectively). This value coincides with the result by Freeman et al. (1983) and is in good agreement with the most recent study of individual stars in this cluster by Grocholski et al. (2006), who find a mean velocity of $+235.2 \text{ km s}^{-1}$ with a velocity dispersion $\sigma_v = 0.9 \text{ km s}^{-1}$ from 17 cluster members.

2.2.1.2 NGC 1978

The intermediate-age cluster population in the LMC corresponds to one of the two peaks in the LMC metallicity distribution at $[\text{Fe}/\text{H}] = -0.37$ (with a spread of $\sigma = 0.15$) reported

⁸ The flattening of a globular cluster is defined as $\epsilon \equiv (a - b)/a$, where a is the major axis and b is the minor axis of the cluster.

by Cole et al. (2005). In a recent work, Mucciarelli et al. (2007a) indeed derived a metallicity of $[M/H] = -0.37$ for NGC 1978. This result is based on the findings from Ferraro et al. (2006), who claimed $[Fe/H] = -0.38 \pm 0.02$ and that $[\alpha/H]$ is almost solar. In contrast to that, Hill et al. (2000) quoted a grossly deviating value of $[Fe/H] = -0.96 \pm 0.20$. They investigated two stars from this cluster (LE8 and LE9, see also Sects. 2.3 and 2.4.2) and concluded that $[O/Fe] = +0.37 \pm 0.10$. These findings have not been reproduced by other groups. Mucciarelli et al. (2008a) rather found a mild depletion in alpha elements on average and ascribe the differences to Hill et al. (2000) to the deviating metallicity. Mucciarelli et al. (2008a), who performed detailed abundance studies of red giants with UVES spectra, also did not confirm the results of Alcaíno et al. (1999), who concluded from multicolour CCD photometry that NGC 1978 consists of two sub-populations differing by 0.2 dex in metallicity. According to their work, the north-western half of the cluster is more metal-rich and younger than the south-eastern half (plus differences of the sub-populations in the helium content). This result has to be seen in conjunction with a peculiarity of the cluster, namely its high ellipticity of $\epsilon = 0.30$ which has been found independently by various groups and was most recently confirmed by Mucciarelli et al. (2007a). A merger event that could explain both the elongated shape and the suspected two sub-populations was, however, ruled out for example by Fischer et al. (1992). A tidal interaction with the host galaxy seems to be a more likely explanation for the high ellipticity (van den Bergh, 2008 and references therein).

Mucciarelli et al. (2007a) derived the cluster age, distance modulus, and turn-off mass by fitting isochrones to the cluster colour-magnitude diagram (CMD). The resulting values are $\tau = 1.9 \pm 0.1$ Gyr, $(m - M)_0 = 18.50$ and $M_{TO} = 1.49 M_{\odot}$, respectively, for the best fit found when using isochrones from the *Pisa Evolutionary Library* (PEL, Castellani et al., 2003). When adopting other isochrones with different overshooting prescriptions, the parameters vary so that one could also derive a somewhat lower turn-off mass ($M_{TO} = 1.44 M_{\odot}$), a lower distance modulus ($(m - M)_0 = 18.38$), and a cluster age from 1.7 to 3.2 Gyr.

The various radial velocity measurements quoted in the literature do widely agree within the error bars, e.g. Olszewski et al. (1991) and Schommer et al. (1992) derived $\langle v_r \rangle = +292 \pm 1.4 \text{ km s}^{-1}$ whereas Ferraro et al. (2006) determined a mean heliocentric velocity of NGC 1978 of $\langle v_r \rangle = +293.1 \pm 0.9 \text{ km s}^{-1}$ and with a velocity dispersion $\sigma_v = 3.1 \text{ km s}^{-1}$.

NGC 1978 harbours a number of red giant stars (Lloyd Evans, 1980) some of which are known to be carbon stars (Frogel et al., 1990). The easiest explanation for such an occurrence is that these C stars are AGB stars undergoing the third dredge-up or, alternatively, that they underwent mass accretion from an old AGB companion, which subsequently evolved into a white dwarf. The results of our analysis of the NGC 1978 targets motivate to discuss more exotic explanations in Sect. 2.5.2.3.

2.2.2 Spectroscopy

The data that we present here were obtained with the Phoenix spectrograph mounted at the Gemini South telescope (Hinkle et al., 1998, 2003). The observing programmes required observations at two different wavelengths, one in the H band and one in the K band. For this purpose, we utilised the Phoenix order sorting filters H6420 and K4220.⁹ The slit width was set to $0''.35$ (the widest slit) which resulted in a spectral resolution of $R = \lambda/\Delta\lambda = 50\,000$. For each target we observed at two or three different positions along the slit to allow for background subtraction. Each night, we also recorded a spectrum of a hot star without intrinsic lines in the respective wavelength regions in order to correct the spectra of our programme stars for telluric lines.

2.2.2.1 NGC 1846

High-resolution, near-infrared spectra of 12 AGB stars in NGC 1846 from the list of Lloyd Evans (1980) were obtained during six half-nights in December 2005. The distribution of the targets within the cluster is illustrated in Fig. 2.1. We observed all 12 targets in the K band between 23620 and 23700 Å. For 10 of them, spectra were also taken in the H band between 15540 and 15587 Å. For most of the targets, the resulting signal-to-noise (S/N) ratio was 65 or better. The total integration times ranged between 45 and 90 minutes per target and wavelength range.

2.2.2.2 NGC 1978

In 2006 we recorded high-resolution, near-infrared spectra of 12 AGB stars in NGC 1978. Ten stars from our target list were already identified by Lloyd Evans (1980) as red stars but largely without information about the spectral type. Frogel et al. (1990) listed a number of AGB stars in NGC 1978, comprising also the stars from LE, and gave information about the spectral type, the cluster membership, and near-infrared photometry data. Based on this information, we selected 10 targets that could be observed with the Phoenix spectrograph using reasonable exposure times. Additionally, we constructed a colour-magnitude diagram from Two Micron All Sky Survey (2MASS, Skrutskie et al., 2006) data and picked 2 more stars that, judging from their K magnitude and $(J - K)$ colour index, are also located on the AGB of NGC 1978. Details about the stars A and B are given in Table 2.1. The distribution of all the targets within the cluster is illustrated in Fig. 2.2.

⁹ The filter H6240 allows to record a certain wavelength range that falls within $15\,470\text{ Å} \approx 6464\text{ cm}^{-1}$ and $15\,680\text{ Å} \approx 6377\text{ cm}^{-1}$. The corresponding range for the filter K4220 runs from $23\,480\text{ Å} \approx 4263\text{ cm}^{-1}$ to $23\,920\text{ Å} \approx 4188\text{ cm}^{-1}$.

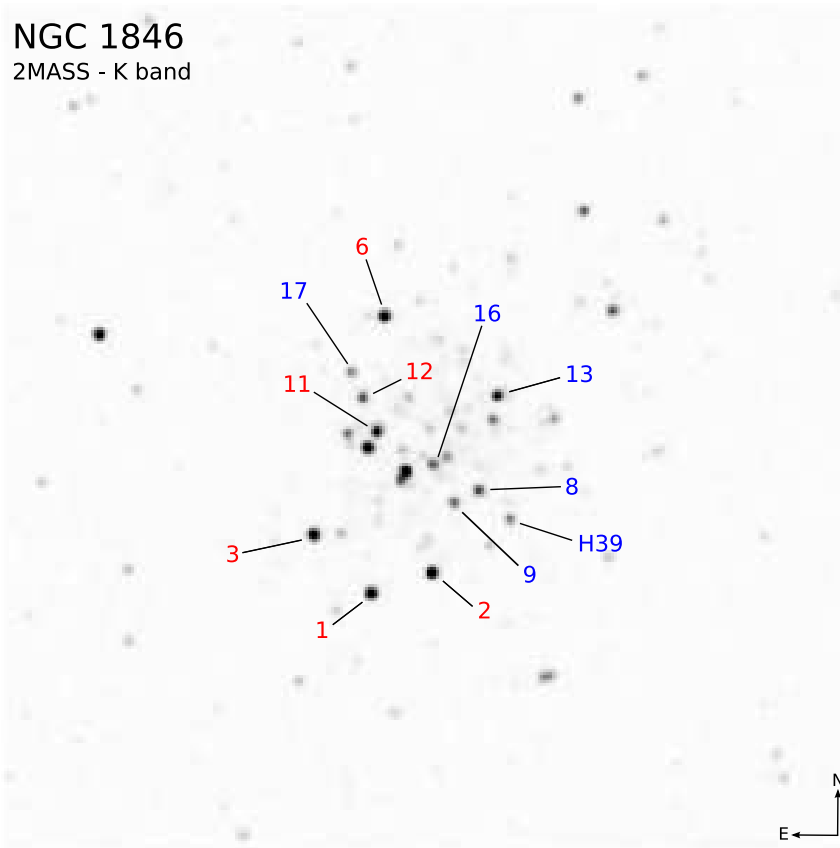


Figure 2.1 Distribution of observed targets in the cluster NGC 1846. The picture was acquired from the 2MASS catalogue using Aladin (Bonnarel et al., 2000). The identifiers refer to the nomenclature of Lloyd Evans (1980). The additional target H39 was selected from the paper of Hodge (1960). The stars 8, 9, 13, 16, 17, and H39 possess an oxygen-rich atmosphere (blue labels), while 1, 2, 3, 6, 11, and 12 are carbon stars (red labels). Compare also Fig. 2.2. The displayed sky region is about $5'.0 \times 5'.0$ wide.

Bad weather conditions in the last of the 4 observing nights in December 2006 prohibited to record H-band spectra for the targets LE2 and LE7. For the star LE9, we obtained spectra from queue mode observations in the semester 2008A. The wavelength settings are similar to the ones described above (Sect. 2.2.2.1), i. e. in the K band our spectra run approximately from 23 580 to 23 680 Å. In the H band (15 530 – 15 600 Å), the spectral region observed was shifted to slightly higher wavelengths compared with NGC 1846 to cover a larger part of the CO 3-0 band head at 15 581.6 Å = 6417.8 cm⁻¹.

The total integration time per target ranged between 20 (LE3) and 120 (LE9) minutes. The resulting S/N ranged from 50 to above 100 per resolution element.

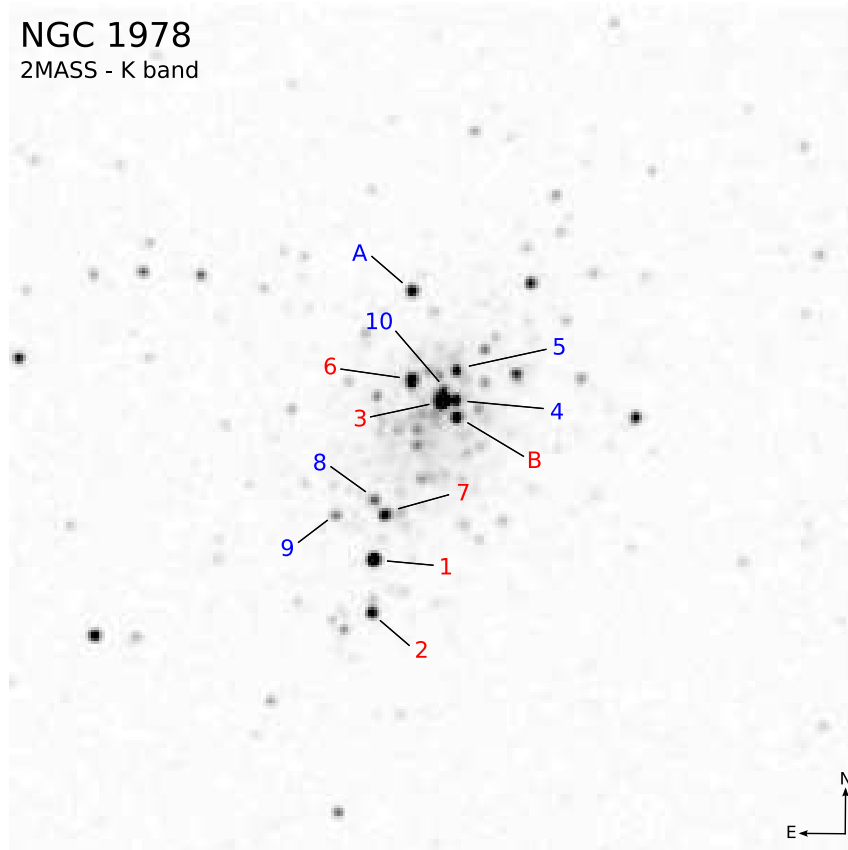


Figure 2.2 Distribution of observed targets in the cluster NGC 1978. Compare also Fig. 2.1. The additional targets A and B (see Table 2.1) were chosen according to their position in the 2MASS colour-magnitude diagram. The stars A, 4, 5, 8, 9, and 10 possess an oxygen-rich atmosphere (blue labels), while B, 1, 2, 3, 6, and 7 are carbon stars (red labels). The cluster is elongated and its major axis stretches roughly from south-east to north-west. The displayed sky region is about $5'.0 \times 5'.0$ wide.

ID	Type	<i>K</i>	<i>J</i> − <i>K</i>	RA	Dec
		2MASS			
A	M	11.116	1.137	05 28 46.43	−66 13 24.80
B	C	11.078	1.289	05 28 43.65	−66 14 09.70

Table 2.1 NGC 1978 additional targets beyond LE.

2.2.3 Data reduction

The data reduction procedure was carried out as described at length for example in Smith et al. (2002) and in the Phoenix data reduction IRAF tutorial¹⁰.

To correct the AGB star spectra for telluric lines, we acquired the spectrum of an early-type star without intrinsic lines. The telluric absorption features were removed using the IRAF task `telluric` in the K band. The H-band spectra are almost free of telluric lines. To allow for a better comparison with synthetic spectra, they were, however, also processed in the same way to remove the fringing.

In the H band, we did the wavelength calibration using a K-type radial velocity standard (HD5457, $v_r = 5.1 \text{ km s}^{-1}$, Wilson, 1953) recorded alongside with the programme stars. Using the Arcturus atlas from Hinkle et al. (1995), we identified several features (OH, Fe, Ti, and Si lines) in the spectrum and derived a dispersion solution. The relation was then applied to the remaining spectra. This procedure allowed us to derive radial velocities from the H-band spectra.

For NGC 1846, the wavelength calibration in the K band was done using the telluric lines of the early-type star. In the case of NGC 1978, we did a direct calibration using the CO lines in the spectrum of an M-type target. The dispersion solutions were then also applied to the carbon star spectra.

2.3 Data analysis

2.3.1 Contents of the observed wavelength ranges

The wavelength ranges were chosen such that from the H-band spectra we could derive the stellar parameters and the C/O ratio. Subsequently, we inferred the carbon isotopic ratio $^{12}\text{C}/^{13}\text{C}$ from the K band. In practice, the parameters are tuned iteratively. The region in the H band is widely used in the literature (e. g. Smith et al., 2002, McSaveney et al., 2007 and Yong et al., 2008) to derive oxygen abundances from the contained OH lines. From the relative change of those features in comparison to the band head from the $^{12}\text{C}^{16}\text{O}$ 3-0 vibration transition, it is possible to determine the C/O ratio in the stellar atmosphere. A weak CN line and a few metal lines (Fe, Ti, Si) aid in the pinning down of the parameters, especially the effective temperature.

The K-band spectra comprise a number of CO lines from first overtone ($\Delta v = 2$) transitions. Beside features from the main isotopomer $^{12}\text{C}^{16}\text{O}$, we also find some $^{13}\text{C}^{16}\text{O}$

¹⁰ Available at <http://www.noao.edu/usgp/phoenix/>. IRAF is distributed by the National Optical Astronomy Observatories, which are operated by the Association of Universities for Research in Astronomy, Inc., under cooperative agreement with the National Science Foundation.

lines in this region. We derived the carbon isotopic ratio by fitting these lines. Apart from the CO lines, there is also a single HF line blended with a ^{13}CO feature.

In Figs. 2.3 and 2.4, we give an overview about our observations. For the oxygen-rich stars, the key features in the H band are marked. In the K band, we indicate the position of the ^{13}CO lines. Moreover, we identify four low-excitation ^{12}CO 2-0 lines. According to Hinkle et al. (1982), low-excitation lines include contributions from the outer atmospheric layers, opposite to high-excitation lines that show characteristics similar to second overtone transitions ($\Delta\nu = 3$). In all the carbon star spectra and for the most luminous oxygen-rich objects, these lines could not be fitted with our synthetic spectra. The calculations underestimate the line strength, suggesting that the extended atmospheres of luminous carbon stars are not well reproduced by our hydrostatic models.

The selection of the wavelength ranges was driven by the oxygen-rich case. From Figs. 2.3 and 2.4 it is obvious that the regions are not well suited for the analysis of carbon star spectra. Both H- and K-band spectra are crowded with features from the CN and C_2 molecules, occurring in addition to the CO lines. The polyatomic molecules C_2H_2 , HCN, and also C_3 contribute to the opacity by means of many weak lines that form a pseudo-continuum (see Sect. 2.3.3). The major part is due to C_2H_2 absorption that increases with decreasing effective temperature. In the H band, the CO band head is strongly affected by neighbouring features. Generally speaking, there is not a single unblended line in the carbon-rich case. The situation in the K band, however, is not that bad. The ^{12}CO lines are still visible, although blended with CN features, but there are only a few C_2 lines. The pseudo-continuum is essentially all due to C_2H_2 , contributions from other molecules are negligible.

2.3.2 Synthetic spectra

We compare our observations with synthetic spectra based on model atmospheres that were calculated with the COMARCS code (details will be given in a forthcoming paper by Aringer et al., 2009). COMARCS is a modified version of the MARCS code (originating from Gustafsson et al., 1975 and Jørgensen et al., 1992, and recently extensively described by Gustafsson et al., 2008). For the analysis of the clusters NGC 1846 and NGC 1978 we calculated more than 1900 atmospheric models. In the model calculations, we deduced the temperature and, accordingly, pressure stratification assuming a spherical configuration in hydrostatic and local thermodynamic equilibrium (LTE). Possible deviations from LTE have a smaller influence on the abundance determination than large deviations from the hydrostatic equilibrium (see for example Johnson, 1994 for a discussion of non-LTE effects in cool star atmospheres). For the stars in our sample, which show only a small variability, we thus expect that hydrostatic models with the assumption of LTE are a reasonable approximation. In the evaluation of the chemical equilibrium, which is a consequence of LTE, we take all relevant opacity sources into account, both in model calculation and spectral synthesis. In the oxygen-rich case H_2O , TiO , CO , and

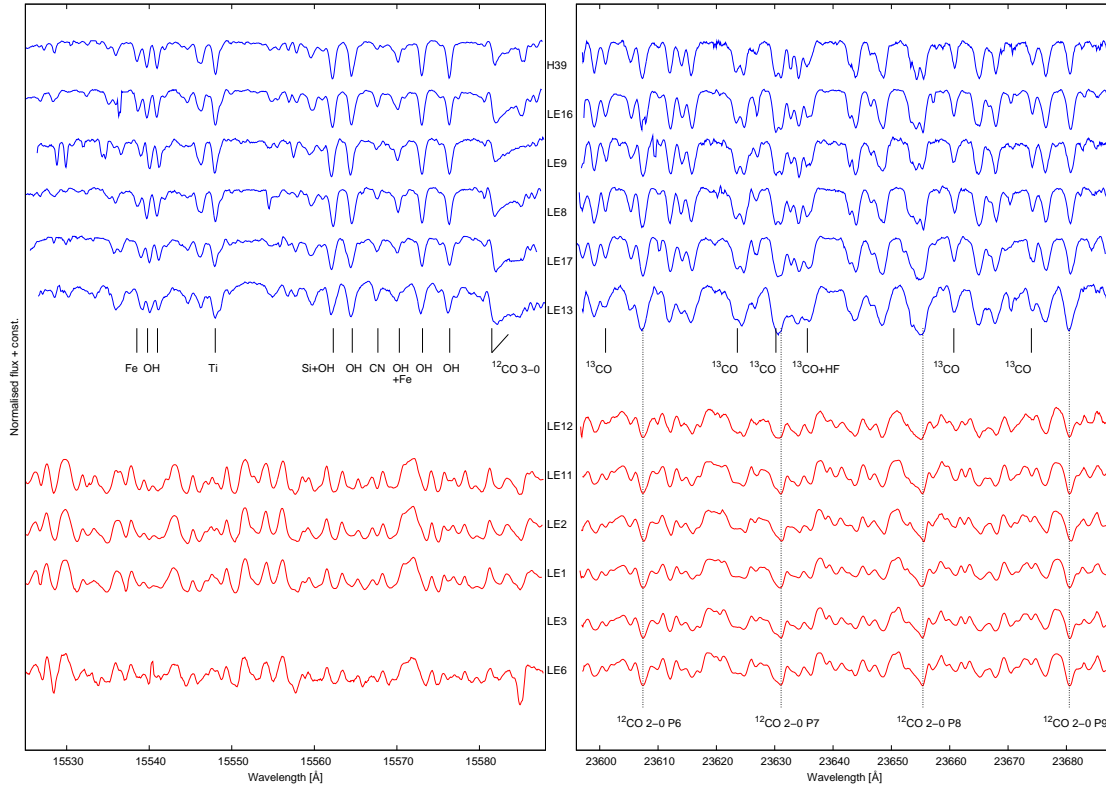


Figure 2.3 Overview about observations of NGC 1846 targets. H-band spectra are shown on the left side, K-band spectra on the right. The spectra are ordered by increasing infrared colour $(J - K)_{2MASS}$ (from top to bottom), respectively. Some features are identified for the oxygen-rich targets (top), for the carbon star spectra we only indicate the position of the low excitation CO lines. The H-band spectra for the targets LE1 and LE11 could not be obtained due to the limited observing time. Note the appearance of the CO band head in the H-band spectra of the oxygen-rich stars (compare also to Fig. 2.4). See text for details.

CN are major opacity contributors, while HCN, C_2H_2 , C_2 (and others) are important in the carbon-rich case. The opacity coefficients utilised by COMARCS were pre-calculated with the COMA code (Aringer, 2000 and Aringer et al., 2009). For each combination of microturbulence and chemical abundances we generated tables with coefficients for a two-dimensional spline interpolation. The applied method is an algorithm developed by Hardy (1971) with the implementation found in the book of Späth (1991). Details about the method are given in appendix A. The interpolation is performed on a grid of temperature and pressure values at 5364 wavelength points. The wavelength grid is the same as the one used by Aringer et al. (1997).

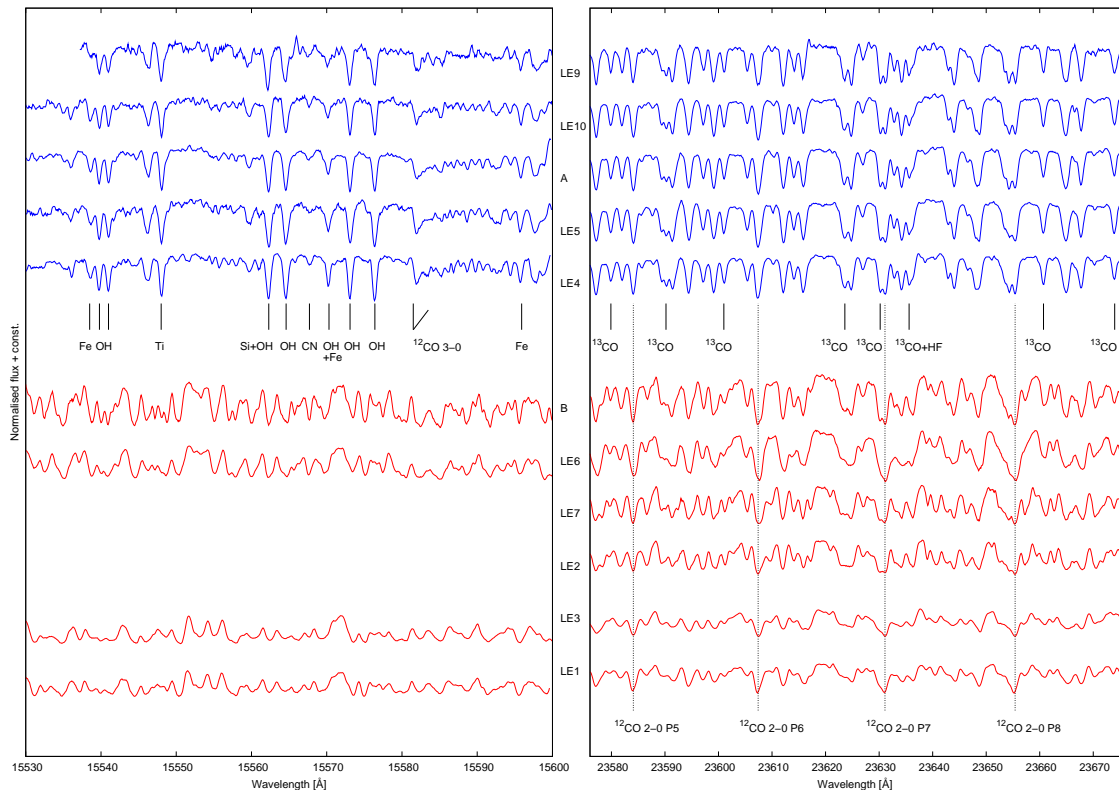


Figure 2.4 Overview about observations of NGC 1978 targets. H-band spectra are shown on the left side, K-band spectra on the right. The spectra are ordered by increasing infrared colour $(J - K)_{2\text{MASS}}$ (from top to bottom), respectively. Some features are identified for the oxygen-rich targets (top), for the carbon star spectra we only indicate the position of the low excitation CO lines. Data of the target LE8 are not shown as they are of poor quality and we did not derive abundances from them. H-band spectra for the targets LE2 and LE7 could not be taken due to bad weather conditions. See text for details.

In the discussion of model atmosphere calculations and spectral synthesis, the question of consistency is stressed frequently. The ideal case is achieved when both model atmosphere and spectrum computations are based upon the same physical principles formulated in the same geometry using the same approximations, methods, and sets of input data. The only difference should actually be the spectral resolution (Höfner et al., 2005). In practice, however, some aspects (such as lines which do not influence the overall atmospheric structure) are omitted in model atmosphere computations for the sake of simplicity. We want to point out that we calculated the model structure and the synthetic spectra in a fully consistent way with respect to spherical geometry and the atomic and molecular input data. Nevertheless, it is important to have a look at the consequences

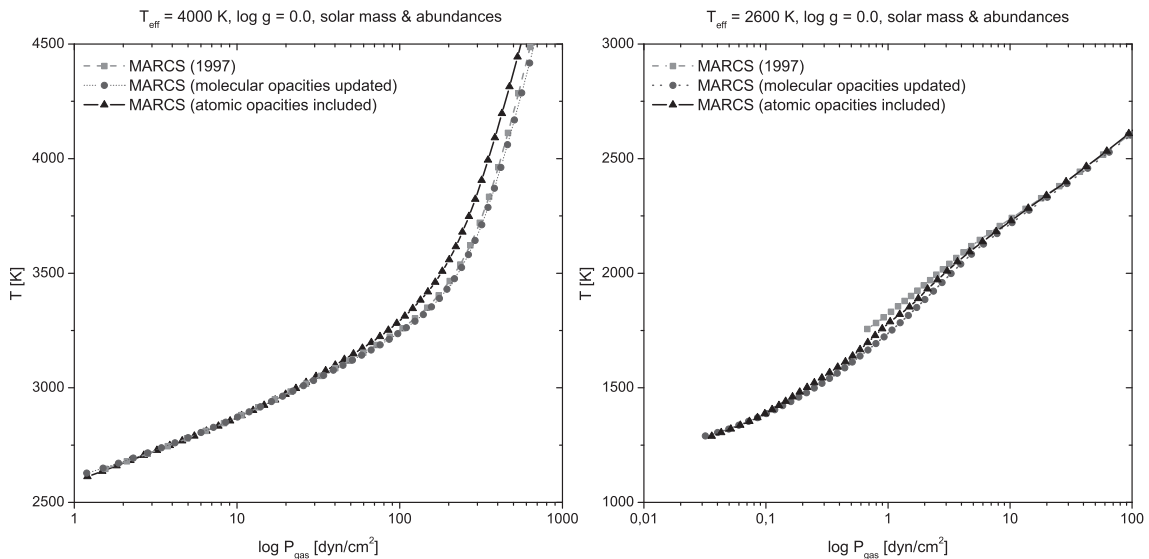


Figure 2.5 Changes in the atmospheric structure due to changed opacity data. The left panel shows a model with $T_{\text{eff}} = 4000$ K, whereas in the right panel $T_{\text{eff}} = 2600$ K. Squares indicate depth points of a MARCS model in the version of Aringer et al. (1997). Circles belong to a model with updated opacities in the far-infrared range. This affects especially cool models that now can be extended to lower optical depths (right panel). The inclusion of atomic opacities (triangles) has the most pronounced effects on the inner region of models with a higher effective temperature (left panel). From Lederer et al. (2006).

arising from inconsistencies. Examples can be found in Aringer (2005), who showed the effect of an inconsistent treatment of sphericity, and in Uttenhaller et al. (2004), where the consequences of a different metallicity in model atmosphere and spectral synthesis calculations are demonstrated.

For this thesis, efforts were made to improve consistency issues. Figure 2.5 illustrates improvements made to MARCS models compared to the version of Aringer et al. (1997). In a first step, opacity data had to be revised in order to overcome difficulties due to a considerably underestimated absorption at wavelengths longward of $12.5 \mu\text{m}$. Furthermore, atomic opacities as well as opacities for VO and OH have been included into model atmosphere computations. The atomic line data were taken from VALD (Kupka et al., 2000), an overview of the molecular line lists used with all the sources documented can be found in Sect. 3.3. Model atmospheres and synthetic spectra that were calculated following the method outlined above have been shown to describe the spectra of cool giant stars appropriately (e. g. Loidl et al., 2001 and Aringer et al., 2002).

From the parameters that determine an atmospheric model, we held the mass and the metallicity constant. The respective values $M = 1.5 M_{\odot}$ and $[M/H] = -0.4$ are

applicable for both clusters and were taken from the literature (see Sect. 2.2.1). In the model calculations, the microturbulent velocity was set to $\xi = 2.5 \text{ km s}^{-1}$, which is in the range that is found for atmospheres of low-mass giants (e.g. Aringer et al., 2002, Smith et al., 2002 and Gautschy-Loidl et al., 2004). Only for the model atmosphere of the star LE13 in NGC 1846 we adopted a value of $\xi = 3.5 \text{ km s}^{-1}$ (cf. also the following sections).

By varying the remaining parameters effective temperature T_{eff} [K], logarithm of the surface gravity $\log(g[\text{cm s}^{-2}])$, and carbon-to-oxygen ratio (C/O), we constructed a grid of model atmospheres and spectra. This was done such that we cover the T_{eff} and $\log g$ range resulting from colour-temperature relations and bolometric corrections applied to our sample stars. The step size in effective temperature was set to 50 K, whilst the surface gravity was altered in steps of 0.25 on a logarithmic scale, i. e. for $\log g$, ranging from 0.0 to +0.5. For some carbon stars in our sample we got $\log g < 0.0$ from the colour transformations and the adopted mass. The spectral features used in the analysis show only a minor dependence on this parameter, as was verified during the analysis of the NGC 1846 data, thus we fixed $\log g = 0.0$ in the analysis of the carbon stars of NGC 1978. In this way we also avoid convergence problems for the atmospheric models.

The element composition is scaled solar (Grevesse and Noels, 1993) with a C/O ratio of 0.48. Motivated by the outcomes of our analysis of NGC 1846 (which are discussed in the forthcoming sections) and by the paper of Hill et al. (2000, see Sect. 2.2.1.2), we assumed an oxygen over-abundance of +0.2 dex for the work on NGC 1978, which was done later than the NGC 1846 investigations. We altered the C/O ratio in steps of 0.05 in the oxygen-rich case and 0.10 in the carbon-rich case. This was done by changing the carbon abundance while leaving the other abundances untouched.

The synthetic spectra cover a wavelength range of $6400 - 6450 \text{ cm}^{-1}$ ($15\,504 - 15\,625 \text{ \AA}$) in the H band and of $4215 - 4255 \text{ cm}^{-1}$ ($23\,500 - 23\,725 \text{ \AA}$)¹¹ in the K band. The spectra were first calculated with a resolution of $R = \lambda/\Delta\lambda = 300\,000$ and then convolved with a Gaussian to match the resolution of our observed spectra ($R = 50\,000$). By applying another convolution with a Gaussian profile we took the macroturbulent velocity into account and fitted this quantity, too. To determine the carbon isotopic ratio $^{12}\text{C}/^{13}\text{C}$ (which is about 89.9 in the sun according to Anders and Grevesse, 1989), we altered this parameter as well. The carbon isotopic ratio has virtually no effect on the model structure and was consequently only considered in the spectral synthesis calculations.

2.3.3 Determination of abundance ratios

We derive the effective temperature T_{eff} , the surface gravity $\log g$, the C/O and $^{12}\text{C}/^{13}\text{C}$ ratio of our targets by fitting synthetic spectra to the observations. The initial guesses

¹¹ $4215-4270 \text{ cm}^{-1}$ ($23420-23725 \text{ \AA}$) in the K band for NGC 1846.

for T_{eff} and $\log g$ were obtained using colour-temperature relations and bolometric corrections from the literature. We converted the $K_{2\text{MASS}}$ and $(J - K)_{2\text{MASS}}$ values into the Johnson system with the formulae given in Carpenter (2001). For the oxygen-rich targets, we estimated T_{eff} and $\log g$ from the relations given by Houdashelt et al. (2000b). In the case of the carbon stars, we utilised the work of Wood et al. (1983) and Bessell et al. (1983) to obtain bolometric corrections (BC_K) and effective temperatures, respectively. From the K magnitude together with BC_K and the distance modulus (see Sects. 2.2.1.1 and 2.2.1.2) we derived $\log L/L_{\odot}$, and subsequently $\log g$ with the obtained T_{eff} and by assuming $M = 1.5 M_{\odot}$. The reddening of the clusters was taken into account, but it is small ($E(B - V) = 0.06$ and $A_K = 0.020$ for NGC 1846, and $E(B - V) = 0.05$ and $A_K = 0.017$ for NGC 1978, Grocholski et al., 2007) and has no significant influence on the transformations.

For each target we fit the parameters in a two-step process. The idea is to fit the spectral ranges at once rather than tuning individual abundances (except for carbon) to fit single spectral features. From the H band, we could in this way constrain the stellar parameters (T_{eff} and $\log g$) and the C/O ratio.¹² Variations in $\log g$ had the smallest effect on the synthetic spectra. A small uncertainty in the stellar mass or radius estimate has thus only a minor influence on the derived abundance ratios.¹³ Using the parameters as obtained from the H band, we then calculated K-band spectra with a varying $^{12}\text{C}/^{13}\text{C}$ ratio to determine this parameter as well. The carbon isotopic ratio does not influence the appearance of the H-band spectrum significantly, as was verified by test calculations.

To match the shape of the spectral features we also had to assume a macroturbulent velocity which reduces the effective resolution of the spectra. The adopted values were generally lower for the oxygen-rich targets. All of the M stars in NGC 1978 and most of the ones in NGC 1846 were fitted by applying a macroturbulent velocity of $v_t = 3 \text{ km s}^{-1}$, whereby we also tested the influence of other values on the quality of the fit. For the fit of LE16 and LE13 in NGC 1846, a macroturbulent velocity of 4 and 7 km s^{-1} , respectively, was necessary to account for the broader lines observed in these stars. For LE13 we also increased the microturbulence to 3.5 km s^{-1} as mentioned before. The carbon stars displayed a stronger broadening of the features (cf. Fig. 2.4). We needed values of $v_t = 8 \text{ km s}^{-1}$ and even up to $v_t = 10 \text{ km s}^{-1}$ (for the fitted NGC 1846 carbon stars and LE6 in NGC 1978) to fit the spectra. We consistently applied the same value for the H and the K band.

We tried to objectify the search for the best fit by applying a least-square fitting method. Although we were in this way able to narrow down the possible solutions to

¹² It was not our aim to measure the metallicity of the stars from our spectra, because the selected wavelength ranges include only a small number of weak or strongly blended metal lines. The chosen metallicity of $[\text{Fe}/\text{H}] = -0.4$ for our models is close to the literature values (see Sects. 2.2.1.1 and 2.2.1.2), and the metallic lines in the synthetic spectra are in reasonable agreement with the observed spectra.

¹³ In the case of NGC 1846, we thus do not have to bother about the small difference in mass between the one derived in Lebzelter and Wood (2007) and the value assumed for calculating the synthetic spectra.

a few candidate spectra quickly, the final decision about our best fit was done by visual inspection. Spectral features with a false strength or position (due to imperfect line data) in the synthetic spectrum, or spectral regions with a high noise level dominate χ^2 and confuse an automatic minimisation algorithm. As the last step in the fitting procedure is done by eye, we assign a formal error to the derived parameters. In the case that the best fit parameters lie in-between our grid values, we quote the arithmetic mean of the candidate models as our fit result. The error bars were estimated from the range of parameters of the model spectra that still gave an acceptable fit.

A considerable part of our discussion will be concerned with the $^{12}\text{C}/^{13}\text{C}$ ratios of our targets. Since the derived isotopic ratios depend on the parameters of the ^{13}CO lines (taken from the list of Goorvitch and Chackerian, 1994), we want to assess possible systematic errors in the line strengths. In the case that the predicted line strengths in the list are too large, one would have to increase $^{12}\text{C}/^{13}\text{C}$ (equivalent to a decrease of the ^{13}C abundance) in order to fit a ^{13}CO feature compared with the case where the predicted strengths are correct. The actual $^{12}\text{C}/^{13}\text{C}$ ratio would then be lower than the derived value. For some oxygen-rich stars in our sample we get carbon isotopic ratios that are close to the value of the CN cycle equilibrium (which is about 4-5). A necessary further reduction is thus not very likely. If the theoretical line strengths are too low, the above argument is reversed. One would assume a lower $^{12}\text{C}/^{13}\text{C}$ ratio to fit the ^{13}CO features, which means that one would underestimate the actual isotopic ratio. Since we, of course, use the same line list for the analysis of both M and C stars, this shifts up the $^{12}\text{C}/^{13}\text{C}$ for all targets in Fig. 2.17. Similar to a $\log g$ uncertainty, the values for the carbon stars would be stronger affected. Hence, underestimated ^{13}CO line strengths would relax the necessity of efficient additional mixing processes on the RGB as discussed in Sect. 2.5.2.

In the next section, we discuss M and C stars separately. The features contained in the spectra depend on the chemistry regime and some issues cannot be discussed in a general way.

M-type stars

In the search for a good fit we took advantage of the way features react to parameter changes. An increasing temperature weakens all features in the H band. The OH/Fe blend at approximately 15 570 Å is a good temperature indicator. The two neighbouring OH lines and the CO band head react less on temperature changes. From the spectral appearance of the band head we conclude that an increase of $\Delta T_{\text{eff}} = +50$ K corresponds to a $\Delta(\text{C}/\text{O}) = +0.01$ change (relative to a baseline model with $T_{\text{eff}} = 3750$ K, $\log g = 0.25$, and $\text{C}/\text{O} = 0.15$). The remaining lines show only a weak dependence on T_{eff} . The K band is largely insensitive to temperature changes, only the ^{13}CO lines show a weak dependence on temperature which adds to the uncertainty in determining the isotopic ratio. The only feature strongly reacting when altering T_{eff} is the blend including the HF line, its strength decreases at higher temperatures.

The HF 1-0 R7 line is blended with a ^{13}CO 2-0 R21 feature. When we compared this line blend in the NGC 1846 spectra with the synthetic ones using the isotopic ratio derived from the two unblended ^{13}CO lines, it turned out that this blend could not be fitted properly. An improvement in the fit could be either achieved by a change in T_{eff} or by a modification of the fluorine abundance. The first option was only possible in a very limited range due to the constraints set by the fit of the H-band spectra. Thus we modified the abundance of F until we achieved a good fit. This was done for the oxygen-rich stars in NGC 1846 only. In the C-star spectra the blend is additionally affected by a nearby CN line.

An increase in C/O enhances the strength of the CO band head and causes stronger CN lines, while the OH lines get slightly weaker, especially the feature blended with an Fe line. Lowering C/O decreases the strength of the CO features in the K band.

The CO band head is also sensitive to changes in $\log g$, while the other features practically are not. A variation of $\Delta \log g = +0.25$ leads to $\Delta(\text{C/O}) = +0.03$ (using the same baseline model as above). Changes in the surface gravity also affect the measured carbon isotopic ratios. A decrease of $\log g$ of 0.25 results in an increase of the derived isotopic ratio of about +2.¹⁴ Two of the ^{13}CO lines in the spectra of the oxygen-rich stars are unblended (^{13}CO 2-0 R18 and ^{13}CO 2-0 R19). Blended ^{13}CO features were used to check the isotopic ratio derived from the clean lines.

The continuum is well defined in the oxygen-rich case. We utilised the least-square method in the process of finding the best fit. In Fig. 2.6 we show an example fit for the oxygen-rich star LE8 in NGC 1846.

C-type stars

Several things make the fitting of carbon stars more difficult compared with the case of M-type stars. Foremost, the quality of the line data for the molecules appearing in the carbon-rich case hampers the qualitative analysis profoundly. For CN, C_3 , and C_2H_2 we used the SCAN database (Jørgensen, 1997a). The line positions in the computed CN list are not accurate enough for modelling high-resolution spectra. With the help of measured line positions for CN that were compiled by Davis et al. (2005), we were able to correct the wavelengths of the strongest lines. While the results were satisfying in the oxygen-rich case, in the carbon star spectra many additional weak lines show up that could not be corrected. The case of C_2 (we used the line data from Querci et al., 1974), producing a wealth of spectral features, is even more problematic: no observed reference line list is available for this molecule, so both line positions and strengths are subject to large uncertainties. We corrected the line list manually by removing five strong features that did not appear in any of our observations. Nine features were shifted to

¹⁴ As a comparison: A decrease in the temperature of 100 K also results in an increase of the derived isotopic ratio of about +2.

other wavelengths where it was evident from the observations that the lines are at the wrong position. Unlike for M stars, the H-band spectra of carbon stars are also affected by the carbon isotopic ratio. Lines from $^{13}\text{C}^{12}\text{C}$ or $^{13}\text{C}^{14}\text{N}$ are important in some blends, however, the quality of the line data for these features could not be assessed for the above described reasons.

The molecules C_2H_2 and C_3 are incorporated into our calculations via low-resolution opacity sampling data. The absorption thus becomes manifest as a pseudo-continuum in the spectra. A possible occurrence of strong lines or regions with particularly low absorption cannot be reproduced with this approach. The pseudo-continuum level reacts sensitively to temperature changes. In general, an increase in T_{eff} reduces the feature strength. The relative changes of different line strength can be used to constrain the temperature range. The lower the temperature gets, the higher the contribution of C_2H_2 and C_3 becomes, whereas C_2H_2 dominates the absorption. An increase in the C/O ratio has the same effect. For example, relative to a model with $T_{\text{eff}} = 3350\text{ K}$, $\log g = 0$, and $\text{C/O} = 1.4$, a change of $\Delta T_{\text{eff}} = +50\text{ K}$ results in $\Delta(\text{C/O}) = +0.10$. Thus, the overall observed line depths can be fitted with a variety of combinations of the parameters T_{eff} and C/O, simply using different scaling factors between the observed and the calculated spectrum. At first glance, a possible continuum point seems to be present close to 15571 \AA . However, closer inspection revealed an absorption feature at this position in the observations that is missing in the synthetic spectra. Therefore, we conclude that this point cannot be used as a reference point. We were limited to tracing relative line depth of features that depend on one or the other of the two parameters. However, this is hampered both by the uncertain line lists as discussed above and by the fact that a deeper CN or C_2 line can either be due to an increase in C/O or a decrease in the temperature. The CO 3-0 band head seems to be the only feature decoupled from this trend. The CO band head weakens relative to its neighbouring features when C/O is increased, and it is almost insensitive to temperature changes. For determining the C/O ratio, we relied on the CO band head and out of the other features in the H band, we particularly took the C_2/CN blend at approximately $15\,553\text{ \AA}$, which is sensitive to both T_{eff} and the C/O ratio, into account. A larger uncertainty of the results compared with the O-rich case was unavoidable.

Another point that we want to stress here is the consequence of the parameter dependence of the pseudo-continuum for the χ^2 method. The absorption in the pseudo-continuum varies with temperature requiring scaling of the observed spectrum before a comparison. Due to this scaling the value of χ^2 changes in the same manner, so that model spectra with lower effective temperatures (causing a lower flux level due to an increased pseudo-continuum) always result in a lower χ^2 , pretending to fit the observations better. This is of course an artificial effect, and thus we cannot rely on the least-square method as objective criterion.

A change in $\log g$ has only small effects on the carbon star spectra. A higher surface gravity produces a higher pseudo-continuum in the K band. In general $\log g$ only

marginally affects the spectral lines. However, in the determination of $^{12}\text{C}/^{13}\text{C}$ the uncertainty in $\log g$ has to be taken into account. In the K band, all ^{13}CO lines are blended with other features. The carbon isotopic ratio is already so high that the strengths of the ^{13}CO lines have become less and less sensitive to changes in this parameter. As a consequence, even the small uncertainties in $\log g$ correspond to large changes in the isotopic ratio, which adds to the errors. In particular, an increase in $\log g$ of 0.25 causes an increase of the isotopic ratio of about +15. As in the oxygen-rich case, an increase in T_{eff} of 100 K has about the same effect.

Variations of the C/O ratio have the strongest impact on the H-band spectra when C/O is slightly above 1. The strength of the CO band head rapidly drops when C/O is increased to 1.3, approximately. Then a saturation sets in and the strength of the CO band head varies slowly with C/O. This behaviour and strong CN features sitting in the band head hamper an accurate C/O determination. The lines of C_2 and CN increase in strength when C/O rises, both in the H and the K band. The CO lines in the K band decrease in strength for higher values of C/O. The changes are, however, small and do not allow for a determination of the C/O ratio from the K-band spectra alone.

Fig. 2.7 is, as an example, a fit for the star B in NGC 1978, which is a carbon star. The star has an effective temperature of about 3350 K (see also Table 2.5 for the other fit parameters). The pseudo-continuum contribution is relatively weak, although there are almost no line-free regions in both spectral bands. A number of features is successfully reproduced by our models, the deviations in other regions are most probably due to uncertain line data. The low excitation CO lines in the K band are not fitted well and can readily be spotted (we refer to the discussion in Sect. 2.3.1).

To measure the $^{12}\text{C}/^{13}\text{C}$ ratio in the carbon star spectra, we utilised a number of blended ^{13}CO lines, since in the vicinity of some other seemingly clean ^{13}CO lines, there are obviously absorption features missing in our synthetic spectra (see e. g. Fig. 2.7). We cannot rule out that our analysis of a limited number of line blends could introduce a systematic error in the inferred carbon isotopic ratios. Therefore, we emphasise that it would be worthwhile to reassess the isotopic ratios in other wavelength regions, particularly in the light of the discussion in Sect. 2.5.2.

2.3.4 Stellar evolutionary models

The stellar evolutionary models presented here have been computed with the FRANEC code (Chieffi et al., 1998). The release we are currently using is optimised to properly compute low-mass models during their AGB phase. Up-to-date input physics, such as low-temperature carbon-enhanced opacities, have been adopted (Cristallo et al., 2007 and Lederer and Aringer, 2009, see also Chap. 3), and physical phenomena, like hydrodynamical instabilities at radiative–convective interfaces and the mass-loss rate, have been properly taken into account (Straniero et al., 2006 and Cristallo et al., 2009). We use

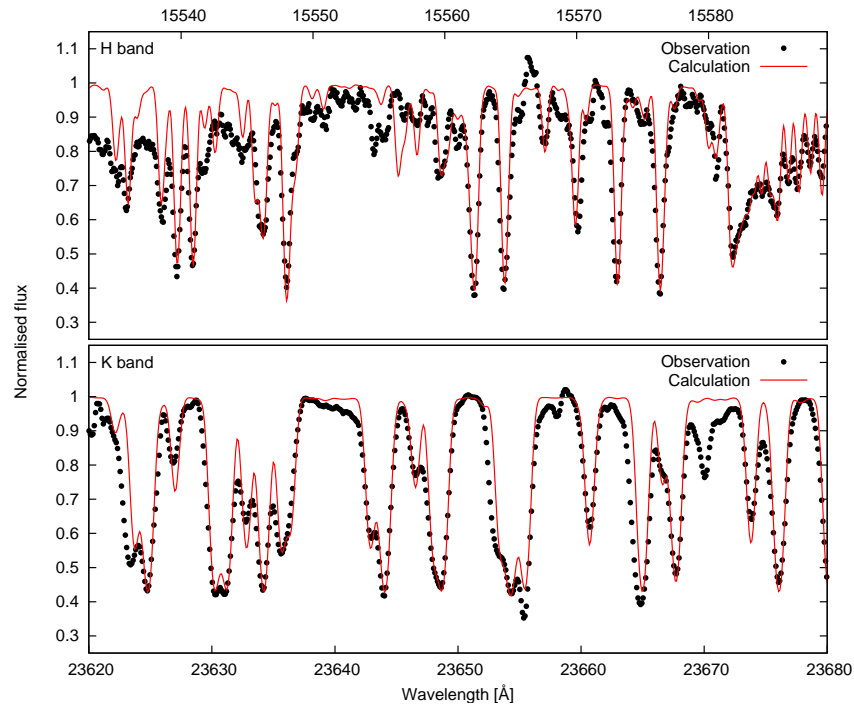


Figure 2.6 Observation and fit of the oxygen-rich star LE8 in NGC 1846. The synthetic spectrum was calculated with $T_{\text{eff}} = 3550 \text{ K}$, $\log g = 0.25$, $\text{C/O} = 0.30$, and a carbon isotopic ratio of 22. For this fit, the fluorine abundance has been reduced (see Sect. 2.5.1).

evolutionary sequences for various initial masses and compositions from Lederer et al. (2009). In particular, models labelled as *scaled solar*, were obtained by scaling the solar abundances derived by Lodders (2003) of a factor Z/Z_{\odot} , where Z is the assumed metallicity (precisely: the metal mass fraction) of the model. Then, *α -enhanced* models were obtained by increasing the initial abundance of O, Ne, Mg, Si, S, Ca, and Ti by a common factor with respect to the corresponding scaled solar values see Piersanti et al., 2007 for details. The inclusion of an additional mixing mechanism taking place below the convective envelope (usually referred to as *extra-mixing*) during the RGB and the AGB phase is described in Sect. 2.5.1.

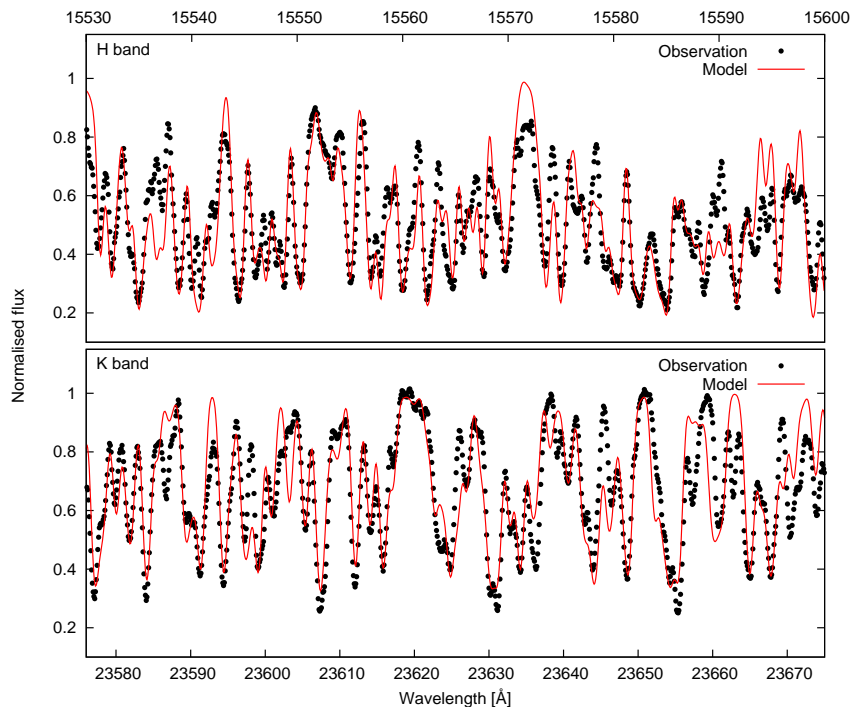


Figure 2.7 Observation and fit of the carbon star B in NGC 1978. The fit parameters are given in Table 2.5. The relatively high effective temperature and low C/O ratio compared with the other carbon stars in our sample allowed a reasonable fit. Deviations can to a large fraction be ascribed to uncertain line data. The strong low excitation CO lines in the K band are not reproduced by the models. See text for details.

2.4 Results

2.4.1 NGC 1846

2.4.1.1 Cluster membership

From the K-band spectra, we measured radial velocities of the target stars from individual lines of CO. Results are presented in Table 2.2. For LE8, Olszewski et al. (1991) give a velocity of $248 \pm 5 \text{ km s}^{-1}$, in excellent agreement with our value. The mean velocity of all investigated AGB stars in NGC 1846 is $248 \pm 2 \text{ km s}^{-1}$ (with a velocity dispersion of $\sigma = 6 \text{ km s}^{-1}$), which is in good agreement with the published values for the cluster. The only star with a larger deviation from the mean velocity is LE17. We repeated the analysis without taking LE17 into account and found a smaller mean velocity ($246 \pm 2 \text{ km s}^{-1}$)

ID	v_r [km s ⁻¹]		
LE1	+251	±	2
LE3	+248	±	3
LE6	+247	±	2
LE8	+250	±	1
LE9	+245	±	1
LE12	+247	±	2
LE13	+242	±	2
LE17	+262	±	1
H39	+242	±	1
LE2	+248	±	2
LE11	+244	±	3
mean	+248	±	2
velocity dispersion (σ)			6
without star LE17			
mean	+246	±	2
velocity dispersion (σ)			3

Table 2.2 Radial velocities and cluster membership of NGC 1846 targets.

and also a smaller velocity dispersion ($\sigma = 3 \text{ km s}^{-1}$). See also Sect. 2.5.1 for a discussion of the cluster membership of LE17.

From Fig. 8 in Grocholski et al. (2007) one can infer that NGC 1846 is in about the same region of the LMC as the field LMC0512-6648 defined in Gallart et al. (2008). Carrera et al. (2008) displays two peaks in the radial velocity distribution of this field. The higher peak is located at 279 km s^{-1} , the other one at 253 km s^{-1} , which roughly agrees with our measurement.

2 Third dredge-up in LMC cluster stars

ID	K 2MASS	$J - K$	$T_{\text{eff},c}$ [K]	L/L_{\odot}	$T_{\text{eff},f}$ [K]	$\log g$	v_t [km s $^{-1}$]	C/O	$^{12}\text{C}/^{13}\text{C}$	[Fe/H]
H39	11.748	1.093	3725	3500	3650	0.25	3	0.20 ± 0.05	12 ± 2	-0.71
LE8	11.230	1.208	3600	3600	3550	0.25	3	0.30 ± 0.05	20 ± 2	-0.35
LE9	11.528	1.143	3600	4000	3650	0.25	3	0.20 ± 0.05	13 ± 2	-0.42
LE13	10.963	1.293	3600	6400	3600	0.00	7	0.65 ± 0.10	60 ± 5	+0.40
LE16	11.429	1.104	3725	4400	3600	0.00	4	0.44 ± 0.05	43 ± 2	-0.20
LE17	11.853	1.225	3650	3100	3700	0.00	3	0.44 ± 0.05	40 ± 4	+0.08
LE2	10.473	1.742	2576	6800	2600	-0.25	10	1.90 ± 0.20	65 ± 15	-
LE11	10.695	1.582	2951	7000	2900	-0.25	10	1.70 ± 0.20	60 ± 10	-

Table 2.3 Data and fit results for oxygen-rich (first group) and carbon-rich (second group) targets in NGC 1846.

2.4.1.2 Stellar parameters and abundance ratios

M stars

The C/O ratio and the $^{12}\text{C}/^{13}\text{C}$ ratio were determined for all six O-rich stars in our sample. Carbon-to-oxygen ratios between 0.2 and 0.65 were found with an uncertainty between ± 0.05 and ± 0.1 , and $^{12}\text{C}/^{13}\text{C}$ isotopic ratios between 12 and 60 were measured. Temperatures of the best fit model spectra agree closely with the T_{eff} values derived from near-infrared photometry (Lebzelter and Wood, 2007) The result for each star is listed in Table 2.3 with the basic parameters of the stellar models used.

The C/O ratio obviously varies significantly from star to star, indicating different amounts of enriched material dredged up to the surface. It would be expected that an increased C/O ratio due to the dredge-up of ^{12}C would be accompanied by an increased isotopic abundance ratio. Indeed we find a nice correlation between C/O and $^{12}\text{C}/^{13}\text{C}$ for the O-rich stars as can be seen from Table 2.3. The values for the C/O and $^{12}\text{C}/^{13}\text{C}$ ratio found are in good agreement with findings from Smith and Lambert (1990) for field stars. The minimum C/O ratio in our sample of 0.2 agrees closely with expectations from first dredge-up.

As described above, one blend including a line of HF (1-0 R7) is covered by our K-band observations. After limiting the various parameters affecting the shape and depth of this blend—mainly the temperature and the carbon isotopic ratio—from other parts of the stellar spectra, we fitted the remaining difference between the observed and the

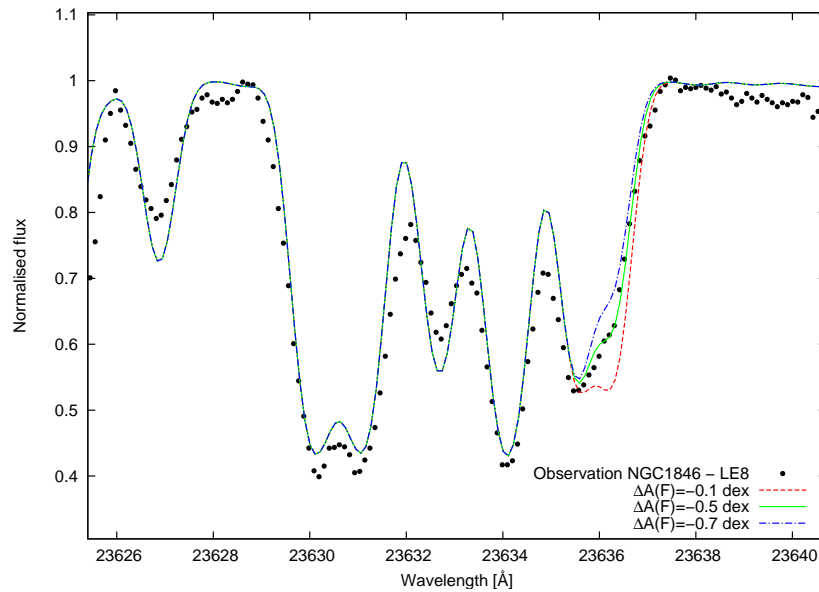


Figure 2.8 Part of the K-band spectrum of LE8 in NGC 1846. Beside the spectrum (dots) three models are plotted with a varying fluorine abundance of $\Delta A(\text{F}) = -0.1$ dex (dashed), -0.5 dex (solid), and -0.7 dex (dash-dotted) relative to a solar value (-7.44) and scaled for the average cluster metallicity, respectively.

calculated blend profile by a change in the F abundance. Due to the rather large uncertainties of the C-star fit we decided to derive the F abundance for the O-rich stars only.

Figure 2.8 shows as an example part of the spectrum of LE8 including the HF line. Three models with different F abundances are plotted. Fluorine is obviously underabundant in LE8 relative to the other metals. It turns out that the F abundance has to be changed from star to star to allow for a reasonable fit of the observed blend. An uncertainty in determining the F abundance comes from both the temperature and the $^{12}\text{C}/^{13}\text{C}$ ratio (via a ^{13}CO line in the blend). We made an estimate of the uncertainty by varying these two parameters around the values determined from other parts of the spectra and then summing in quadrature the respective uncertainties (the error bars are shown in Fig. 2.14). Taking into account this uncertainty and the fact that we have only one HF line to derive the abundance, the results have to be taken with some caution. Confirmation from other HF lines is needed to limit the possible effect of unidentified lines on the profile of the blend and the derived abundances. We have acquired more data and will present a detailed analysis of the fluorine abundances in NGC 1846 elsewhere.

C stars

The C/O ratio was derived for two C-rich stars, LE11 and LE2. For the other C-rich stars, either no H-band spectra were available (as a result of limited observing time) or no acceptable fit of the spectrum could be achieved. For the latter case, the starting influence of stellar variability on the stellar spectrum may play some role besides the above-mentioned problems.

The derived T_{eff} and C/O for the C-rich star LE11 come with a much larger uncertainty. From the strength of the CO 3-0 band head, we exclude a C/O of less than 1.4. A macroturbulent velocity of 10 km s^{-1} is needed to both fit the width of the features and their strength. The temperature can be constrained even less. If we use the value from near-infrared photometry, we get a T_{eff} of 2950 K. As noted by Lebzelter and Wood (2007), this temperature is likely to be too low as pulsation properties instead suggest a value close to 3150 K. We produced model spectra around both temperatures. A value of $T_{\text{eff}} = 2950 \text{ K}$ seems to give the better fit, but the sensitivity of the synthetic spectrum on this parameter is not very high.

Concerning an upper limit of the C/O ratio, an overall fit of the spectrum of similar quality can be reached for various combinations of C/O and T_{eff} with a higher temperature requiring a higher C/O ratio. At temperatures around 3000 K, an increase in T_{eff} by 100 K can, as a rule of thumb, be compensated by an increase of C/O by 0.1 in the parameter region under consideration. Taking the uncertainties of the line lists into account we cannot exclude a C/O ratio as high as 2.0, but an upper limit of 1.9 seems reasonable due to constraints set by the range of possible temperatures defined by the K-band spectrum, the near-infrared colour and the pulsation behaviour, respectively.

With this value we derived a $^{12}\text{C}/^{13}\text{C}$ ratio of about 60 from the K-band spectrum. The derived isotopic ratio depends on the temperature, the C/O ratio, and the selection of the point in the synthetic spectrum to which the observed one is scaled. The C/O ratio has the least influence and, within the constraints set by the H-band spectrum, its uncertainty can be neglected. The temperature is an important parameter for T_{eff} above 2900 K. Below that value, uncertainties in this parameter affect the resulting $^{12}\text{C}/^{13}\text{C}$ ratio less and less. The selection of the pseudo-continuum is of high importance in this low temperature regime. From a comparison between the observed spectra and synthetic spectra by varying the mentioned parameters, we derive a possible range for the isotopic ratio of ± 10 around the mean value.

Additionally we were able to produce a reasonable fit for the spectra of LE2 when using a temperature between 2600 and 2850 K, the H-band spectrum indicates a C/O ratio of 1.9 ± 0.2 . The lower temperature nicely corresponds to the one derived from the $J - K$ value (Lebzelter and Wood, 2007). The resulting $^{12}\text{C}/^{13}\text{C}$ ratio is close to 65 ± 15 .

While we were not able to make a good fit of the H- and K-band spectra of LE1, we made a qualitative comparison of LE1 and LE2. Both wavelength ranges indicate that

LE1 has a higher C/O ratio than LE2. Unfortunately, a quantitative estimate was not possible.

2.4.2 NGC 1978

2.4.2.1 Cluster membership

We derived the heliocentric radial velocity by cross-correlating the H-band spectra with a template spectrum (using the IRAF task `fxcor`). Data for the star LE9 were taken in the semester 2008A, and no radial velocity standard (K-type star) was recorded, so no information could be deduced for this target, because the stellar lines had to be used for the wavelength calibration. While the quality of our LE8 data is too low to derive abundance ratios, it is still adequate to measure the radial velocity (only with a slightly higher error than for the other targets). The sample shows a relatively homogeneous radial velocity distribution, the spread is quite small, so we conclude that all our targets are actually cluster members. The results are summarised in Table 2.4. The value $v_r = +292.9 \pm 1.3 \text{ km s}^{-1}$ (with a velocity dispersion of $\sigma_v = 2.6 \text{ km s}^{-1}$) we find is well in line with earlier determinations (see Sect. 2.2.1.2). As a comparison, Carrera et al. (2008) measured radial velocities in four fields with different distances to the LMC centre. The mean values found in the individual fields range from +278 to +293 km s^{-1} . The velocity dispersion in the metallicity bin with $[\text{Fe}/\text{H}] \geq -0.5$ is $\sigma_v = 20.5 \text{ km s}^{-1}$.

The errors for the carbon stars are systematically higher than for the oxygen-rich stars. This can easily be understood by looking at Fig. 2.4. The features in the C-rich case are usually broader and consequently the peak in the cross-correlation function (and thus the FWHM) is broader, too.

2.4.2.2 Stellar parameters and abundance ratios

We summarise our fit results in Table 2.5. In the first column, we list the star identifier (compare Fig. 2.2), followed by the K magnitude and the colour index ($J - K$) taken from the 2MASS database. In the next two columns, we quote the effective temperature and luminosity (rounded to $100 L_\odot$) resulting from the respective colour calibrations and bolometric corrections (see Sect. 2.3.3). The parameters resulting from our fitting procedure (T_{eff} , $\log g$, v_t , C/O, $^{12}\text{C}/^{13}\text{C}$) are listed in the subsequent columns. We note that none of our target stars is a large amplitude variable, thus the influence of variability on the stellar parameters can be safely ignored. A detailed discussion of the small amplitude variability (1.5 mag in R) will be given elsewhere (Wood & Lebzelter, in preparation).

The derived effective temperatures are systematically higher than the T_{eff} values inferred from the infrared colour transformations. Better agreement between the two temperature scales is found when we adopt a scaled solar oxygen abundance rather than an

ID	v_r [km s ⁻¹]
A	+295.6 ± 1.0
LE4	+296.4 ± 0.8
LE5	+292.9 ± 0.9
LE8	+290.4 ± 1.3
LE10	+292.5 ± 0.7
B	+290.6 ± 1.3
LE1	+297.5 ± 1.6
LE3	+291.5 ± 1.9
LE6	+290.2 ± 1.7
mean	+292.9 ± 1.3
velocity dispersion (σ)	2.6

Table 2.4 Radial velocities and cluster membership of NGC 1978 targets.

ID	K 2MASS	$J - K$	$T_{\text{eff},c}$ [K]	L/L_\odot	$T_{\text{eff},f}$ [K]	$\log g$	v_t [km s ⁻¹]	C/O	¹² C/ ¹² C
A	11.116	1.137	3600	5300	3825	0.50	3	0.23 ± 0.05	16 ± 3
LE4	11.199	1.148	3600	5000	3725	0.38	3	0.18 ± 0.03	13 ± 4
LE5	11.387	1.140	3600	4200	3775	0.25	3	0.18 ± 0.05	6 ± 2
LE9	12.259	1.056	3800	2000	3900	0.38	3	0.13 ± 0.03	12 ± 2
LE10	11.802	1.115	3700	3300	3900	0.38	3	0.18 ± 0.05	9 ± 3
B	11.078	1.289	3176	4400	3350	0.00 [†]	8	1.35 ± 0.10	175 ± 25
LE1	10.467	1.815	2554	6200	2600	0.00 [†]	8	> 1.50	> 200
LE3	9.676	1.814	2556	12900	2600	0.00 [†]	8	> 1.50	> 200
LE6	10.707	1.383	3043	5800	3100	0.00 [†]	10	1.30 ± 0.10	150 ± 50

Table 2.5 Data and fit results for oxygen-rich (first group) and carbon-rich (second group) targets in NGC 1978. Values marked with [†] were fixed in the analysis.

over-abundance of 0.2 dex, which was our standard choice in the analysis (we refer to Sects. 2.2.1.2 and 2.3.2 for details). We want to mention that the results from Smith et al.

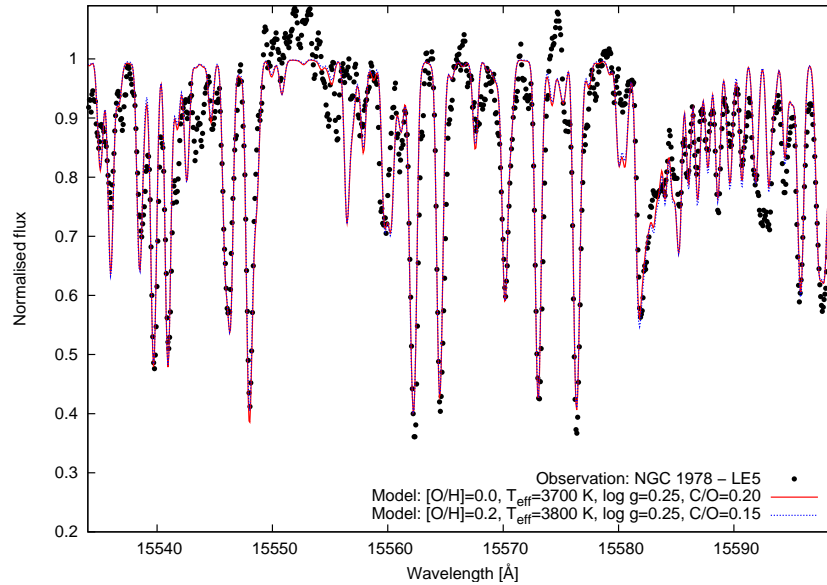


Figure 2.9 Fit of the H-band spectrum of the target LE5 in NGC 1978 adopting different oxygen abundances. A value of $[O/Fe] = 0.2$ (which we used in our analysis) leads to a higher temperature and a lower C/O ratio compared with a scaled solar oxygen abundance ($[O/Fe] = 0.0$). The two model spectra both give reasonable fits to the observations, thus a decision about the actual oxygen abundance cannot be made from our data. However, lower effective temperatures (and thus the "no oxygen over-abundance" scenario) agree better with the values derived from colour-temperature relations.

(2002, their Fig. 8) imply $[O/Fe] \leq 0.0$ for the LMC, contrary to our assumption. Also, Mucciarelli et al. (2008a) found that the other alpha-element abundances are roughly scaled solar ($[\alpha/Fe] \approx 0.0$) in NGC 1978. Apart from the influence on the temperature scale, a higher oxygen abundance shifts the derived C/O ratios only to slightly higher values (Fig. 2.9). The derived carbon isotopic ratios are marginally affected by an oxygen over-abundance.

M stars

We found that for the five oxygen-rich stars within our sample the C/O ratio is varying little, the values range from 0.13 to 0.18 with a typical uncertainty of ± 0.05 . The isotopic ratios vary in the range between 9 and 16 with an uncertainty ranging up to ± 4 . Considering the error bars, all M stars occupy more or less the same region in Fig. 2.10, where we display the measured C/O and $^{12}\text{C}/^{13}\text{C}$ of our sample stars. No target is offset from the spot marking the abundance ratios expected after the evolution on the first giant branch (C/O ≈ 0.2 , $^{12}\text{C}/^{13}\text{C} \approx 10$). In other words, we do not find conclusive signs of

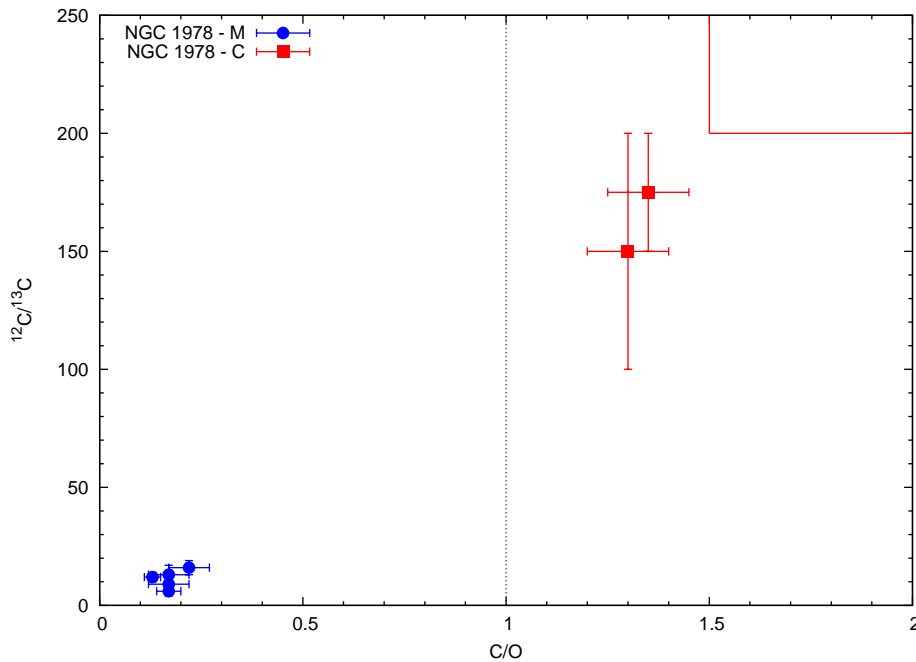


Figure 2.10 Measured abundances ratios for the targets in NGC 1978. Oxygen-rich targets appear to the left of the dotted line at $C/O = 1$, carbon-rich targets are on the right. The box in the upper right corner marks the lower limits for the targets LE1 and LE3. There are no obvious signs of TDU among the M stars, S stars are completely lacking in this cluster. Additionally, from the carbon star data we cannot detect a saturation level for the carbon isotopic ratio which would hint at the occurrence of extra-mixing.

third dredge-up among the oxygen-rich stars in the cluster. This is also consistent with the results from Lloyd Evans (1983) who did not find S-type stars in NGC 1978. The total number of our targets is small, so general statements based on our results are rather weak due to the bad statistics. However, the fact that we find oxygen-rich stars, in which the TDU seems not to be active, does not exclude that this phenomenon is at work in other stars of the cluster.

C stars

In fact, we also identify a sub-sample of carbon-rich stars belonging to NGC 1978. Satisfactory fits could only be achieved for the two hottest carbon stars (B and LE6) in our sample. We also derived C/O and $^{12}\text{C}/^{13}\text{C}$. The error bars are larger than for the M stars, the reasons for that are outlined in the previous sections. For the two cool objects LE1 and LE3, we could only derive lower limits for C/O and $^{12}\text{C}/^{13}\text{C}$. For an increasing carbon content, the features saturate, thus we cannot give a reliable upper limit for C/O .

The C/O ratios that we found are in line with the results obtained by other groups. Matsuura et al. (2005) adopted $C/O \geq 1.4$ to explain molecular features in low-resolution spectra of LMC carbon stars. Investigations of planetary nebulae in the LMC exhibit a range of C/O ratios from slightly above 1 up to even 5 (e.g. Stanghellini et al., 2005). We are not aware of measurements of the carbon isotopic ratio directly from carbon-rich AGB stars in the LMC other than the ones presented here. Reyniers et al. (2007) analysed the post-AGB object MACHO 47.2496.8 ($[Fe/H] = -1.4$) in the LMC and derived $C/O > 2$ and $^{12}C/^{13}C \sim 200$. A peculiar combination of C/O and $^{12}C/^{13}C$ values even more extreme than those of our carbon-rich targets was presented by de Laverny et al. (2006). They found $C/O \leq 1.2$ and $^{12}C/^{13}C > 300$ for BMB-B 30 (with $[M/H] = -1.0$) in the SMC.

Qualitative estimates based on the K-band spectra of the targets LE2 and LE7 suggest that those have an effective temperature between the two groups LE1–LE3 and B–LE6 (see Fig. 2.4). Except for the target B, the difference between the derived effective temperature and the T_{eff} value obtained from the colour transformation is not quite as large as in the oxygen-rich case (about 50 K). We repeated the analysis for the star B with a scaled solar oxygen abundance (as for LE5, Fig. 2.9) and also found a lower T_{eff} , whereas the C/O ratio remained basically unchanged. Almost all spectral features in the carbon-rich case do react sensitively to temperature changes, therefore T_{eff} can be better defined than the C/O ratio. A remarkable result is that—opposite to our findings for NGC 1846 (see Sect. 2.4.1.2)—we do not find a saturation level for the carbon isotopic ratio.

Abundances and infrared photometry

In Fig. 2.11 we show a CMD of NGC 1978 with the respective values for C/O and $^{12}C/^{13}C$ indicated. We do not plot the bolometric magnitudes on the ordinate because of the inconsistent bolometric corrections applied to the targets. The oxygen-rich stars seem to form a sequence with a C/O ratio increasing with luminosity which might hint at a mild dredge-up. However, this could be misleading, as we have to take the error bars quoted in Table 2.5 into account. Moreover, the isotopic ratios do not appear in an ordered sequence. The carbon stars are brighter in *K* and have significantly redder colours. For the stars LE1 and LE3, having the highest (*J* – *K*) values, the indicated numbers refer to lower limits for the abundance ratios. The two carbon stars without labels are LE2 and LE7 which were excluded from our analysis. Both have luminosities comparable to the brightest oxygen-rich stars. A possible explanation is that these stars are in a post-flash dip phase, displacing them about 1 magnitude down from the average luminosity in this evolutionary stage in the CMD (see also the discussion in Sect. 2.5.1.1).

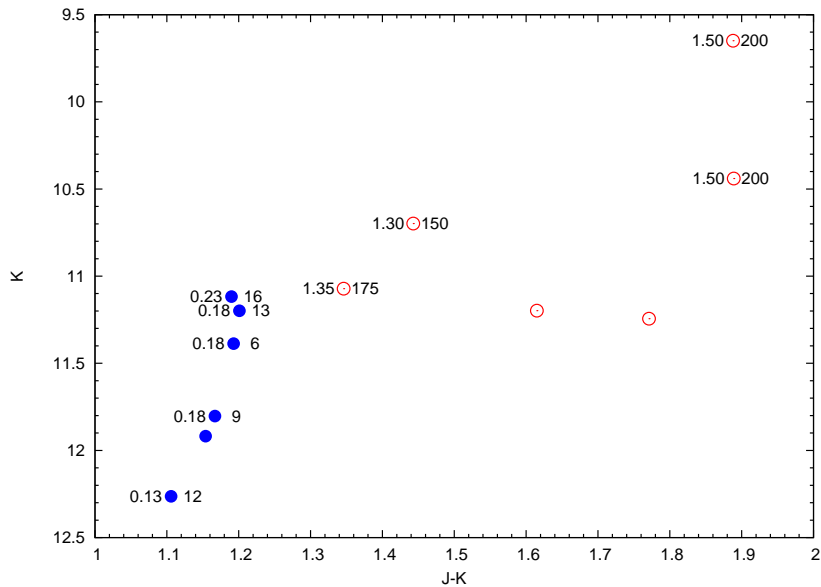


Figure 2.11 Colour-magnitude diagram based on 2MASS data for NGC 1978. The derived C/O and $^{12}\text{C}/^{13}\text{C}$ values are indicated (left and right of the symbols, respectively). Filled symbols refer to oxygen-rich objects, empty symbols depict carbon stars. Points without labels are LE8, LE7, and LE2 (from left to right). Again, the values quoted for the targets with $(J - K) \simeq 1.9$ are lower limits. Compare also Table 2.5. Details are discussed in the text.

2.5 Discussion

2.5.1 NGC 1846

2.5.1.1 Dredge-up along the AGB

In Fig. 2.12 we show the location of the oxygen-rich stars of our sample in a colour-magnitude diagram. The data points are labelled with their respective C/O ratio. Colour and m_{bol} values used here are taken from Lebzelter and Wood (2007). As shown in that paper, the colour variations of these stars are very small and can be neglected in the present discussion. The m_{bol} values are derived from the near-infrared magnitudes using the transformations in Houdashelt et al. (2000a, 2000b). For details we refer to Lebzelter and Wood (2007). The sample stars cover a significant range in brightness along the AGB, thus allowing us to look for changes in the C/O and $^{12}\text{C}/^{13}\text{C}$ ratios with increasing luminosity. We can exclude that these stars belong to the RGB. Indeed, the RGB tip observed by Lebzelter and Wood (2007) is definitely fainter than the faintest star in the

sample, LE17. This occurrence is confirmed by our evolutionary models (see below). Actually, LE17 is only slightly brighter than the RGB tip of the $1.5 M_{\odot}$ model, but its $^{12}\text{C}/^{13}\text{C}$ ratio (30) is definitely greater than expected for the brightest RGB stars (see Sneden, 1991 and Gratton et al., 2000b). LE13, the brightest star in the NGC 1846 sample, is also the brightest O-rich AGB star known in this cluster. However, the resulting picture is far from clear. Indeed we find the star with the highest C/O value at the top. But the two stars with a C/O ratio close to 0.44 (LE16 and LE17) do not seem to fit into a steady increase with luminosity at all. They also seem to be offset from the other stars, which seem to form some sequence in the CMD. Lebzelter et al. (2008a) also found a possible correlation between the C/O ratio and the pulsation mode. The differences in the pulsation mode may also help to explain the observed scatter in C/O along the AGB of the cluster.

We note here that the luminosity at which an AGB star is observed does not necessarily have to be representative of its evolutionary state along the AGB. During thermal pulses the brightness can change significantly both to lower and to higher values. It was suggested by Lebzelter and Wood (2007) that at least the atypically low luminosity of two of the carbon stars in this cluster can be explained by a deviation from the mean interpulse luminosity during a thermal pulse.

The star LE17 seems to be an outlier in various aspects. Assuming that it is a cluster member, its low luminosity, coupled to its large $J - K$, could be explained if this star is undergoing a post-flash dip phase (Iben and Renzini, 1983). The expansion powered by a thermal pulse indeed causes a significant decrease in the luminosity and in the effective temperature. From our models, we derive that variations up to 1 mag and 200 K (in M_{bol} and T_{eff} , respectively) have to be expected. Alternative scenarios for explaining the characteristics of LE17 could be either an unresolved binary or a long secondary period similar to the ones already found in several AGB stars (e.g. Wood et al., 2004). The observed offset in velocity of LE17 from the other AGB stars in our sample could be consistent with both of these scenarios. The star's obvious enrichment in ^{12}C , however, could be best explained by the post-flash dip scenario.

An alternative would be that LE17 is not a cluster member but a background star. Indeed this solution cannot be ruled out. Frogel et al. (1990) list the star as a cluster member based on its projected distance to the cluster center. Lebzelter and Wood (2007) used the location of the star in the colour-magnitude diagram as an argument in favour of the cluster membership. On the other hand, the radial velocity of the star is offset from the other AGB stars measured by almost 20 km s^{-1} . In their work on the velocity dispersion in LMC clusters, Grocholski et al. (2006) chose a range in velocity of $\pm 10 \text{ km s}^{-1}$ around the mean cluster velocity to separate members from non-members. According to this criterion, LE17 would not be a member. Based on the present data, it is difficult to distinguish between the two possibilities.

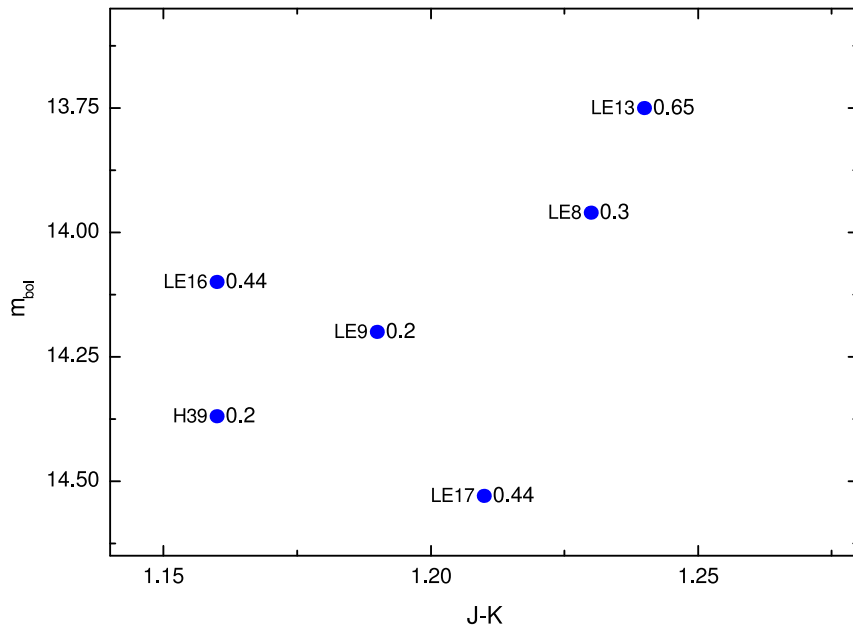


Figure 2.12 Colour-magnitude diagram of the oxygen-rich stars in the NGC 1846 sample. The C/O ratio of each data point is given.

Concerning the other "anomalous" star, LE16, one could speculate that the observed AGB stars may belong to two sequences, one including the stars with C/O ratios between 0.2 and 0.3, and another one, shifted to the blue, with the two remaining stars. We come back to this point below.

As mentioned above there is a qualitative agreement in the derived abundances between the increase in C/O and $^{12}\text{C}/^{13}\text{C}$. Thus, a wrong abundance for the two deviating stars is not very likely. Note that all the stars with C/O > 0.2 and $^{12}\text{C}/^{13}\text{C} > 15$ but LE17 are brighter than the minimum luminosity for the occurrence of the third dredge-up, as predicted by our models. Taking the mean luminosity of the interpulse period just after the occurrence of the first TDU episode, we find that all stars with m_{bol} brighter than 14.1 mag should be ^{12}C enhanced. Once again, the anomaly of LE17 could be solved if the star was in the post-flash dip.

We illustrate the relation between C/O and $^{12}\text{C}/^{13}\text{C}$ in Fig. 2.13. While there is some scatter, a relation between these two quantities can clearly be seen. In the same figure, we also plotted the expected relations from evolutionary models. The magenta solid line represents our reference model: $M = 1.9 M_{\odot}$ (1.8 at the beginning of the TP-AGB phase), $Z=0.006$, $[\alpha/\text{Fe}] = 0.2$, $Y=0.27$. The mass has been chosen according to the mass derived from the pulsation behaviour by Lebzelter and Wood (2007), while the moderate enhancement of the α elements corresponds to the value claimed for the Large Magellanic

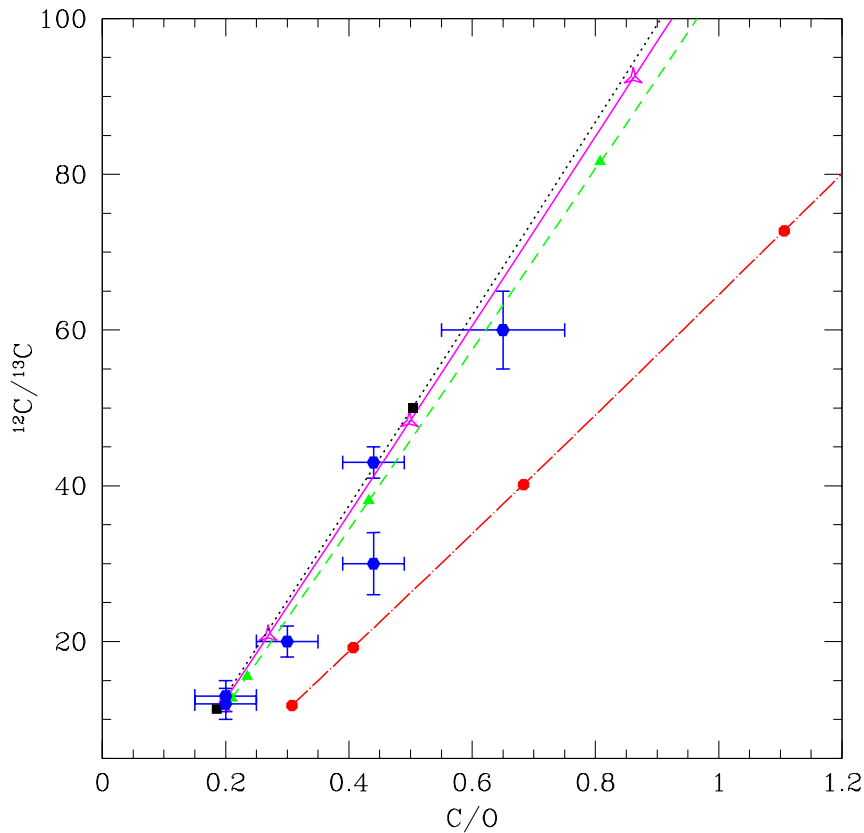


Figure 2.13 C/O versus $^{12}\text{C}/^{13}\text{C}$ for the oxygen-rich stars in the NGC 1846 sample. For comparison predicted values from our evolutionary models are shown. The lines connect individual interpulse values for four sets of model parameters. See text for details.

Cloud (e.g. Hill et al., 2000). The C/O ratio of the two less evolved stars in our sample, H39 and LE9, supports such an assumption. Indeed, the expected C/O ratio after the first dredge-up is 0.35, for a scaled solar composition, and 0.2 when $[\text{O}/\text{Fe}] = +0.2$. In this case, the total metallicity ($Z=0.006$) would imply $[\text{Fe}/\text{H}] = -0.5$, in agreement with the latest spectroscopic determination for NGC 1846 (Grocholski et al., 2006). To evaluate the effects of possible variations of these model parameters, we also report the relations obtained by changing the mass ($1.5 M_{\odot}$, green dashed line), the total metallicity ($Z=0.003$, black dotted line), and the initial abundance ratios (scaled solar instead of alpha-enhanced, red dot-dashed line).

It can be seen that all data points are found very close to the theoretical relation for the reference model, even if LE17 presents a lower carbon isotopic ratio (or too high

C/O)¹⁵. Changes in initial mass and metallicity have little effect, so that the uncertainties of the present spectroscopic analysis do not allow us to distinguish among the different relations reported in Fig. 5. The model with a solar-scaled composition can instead be safely excluded. The boxes along the relations mark the interpulse values after each dredge-up event. Close to these values we should have the highest probability of finding a star. In general, the agreement is remarkably good, with one exception (LE13).

Concerning the abundance of the light element F, we observe, as shown in Fig. 2.14, a change from a fluorine under-abundance to a fluorine over-abundance with increasing C/O (relative to the solar value scaled to the iron abundance of the cluster). Accordingly, there is also a similar trend with the luminosity, as found for the C/O ratio. Measurements of HF lines are a critical source for obtaining the F abundance in stars. Various hypotheses on the origin of this element have been discussed in the literature (see Schuler et al., 2007 for a recent overview). In particular, from a correlation of the carbon abundance with the F abundance, Jorissen et al. (1992) showed that nucleosynthesis in AGB stars is one likely alternative for the production of this element. Schuler et al. (2007) come to a similar result from F abundance measurements of a carbon-enhanced, metal-poor star. A positive correlation between F and C/O has also been confirmed in a planetary nebula (Zhang and Liu, 2005). Our data of NGC 1846 AGB stars clearly support the production and dredge-up of F during the AGB evolution. The two lines in the figure represent the predictions of the reference model. The only difference between the two lines is in the initial fluorine abundance. We have assumed $[F/Fe] = 0$ and $[F/Fe] = -0.71$ at the beginning of the evolutionary sequence, for the solid and the dashed lines, respectively. The lower value corresponds to the one of the less evolved AGB star in our sample (H39). Note that Cunha et al. (2003) report similar fluorine under-abundances in LMC giants. Our models predict a negligible variation in the surface F abundance after the first dredge-up. It should be noted that only an "extreme" extra-mixing during the RGB may induce a sizeable fluorine depletion (see e. g. Denissenkov et al., 2006). In contrast, during the AGB fluorine is produced by alpha-captures on ¹⁵N in the convective zone generated by a thermal pulse and, later on, dredged up. Part of the ¹⁵N seeds are in the ashes of the CNO burning (about 50%), while the remaining part is synthesised in the ¹³C pocket. In both cases, ¹⁵N is released by the ¹⁸O(p, α)¹⁵N reaction (for more details see Cristallo et al., 2006). However, even if models account for a substantial AGB production, we confirm the previous claim by Jorissen et al. (1992) that the theoretical predictions underestimate the fluorine over-abundance observed in evolved AGB stars. A possible solution may be a more efficient production of ¹⁵N in the He-rich inter-shell zone. Perhaps, an additional and different source of fluorine should be sought. We have

¹⁵ Note that the abundances have been determined with a model atmosphere without O enhancement. To see if this has any effect on the derived ratios, we calculated a test model with O enhanced by +0.1 and +0.2 dex, respectively. It turned out that this enhancement only has a weak effect on the spectra which can be compensated for by small changes in the temperature. The C/O and the ¹²C/¹³C ratios remain almost unchanged. See also Sect. 2.4.1.2.

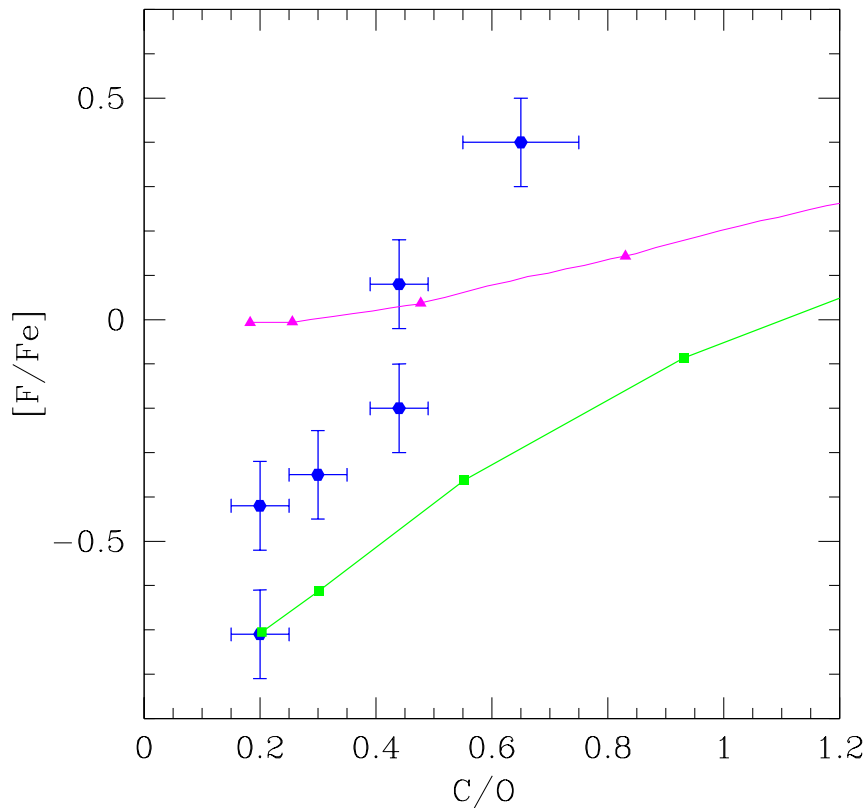


Figure 2.14 Fluorine abundances of the oxygen-rich sub-sample of NGC 1846 as a function of the C/O ratio. The solid line corresponds to the reference theoretical model, while the dashed line represents a model for which the initial [F/Fe] is -0.71 instead of 0.

to note, of course, that, as the fluorine abundance in the NGC 1846 stars has been derived from only one line blend, a systematic error cannot be excluded.

2.5.1.2 The S-type stars

An interesting case is LE13. This star has been classified as spectral type S3/3 by Lloyd Evans (1983). Indeed the ZrO band head at 6345 \AA is clearly visible in the spectrum presented by him (see his Fig. 1). According to its spectral classification, TiO bands and ZrO bands should be of similar strength (Keenan and Boeshaar, 1980). YO should occur, but is not covered by the spectra shown by Lloyd Evans (1983). As expected for a star with S-type spectral characteristics, the C/O ratio is clearly enhanced in LE13 with a value between 0.6 and 0.7. In Fig. 2.15, we compare the observed spectrum with our model for both cases ($C/O = 0.6$ and $C/O = 0.7$). The model fits the observation reasonably well. As mentioned above, this model was calculated with an increased microturbulent

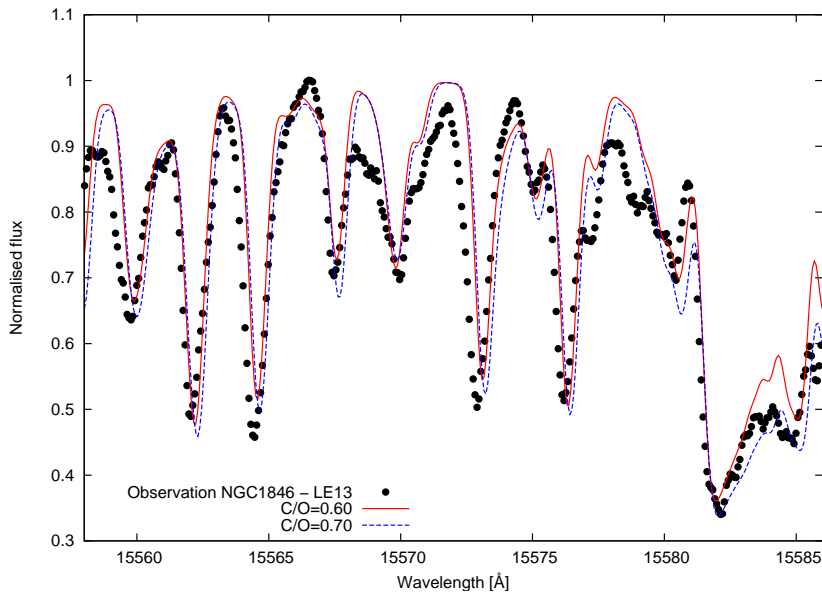


Figure 2.15 H-band spectrum of LE13 in NGC 1846. The observational data are compared with models of $T_{\text{eff}} = 3600$ K, $\log g = 0$, $C/O = 0.6$ (solid line) and 0.7 (dotted line), respectively.

velocity to allow for a reasonable fit of the observed line profiles. A change in the C/O ratio to 0.7 gives a similar fit, but a further increase in the C/O ratio gets problematic as the CN lines, especially the one at 15567 \AA , become too strong. Compensating for this with a higher temperature would give a bad fit of the OH line close to 15570 \AA and too strong a CO band head. Similarly, changes in $\log g$ cannot compensate for a C/O value close to one. LE13 is thus an S-type star with C/O clearly below 1.

Lloyd Evans (1983) also classified a second star in this cluster as of spectral type S3/1, namely LE8. LE8 has an even lower C/O ratio of only about 0.3 . Direct comparison with the spectra of LE9 and H39 does indicate that the star has an increased C/O ratio, but it is far below the expectations for an S-star. Unfortunately, Lloyd Evans (1983) presented no visual spectrum of this star.

A C/O ratio of only 0.65 for an S-type star is in agreement with the oxygen overabundance in the Magellanic Cloud discussed above. If this the case for NGC 1846, and the comparison of the other stars with the expectations from the model suggests this, then we would require more dredge-up events to produce a C/O ratio close to one than in the case of a solar abundance pattern. In other words, the abundance of s -process enriched material on the surface may be high enough to see ZrO bands, for instance, but the amount of C dredged up does not yet equal the amount of O due to the high starting value of the oxygen abundance. Comparing the C/O ratio of LE13 and LE8, we would

expect to see less ZrO in LE8, which indeed agrees with the spectral classes from Lloyd Evans (1983).

Piccirillo (1980) pointed out that only for stars with $T_{\text{eff}} < 3000$ K we would expect a correlation of the occurrence of ZrO bands with a C/O close to one. For hotter stars, an increased abundance of zirconium is the main reason for a visibility of ZrO in the spectrum. As the stars in our sample all have temperatures above 3000 K, the occurrence of ZrO bands is not surprising. We think that a combination of this effect and an enhancement of O in the pre-AGB composition of the star explains the observed C/O ratio. In this context we also note that Smith and Lambert (1990) report a C/O ratio for the two intrinsic (i. e. AGB, see Jorissen et al., 1993) S-stars NQ Pup and V679 Oph of 0.29 and 0.75, respectively. Thus the C/O values we found for the two S-type stars in NGC 1846 look realistic.

2.5.1.3 The carbon stars

The study of the C stars in this cluster was hampered by the above mentioned difficulties deriving basic parameters and abundances. Still a few points can be noticed. The C/O ratio we find is rather high. There is quite a gap in our sample between the highest C/O ratio of an O-rich star (LE13, 0.65) and the lowest value of a C-rich star (LE11, 1.7). There are still two candidates in the cluster, LE12 and LW2 (see Lebzelter and Wood, 2007), which may fill this gap, but unfortunately we have no data for these stars. The value is also high compared to the values found by Lambert et al. (1986, see also Smith and Lambert, 1990) for field stars, where the maximum C/O is 1.6. Such an occurrence is not surprising, however, since the oxygen content is lower in NGC 1846, even considering $[O/Fe] = 0.2$, when compared to field stars. From the abundance of HCN and C_2H_2 , Matsuura et al. (2006) find that the C/O ratio in their sample of LMC carbon stars should be higher than 1.7, which would agree with our findings.

Of particular interest is the carbon isotopic ratio derived for the two carbon stars in our sample. Although the C/O ratio increases, the $^{12}\text{C}/^{13}\text{C}$ remains close to the highest value found for the O-rich stars in this cluster. Basing on the only two carbon stars in the sample, we can tentatively conclude that some saturation level exists around 60 for the carbon isotopic ratio. In contrast to this figure, the evolutionary models predict a continuous increase in the $^{12}\text{C}/^{13}\text{C}$ ratio, as due to the dredge-up of primary¹⁶ ^{12}C . Indeed, for $C/O > 1$, our reference model predicts values definitely higher than 100. Our finding confirms what has already been observed in galactic C stars (Smith and Lambert, 1990 and Abia et al., 2001), which shows a clustering between 50 and 70.

The most obvious explanation for this observational pattern is the occurrence of a mixing process able to bridge the radiative gap between the relatively cool bottom of

¹⁶ *Primary* indicates that the amount of the element produced does not depend on the presence of any seed nuclei, but proceeds from the initial hydrogen content (Habing and Olofsson, 2003).

the convective mantle and the hot hydrogen-burning zone. It is usually referred to as *extra-mixing* or *deep mixing*. We refer to Chap. 1 for detailed information.

The scenario emerging from the evolutionary sequence of $^{12}\text{C}/^{13}\text{C}$ versus C/O in NGC 1846 is that of a moderate deep mixing, affecting the ^{13}C surface abundance in the late part of the AGB only, when stars become carbon-rich. Indeed, while the abundance derived from O-rich stars in NGC 1846 are all compatible with the prediction of models with no extra-mixing, the $^{12}\text{C}/^{13}\text{C}$ ratios we find for the two C stars indicate that their envelope material could have been exposed to a temperature on the order of $30\text{--}40 \times 10^6$ K. At that temperature and on an AGB timescale, ^{12}C is partially converted into ^{13}C , but only marginally into ^{14}N .

From the models, we find that, during the AGB the bottom of the convective envelope, whose temperature never exceeds 4×10^6 K, moves closer to the H-burning zone. Just before the first thermal pulse, a region as large as $2.2 \times 10^{-3} M_{\odot}$ separates the innermost convectively unstable layer from the shell where the temperature is 40×10^6 K, but before the tenth TP, this region is reduced to $4 \times 10^{-4} M_{\odot}$. Such an occurrence suggests that the effect of a possible extra-mixing should be stronger in the late part of the AGB than at the beginning.

To simulate such a scenario, we calculated an additional model with the same input parameters as the reference model, but artificially including an extra-mixing. We assume that such an extra-mixing is confined within a region as large as $10^{-3} M_{\odot}$ below the convective envelope, but only if the temperature is lower than a maximum value (T_{lim}). The average convective velocity is fixed to 100 cm s^{-1} .¹⁷ Here the most important parameter is the value of the maximum temperature, as shown in Fig. 2.16, where we reported the $^{12}\text{C}/^{13}\text{C}$ versus C/O relations obtained for $T_{\text{lim}} = 35 \times 10^6$ and 40×10^6 K.

This phenomenological model is useful for inferring the extension of the region affected by the supposed extra-mixing and its maximum temperature, but a more physical description of the mechanism supporting this phenomenon is needed to derive more quantitative results. Either way, we stress that the $^{12}\text{C}/^{13}\text{C}$ versus C/O sequences for intermediate-age clusters are the best way to understand and to constrain the deep mixing in AGB stars.

2.5.2 NGC 1978

We seek to explain the following observed features of NGC 1978:

¹⁷ This is a slow mixing, when compared to the typical convective velocity in the envelope of an AGB star, which is of the order of 10^5 cm s^{-1} . We have verified, however, that the C/O and $^{12}\text{C}/^{13}\text{C}$ ratios are only marginally affected by the choice of this parameter.

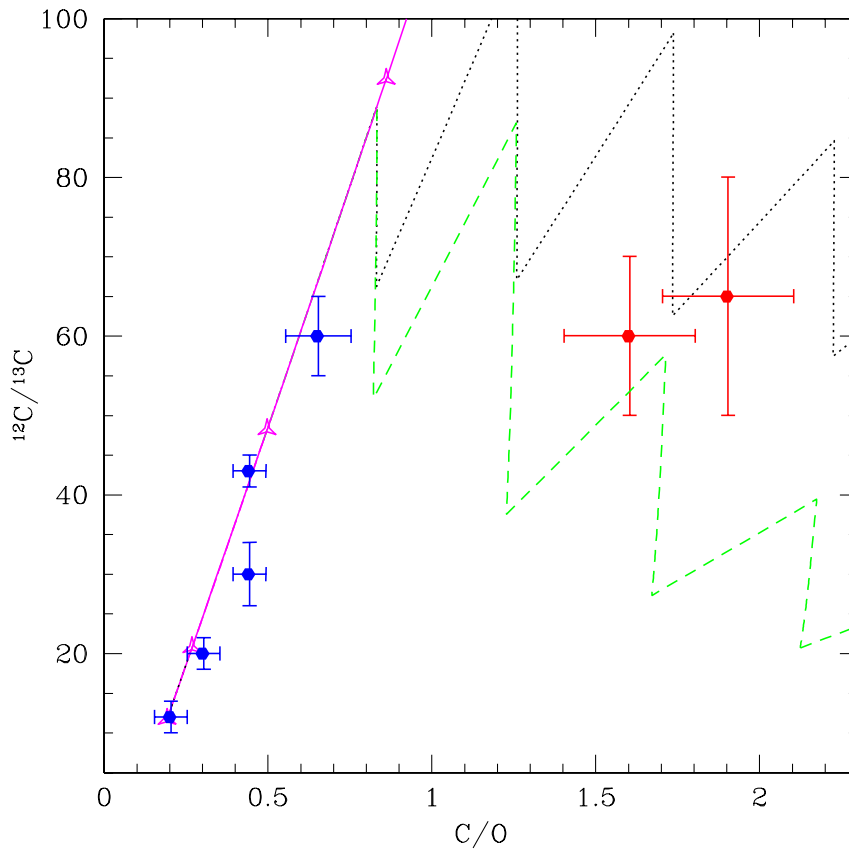


Figure 2.16 C/O versus $^{12}\text{C}/^{13}\text{C}$ for the full sample of NGC 1846. Predicted values from models with and without extra-mixing are shown. The solid line refers to our reference model, while the dotted and dashed ones refer to models with $T_{\text{lim}} = 35 \times 10^6$ K and $T_{\text{lim}} = 40 \times 10^6$ K, respectively (see text for details).

- The cluster harbours carbon stars.
- The M stars do not show conclusive signs of third dredge-up.
- There is no saturation of the carbon isotopic ratio.

Except for the first point, this is more or less the opposite of what we found for the cluster NGC 1846 (see Sect. 2.4.1.2), the composition of which is similar to the one of NGC 1978, even if NGC 1846 is slightly younger and, as a consequence, harbours more massive AGB stars (with a mass of about $1.8 M_{\odot}$). To recall the findings from Sect. 2.5.1, the M stars in NGC 1846 span a range in C/O from 0.2 to 0.65, and $^{12}\text{C}/^{13}\text{C}$ —initially rising together with C/O—does not exceed 60 to 70, even in the carbon stars.

The first point in the list is a clear indication of ongoing TDU in the cluster. The second point may at first seem to contrast this statement, while low number statistics could resolve this apparent contradiction: the lifetime of a thermally pulsing AGB star is short, so in a sample of a few stars we do not necessarily have to find a star with an enhanced carbon abundance. This possibly explains the large gap between the M and the C stars in terms of C/O (see Fig. 2.10). An alternative scenario where the TDU is so efficient that the star becomes carbon-rich after a single dredge-up episode occurs only at much lower metallicity (e. g. Herwig et al., 2000).

Let us put aside the C/O error bars for a moment and speculate about the group of M stars. The 2MASS data come with uncertainties in K of lower than 0.05, except for LE10 where the error is 0.076.¹⁸ In any case, the luminosity sequence that the stars form is conserved. The star LE9 is the faintest at K , with $m_K = 12.3$, in the sample and also the star with the lowest C/O ratio. Cioni et al. (2000) identify the RGB tip in the LMC at $K_0 = 12.1$ mag. According to this value, LE9 could as well be an RGB star or located at the early-AGB. The targets LE5 and LE10 are possibly at the very beginning of the thermally pulsing asymptotic giant branch (TP-AGB) star phase. The case of LE4 and, in particular, A is more difficult. Comparing these stars with those of similar luminosity in the sample of NGC 1846, we note that the latter are classified as S stars and present C/O ratios of 0.4 or even larger. The C/O ratio we find for the star A (0.23) is slightly larger than the average of the other stars, perhaps compatible with just one (the first) TDU episode. The bolometric magnitude of A also roughly corresponds to the limit we found for the onset of the TDU in NGC 1846 ($m_{\text{bol}} = 14.1$ mag).

2.5.2.1 Toy models

In the following sections we discuss various evolutionary sequences in the $^{12}\text{C}/^{13}\text{C}$ versus C/O plane.¹⁹ The sequences were obtained starting from different assumptions for the initial composition and for the efficiency of extra-mixing phenomena, which are possibly operating during the RGB and the AGB phase. Some simple considerations may help to understand the trend of these evolutionary sequences. The simplest picture is that the TDU only adds ^{12}C to the envelope, leaving ^{13}C and ^{16}O (which makes up almost all of the oxygen) unchanged. In this case, the "evolution track" is a straight line in the plot under consideration, as both axes depend linearly on ^{12}C . The slope of this straight line is $k = ^{16}\text{O}/^{13}\text{C}$, which can be easily derived from the following relation.

$$\frac{\text{C}}{\text{O}} = \frac{^{12}\text{C} + ^{13}\text{C}}{^{16}\text{O}} = \frac{^{13}\text{C}}{^{16}\text{O}} \left(\frac{^{12}\text{C}}{^{13}\text{C}} + 1 \right) \quad (2.1)$$

¹⁸ The errors for $(J - K)$ are higher, ranging up to and being even greater than 0.1. This could also affect the differences between the effective temperature scales discussed in Sect. 2.4.2.

¹⁹ Here the element symbols represent the number abundances of the respective elements.

Solving this equation for $^{12}\text{C}/^{13}\text{C}$ results in

$$\frac{^{12}\text{C}}{^{13}\text{C}} = \frac{^{16}\text{O}}{^{13}\text{C}} \frac{\text{C}}{\text{O}} - 1. \quad (2.2)$$

We identify C/O with the x -axis and $^{12}\text{C}/^{13}\text{C}$ with the y -axis of the plots shown in Figs. 2.18 and 2.19. According to our premises, the slope $^{16}\text{O}/^{13}\text{C}$ is constant and fully determined by an initial²⁰ pair of C/O and $^{12}\text{C}/^{13}\text{C}$ values.

The situation changes when oxygen is also dredged up. Then the curve bends upwards and the curvature is dependent on the amount of oxygen dredge-up. To extend our simple picture of the TDU, we assume that per dredge-up episode the oxygen abundance in the mantle changes by an amount of $\Delta^{16}\text{O}$. Correspondingly, the abundance of the main carbon isotope changes by $\Delta^{12}\text{C}$. Furthermore, we request that the Δ -values remain constant during the whole TP-AGB phase. This implies that also the ratio of the abundances changes remains constant and we define

$$\beta \equiv \left. \frac{\Delta^{16}\text{O}}{\Delta^{12}\text{C}} \right|_{1 \text{ TDU episode}} = \frac{^{16}\text{O}_{\text{after}} - ^{16}\text{O}_{\text{before}}}{^{12}\text{C}_{\text{after}} - ^{12}\text{C}_{\text{before}}}. \quad (2.3)$$

The indices *before* and *after* relate to the abundances changes in the course of one single dredge-up episode. From the numerical AGB models (Sect. 2.5.2.2), we find $\beta = \mathcal{O}(10^{-2})$ per dredge-up episode (the relation is indeed roughly linear).

To obtain an expression for the curves shown in Fig. 2.17 we first consider the factors by which the abundances of ^{12}C and ^{16}O change.

$$\tilde{s} = \frac{^{16}\text{O}_{\text{after}}}{^{16}\text{O}_{\text{before}}} \quad (2.4)$$

$$\tilde{t} = \frac{^{12}\text{C}_{\text{after}}}{^{12}\text{C}_{\text{before}}} \quad (2.5)$$

Using the expressions for \tilde{s} and $\tilde{t}(> 1)$, we can rewrite Eq. 2.3 as

$$\beta = \frac{\tilde{s} - 1}{\tilde{t} - 1} \frac{^{16}\text{O}_{\text{before}}}{^{12}\text{C}_{\text{before}}}. \quad (2.6)$$

A function $y(x)$ in which x and y have the same meaning as described above can be found by interpreting $^{12}\text{C}_{\text{before}}$ and $^{16}\text{O}_{\text{before}}$ as initial values (i. e. the ones attained at the RGB tip) for our artificial AGB evolution track. Moreover, we consider s and t as parameters that can freely vary as long as they are ≥ 1 . We thus drop the tilde and the index *before* at this point. The axes of our plot then represent quantities that can be written as

²⁰ More precisely, the values at the beginning of the TP-AGB phase.

$$x = \frac{t \, {}^{12}\text{C} + {}^{13}\text{C}}{s \, {}^{16}\text{O}}, \text{ and} \quad (2.7)$$

$$y = \frac{t \, {}^{12}\text{C}}{{}^{13}\text{C}}. \quad (2.8)$$

The parameters s and t are related to the relative rate of oxygen dredge-up (Eq. 2.6). The parameter s that indicates the change of the oxygen abundance can thus be written as

$$s = \beta(t - 1) \frac{{}^{12}\text{C}}{{}^{16}\text{O}} + 1. \quad (2.9)$$

We replace s in Eq. 2.7 with the expression from Eq. 2.9 and transform all occurrences of isotope abundances to ratios that we can measure, which leads to

$$x = \frac{t \frac{{}^{12}\text{C}}{{}^{13}\text{C}} + 1}{\beta(t - 1) \frac{{}^{12}\text{C}}{{}^{13}\text{C}} + \frac{1}{\text{C/O}} \left(\frac{{}^{12}\text{C}}{{}^{13}\text{C}} + 1 \right)}, \quad (2.10)$$

$$y = \frac{t \, {}^{12}\text{C}}{{}^{13}\text{C}}. \quad (2.11)$$

Alternatively, we can also use the parameter-free form

$$y = \frac{x \left[\frac{1}{\text{C/O}} \left(\frac{{}^{12}\text{C}}{{}^{13}\text{C}} + 1 \right) - \beta \frac{{}^{12}\text{C}}{{}^{13}\text{C}} \right] - 1}{1 - \beta x}, \quad (2.12)$$

with $x \geq \text{C/O}$, consequently. In the case that $\beta = 0$ (no oxygen dredge-up), this formula reduces to the expression given in Eq. 2.2.

In Fig. 2.17 we show the curves described above for different pairs of initial C/O and ${}^{12}\text{C}/{}^{13}\text{C}$, and also for different $\beta = \Delta {}^{16}\text{O}/\Delta {}^{12}\text{C}$. For each pair, we display the case where only ${}^{12}\text{C}$ is added to the envelope, and additionally we plot curves for two different relative rates of oxygen dredge-up. The straight lines originating from the C/O - ${}^{12}\text{C}/{}^{13}\text{C}$ pairs that roughly correspond to the stars A and LE4 of our sample fail to arrive at the carbon star data points. Assuming that the observed carbon isotopic ratio of the C stars in NGC 1978 originates from the third dredge-up operating in these stars, there are three possibilities that may be invoked—in combination—to reproduce the observations. This is either an extensive oxygen dredge-up, or a lower initial C/O ratio, or a larger initial ${}^{12}\text{C}/{}^{13}\text{C}$ ratio. As for the case of an oxygen enhancement, extra-mixing operating during the RGB or the AGB, which causes a decrease of the ${}^{12}\text{C}/{}^{13}\text{C}$ in the envelope, would go in the wrong direction.

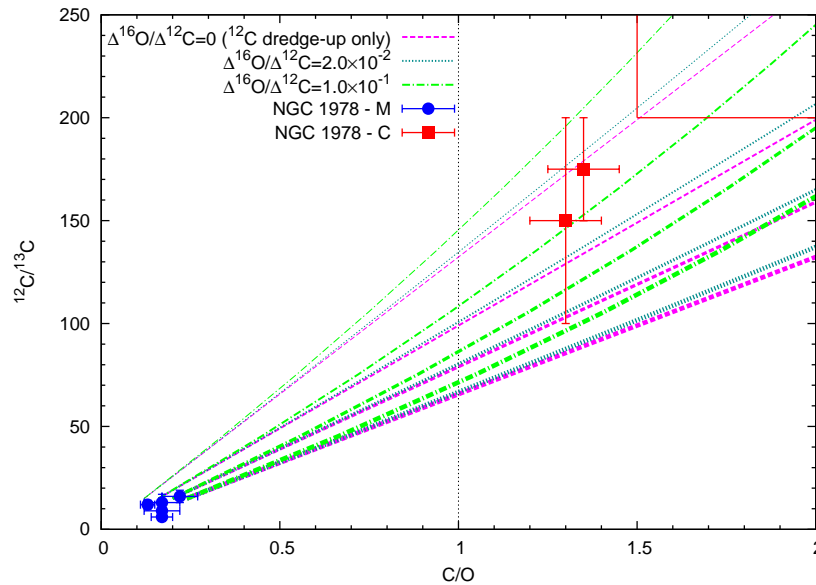


Figure 2.17 Simplistic picture of the third dredge-up. If only ^{12}C is added to the atmosphere by the TDU, then an oxygen-rich star evolves along a straight line to the carbon star stage (magenta dashed lines). The slope $k = {}^{16}\text{O}/{}^{13}\text{C}$ is fully determined by the values of C/O and ${}^{12}\text{C}/{}^{13}\text{C}$ after the RGB phase. If also ${}^{16}\text{O}$ is dredged up, the curves bend up (two different relative rates of oxygen dredge-up are depicted by blue dotted and green dash-dotted lines, respectively). We show curves for four different values of initial C/O (0.12, 0.16, 0.20, and 0.24) with ${}^{12}\text{C}/{}^{13}\text{C} = 15$ always. The line width of the tracks discriminates between the individual initial C/O ratios. More information is given in the text.

2.5.2.2 Stellar evolutionary models

In this section we present theoretical tracks computed with the FRANEC code, and we compare them with observations. In the left panel of Fig. 2.18, we report the evolution of the ${}^{12}\text{C}/{}^{13}\text{C}$ versus C/O curves from the pre-main sequence up to the early-AGB phase in the region where the M stars of NGC 1978 lie. In practice, the end point of each curve (marked by a symbol in the left panel of Fig. 2.18) represents the value attained at the tip of the RGB phase, which is conserved up to the onset of the first thermal pulse. In the right panel, instead, we extend the axes to also include the C-rich stars. We plot the whole AGB evolutionary tracks and mark the values attained after each TDU episode.

We firstly concentrate on the O-rich stars of our sample. We carry on our analysis under the assumption that these stars have not experienced TDU, because they still are at the beginning of the TP-AGB phase or because they arrived on the AGB with a too small envelope mass. In this case, their initial surface composition has been modified by

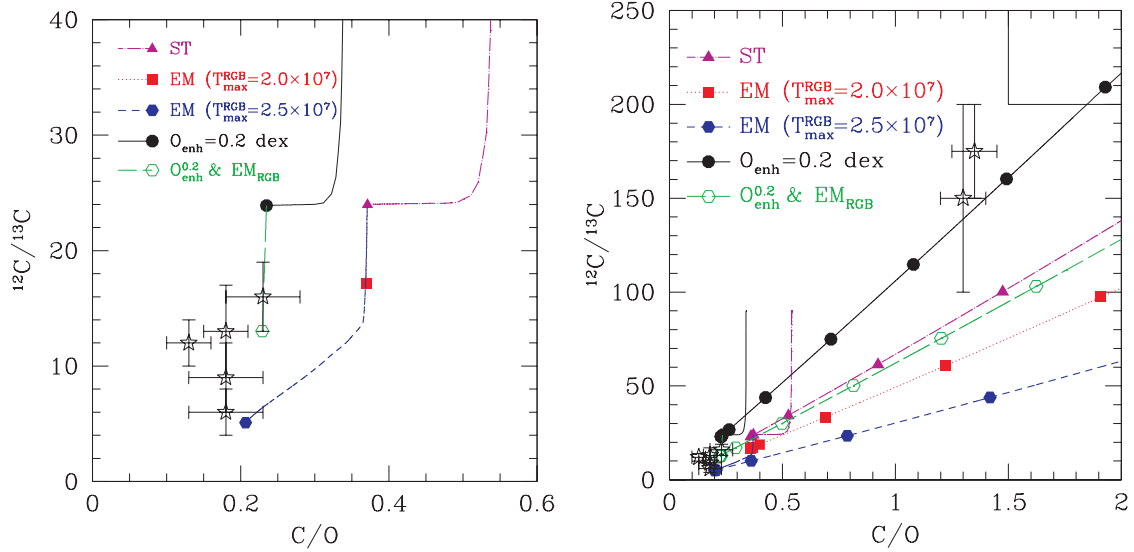


Figure 2.18 Comparison between observational data and theoretical models. $^{12}\text{C}/^{13}\text{C}$ isotopic ratios vs. C/O ratios are reported. In the left panel we report the range of O-rich stars only, while in the right panel the whole sample has been considered. The star symbols with error bars indicate our observations. The red dotted, the blue dashed, and the green long-dashed curves in the left panel are partly covered by other tracks in the plot. In the right panel, the symbols indicate the values attained during the interpulse phases, which are on the order of 10^3 times longer than the TDU episodes. See text for details.

the occurrence of the FDU only and, eventually, by an additional slow mixing operating below the convective envelope during the RGB phase (the so-called *extra-mixing*, see Sect. 1.4.2). Our reference model (ST, dash-dotted magenta curve) has an initial mass $M = 1.5 M_{\odot}$ with $Z = 0.006$, corresponding to $[\text{Fe}/\text{H}] = -0.36$. We assume an initial solar-scaled composition, which implies $\text{C}/\text{O} = 0.5$ and $^{12}\text{C}/^{13}\text{C} = 90$. After the FDU, the surface values attain $\text{C}/\text{O} = 0.36$ and $^{12}\text{C}/^{13}\text{C} = 24$. This is due to the fact that the convective envelope penetrates into regions where partial hydrogen-burning occurred before. No extra-mixing has been included in the ST case. The values so obtained clearly disagree with the M stars observations, which show an average $\text{C}/\text{O} = 0.18$ and an average $^{12}\text{C}/^{13}\text{C} = 11$. Thus, we explored the possibility of an occurrence of extra-mixing on the RGB.

This hypothesis is supported by the bulk of observations of RGB stars in the galactic field, as well as in open and globular clusters (see e. g. Gratton et al., 2000a). These observations show that this additional mixing occurs in low-mass stars ($M < 2 M_{\odot}$) during

the first ascent along the Red Giant Branch. Moreover, Eggleton et al. (2008) identified a mixing-mechanism driven by a molecular weight inversion ($\delta\mu$ -mixing) in three-dimensional stellar models that must operate in all low-mass stars while they are on the RGB. The operation of this RGB extra-mixing is also required to explain the relatively low $^{12}\text{C}/^{13}\text{C}$ ratios in the M stars of NGC 1846 (Sect. 2.5.1).

As in Sect. 2.5.1, we include this additional mixing right after the RGB luminosity bump. The extension of the zone in which this additional mixing takes place is fixed by prescribing the maximum temperature the material is exposed to ($T_{\text{RGB}}^{\text{max}}$). The circulation rate is tuned by setting the mixing velocity to a value that is a small fraction of the typical convective velocities in the envelope of an RGB star (see Sect. 2.5.1). As discussed in Sect. 2.5.1, the carbon isotopic ratio largely depends on $T_{\text{RGB}}^{\text{max}}$. In Fig. 2.18 we report two models, characterised by $T_{\text{RGB}}^{\text{max}} = 2.0 \times 10^7$ K (red dotted curve) and $T_{\text{RGB}}^{\text{max}} = 2.5 \times 10^7$ K (blue short-dashed curve). In the first case, the final $^{12}\text{C}/^{13}\text{C}$ ratio decreases, reaching a value in good agreement with those observed in the M stars of NGC 1978. Notwithstanding, the C/O ratio remains unaltered and higher than the observed one. An increase of $T_{\text{RGB}}^{\text{max}}$ up to 2.5×10^7 K leads to a lower C/O ratio of about 0.21, which is in better agreement with the observations. However, the corresponding $^{12}\text{C}/^{13}\text{C}$ ratio is 5, which is definitely lower than the average value (11). Note that only LE5 shows such a low value ($^{12}\text{C}/^{13}\text{C} = 6$).

Then, we explored the possible effect of an oxygen enhancement (see the discussion in Sect. 2.2.1.2). The black solid line in Fig. 2.18 represents a model similar to the ST case, but with $[\text{O}/\text{Fe}] = 0.2$. As for the ST case, the effects of the FDU are clearly recognisable. An additional model, as obtained by including an RGB extra-mixing ($T_{\text{RGB}}^{\text{max}} = 2.1 \times 10^7$ K) is also reported (green line). The final surface composition of this model (C/O = 0.23 and $^{12}\text{C}/^{13}\text{C} = 13$) is close to the average values of the observed sample (C/O = 0.18 and $^{12}\text{C}/^{13}\text{C} = 11$). Thus, a first conclusion is that moderate RGB extra-mixing ($2.1 \times 10^7 < T_{\text{RGB}}^{\text{max}} < 2.3 \times 10^7$ K) coupled to moderate oxygen enhancement appears to nicely reproduce the observed average composition of the M stars in NGC 1978. The same conclusion has been reached in the case of NGC 1846 (see Fig. 2.19 and Sect. 2.5.1).

What are the implications of this scenario when applied to the whole observational sample (O-rich and C-rich stars)? We carry on our analysis assuming that the carbon stars are intrinsic, i. e. that their surface composition, in particular the large C/O and carbon isotopic ratios, is the result of nucleosynthesis and mixing processes occurring during the thermally pulsing AGB evolution.

In the right panel of Fig. 2.18 we report the same models as shown in the left panel. The tracks can be compared to the toy model presented in Sect. 2.5.2.1. None of the theoretical tracks can simultaneously reproduce the abundance ratios of the M and C stars. The large values of the C-star carbon-isotopic ratio can only be reproduced by the oxygen-enhanced model with no RGB extra-mixing. All the other models predict too low $^{12}\text{C}/^{13}\text{C}$ ratios. The situation appears even more peculiar when compared with the case

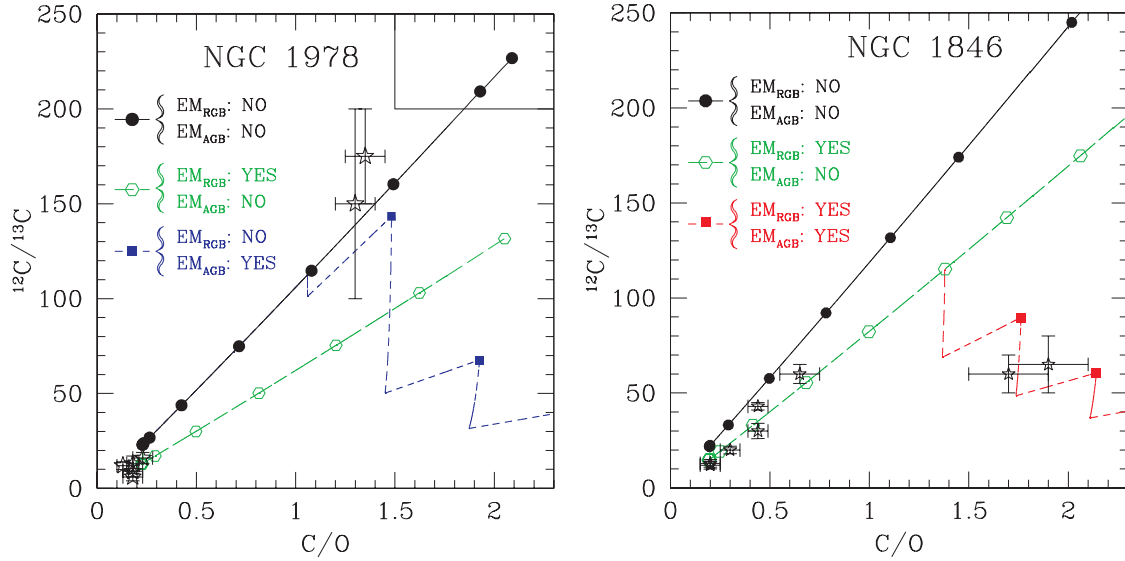


Figure 2.19 Comparison between observational data and theoretical models. $^{12}\text{C}/^{13}\text{C}$ isotopic ratios vs. C/O ratios are reported. In the left panel, we report observational data of the cluster NGC 1978, accompanied by selected theoretical tracks. As a comparison, in the right panel, we report the fitting curve for another LMC cluster (NGC 1846). The symbols along the tracks indicate the values attained during the interpulse phases (see also Fig. 2.18). The star symbols with error bars indicate our observations. See text for details.

of NGC 1846, for which we found C stars with larger values of C/O, but with $^{12}\text{C}/^{13}\text{C}$ between 60 and 70, so that an AGB extra-mixing (in addition to the RGB extra-mixing) was invoked to reproduce the observations. The vast difference between the two clusters is illustrated in Fig. 2.19. In the left panel, data for NGC 1978 are compared with three models computed under different assumptions for the RGB and the AGB extra-mixing, namely no extra-mixing (black solid line), moderate RGB extra-mixing only (green long-dashed line), and moderate AGB extra-mixing only (blue dashed line). All the three models have $M = 1.5 M_{\odot}$ and $[\text{O}/\text{Fe}] = 0.2$. In the right panel, data for NGC 1846 are compared with similar models. In this case, the mass is $1.8 M_{\odot}$ and the red dashed line refers to a model with both RGB and AGB extra-mixing (see Sect. 2.5.1 for more details on models with AGB extra-mixing). In summary, the large carbon isotopic ratio observed for the C stars of NGC 1978 ($^{12}\text{C}/^{13}\text{C} > 150$) rules out both RGB and AGB extra-mixing, which are instead required to reproduce the evolutionary sequence of M, S, and C stars in NGC 1846.

2.5.2.3 Alternative scenarios

In the previous section, we did not identify a theoretical scenario that satisfactorily reproduces the whole set of stars belonging to NGC 1978 (including both the O-rich and the C-rich sub-sample). Moreover, the intermediate-age LMC cluster NGC 1846, which we discussed in Sect. 2.5.1, presents a totally different abundance pattern, which cannot be ascribed to the same theoretical scenario. The lack of S stars is an additional peculiarity of NGC 1978. So far, our arguments have been based on the assumption that the stars in our sample possess the same initial composition, mass, and age so that they form an evolutionary sequence, in which the variations of the surface composition are due to intrinsic processes only. In this section, we speculate about possible alternative scenarios, namely

- the existence of two stellar populations having different ages,
- the existence of rejuvenated stars, or
- the activation of additional mixing at the base of the convective zones generated by a thermal pulse.

The existence of two populations proposed by Alcaíno et al. (1999) is an attractive possibility, because it might explain the dichotomy between the M and the C stars. The M stars would then belong to the older population. Their mass is sufficiently low for the occurrence of the RGB extra-mixing, but too low for the occurrence of the TDU during the AGB. On the contrary, the C stars are younger (less than 1 Gyr) and more massive ($M > 2 M_{\odot}$). For these stars, the persistence of the μ -barrier at the base of the hydrogen-rich envelope prevented the RGB extra-mixing, whilst, during the AGB, TDU accounts for the observed large C enhancement. However, this scenario seems unlikely. First of all, a number of other studies did not find significant metallicity, mass or age differences. Second, a cluster merger creating two populations is not considered to be a valid option (see Sect. 2.2.1.2). Alcaíno et al. (1999) argue that the north-western half could be more metal-rich and maybe slightly younger. The distribution of our targets in Fig. 2.2 does not support this idea. The M stars are distributed equally around the cluster centre. The carbon stars in our sample lie either in the centre or in the south-eastern half of the cluster. According to Lloyd Evans (1980), there is another carbon star (LE11) located in the north-western half. Although the C stars appear to line up along the cluster's major axis, there is no indication that they concentrate in a certain region. We also do not see a signature of the lower AGB of the supposed younger population. A large spread in metallicity would have shown up in the fitting process, yet we were able to obtain reasonable results for both oxygen-rich stars and the hottest carbon-stars with a single value for the metallicity.

The evidence for a single age stellar population does not exclude the existence of rejuvenated stars. Merging, coalescence, or mass accretion processes are often invoked to

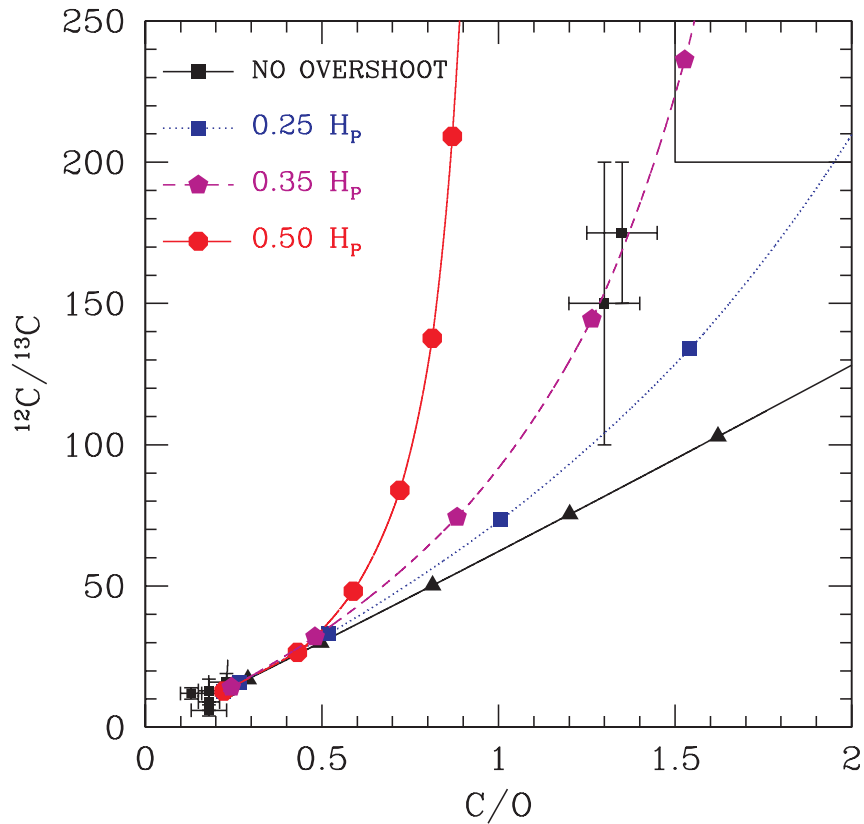


Figure 2.20 C/O ratio for a series of models including an overshoot at the base of convective zone generated by the TPs. The extension (in fraction of the pressure scale height) of the overshoot zone is indicated in the legend.

explain the Blue Stragglers observed in many GCs. Actually, a non-negligible number of stars lie above the turn-off and the sub-giant branch in the colour-magnitude diagram of NGC 1978 (Mucciarelli et al., 2007a), although we cannot exclude that those are field stars or the result of unresolved pairs. If the product of one of the above mentioned processes is a star with a mass larger than $2 M_{\odot}$, or if the rejuvenating process leaves the envelope composition enriched with heavy elements, the efficiency of the RGB extra-mixing is significantly reduced (Charbonnel and Zahn, 2007). Such a scenario might explain the large carbon isotopic ratio of the C stars, but the lack of S stars remains a mystery. Moreover, even if we do not have a detailed statistics of the number of binary systems in NGC 1978²¹, it seems unlikely that two merger events occur nearly simultaneously to produce the stars B and LE6, for instance. Indeed, since the carbon star phase is a comparably short period during stellar evolution, *all* the merger events that produced the C stars would have had to take place within a short time interval.

²¹ Estimated binary fractions in other LMC and SMC clusters range from 10 (NGC 1783, Mucciarelli et al., 2007b) to ≤ 30 per cent (Chiosi and Vallenari, 2007).

The last alternative scenario we have investigated regards the possible modification of the efficiency of the mixing processes taking place during the AGB phase, which is responsible for the increase of ^{12}C and ^{16}O in the envelope. A deeper TDU would increase both the carbon isotopic ratio and the C/O ratio, thus leaving the slope of the curves in the right panel of Fig. 2.18 unaltered. In this scenario, the possibility of producing S stars as a consequence of the TDU is reduced, since the transition to the C-star stage is more rapid. We recall that the TDU depth basically depends on the strength of the thermal pulses: stronger TPs push outward the external layers more easily, therefore inducing deeper dredge-up episodes. In turn, the strength of a thermal pulse depends on many physical and chemical properties, such as the core and the envelope mass, or the CNO content in the envelope (Straniero et al., 2003). On the other hand, an increase of the primary oxygen that is dredged up might limit the increase of the C/O at the surface and steepen the $^{12}\text{C}/^{13}\text{C}$ -C/O relation. The fraction of oxygen produced by the $^{12}\text{C} + \alpha$ reaction increases toward the centre. Therefore, an additional mixing process, as due to a ballistic overshoot or to non-standard mechanisms (such as rotation or the effects of magnetic fields), that moves primary O (and C) from the deep interior to the He-rich inter-shell, may indirectly explain the large carbon isotopic ratio of the carbon stars in NGC 1978. To shed light on this possibility, we computed some additional models, in which we applied an artificial overshoot at the base of the convective zone generated by the TPs. The initial mass adopted in the models is $1.5 M_{\odot}$, and the initial composition is oxygen-enhanced (+0.2 dex). A moderate RGB extra-mixing ($T_{\text{RGB}}^{\text{max}} = 2.1 \times 10^7$ K, corresponding to the case of the green long-dashed line in Fig. 2.18) has been included. We parametrise the additional mixing by limiting the extension of the overshoot layer to a fraction of the pressure scale height of the most internal convective mesh point. In Fig. 2.20, we report the resulting $^{12}\text{C}/^{13}\text{C}$ isotopic ratios as a function of C/O.

Even if these models apparently provide a simultaneous reproduction of the composition of both M and C stars, we have to stress the many theoretical and observational evidences against such a process. At the He-flash peak, the inner border of the convective zone already reaches the layer where the temperature attains its maximum value. Below this point, due to the neutrino energy loss, the temperature (and the entropy) decreases, so that the deceleration due to the buoyancy is quite strong. Herwig et al. (2006) showed that even if the pressure and the entropy barrier at the base of the convective shell generated by a TP is stiff, convective plumes can penetrate into the underlying radiative layers due to g -mode oscillations. These structures reach down to about 2×10^8 cm below the formal convective border (see their Fig. 24), and develop mean vertical velocities that are about 1000 times smaller than the average convective velocities. The extension of this penetration has the same order of magnitude as the overshoot zone in our models, namely 1.0×10^7 cm, 1.2×10^8 cm, and 1.5×10^8 cm, for $0.25 H_p$, $0.35 H_p$, and $0.5 H_p$, respectively (these are mean values). However, if in our 1D models the whole mass of the spherical overshoot region is efficiently mixed, the amount of mass contained in the penetrating plumes of the 3D model is certainly lower. In addition, the result of the 3D

model may be affected by the assumed boundary conditions. As was stressed by Herwig et al. (2006), their models ignore μ -gradients, which increase the stability and reduce mixing across the formal convective boundaries. Moreover, they found that the amplitude of the gravity waves depends both on the resolution adopted in the simulation and on the choice of the heating rate.

On the other hand, the bulk of the C stars in the Milky Way as well as those in NGC 1846 have $^{12}\text{C}/^{13}\text{C}$ ratios in the range from 40 to 70, and only in a few cases up to 100 (Lambert et al., 1986). This occurrence leads us to the conclusion that such an overshoot is supposedly an uncommon process. Note that the occurrence of an overshoot below the convective zone generated by a TP causes considerable changes of the physical conditions in the He-rich inter-shell. In particular, larger temperatures develop at the pulse peak and, therefore, the $^{22}\text{Ne}(\alpha, n)^{13}\text{C}$ reaction rate becomes an important neutron source, even in low-mass AGB stars. In such a case, the resulting *s*-process nucleosynthesis would be characterised by an overproduction of neutron-rich isotopes. For instance, the expected isotopic compositions of strontium, zirconium, molybdenum, and barium would substantially differ from those measured in pre-solar SiC grains, which were produced in the cool circumstellar envelope of a past generation of C stars (see Lugaro et al., 2003). Additionally, calculated element abundances ratios such as Rb/Sr would not match observations obtained from carbon stars (see Abia et al., 2001). For these reasons, if the overshoot from the base of the convective zone generated by TPs is non-negligible, it should be a rare event.

In summary, a clear and coherent picture of the AGB stars in the cluster NGC 1978 within the more general context of low-mass AGB stellar evolution and nucleosynthesis cannot be easily achieved. Once again, we stress the uniqueness of the C star sample of NGC 1978 with respect to other LMC clusters.

2.6 Conclusions

We derived C/O ratios and $^{12}\text{C}/^{13}\text{C}$ ratios for our targets in the LMC clusters NGC 1846 and NGC 1978, and tested how the third dredge-up events change the surface abundances in these two homogeneous AGB-star samples.

In NGC 1846 we identified oxygen-rich stars with clear indications of the TDU from enhanced values of the carbon-to-oxygen and carbon isotopic ratio. The respective values lie between 0.2 and 0.65 for C/O, and 12 and 60 for $^{12}\text{C}/^{13}\text{C}$. The cluster also contains a few carbon stars, but only rather uncertain values for the C/O ratio could be derived. An analysis of the two carbon stars LE11 and LE2 was possible leading to C/O = 1.7 and 1.9 and $^{12}\text{C}/^{13}\text{C} = 60$ and 65, respectively. As expected, the C/O ratio is correlated with the $^{12}\text{C}/^{13}\text{C}$ ratio. We found a good agreement with model predictions for both ratios assuming an oxygen over-abundance of +0.2 dex in the cluster. The measured C/O ratios are in reasonable agreement with the predicted values during the interpulse phases.

This is the first direct test of the models concerning dredge-up before the stars become carbon stars.

An increase in the fluorine abundance along the AGB of NGC 1846 has been found. This confirms nucleosynthesis in AGB stars as one of the origins of this element.

Two stars in the cluster NGC 1846, namely LE13 and LE8, were classified as having spectral type S in the past. We find a C/O of 0.65 and 0.3 for these objects. While the C/O ratio is thus clearly less than 1, we argue that the comparably high temperature of the stars allows for S-type characteristics at this value of C/O.

The $^{12}\text{C}/^{13}\text{C}$ ratio found in the carbon stars of NGC 1846 cannot be explained with standard models for the third dredge-up. They indicate the need for a moderate extra-mixing, affecting the late part of the AGB evolution.

The second cluster for which we presented a sample of AGB stars was NGC 1978, which is also located in the LMC. Again, we derived the C/O and the $^{12}\text{C}/^{13}\text{C}$ ratios for the target stars where it was possible. Like in the case of NGC 1846, the spectroscopic data reveal the presence of two sub-samples, one where $\text{C/O} < 1$ in the stellar atmosphere (oxygen-rich or M-type stars), and the other with $\text{C/O} > 1$ (carbon-rich or C-type stars). The oxygen-rich stars present low values for the C/O ratio (mean value 0.18) and the $^{12}\text{C}/^{13}\text{C}$ ratio (mean value 11). The spread in the C/O ratio is restricted, all values are consistent with the mean value within the error bars. We observe a larger spread in the $^{12}\text{C}/^{13}\text{C}$ ratios. We conclude from the spectroscopic data in comparison to our evolutionary models that the TDU mechanism is not (yet) working in these stars. This is a clear contrast to our results concerning NGC 1846. The carbon-rich stars of our sample instead show C/O values and $^{12}\text{C}/^{13}\text{C}$ ratios consistent with the occurrence of TDU. A lack of S stars, with C/O ratios between those of the O-rich stars and the C-rich stars, has been highlighted.

We did not find a theoretical scheme that is able to satisfactorily reproduce the chemical abundance pattern in NGC 1978. By claiming the existence of a non-standard mixing mechanism, we postulated some possible solutions. However, we are aware that too many *ad hoc* assumptions make our analysis objectionable, taking into account that some of them are strongly limited by observational constraints. In particular, a more consistent picture of all the additional mixing mechanisms, which are active during the RGB and the AGB phase, is required. This has to be emphasised all the more in the context of our findings for NGC 1846. This cluster shows a different abundance pattern, although it is comparable to NGC 1978 in terms of metallicity, age, and the stellar mass. We also discussed the scenario of multiple stellar populations and rejuvenated stars.

Narrower constraints for stellar evolutionary models could be derived from atmospheric models including a set of more accurate molecular line data, especially in the case of carbon stars. Additionally, the more evolved a star is (thus having a higher luminosity and C/O ratio), the more dynamic effects influence the spectral appearance, which could lead to uncertainties in the abundance determination. From the observational point of

view, improvements could be achieved by means of the choice of the observed wavelength regions, some of which are less crowded with molecular lines. Moreover, a comparison between low-resolution data and high-resolution data should be explored further (cf. Wahlin et al., 2006). If low-resolution data deliver robust C/O ratios (and stellar parameters), the isotopic ratios could be derived in the high-resolution spectra more accurately. Future infrared spectrographs will also allow to record wider wavelength intervals (e. g. Oliva and Origlia, 2008). In this way, a larger number of molecular features can be analysed simultaneously, which will consequently lead to a reduction of the error bars.

In conclusion, we affirm that there is much room for improvement. As a first step, we are currently acquiring new data to increase our statistics by studying more AGB stars in other LMC globular clusters. In this way, we could shed light on the puzzling abundance pattern that we found in NGC 1978, for instance, and put our results in the overall picture of nucleosynthesis and mixing during the late stages of stellar evolution.

3 Low-temperature Rosseland opacities

This chapter is based on the following publication.

- Lederer, M. T. and Aringer, B. 2009, *A&A*, 494, 403-416

3.1 Introduction

Radiative energy transport within a medium plays a role in a wealth of astrophysical scenarios. When the photon mean free path is short compared with the typical scale height of the medium, irrespective of the photon wavelength, this problem can be modelled by the diffusion approximation. By assuming local thermodynamic equilibrium (LTE), the definition of a harmonic mean opacity coefficient—the so-called Rosseland mean (Rosseland, 1925)—emerges naturally from the evaluation of the integrated radiative flux (see appendix B), and this mean then characterises the interaction between radiation and matter. Rosseland stated that the derivation of the analytical expression for this "characteristic function of the medium regarding its power of transmitting radiation *en bloc*" is not difficult, yet the actual calculation is. This is because one usually has to account in detail for a wide variety of absorbers. Typical applications of Rosseland mean opacities are stellar structure and evolution calculations, which span orders of magnitude in temperature and density and require the inclusion of numerous absorption and scattering processes.

As an example, we consider a low mass star in the late phase of its evolution on the asymptotic giant branch (AGB). Data for electron thermal conductivity, a basic energy transport process in the inert C–O core, are available from Cassisi et al. (2007). Tabulated high temperature opacity data (ranging from a few thousand to a few hundred million Kelvin) are provided by the OPAL collaboration (Iglesias and Rogers, 1996) and the Opacity Project (OP, Seaton, 2005). Both groups provide their data publicly through web interfaces^{22,23} where in general single element abundances can be varied. OPAL also allows to produce so-called Type II tables: starting from a given element mixture, the abundances of two elements (e. g. C and O) are enhanced by adding constant mass fractions in each case. Apart from H₂, however, no molecular contributions to the Rosseland mean are taken into account in both the OPAL and OP databases. Molecules become the dominant opacity source at temperatures lower than about 4000-5000 K, which occur in the outer envelope and atmosphere of a star on one of the giant branches—either the Red Giant Branch (RGB) or the AGB—, or in protoplanetary accretion disks. At even

²² OPAL: <http://www-phys.llnl.gov/Research/OPAL/>

²³ OP: <http://opacities.osc.edu>

lower temperatures (below approximately 1500 K), dust can be responsible for the bulk of opacity.

One of the first papers giving a detailed discussion about low-temperature mean opacities (and also summarising earlier efforts on this topic) was Alexander et al. (1983). This work evolved further and resulted in the extensive database of Alexander and Ferguson (1994) and the updated version of Ferguson et al. (2005)—henceforth AF94 and F05, respectively—that has become a standard for low-temperature opacities in the past few years. These data are based on scaled solar metal compositions (plus some tables for enhanced alpha element abundances). Returning to our AGB star example, the problem is that the chemical composition in the envelope of such an object varies. Products of the ongoing nucleosynthesis in the stellar interior are brought to the surface by a series of mixing events. The entire mechanism is dubbed third dredge-up (TDU, for a review see Busso et al., 1999 and also Sect. 1.4.1). The main burning products dredged up are freshly synthesised carbon and elements produced by the slow neutron capture process. Alterations to the element mixture result in significantly different opacity coefficients. The corresponding implications for the stellar evolution calculations were emphasised by Alexander et al. (1983). The authors provide some examples of how the Rosseland mean opacity changes when the number ratio of carbon to oxygen atoms (C/O) varies. The important role of the C/O ratio is due to the fact that of all the abundant molecules, carbon monoxide (CO) has the highest binding energy (Russell, 1934). The partial pressure of CO hardly varies with the C/O ratio in a plasma at constant temperature and pressure. In a chemical equilibrium situation, the less abundant species of carbon and oxygen are almost completely locked in the CO molecule. The remaining fraction of the more numerous atoms is free to form other molecules. The absolute number of free atoms (i. e. not bound in CO) of either oxygen or carbon primarily determines the magnitude and characteristics of the Rosseland mean opacity since CO contributes on average less than other molecular species (such as H₂O, TiO, C₂H₂, and HCN).

Although the above facts have been in principle known for a long time, they have not been accounted for in stellar evolution models, due to the lack of adequate opacity data. From the tabulated low-temperature opacities that can be found in the literature (other than AF94 and F05, e. g. Neuforge, 1993, Semenov et al., 2003, Weiss et al., 2006, Sharp and Burrows, 2007 and Freedman et al., 2008, partly monochromatic and focused on special objects such as brown dwarfs and extrasolar planets), only Helling et al. (2000) considered a case in which C/O = 1.8 in simulating winds of carbon-rich AGB stars. Dotter et al. (2007) investigated single element abundance variations and the influence on low and high temperature opacities exemplarily. Subsequently, the sensitivity of stellar evolution models to these changes was analysed and both effective temperatures and stellar lifetimes depend clearly on opacity changes due to abundance variations.

A dramatic improvement in evaluating molecular opacities with a varying amount of carbon was achieved by Marigo (2002) who illustrated how a correct treatment of opacity can affect stellar evolution tracks by using analytical AGB star models. The principle

outcomes were that observations of carbon stars can be reproduced more accurately than before and the models appear to imply that the carbon star phase is shortened considerably with a consequent reduction in the stellar yields. The opacities were estimated by chemical equilibrium calculations and analytical fits for molecular contributions to the Rosseland mean, which were combined by a simple linear summation. This was the main problem of this approach. The non-linear nature of the Rosseland mean by definition renders the method of adding up opacity contributions a fragile approximation. Moreover, the derived molecular contributions are not unique because they cannot be determined in a non-ambiguous way. The Rosseland mean emphasises transparent spectral regions, and the gaps between absorption lines from a specific molecule can be filled by other species depending on the chemistry. Thus, this interplay crucially influences the total opacity. Finally, not all relevant molecular absorbers have been taken into account in the work described above.

From this overview, we conclude that the stellar evolution community require a complete, homogeneous database containing Rosseland mean opacity coefficients with varied abundances of carbon. The aim of this work is to fill this gap. We also included abundance variations in nitrogen, since in low and intermediate mass stars mechanisms might activate the CN cycle and trigger the reconversion of carbon isotopes into nitrogen. The corresponding mechanism acting in stars of mass lower than $4 M_{\odot}$ is dubbed Cool Bottom Process (Wasserburg et al., 1995) or *extra-mixing* (see Sect. 1.4.2) which is a slow, deep circulation at the bottom of the convective envelope. Its origin is still unknown, although a number of driving mechanisms have been proposed (e. g. rotationally induced instabilities, magnetically induced circulation, gravity waves or thermohaline mixing – we refer to Busso et al., 2007 for an overview). In more massive AGB stars ($M > 4 M_{\odot}$), the "analogous" process (in the sense of converting primary carbon into nitrogen) is known as hot bottom burning (Iben, 1973).

A preliminary version of the opacity data presented in the following was applied successfully by Cristallo et al. (2007, 2008) and Lebzelter et al. (2008a) and Lederer et al. (2009), see also Chap. 2. Cristallo et al. (2007) considered a low metallicity ($Z = 1 \times 10^{-4}$) stellar model with $M = 2 M_{\odot}$. By using the new opacity coefficients, the model was able to reproduce observational data more accurately than earlier models in terms of physical properties (such as for instance the effective temperature) and the abundance pattern of the heavy elements. Information that is complementary to the data considered here can be found in Lederer and Aringer (2008a).

This chapter is structured as follows. In Sect. 3.2, we describe the tools used to generate our opacity tables. Section 3.3 summarises all data adopted in our calculations, i. e. abundances as well as atomic and molecular opacity data. We describe and justify the design of our tables in Sect. 3.4. We discuss the results in detail in Sect. 3.5, before concluding and providing a perspective on future work in Sect. 3.6.

Wavenumber interval [cm ⁻¹]		Δk [cm ⁻¹]	Number of points	
200	–	1000	5	161
1000	–	16000	4	3752
16000	–	25000	10	901
25000	–	30000	20	251
30000	–	40000	40	261
40000	–	200000	500	319
				5645

Table 3.1 Wavenumber grid

3.2 Tool and method

To generate the data presented in this work, we used the COMA code developed by Aringer (2000). For a description of improvements since the initial version, we refer to a forthcoming paper of Aringer et al. (2009); see also Sect. 2.3.2. Assuming local thermodynamic equilibrium, the program solves for the ionisation and chemical equilibrium (using the method of Tsuji, 1973) at a given temperature and density (or pressure) combination for a set of atomic abundances. From the resulting partial pressures for the neutral atoms, ions, and molecules, the continuous and line opacity is calculated at the desired wavelengths using the data listed in Sect. 3.3. The main purpose of the COMA code was originally to provide monochromatic absorption coefficients for dynamical model atmospheres of cool giants (Höfner et al., 2003). However, it has been used in a wide range of applications, for example in the process of calculating low and high resolution spectra (e. g. Aringer et al., 2002 and Lebzelter et al., 2008a, respectively) and line profile variations (Nowotny et al., 2005).

Once the monochromatic opacities $\kappa_\nu(T, \rho) \equiv \kappa(\nu, T, \rho)$ are known (T stands for the temperature and ρ for the density), the calculation of a mean opacity coefficient such as the Rosseland mean is straightforward. One has to perform a weighted integration of κ_ν over the relevant frequency range. For the Rosseland mean $\kappa_R = \kappa_R(T, \rho)$, the relation is given by

$$\frac{1}{\kappa_R} = \int_0^\infty \frac{1}{\kappa_\nu} \frac{\partial B_\nu(T)}{\partial T} d\nu \bigg/ \int_0^\infty \frac{\partial B_\nu(T)}{\partial T} d\nu, \quad (3.1)$$

where the weighting function is the partial derivative of the Planck function with respect to the temperature. The main subject of this chapter is to study not only the dependence of κ_R on the thermodynamic quantities T and ρ , but in addition the chemical composition.

In practice, the integration over ν in Eq. 3.1 must be performed at a predefined discrete frequency (or wavelength) grid. We use a grid that is based on the one described by Jørgensen et al. (1992), but we extend the wavelength range to have boundaries at $200,000 \text{ cm}^{-1}$ ($500 \text{ \AA} = 0.05 \mu\text{m}$) and 200 cm^{-1} ($50 \mu\text{m}$). This results in a total number of 5645 wavelength points at which we calculate the opacity (see Table 3.1). Helling and Jørgensen (1998) proposed to use a number of opacity sampling points for the accurate modelling of atmospheres of late-type stars that is roughly four times larger than the value used here. The same is true for the number of wavelength points in F05, who use more than 24,000 points. However, the error introduced when using a lower resolution is generally small compared with other uncertainty sources (see Sect. 3.5.3), and a smaller number of grid points has the advantage of a reduced computing time. We note that the opacity sampling technique remains—regardless of the precise number of points—a statistical method. To arrive at a realistic and complete description of the spectral energy distribution, one would need a far higher resolution ($R \approx 200,000$). In any case, the grid is sufficiently dense for a rectangle rule to be sufficient in carrying out the wavelength integration. This can be justified by comparing the numerically obtained value of the normalisation factor on the right-hand side of Eq. 3.1 with its analytical value. The formal integration limits in the definition of the Rosseland mean have to be replaced by cut-off wavelengths. These are determined by the weighting function $\partial B_\nu(T)/\partial T$ that constrains the relevant wavelength range. Like the Planck function itself, the maximum of its derivative shifts to shorter wavelengths with decreasing temperature and vice versa. At the upper wavelength limit adopted here ($50 \mu\text{m}$) and for the lowest temperature at which we generate data (about 1600 K), the weighting function has decreased to less than 1/100 relative to its maximum value. Accordingly, at the high temperature edge the weighting function at the same wavelength has dropped to almost 1/10,000 of its maximum value. Since we do not include grain opacity in our calculations that would require going to even longer wavelengths (as in F05), we definitely cover the relevant spectral range for the calculation of κ_R within the adopted parameter range. The decline in the weighting function towards shorter wavelengths (or higher frequencies) is far steeper, so that the above argument is also fulfilled at the short-wavelength cut-off.

3.3 Data sources

In the following, we briefly summarise the sources of the data entering the opacity calculations. The basic ingredient in this procedure is the relative amount of elements contained in the mixture for which we would like to know the opacity (see appendix C for details on the conversion between abundance scales). In this work, we chose to use the set of recommended values for solar element abundances compiled by Lodders (2003), which imply a solar C/O ratio of 0.501. The values for the elements C, N, and O are close to the values given by Grevesse et al. (2007); using their abundances results in $(\text{C/O})_\odot = 0.537$. The authors derive these values from a 3D hydrodynamic model of the

Ion and process	Reference
HI b-f and f-f	Karzas and Latter (1961)
H ⁻ b-f	Doughty et al. (1966)
H ⁻ f-f	Doughty and Fraser (1966)
H+H (Quasihydrogen)	Doyle (1968)
H ₂ ⁺ f-f	Mihalas (1965)
H ₂ ⁻ f-f	Somerville (1964)
C I, Mg I, Al I, Si I, He I f-f	Peach (1970)
He ⁻ f-f	Somerville (1965)
continuous e ⁻ scattering	Mihalas (1978)
Rayleigh scattering from H I	Dalgarno, quoted by Gingerich (1964)
Rayleigh scattering from H ₂	Dalgarno and Williams (1962)

Table 3.2 Continuous opacity sources

solar atmosphere, a technique that caused a downward revision of the solar CNO abundances in recent years. However, these values are still disputed. For instance, Centeno and Socas-Navarro (2008a) used spectro-polarimetric methods to argue for an oxygen abundance that is higher than claimed by Grevesse et al. (2007) and closer to previously accepted values (e. g. Grevesse and Sauval, 1998 with $(C/O)_{\odot} = 0.490$). that agree with values derived from helioseismology (e. g. Basu and Antia, 2008).

However, the data presented depend to first order only on the relative amount of carbon and oxygen, which does not differ significantly from that for the various abundance sets mentioned above. Therefore and due to the fact that C/O is a variable quantity, the current tables can serve as an approximation for applications that use abundances other than Lodders (2003), until we generate further data.

3.3.1 Continuous opacity

The routines for the calculation of the continuum opacity in COMA are based on an earlier version of the MARCS code (Jørgensen et al., 1992). The latest MARCS release was described by Gustafsson et al. (2008). We adopt the format of their Table 1 to ease comparison with their updated set of continuous opacity sources. The data that we use (and list in Table 3.2) are not as extensive. However, the most relevant sources are included, and in the low-temperature region of the presented tables in particular the molecular contribution to κ_R dominates over the continuum by several orders of magnitude.

3.3.2 Atomic lines

Atomic line data are taken from the VALD database (Kupka et al., 2000)²⁴, where we use updated version 2 data (from January 2008) here. For the atomic lines, we adopt full Voigt profiles derived from the damping constants listed in VALD. The only exception is hydrogen for which we use an interpolation in tabulated line profiles from Stehle (1995). The atomic partition functions are taken from the work of Irwin (1981), although the data for boron have been modified (Gorfer, 2005). The number of atomic lines included is 16,059,201. Split into their respective ionisation stages the numbers are: I 4,028,995, II 5,347,990, and III 6,682,216. For the ionisation energies, we refer to Stift (2000) since we use the same reference data quoted there in the current work.

3.3.3 Molecular data

In the calculation of low-temperature opacities, molecules play a critical role. We list the data that we used to calculate the tables containing Rosseland mean opacity coefficients in Table 3.3. References to the thermodynamic data (i. e. the partition function) and the line data for each molecule (displayed in the first column) are as indexed in the columns two and four, respectively. The number of lines entering the calculation is given in the third column (the original lists contained more lines). For some molecules, there is more than one line list available. The line lists that we use were selected during other projects (cited at the beginning of Sect. 3.2) proven to deliver viable results. In the case of the OH line list, the measured data from the HITRAN database contain more lines than that from Schwenke (1997). We performed some test calculations after completing the database with OH data from HITRAN. The change in our results was, however, hardly perceptible. As long as the overall opacity distribution is reproduced reasonably, the line positions do not have to be precisely correct in calculating κ_R (as opposed to applications relying on high-resolution spectral synthesis).

For the molecules C_2 and CN, we introduced some modifications to the line data. Jørgensen (1997a) suggested a scaling of the gf values for C_2 in a certain wavelength region (details are given in Loidl et al., 2001). We followed this suggestion but also investigated the effect on κ_R of not applying this scaling (see Sect. 3.5.3). The modifications to the CN line list are not crucial to the calculation of the Rosseland mean. We corrected the line positions of approximately 18,000 lines using measurements listed in the catalogue of Davis et al. (2005). The data for the molecules C_3 and C_2H_2 from Jørgensen (1997a) are only available in the form of an opacity sampling. For the generation of these data, a microturbulent velocity of 2.5 km s^{-1} was adopted. As for the calculation of the molecular line opacity, we assume Doppler profiles in each case, since there is little information about the damping constants of molecular transitions. Additionally, for the species

²⁴ VALD: <http://ams.astro.univie.ac.at/~vald/>

3 Low-temperature Rosseland opacities

Molecule	Thermodynamic data ¹	Number of Lines	Line data ²
CO	1	131 859	7
CH	2	229 134	8
C ₂	1	360 887	9
SiO	2	85 788	10
CN	1	2 533 040	8
TiO	1	22 724 670	11
H ₂ O	3	27 693 367	12
HCN/HNC	4	33 454 021	13
OH	1	36 601	14
VO	1	3 171 552	15
CO ₂	2	1 032 266	16
SO ₂	5	29 559	17
HF	1	462	18
HCl	1	447	17
ZrO	1	16 391 195	19
YO	1	975	20
FeH	6	116 300	6
CrH	1	13 824	21
C ₂ H ₂	-	opacity sampling	22
C ₃	-	opacity sampling	22

¹ (1) Sauval and Tatum (1984), (2) Rossi et al. (1985), (3) Vidler and Tennyson (2000), (4) Barber et al. (2002), (5) Irwin (1988), (6) Dulick et al. (2003)

² (7) Goorvitch and Chackerian (1994), (8) Jørgensen (1997a), (9) Querci et al. (1974), (10) Langhoff and Bauschlicher (1993), (11) Schwenke (1998), (12) Barber et al. (2006), (13) Harris et al. (2006), (14) Schwenke (1997), (15) Alvarez and Plez (1998), (16) Rothman et al. (1995), (17) Rothman et al. (2005), (18) Tipping (2007), (19) Plez (2007), (20) Littleton (2007), (21) Bauschlicher et al. (2001), (22) Jørgensen et al. (1989)

Table 3.3 Molecular line data

Metallicity	Enhancement factors											
Z	¹² C								¹⁴ N			
0.04	1.0	1.2	1.5	1.8	2.0	2.2	3.0		1.0	1.2	1.5	
0.02	1.0		1.5	1.8	2.0	2.2	3.0	5.0	1.0	1.5	2.0	
0.01	1.0		1.5	1.8	2.0	2.2	5.0	10.0	1.0	1.5	3.0	
0.008	1.0			1.8	2.0	2.2	5.0	10.0	20.0	1.0	2.0	4.0
0.006	1.0			1.8	2.0	2.2	5.0	10.0	30.0	1.0	2.5	5.0
0.005	1.0			1.8	2.0	2.2	5.0	10.0	30.0	1.0	2.5	5.0
0.004	1.0			1.8	2.0	2.2	5.0	10.0	30.0	1.0	2.5	5.0
0.003	1.0			1.8	2.0	2.2	6.0	20.0	70.0	1.0	3.0	8.0
0.002	1.0			1.8	2.0	2.2	6.0	20.0	70.0	1.0	3.0	8.0
0.001	1.0			1.8	2.0	2.2	8.0	35.0	150.0	1.0	4.0	16.0
0.0003	1.0			1.8	2.0	2.2	12.0	75.0	500.0	1.0	7.0	50.0
0.0001	1.0			1.8	2.0	2.2	18.0	150.0	1500.0	1.0	12.0	150.0
0.00003	1.0			1.8	2.0	2.2	27.0	350.0	5000.0	1.0	22.0	500.0
0.00001	1.0			1.8	2.0	2.2	40.0	750.0	15000.0	1.0	40.0	1500.0

Table 3.4 Metallicities and enhancement factors

dominating the overall opacity and in regions close to bandheads, even the wings of the strongest lines will contribute less to the opacity than the Doppler cores of the numerous overlapping neighbour lines.

The chemical equilibrium constants used in calculating the molecule partial pressures are those from Tsuji (1973) with updates described in Helling et al. (1996). In the case of C₃, we utilised data published by Irwin (1981). All molecules (a total number of 314 species) enter into the equation of state.

3.4 Table design

We tabulate the logarithm of the Rosseland mean opacity $\log \kappa_{\text{R}} [\text{cm}^2 \text{g}^{-1}]$ as a function of $\log T [\text{K}]$, the logarithm of the gas temperature, and $\log R [\text{g cm}^{-3} \text{K}^{-3} 10^{18}]$, where $R \equiv \rho/T_6^3$.²⁵ ρ and T_6 represents the density in units of g cm^{-3} and the temperature in millions of Kelvin, respectively. The ranges covered are $3.2 \leq \log T [\text{K}] \leq 4.05$ with a step size

²⁵ The auxiliary quantity R allows to cover the relevant T - ρ region on a compact rectangular grid. Mayer and Duschl (2005) emphasise that there is also a physical meaning to R , namely that it represents constant ratios of gas to radiation pressure. At $R \approx -4.5$ gas and radiation pressure are approximately equal.

of 0.05, and $-7.0 \leq \log R \leq 1.0$ with a step size of 0.5 (see also showcases 3.2 and 3.3, as well as Fig. 3.4). The low-temperature cut-off was set to be the temperature at which grains may become the major opacity source (cf. e. g. F05). However, typical AGB stellar evolution models do not attain such low temperatures. We would like to emphasise that dust formation is usually not an equilibrium process (Gail and Sedlmayr, 1988), and thus an a priori tabulation of grain opacities can be affected by large uncertainties. At the highest value of $\log T$, the contribution of molecules to the mean opacity vanishes and a smooth transition to high temperature opacity data is possible (see Sect. 3.5.1). Data are available for 14 different values of Z (cf. Table 3.4) that depicts the total mass fraction of all elements heavier than helium. The metallicity spans a range from $Z = 1 \times 10^{-5}$ to the Magellanic clouds metallicity range ($Z \approx 1 \times 10^{-3} - 1 \times 10^{-2}$ van den Bergh, 2000a, 2000b), where the grid is a bit denser in terms of Z , and the solar metallicity to super-solar metallicity ($Z = 0.04$). We calculated tables for three different mass fractions of hydrogen ($X \in \{0.5, 0.7, 0.8\}$). Thus, the data cover the supposedly prior field of application, namely the outer layers of an AGB star, where such values of X occur. Initially, we calculated a master table for each metallicity, in which the metal composition was linearly scaled from the abundances given by Lodders (2003) to arrive at the respective Z value. From these abundances, we then enhanced the mass fractions of ^{12}C and ^{14}N in steps that depended on the initial metallicity (see Table 3.4). Since this produced an increase in the overall metallicity Z , we followed the OPAL approach and reduced the mass fraction of ^4He to fulfil $X + Y + Z = 1$.

The number of enhancement factors is constrained by a trade-off between numerical accuracy and computational costs in the generation and application of the tables. Due to the special role of carbon in conjunction with oxygen (see Sect. 3.1), the number of enhancement factors is higher than for nitrogen.²⁶ We calculated opacities for 7 different mass fractions of ^{12}C . The starting point was the mass fraction that results from scaling all element abundances to the metallicity under consideration. All other carbon mass fractions resulted from multiplying this mass fraction by factors chosen as follows. For each metallicity, we use the factors 1.8, 2.0, and 2.2. The C/O ratio emerging from the adopted scaled solar abundances was about 0.5. Thus, multiplying the initial $X(^{12}\text{C})$ by 2.0, we inferred that $\text{C/O} \approx 1$, where the molecular opacity in general reaches a minimum at low temperatures. As one can see for example in Fig. 3.9, the molecular absorption increased sharply on both sides of this minimum, while, towards much higher and lower C/O ratios, there was some type of saturation. To resolve this sharp turnaround, we included the factors 1.8 and 2.2 (corresponding to $\text{C/O} \approx 0.9$ and 1.1, respectively). In stellar evolution models of low metallicity AGB stars this is probably of minor importance because the transition to a carbon star is usually rapid and occurs within a few

²⁶ Here we deviate from the original design used in Cristallo et al. (2007) and Lederer and Aringer (2008a), where we adopted 5 enhancement factors for both carbon and nitrogen.

dredge-up episodes (e. g. Marigo and Girardi, 2007). The respective highest enhancement factor is related to the initial metallicity. From the work of Abia et al. (2003) and references therein and the first application of our data by Cristallo et al. (2007, 2008), we derived information about the final carbon abundances reached in AGB stars. These determined the maximum enhancement factors in our tables for the metallicities under consideration (for instance $Z = 1 \times 10^{-2}, 1 \times 10^{-3}, 1 \times 10^{-4}$). At all other metallicities, we derived the highest factors using a roughly linear relation between $\log Z$ and $\log f_{C,\max}$ (where we denote the enhancement factor as f). The remaining two factors for carbon are distributed almost equispaced on a logarithmic scale between $f = 2$ and $f_{C,\max}$ at the lower metallicities. For high Z with low final enhancements, we shifted factors from the carbon-rich regime to the region in which $C/O < 1$. For ^{14}N , we introduced two additional factors beyond the initial abundance. The expected final overabundance of nitrogen is much lower than for carbon, and we set $f_{C,\max}/f_{N,\max} = 10$ for the lowest values of Z , decreasing this value for increasing Z . The intermediate enhancement factor for nitrogen was set to bisect the logarithmic interval approximately between the two other factors. An overview of all enhancement factors at each metallicity is given in Table 3.4.

We have not yet considered varied alpha element abundances, although one expects an increased value of $[O/Fe]$ at low metallicities (e. g. Hill et al., 2000). The reason is the sharp increase in the number of tables, if one retains the previously outlined data structure. In its current version, the database contains $3 \times 7 \times 3 = 63$ tables per metallicity. Varying the abundance of oxygen also influences the C/O ratio, which is the decisive quantity for the molecular opacity at low temperatures. This in turn requires alterations to the enhancement factors of carbon, since one wishes to retain at least one point where $C/O = 1$, even for an enhanced oxygen abundance. Establishing a scheme with a minimal number of enhancement factors for three elements (or element groups) is therefore not straightforward if one is attempting to retain as much information as possible with respect to the role of the C/O ratio. In place of enhancement factors, one could add constant amounts of one element (group) in terms of a mass fraction, as completed in the OPAL Type II tables. Only the application of the data in their current form will provide us with information about the feasibility of our approach and whether the data should be arranged in a different way. Future work will be dedicated to these questions.

3.5 Results and discussion

The calculation of Rosseland mean opacities for scaled solar metal mixtures has been discussed extensively in many papers (see Sect. 3.1 for citations). Since we find good agreement with data from other groups (see Sect. 3.5.1), we only briefly restate the main points of this procedure. In Fig. 3.1, we provide an overview of the contents of the Rosseland opacity database using examples. We refer to individual panels in the following paragraphs. Generally speaking, molecules cause the mean opacity to vary dramatically as a

function of temperature in a similar way for each hydrogen mass fraction X and metallicity Z (left panels of Fig. 3.1) that we include in our database. Beyond a temperature corresponding to $\log T = 3.6$ to 3.7 (depending on Z and $\log R$), the contribution of molecules to κ_R vanishes and only continuous sources and atomic lines block the radiation field.

AF94 provided an in-depth discussion about which type of opacity is dominant in different regions of the parameter space. They presented a detailed treatment of the main molecular opacity sources, which were in this case water (H_2O)—accounting for the large bump at low temperatures—and titanium oxide (TiO). They also provided information about the monochromatic absorption coefficients of these molecules. Beside H_2O and TiO , there is a number of other molecules that deliver non-negligible contributions to the Rosseland opacity in the oxygen-rich case (cf. Lederer and Aringer, 2008a). At higher temperatures, CN and CO contribute to κ_R , and VO , OH , and SiO (ordered by decreasing importance) should also be taken into account. Calculations based on these 7 molecules result in opacity coefficients that are accurate to about 10 per cent compared with the full dataset when the metal mixture is oxygen-rich. The further inclusion of CrH and YO reduces this error to below 3 per cent on average. The temperature ranges in which different molecules contribute to κ_R indicated in the bottom right panel of Fig. 3.1 are estimated by omitting the respective molecules in the calculation of κ_R and by checking where the change in this quantity exceeds 5 per cent with respect to the complete dataset. However, the limits derived from this criterion vary with the value of $\log R$ under consideration. We use $\log R = -1.5$, which is typical of the envelopes of AGB stars (Sergio Cristallo, private communication).

An increase in the carbon content of the metal mixture while the amount of oxygen remains at its original value (i. e. an increase in the C/O ratio) has distinct effects on the Rosseland mean opacity. We refer to Sect. 3.1 and the previous section for a description of the respective mechanism. In the transition from the oxygen-rich regime (Fig. 3.1, top left) to the carbon-rich regime (Fig. 3.1, top right), one can distinguish between two cases. At lower temperatures (below $\log T = 3.4$; we refer in the following to the case shown in Fig. 3.2, i. e. $\log R = -3.0$), the opacity first decreases, due to the above described property of CO , which causes the following mechanism. As C/O increases from its initial value of about 0.5 and approaches 1, more oxygen becomes bound in CO and fewer oxygen atoms are free to form molecules with a large overall absorption such as H_2O . Close to $\text{C/O} = 1$ (not necessarily at an exact equal amount of C and O), the opacity reaches a minimum as the partial pressures of oxygen-bearing molecules drop substantially, while the abundances of carbon-bearing molecules only begin to rise to significant levels. As the amount of carbon continues to increase, thus incrementing C/O beyond 1, the opacity increases due to the formation of polyatomic carbon-bearing molecules such as C_2H_2 or HCN . These polyatomic molecules are obviously most relevant at lower temperatures. In addition, C_3 and C_2 produce a bump in the opacity at high carbon enrichments.

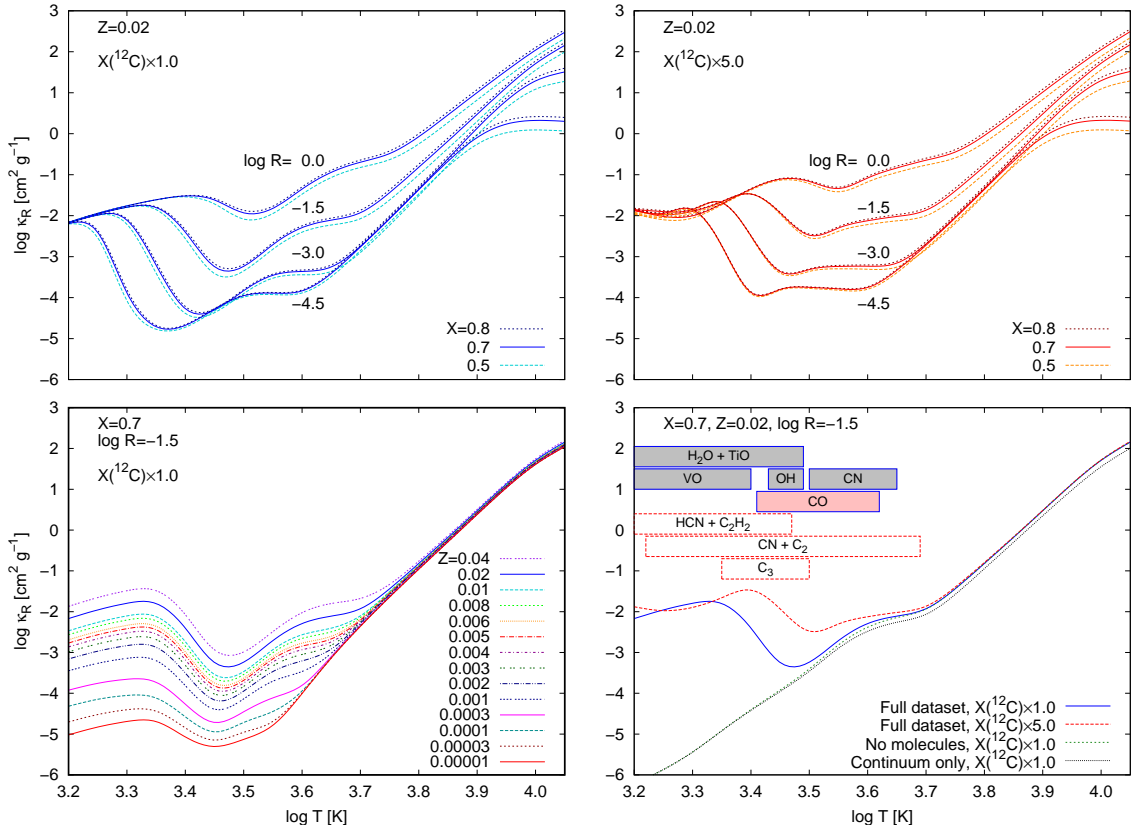


Figure 3.1 Contents of the opacity database in some showcases. Top left panel: Roseland mean opacities at constant $\log R$ for $Z = 0.02$ as a function of $\log T$ for different values of X . The qualitative behaviour is fairly independent of X and Z and varies smoothly with $\log R$ at fixed abundances of carbon and nitrogen (the latter is not enhanced in any of the panels shown in this figure). Bottom left panel: The molecular opacity decreases when lowering the metallicity, but the structure with a bump at low temperatures due to the molecular contribution to the opacity is conserved. Top right panel: For the case where carbon is enhanced the molecules also produce high opacities at low $\log T$, although the shape of the curve differs noticeably from the standard case. Bottom right panel: The reason for the different structure in the opacities is that different molecules contribute to the opacity in the carbon-rich case (white boxes), in contrast to the oxygen-rich case (dark-grey boxes). The CO molecule contributes in both cases as well as CN, although at different orders of magnitude in each case. The extension of each box provides an indication of the temperature where the sources contribute but does not contain information about the order of magnitude of the contribution. The total contribution of molecules and atoms is assessed by leaving out these opacity sources in the calculations. All curves have been smoothed using cubic splines. See text for details.

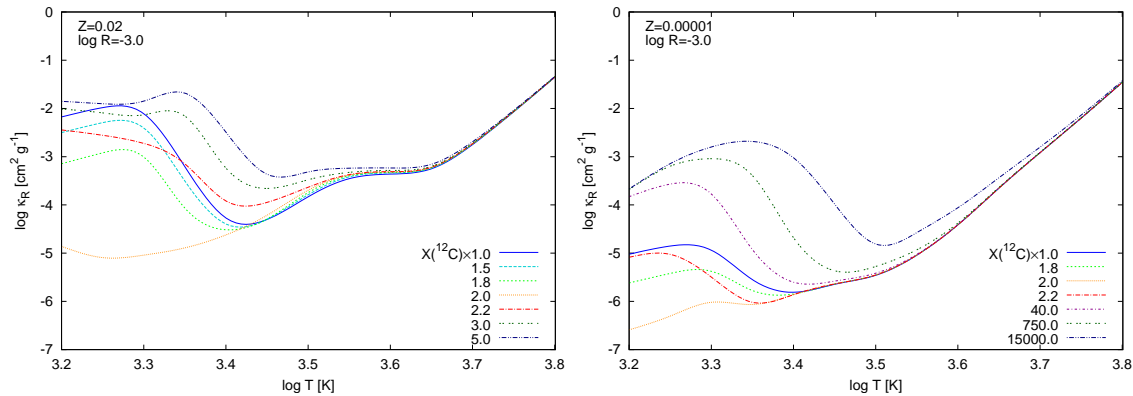


Figure 3.2 Rosseland opacity changing with the carbon content in the metal mixture as a function of temperature. We show curves for two metallicities, $Z = 0.02$ and the lowest metallicity in this database $Z = 0.00001$, at a value of $\log R = -3.0$. The full line represents the solar scaled metal mixture with $C/O \approx 0.5$. An increase in the carbon mass fraction first causes a drop in κ_R at low temperatures as C/O approaches 1 ($X(^{12}\text{C}) \times 2.0$, dotted line), because more oxygen atoms get bound in CO and less other molecular opacity carriers can be formed. When C/O rises beyond 1 this trend is reversed and the mean opacity increases again due to the formation of carbon-bearing molecules. At higher temperatures the opacity is growing monotonically due to CO, CN and atomic carbon. See also Fig. 3.9. All curves have been smoothed using cubic splines.

The situation at higher temperatures (up to $\log T = 3.7$) is, however, different. Besides CO, the contribution of which remains almost constant, only CN and C_2 are relevant opacity sources (cf. Fig. 3.1, bottom right panel), while other molecules that are important to the Rosseland opacity are dissociated at these temperatures. The partial pressures of these molecules rise monotonically with the carbon abundance and thus the opacity at high $\log T$ increases in the same manner. At intermediate temperature (around $\log T = 3.4$) where many different opacity sources contribute, the aforementioned mechanisms compete and the behaviour of κ_R is a more complex function of C/O .

Briefly summarised, changes in the chemistry alter the Rosseland mean opacity, whereas variations in the C/O ratio have the most pronounced effect. An oxygen-rich composition ($C/O < 1$) results in a different group of molecules accounting for the opacity than in the carbon-rich case ($C/O > 1$). Furthermore, carbon-bearing molecules have different spectral appearances from the oxygen-bearing ones and thus cause κ_R to have a different functional behaviour. Helling et al. (2000) provided examples of monochromatic absorption coefficients for carbon-bearing molecules. The only two molecules that contribute significantly for either chemistry are CO and CN.

As emphasised earlier, the presented data are primarily relevant to the envelopes of evolved low mass stars. Chemical composition variations due to the TDU acting in AGB

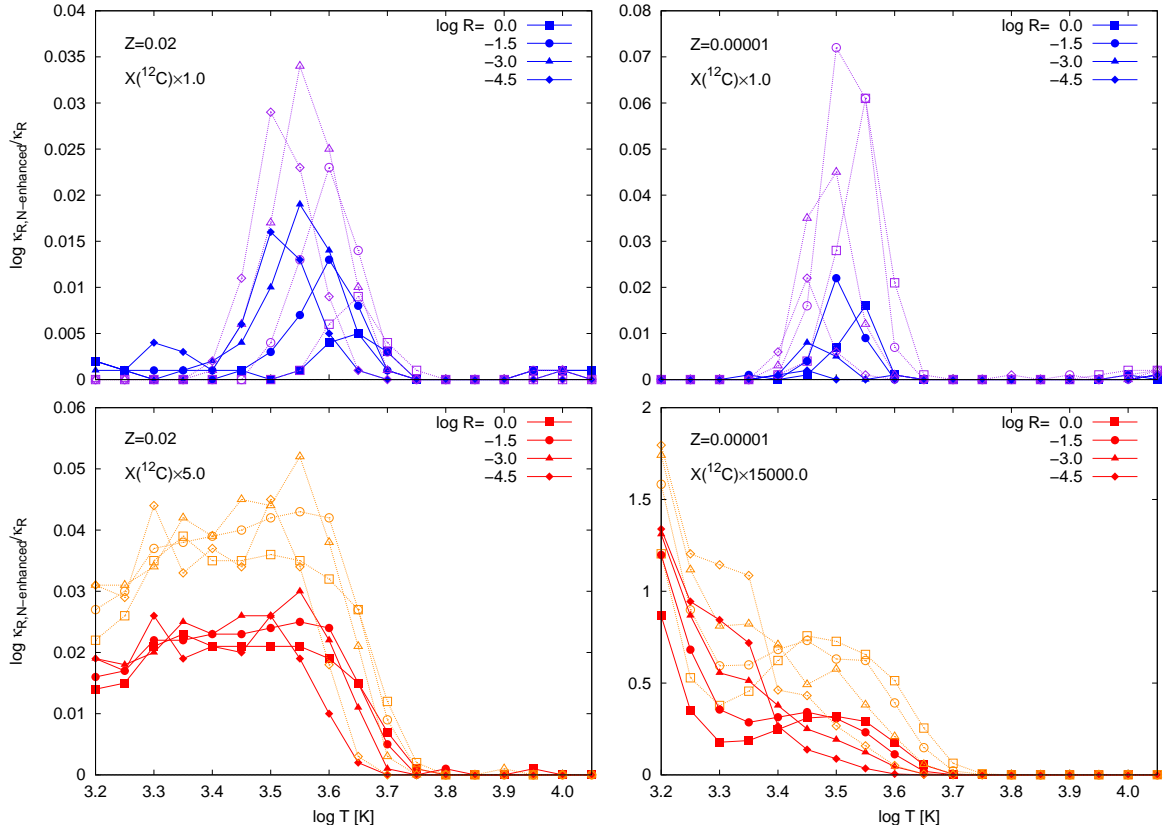


Figure 3.3 Effects of an increased nitrogen abundance on the Rosseland mean opacity at various $\log R$ values relative to the case without any nitrogen enhancement. The filled and empty symbols refer to intermediate and maximum enhancement factors of ^{14}N , respectively. For $Z = 0.02$ (left panels), these are 1.5 and 2, whereas for $Z = 0.00001$ (right panels), we have 40 and 1500. On the top, we show the cases for the oxygen-rich case (default carbon abundance). Here the increase in opacity is due to the CN molecule. The bottom panels refer to maximum enhanced ^{12}C (i. e. the carbon-rich case), where HCN also contributes to the mean opacity at lower temperatures. Note the different scales on the y-axis.

stars concern mostly the enrichment in carbon. However, the dredged-up carbon in the envelope can be inputted back into the CN cycle, which partly converts ^{12}C to ^{14}N (see Sect. 3.1). By varying the abundance of nitrogen (more precisely ^{14}N), we add a further dimension to our data tables. These alterations have more direct consequences on the behaviour of the Rosseland mean in the sense that an increase in nitrogen always causes an increase in the opacity (in contrast to an increase in carbon, which can lower κ_R for a certain parameter range; see above). Nitrogen is present only within two molecules being considered here, i. e. CN and HCN, and can directly influence the Rosseland

opacity only via these compounds. Other molecules containing nitrogen indirectly affect the opacity by altering the molecular partial pressures in chemical equilibrium. In the oxygen-rich case, the effect of an increase in ^{14}N is relatively moderate, because the partial pressure of CN is in general low. In the carbon-rich case, the abundance of CN is however much higher, HCN is also present in significant amounts, and, as a consequence, the opacity can increase considerably. These properties of κ_{R} are illustrated in Fig. 3.3 for the two enhancement factors of ^{14}N . On top, we present results for two different metallicities without any carbon enhancement, where the increase in opacity is due to CN only. In the respective bottom panels, the carbon abundance has been enhanced to its maximum value and HCN causes a considerable rise in κ_{R} at lower temperatures. In the high temperature range, some minor contributions from atomic nitrogen to the opacity are evident.

The results discussed above are condensed into the form of 14 separate files, one for each metallicity.²⁷ Each file consists of a header indicating the abundances used, the initial metallicity, the initial mass fractions for ^{12}C , ^{14}N , and the alpha elements, and a look-up table for the true data block. An example header is shown in showcase 3.1 for the tables with initial metallicity $Z = 0.02$. The final file consists of 63 rectangular data arrays, where $\log \kappa_{\text{R}}$ is tabulated as a function of $\log T$ and $\log R$. Two examples of such data arrays are given in the showcases 3.2 and 3.3, the content of which is visualised in Fig. 3.4. The tables are ordered such that the mass fraction $X(^{12}\text{C})$ varies the most rapidly followed by the hydrogen mass fraction and $X(^{14}\text{N})$. For future compatibility, a data field for the alpha element enhancement factor was introduced into the look-up table.

3.5.1 Comparison with other data

We compare our tables based on a scaled solar metal mixture with data from F05 based on the same abundances as in this work. A direct comparison with AF94 is not possible because there are, of course, no tables based on the Lodders (2003) abundances. We refer to F05 for a comparison of AF94 and F05. In general, when we compare our values to other opacity tables in the following figures, we always depict data from our database as κ_{COMA} , while the respective reference values are labelled κ_{R} . Despite the numerous differences between the COMA and F05 approach, we find reasonable agreement between both sets of data. For the case shown in Fig. 3.5 ($Z = 0.02$), the difference between the COMA and F05 values does not exceed 15 per cent for temperatures as low as $\log T = 3.5$. The discrepancies at lower temperatures are higher (up to 35 per cent) and can in fact be ascribed to several things. First and foremost, the use of different sets

²⁷ The tables are only available in electronic form at the CDS via anonymous ftp to [cdsarc.u-strasbg.fr](ftp://cdsarc.u-strasbg.fr) (130.79.128.5) or via <http://cdsweb.u-strasbg.fr/cgi-bin/qcat?J/A+A/>. Due to the CDS data policy, the data structure is different from the one described in this work. The files in the format that is referred to here will be provided on request.

```
#####
# ROSSELAND MEAN OPACITY COEFFICIENTS #
#-----#
# Lodders 2003 # Abundances #
# Z = 0.02 # Initial metallicity #
#-----#
# X( 12C ) = 3.28816E-03 # Initial mass fractions #
# X( 14N ) = 1.06473E-03 #
# X( 16O ) = 8.82187E-03 #
# X( 20Ne ) = 1.55487E-03 #
# X( 24Mg ) = 7.58811E-04 #
# X( 28Si ) = 1.00991E-03 #
# X( 32S ) = 5.31113E-04 #
# X( 40Ca ) = 9.56690E-05 #
# X( 48Ti ) = 3.31868E-06 #
#####

# TABLE SUMMARY #####
## X Y Z C/O 12C 14N Alpha
1 0.5 0.480000 0.020000 0.501 1.0 1.0 1.0
2 0.5 0.478356 0.021644 0.749 1.5 1.0 1.0
3 0.5 0.477369 0.022631 0.898 1.8 1.0 1.0
4 0.5 0.476712 0.023288 0.997 2.0 1.0 1.0
5 0.5 0.476054 0.023946 1.096 2.2 1.0 1.0
6 0.5 0.473424 0.026576 1.492 3.0 1.0 1.0
7 0.5 0.466847 0.033153 2.484 5.0 1.0 1.0
8 0.7 0.280000 0.020000 0.501 1.0 1.0 1.0
9 0.7 0.278356 0.021644 0.749 1.5 1.0 1.0
10 0.7 0.277369 0.022631 0.898 1.8 1.0 1.0
11 0.7 0.276712 0.023288 0.997 2.0 1.0 1.0
12 0.7 0.276054 0.023946 1.096 2.2 1.0 1.0
13 0.7 0.273424 0.026576 1.492 3.0 1.0 1.0
14 0.7 0.266847 0.033153 2.484 5.0 1.0 1.0
15 0.8 0.180000 0.020000 0.501 1.0 1.0 1.0
16 0.8 0.178356 0.021644 0.749 1.5 1.0 1.0
17 0.8 0.177369 0.022631 0.898 1.8 1.0 1.0
18 0.8 0.176712 0.023288 0.997 2.0 1.0 1.0
19 0.8 0.176054 0.023946 1.096 2.2 1.0 1.0
20 0.8 0.173424 0.026576 1.492 3.0 1.0 1.0
21 0.8 0.166847 0.033153 2.484 5.0 1.0 1.0
22 0.5 0.479468 0.020532 0.501 1.0 1.5 1.0
23 0.5 0.477824 0.022176 0.749 1.5 1.5 1.0
24 0.5 0.476837 0.023163 0.898 1.8 1.5 1.0
25 0.5 0.476179 0.023821 0.997 2.0 1.5 1.0
26 0.5 0.475522 0.024478 1.096 2.2 1.5 1.0
27 0.5 0.472891 0.027109 1.492 3.0 1.5 1.0
28 0.5 0.466315 0.033685 2.484 5.0 1.5 1.0
29 0.7 0.279468 0.020532 0.501 1.0 1.5 1.0
30 0.7 0.277824 0.022176 0.749 1.5 1.5 1.0
31 0.7 0.276837 0.023163 0.898 1.8 1.5 1.0
32 0.7 0.276179 0.023821 0.997 2.0 1.5 1.0
33 0.7 0.275522 0.024478 1.096 2.2 1.5 1.0
34 0.7 0.272891 0.027109 1.492 3.0 1.5 1.0
35 0.7 0.266315 0.033685 2.484 5.0 1.5 1.0
36 0.8 0.179468 0.020532 0.501 1.0 1.5 1.0
37 0.8 0.177824 0.022176 0.749 1.5 1.5 1.0
38 0.8 0.176837 0.023163 0.898 1.8 1.5 1.0
39 0.8 0.176179 0.023821 0.997 2.0 1.5 1.0
40 0.8 0.175522 0.024478 1.096 2.2 1.5 1.0
41 0.8 0.172891 0.027109 1.492 3.0 1.5 1.0
42 0.8 0.166315 0.033685 2.484 5.0 1.5 1.0
43 0.5 0.478935 0.021065 0.501 1.0 2.0 1.0
44 0.5 0.477291 0.022709 0.749 1.5 2.0 1.0
45 0.5 0.476305 0.023695 0.898 1.8 2.0 1.0
46 0.5 0.475647 0.024353 0.997 2.0 2.0 1.0
47 0.5 0.474989 0.025011 1.096 2.2 2.0 1.0
48 0.5 0.472359 0.027641 1.492 3.0 2.0 1.0
49 0.5 0.465783 0.034217 2.484 5.0 2.0 1.0
50 0.7 0.278935 0.021065 0.501 1.0 2.0 1.0
51 0.7 0.277291 0.022709 0.749 1.5 2.0 1.0
52 0.7 0.276305 0.023695 0.898 1.8 2.0 1.0
53 0.7 0.275647 0.024353 0.997 2.0 2.0 1.0
54 0.7 0.274989 0.025011 1.096 2.2 2.0 1.0
55 0.7 0.272359 0.027641 1.492 3.0 2.0 1.0
56 0.7 0.265783 0.034217 2.484 5.0 2.0 1.0
57 0.8 0.178935 0.021065 0.501 1.0 2.0 1.0
58 0.8 0.177291 0.022709 0.749 1.5 2.0 1.0
59 0.8 0.176305 0.023695 0.898 1.8 2.0 1.0
60 0.8 0.175647 0.024353 0.997 2.0 2.0 1.0
61 0.8 0.174989 0.025011 1.096 2.2 2.0 1.0
62 0.8 0.172359 0.027641 1.492 3.0 2.0 1.0
63 0.8 0.165783 0.034217 2.484 5.0 2.0 1.0
#####
```

Showcase 3.1 Table header of the file 103.Z.02.karo. It consists of information about the adopted solar abundances, the initial metallicity, and the mass fractions of the main isotopes of carbon, nitrogen, and the alpha elements. Moreover, it contains a look-up table for the actual data blocks (compare showcases 3.2 and 3.3).

3 Low-temperature Rosseland opacities

##	X	Y	Z	C/O	12C	14N	Alpha										
8	0.7	0.280000	0.020000	0.501	1.0	1.0	1.0										
log R																	
log T	-7.000	-6.500	-6.000	-5.500	-5.000	-4.500	-4.000	-3.500	-3.000	-2.500	-2.000	-1.500	-1.000	-0.500	0.000	0.500	1.000
3.200	-3.906	-3.180	-2.602	-2.314	-2.222	-2.194	-2.184	-2.179	-2.176	-2.174	-2.172	-2.169	-2.167	-2.164	-2.161	-2.158	-2.155
3.250	-4.968	-4.773	-4.330	-3.662	-2.956	-2.407	-2.119	-2.017	-1.983	-1.969	-1.962	-1.957	-1.952	-1.948	-1.943	-1.938	-1.933
3.300	-4.943	-4.929	-4.893	-4.775	-4.459	-3.885	-3.181	-2.545	-2.108	-1.900	-1.823	-1.794	-1.779	-1.769	-1.761	-1.753	-1.744
3.350	-4.686	-4.772	-4.824	-4.836	-4.807	-4.710	-4.438	-3.902	-3.207	-2.556	-2.072	-1.800	-1.685	-1.637	-1.612	-1.595	-1.579
3.400	-4.269	-4.348	-4.443	-4.543	-4.629	-4.677	-4.667	-4.560	-4.271	-3.730	-3.042	-2.402	-1.928	-1.650	-1.519	-1.455	-1.416
3.450	-4.069	-4.076	-4.104	-4.151	-4.213	-4.284	-4.345	-4.362	-4.302	-4.124	-3.775	-3.245	-2.618	-2.037	-1.617	-1.371	-1.240
3.500	-4.056	-4.040	-4.014	-3.986	-3.965	-3.954	-3.941	-3.906	-3.832	-3.706	-3.510	-3.237	-2.879	-2.434	-1.931	-1.470	-1.143
3.550	-3.874	-3.945	-3.979	-3.979	-3.950	-3.890	-3.791	-3.646	-3.455	-3.226	-2.973	-2.709	-2.436	-2.144	-1.822	-1.465	-1.098
3.600	-3.272	-3.445	-3.600	-3.726	-3.811	-3.837	-3.782	-3.626	-3.361	-3.020	-2.651	-2.292	-1.958	-1.648	-1.351	-1.056	-0.760
3.650	-2.503	-2.719	-2.923	-3.113	-3.280	-3.412	-3.477	-3.434	-3.251	-2.937	-2.538	-2.109	-1.690	-1.300	-0.943	-0.616	-0.311
3.700	-1.752	-1.978	-2.199	-2.410	-2.604	-2.764	-2.862	-2.861	-2.750	-2.546	-2.269	-1.928	-1.532	-1.110	-0.695	-0.305	0.053
3.750	-1.099	-1.305	-1.515	-1.722	-1.914	-2.072	-2.168	-2.169	-2.071	-1.901	-1.686	-1.439	-1.162	-0.846	-0.484	-0.090	0.306
3.800	-0.654	-0.771	-0.920	-1.083	-1.239	-1.366	-1.439	-1.436	-1.354	-1.210	-1.027	-0.818	-0.591	-0.344	-0.072	0.233	0.574
3.850	-0.503	-0.502	-0.519	-0.562	-0.620	-0.673	-0.698	-0.679	-0.611	-0.500	-0.353	-0.179	0.016	0.228	0.459	0.712	0.989
3.900	-0.485	-0.444	-0.379	-0.287	-0.184	-0.092	-0.015	0.057	0.134	0.226	0.339	0.475	0.632	0.809	1.005	1.222	1.461
3.950	-0.493	-0.449	-0.364	-0.222	-0.015	0.235	0.476	0.665	0.806	0.919	1.021	1.127	1.245	1.382	1.538	1.718	1.921
4.000	-0.498	-0.462	-0.383	-0.234	0.003	0.324	0.688	1.026	1.288	1.473	1.604	1.710	1.810	1.917	2.039	2.182	2.350
4.050	-0.478	-0.457	-0.396	-0.264	-0.032	0.302	0.707	1.129	1.509	1.804	2.011	2.157	2.270	2.371	2.475	2.592	2.727

Showcase 3.2 Example data block from the file 103.Z.02.karo with $Z = 0.02$, $X = 0.7$, and scaled solar carbon and nitrogen abundances. The contents of this table are visualised in Fig. 3.4 (left panel). The headline is reproduced from the look-up table (showcase 3.1).

##	X	Y	Z	C/O	12C	14N	Alpha										
35	0.7	0.266315	0.033685	2.484	5.0	1.5	1.0										
log R																	
log T	-7.000	-6.500	-6.000	-5.500	-5.000	-4.500	-4.000	-3.500	-3.000	-2.500	-2.000	-1.500	-1.000	-0.500	0.000	0.500	1.000
3.200	-2.098	-2.053	-1.999	-1.928	-1.869	-1.837	-1.825	-1.825	-1.832	-1.841	-1.853	-1.864	-1.871	-1.869	-1.852	-1.817	-1.755
3.250	-2.198	-2.060	-1.991	-1.958	-1.944	-1.928	-1.897	-1.879	-1.884	-1.905	-1.932	-1.958	-1.980	-1.997	-2.004	-1.993	-1.956
3.300	-3.894	-3.319	-2.715	-2.216	-1.927	-1.823	-1.810	-1.825	-1.829	-1.828	-1.841	-1.873	-1.914	-1.953	-1.983	-1.999	-1.993
3.350	-4.294	-4.294	-4.160	-3.818	-3.304	-2.713	-2.158	-1.789	-1.657	-1.641	-1.641	-1.637	-1.640	-1.658	-1.689	-1.720	-1.741
3.400	-4.023	-4.024	-4.033	-4.039	-4.008	-3.854	-3.522	-3.035	-2.469	-1.930	-1.578	-1.448	-1.396	-1.356	-1.329	-1.322	-1.329
3.450	-3.983	-3.947	-3.909	-3.867	-3.825	-3.782	-3.720	-3.590	-3.339	-2.953	-2.451	-1.908	-1.452	-1.205	-1.087	-1.013	-0.981
3.500	-4.011	-3.980	-3.931	-3.873	-3.807	-3.724	-3.614	-3.470	-3.290	-3.064	-2.785	-2.454	-2.060	-1.598	-1.143	-0.906	-1.032
3.550	-3.759	-3.860	-3.911	-3.908	-3.858	-3.767	-3.634	-3.451	-3.209	-2.916	-2.597	-2.277	-1.963	-1.646	-1.317	-0.977	-0.937
3.600	-3.164	-3.330	-3.488	-3.624	-3.718	-3.743	-3.674	-3.496	-3.212	-2.858	-2.479	-2.100	-1.735	-1.390	-1.061	-0.745	-0.536
3.650	-2.474	-2.676	-2.866	-3.043	-3.204	-3.331	-3.390	-3.336	-3.147	-2.831	-2.433	-2.004	-1.585	-1.191	-0.821	-0.472	-0.167
3.700	-1.746	-1.968	-2.184	-2.387	-2.571	-2.723	-2.813	-2.807	-2.689	-2.479	-2.200	-1.862	-1.472	-1.054	-0.640	-0.249	0.115
3.750	-1.098	-1.302	-1.511	-1.716	-1.904	-2.057	-2.147	-2.143	-2.040	-1.865	-1.646	-1.398	-1.120	-0.805	-0.447	-0.057	0.338
3.800	-0.653	-0.770	-0.919	-1.081	-1.235	-1.360	-1.430	-1.423	-1.338	-1.191	-1.005	-0.794	-0.565	-0.317	-0.044	0.261	0.601
3.850	-0.502	-0.501	-0.518	-0.560	-0.618	-0.670	-0.693	-0.672	-0.603	-0.489	-0.341	-0.166	0.030	0.244	0.475	0.729	1.008
3.900	-0.484	-0.443	-0.378	-0.285	-0.183	-0.090	-0.012	0.060	0.138	0.232	0.346	0.483	0.641	0.818	1.015	1.233	1.473
3.950	-0.492	-0.447	-0.363	-0.220	-0.013	0.237	0.479	0.669	0.810	0.923	1.027	1.134	1.252	1.389	1.546	1.726	1.930
4.000	-0.497	-0.460	-0.381	-0.232	0.006	0.327	0.692	1.031	1.295	1.480	1.612	1.719	1.819	1.926	2.048	2.192	2.360
4.050	-0.477	-0.455	-0.394	-0.261	-0.028	0.307	0.714	1.138	1.520	1.818	2.027	2.175	2.288	2.390	2.494	2.612	2.748

Showcase 3.3 Example data block from the file 103.Z.02.karo for an initial metallicity $Z = 0.02$, $X = 0.7$, and with $X(^{12}\text{C}) \times 5.0$ and $X(^{14}\text{N}) \times 1.5$. The contents of this table are visualised in Fig. 3.4 (right panel). The headline is reproduced from the look-up table (showcase 3.1).

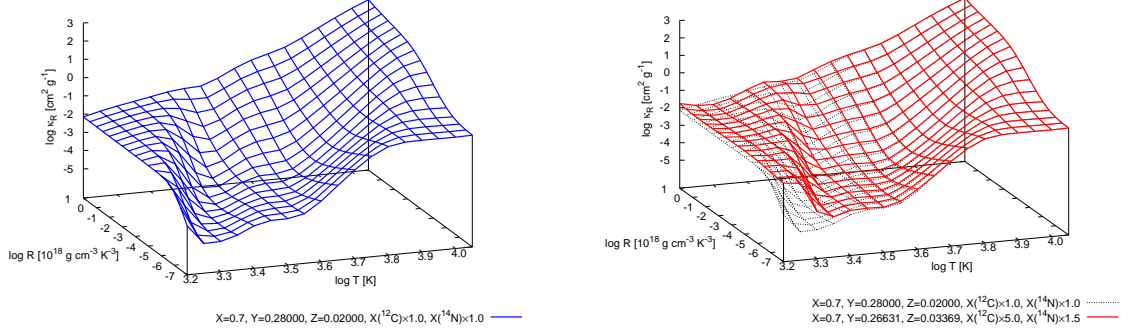


Figure 3.4 Graphical representation of two opacity tables that belong to the set with initial metallicity $Z = 0.02$. Left panel: Opacities for $Z = 0.02$, $X = 0.7$, and scaled solar carbon and nitrogen abundances (compare showcase 3.2). Right panel: Opacities for an initial metallicity $Z = 0.02$, $X = 0.7$, and with $X(^{12}\text{C}) \times 5.0$ and $X(^{14}\text{N}) \times 1.5$ (compare showcase 3.3). We also indicate the data that are shown in the left panel (dotted lines) to ease the comparison.

of molecular data in the calculations (cf. our Table 3.3 and their Tables 3 and 4) produces a deviation in the resulting mean opacity coefficients. Second, we adopt a microturbulent velocity of 2.5 km s^{-1} , while F05 use 2.0 km s^{-1} . The choices for this parameter are (within a certain range that is found for atmospheres of low mass giants) somewhat arbitrary and cause perceptible changes in κ_R , especially at lower temperatures. Third, F05 use a denser wavelength grid for the evaluation of κ_R . We discuss these issues in more detail in Sect. 3.5.3. From a comparison of Fig. 3.5 with Figs. 3.11 (showing a comparable order of magnitude of the deviations) and 3.12, it is, however, clear that the numerous differences in the physical input data are responsible for the major part of the discrepancies. The resolution and microturbulent velocity influence κ_R not quite as much. The large deviations in the data at the lowest temperatures are due to grain opacity that we do not take into account in our calculations, but dust is usually not formed under equilibrium conditions (as assumed by F05, see Sect. 3.1). Moreover, F05 adopted a finer grid in $\log T$ below 3.5. For the oxygen-rich case, a cubic spline interpolation (see Fig. 3.5, dotted lines) on the coarser grid we adopted (and also used by AF94) provides reasonably accurate values.

The comparison with high temperature data such as that from OPAL or OP is limited to the temperature regions where the tables overlap. Moreover, it is this region where a transition between low and high temperature opacities has to be made for applications covering a wide temperature range. OP data stretch down to $\log T = 3.5$, whereas the OPAL tables end at $\log T = 3.75$. The comparison for a standard scaled solar composition in Fig. 3.6 shows a growing deviation for lower temperatures because both OPAL and OP

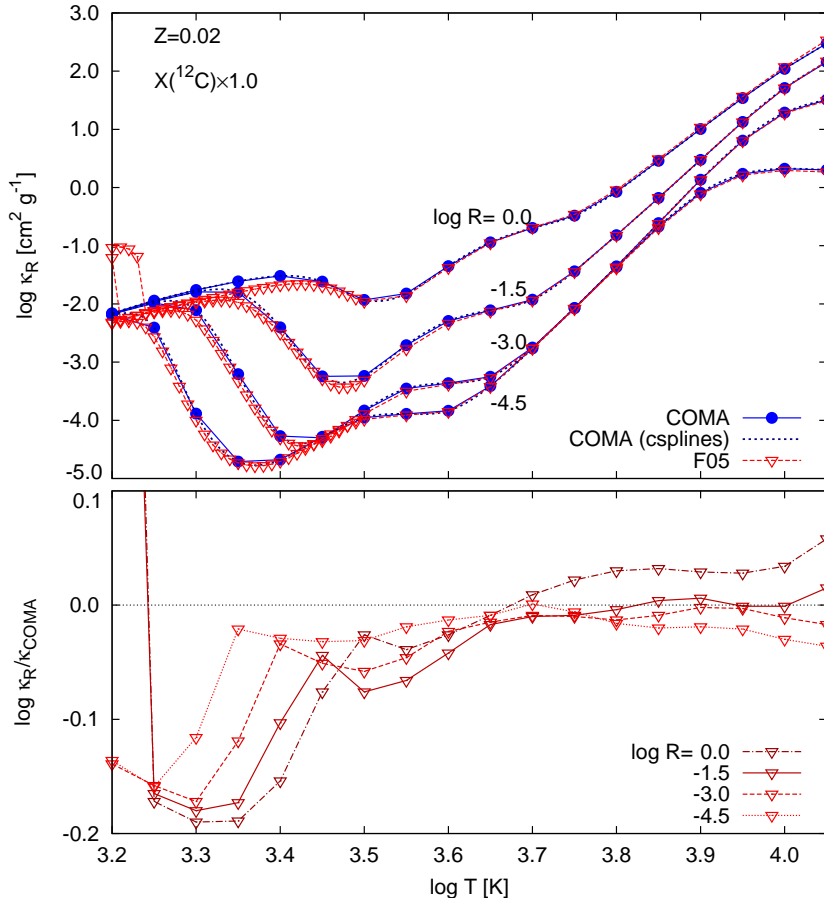


Figure 3.5 Comparison of COMA (filled circles) and F05 (empty triangles) values at a metallicity of $Z = 0.02$. The top panel shows absolute values, whereas in the bottom panel the differences between F05 and COMA values are indicated on a relative scale. Here and in the following figures, κ_{COMA} refers to data contained in our database, while the respective comparison values are always labelled κ_R . The overall agreement down to $\log T = 3.5$ is gratifying. The growing discrepancies towards lower temperatures are most probably due to the deviating set of molecular data in the respective calculations. The step increase in κ_R in the F05 data below $\log T = 3.25$ is due to dust grains that are not accounted for in our data. Below $\log T = 3.5$, F05 use a smaller temperature spacing than we do. The regions between the grid points can be reasonably well reconstructed by a cubic spline interpolation in $\log T$ (dotted lines in top panel). In the bottom panel, we compare values at the COMA grid points only.

do not include molecular absorbers (except H_2). This plot indicates that in the region between $\log T = 3.8$ and the high temperature end of the COMA data, a smooth transition to high temperature data is possible. Again, from the dimension of the differences, we

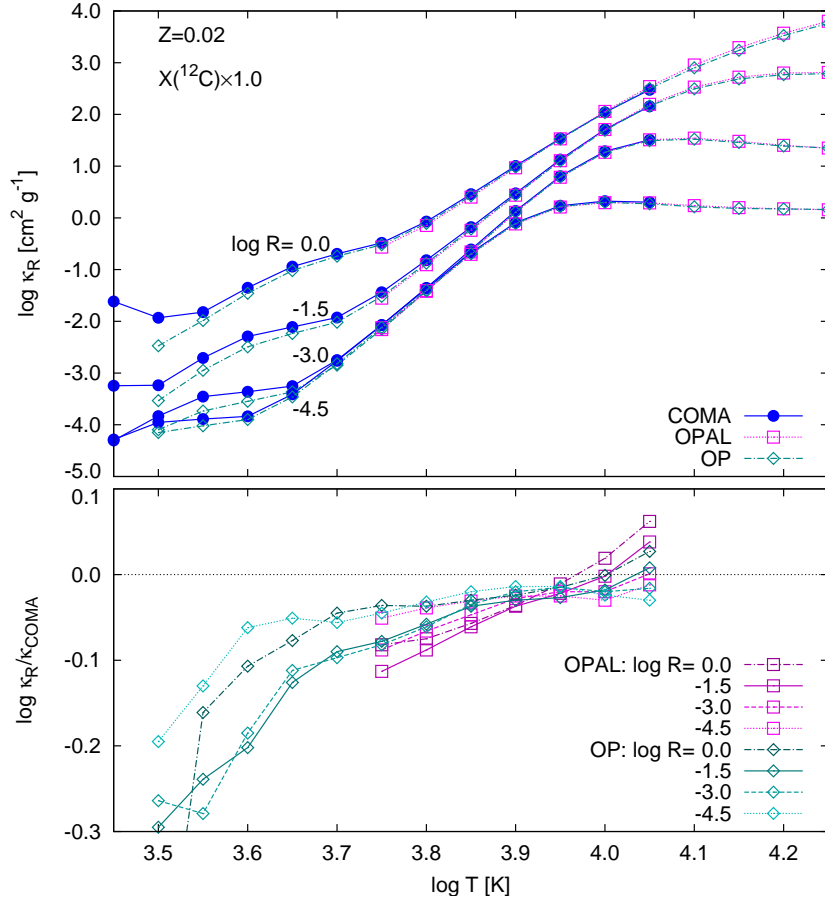


Figure 3.6 Comparison of COMA values with OP and OPAL for $Z = 0.02$. The top panel shows absolute values, whereas in the bottom panel the differences in the overlapping region are again indicated on a relative scale. The high temperature data do not include the relevant molecular opacity sources. Therefore, the discrepancies increase the lower the temperature becomes. OP data range down to $\log T = 3.5$, whereas the OPAL tables end at $\log T = 3.75$. The transition between low and high temperature data can be done close to the upper temperature border of the COMA data, where agreement between the values shown here is fairly good. See also Figs. 3.7 and 3.8.

conclude that these are due to different physical input data rather than other parameters (see Sect. 3.5.3). To assess which temperature region renders itself to such a crossover we plot the logarithmic difference between our opacities and those of OPAL and OP, respectively, as a function of $\log R$ in Fig. 3.7. The deviations are in general moderate and the closest agreement is found around temperatures of 10,000 K. A few comments about the differences are required here. For a metallicity of $Z = 0.02$, the values from COMA are systematically higher than both OPAL and OP. This discrepancy almost vanishes at the

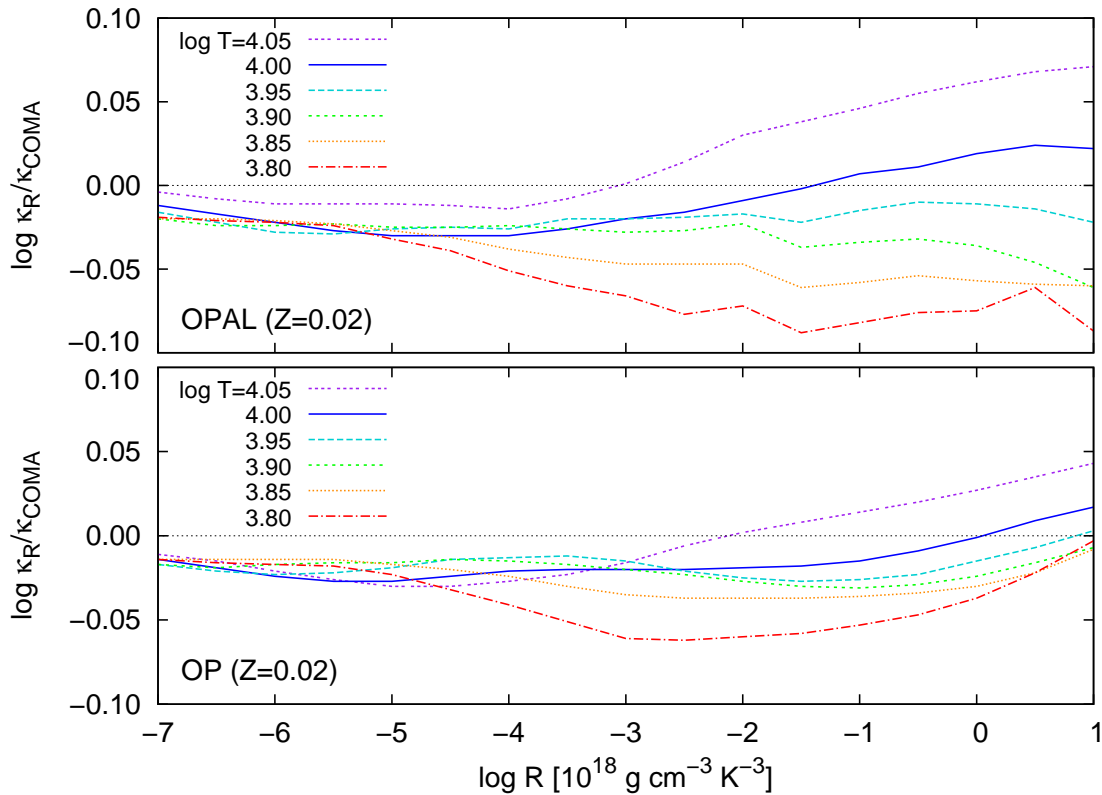


Figure 3.7 Comparison of COMA values with OP and OPAL. Our opacity coefficients are systematically higher for a metallicity of $Z = 0.02$. This constant offset vanishes for lower metallicities (see Fig. 3.8), which implies that atomic opacities (lines and continuum) of the metals are the cause. For high values of $\log R$ where the pressure broadening of the spectral lines becomes important, we find increasingly divergent results. The plots appear to imply that the low and high temperature data should be merged around $\log T = 4.0$ (solid line).

lowest metallicity considered ($Z = 0.00001$, Fig. 3.8). It must therefore be related to the metallicity, which leaves either the metal lines or the differing continuum opacity as a reason. As for the first possibility, OPAL and OP use a restricted set of the most abundant elements, while we use all data that are contained in VALD. Whether this can cause the differences is a question to be answered by further analysis. Moreover, either OPAL and OP data do not include line broadening due to microturbulence, although this alone cannot account for the difference in κ_R .

Beside the constant offset, we recognise a growing discrepancy at increasing $\log R$, which is supposedly to be linked to the pressure broadening of the atomic lines. As mentioned earlier, the damping constants are those from VALD. Additionally, the adopted

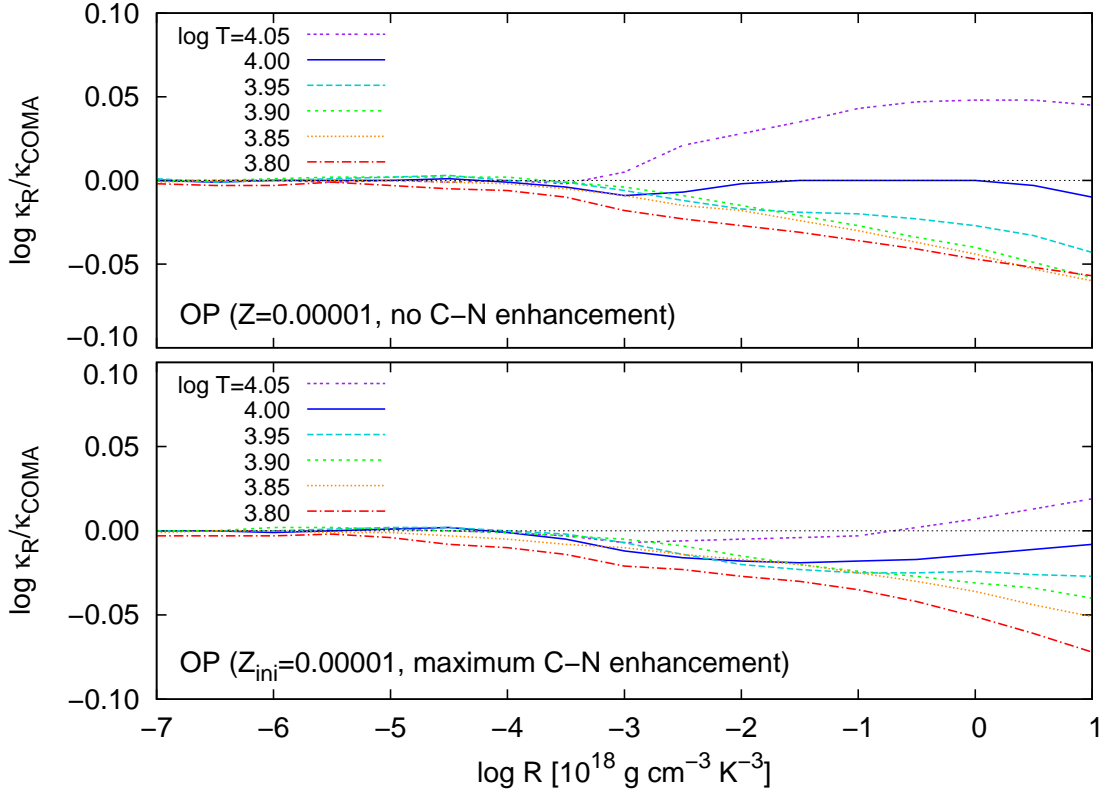


Figure 3.8 Comparison of COMA with OP at a low metallicity ($Z = 0.00001$) with scaled solar abundances of carbon and nitrogen, and with C and N enhanced to the maximum values (which results in a higher metallicity). The data agree quite well, the discrepancies remain within 5 per cent around 10,000 K (solid line). Again, at high $\log R$ the deviations are higher, obviously due to a deviant treatment of the pressure broadening of spectral lines. From a comparison between OP and OPAL (see text) we draw the same conclusions for OPAL data.

tabulated hydrogen line profiles could play a role since hydrogen lines contribute significantly to the Rosseland mean at high temperatures (cf. e. g. AF94). A deeper investigation of this issue is still to be completed, although the differences remain on an overall satisfactorily small scale.

For a mixture enriched in carbon and nitrogen, we also performed tests. We switched to the lowest metallicity in our database where the effects should be most pronounced due to the high enhancement factors. Here we restrict ourselves to a comparison with OP data since these can be produced quite easily using the software contained in the OPCD (version 3.3). Based on the same mass fractions that we used in COMA, we generated opacity tables with the aforementioned program set and compared them with ours. The

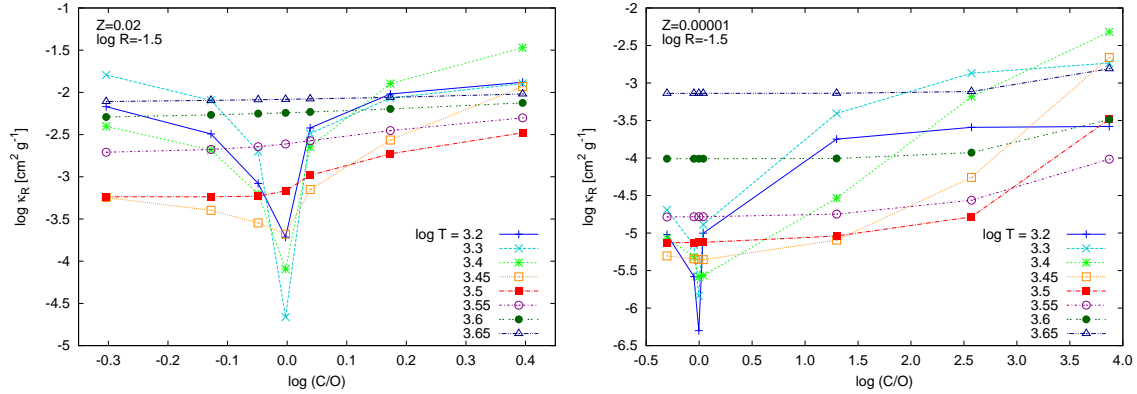


Figure 3.9 Evolution of the Rosseland mean as a function of the C/O ratio for different metallicities ($Z = 0.02$ and $Z = 0.00001$) and a representative value of $\log R = -1.5$. To obtain opacities at enhanced carbon abundances in-between grid points we recommend a linear interpolation scheme in $\log \kappa_R$ and $\log X(^{12}\text{C})$ as indicated by the lines. The largest relative errors have to be expected at low metallicities and temperatures between $X(^{12}\text{C}) \times 2.2$ and the successive enhancement factor. For a description of the mechanism that makes κ_R drop to a minimum value at $\text{C/O} = 1$ and then rise again we refer to Sect. 3.5.

results are shown in Fig. 3.8. We refer to the discussion in the above paragraph concerning the differences but we emphasise again that the quantity $\log \kappa_R / \kappa_{\text{COMA}}$ measuring the differences in the logarithmic opacity in dex remains within a reasonable range, i. e. $\Delta < 0.05$ dex. In these plots, it is evident that the transition from the COMA coefficients to OP data should occur around a temperature of $\log T = 4.0$. From the work of F05 who provided more details about the relation between the low and high temperature opacities, and Seaton and Badnell (2004) who completed an in-depth comparison between OP and OPAL, we conclude that the above statement also holds for OPAL data.

To sum up, despite the differences in the calculation of Rosseland opacities with respect to input data and methods, we nevertheless find a satisfactory agreement of results from other groups in comparison with our values.

3.5.2 Interpolation

The interface between the opacity tables and the various application codes in which they are used are the interpolation routines. Concerning the temperature and $\log R$, it has become sort of a standard to interpolate in these dimensions using cubic splines (e. g. Seaton, 1993, 1996) or quadratic fits (in the Fortran subroutines from Arnold I. Boothroyd²⁸). The results are quite satisfactory, but we want to emphasise that, in the

carbon-rich case, problems can occur. At low values of $\log R$ and a high carbon enhancement, a cubic spline interpolation in the $\log T$ dimension might overshoot and produce spurious results. We strongly advise always checking separately the quality of the fit for each table (or relevant parts thereof) used.

The problem now is how to account for the element enhancements. As outlined in Sect. 3.5, the special role of the C/O ratio bisects the parameter range at $C/O = 1$ at low temperatures, and κ_R is not a continuous function of the carbon content at this point (Fig. 3.9). To resolve the sharp turnaround in the Rosseland mean, we require some grid points close to $C/O = 1$. Overall, the number of enhancement factors is too low and the grid too coarse to apply any other interpolation scheme than a linear one. As shown in Fig. 3.9 for the solar case and at low metallicity, linear interpolation in $\log \kappa_R$ and $\log X(^{12}\text{C})$ delivers quite gratifying results beyond a certain temperature, where molecules cease to play an important role in determining the value of the Rosseland opacity. The lower the temperature becomes, the sharper the turnaround in the functional behaviour of κ_R . Due to the sudden drop in opacity when the amount of carbon and oxygen atoms become approximately equal, linear interpolation misses out a certain fraction of information. At high metallicities the situation is not so serious, although the case shown in the right panel of Fig. 3.9 ($Z = 0.00001$) reveals this shortcoming clearly. Once the element mixture is carbon-rich ($\log C/O > 0$), the opacity first increases sharply but flattens at high carbon enhancement values. Due to the construction of our tables (see Sect. 3.4), the spacing of the enhancement factors in the carbon-rich regime increases at lower metallicities. Between the $X(^{12}\text{C}) \times 2.2$ and the successive enhancement factor, an additional grid point would be favourable. For the case of nitrogen enhancement, linear interpolation in both $\log \kappa_R$ and $\log X(^{14}\text{N})$ is a good approximation, because the relation between the nitrogen content and the opacity has a simpler behaviour.

3.5.3 Sources of uncertainties

The definition of the Rosseland mean opacity in Eq. 3.1 leaves only some ambiguity about how to evaluate this quantity in terms of numerical methods. However, the considerable uncertainties in published opacity coefficients originate in data entering the calculations. In the case of low-temperature opacities, there is, in particular, a good amount of physical data of different quality that must be combined into one quantity. The summary in the following paragraphs is not exhaustive but discusses the accuracy of the data presented here and elsewhere.

3.5.3.1 Adopting different solar element abundances

Hitherto, it has been emphasised that low-temperature Rosseland opacities are to a large extent determined firstly by the total metallicity of the element mixture Z and secondly

²⁸ <http://www.cita.utoronto.ca/~boothroy/kappa.html>

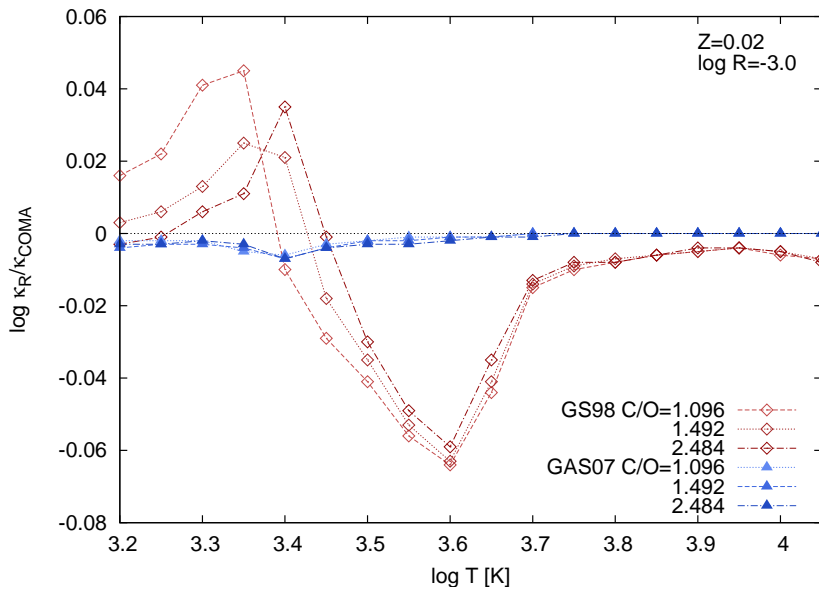


Figure 3.10 Changes in the Rosseland opacity when using different sets of solar element abundances, for instance Grevesse and Sauval (1998, GS98) and Grevesse et al. (2007, GAS07). Data shown here are for the carbon-rich case and $Z = 0.02$ at $\log R = -3.0$. The C/O ratios were set to match the values contained in our database using Lodders (2003, L03) abundances resulting from $X(^{12}\text{C}) \times 2.2, 3.0, 5.0$. GAS07 is in many respects very similar to L03 (e. g. regarding the C, N and O abundances and the share of these elements in Z) and thus results in almost identical opacity coefficients. The abundances given by GS98 deviate much more from L03. The differences become manifest in the opacities at high temperatures, and also at low $\log T$ by means of the chemical equilibrium. Other uncertainties discussed in the text have a comparable order of magnitude.

by the C/O ratio. The individual element abundances play a role as well but do not change the opacity on an order-of-magnitude scale when the aforementioned parameters are kept fixed. Concerning the oxygen-rich case, we refer to a discussion of this topic given by Dotter et al. (2007). For the carbon-rich case, we exemplarily calculated opacity coefficients starting from solar element abundances other than Lodders (2003, L03), that is Grevesse and Sauval (1998, GS98)[GS98] and Grevesse et al. (2007, GAS07)[GAS07]. The results of our comparison are shown in Fig. 3.10 (for $Z = 0.02$ at $\log R = -3.0$). The solar abundances given by GAS07 are very similar to those of L03, and it is therefore unsurprising to uncover virtually identical opacity coefficients for our test case. The situation is different when we consider the GS98 abundances, which provide higher values for C, N, and O than L03 and GAS07. These elements also make up a higher fraction of Z than in the other cases. In turn, when the metals are scaled to obtain $Z = 0.02$, metals

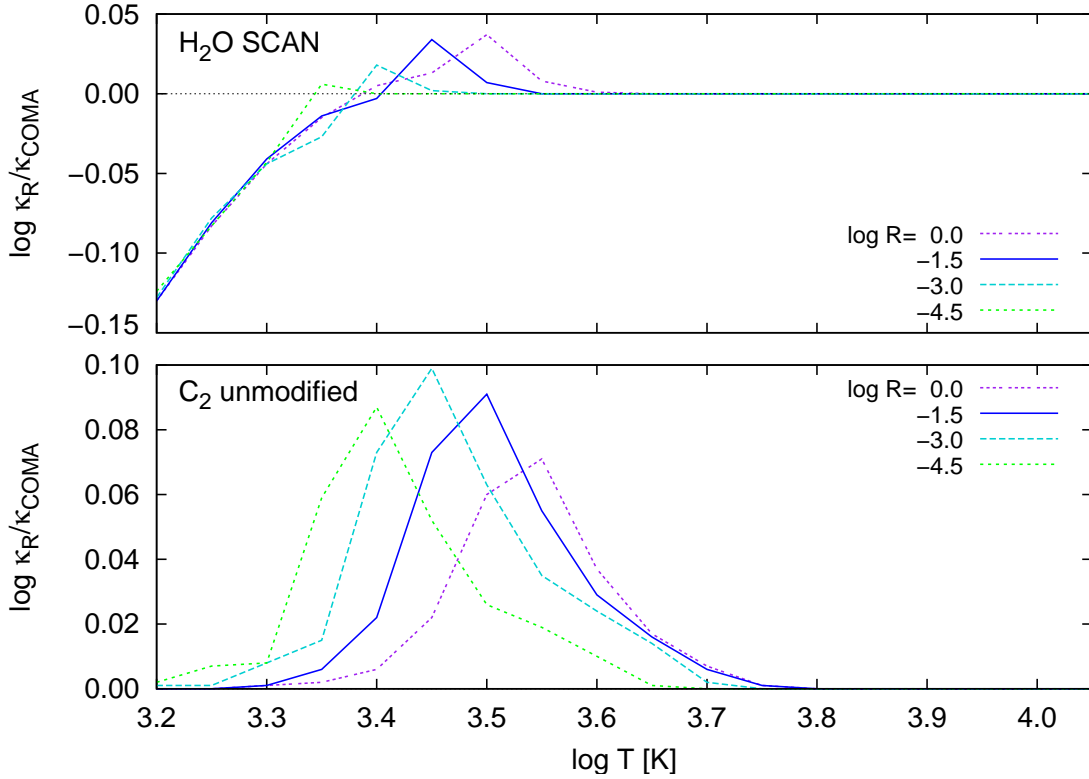


Figure 3.11 Uncertainties in the molecular data that affect the mean opacity. Top panel: Using a different line list for water which is the main source of opacity at low temperatures in the oxygen-rich case causes considerable changes in κ_R . As a test we substituted the BT2 water line list by the one from SCAN and plot the relative changes compared to the default setup. Bottom panel: For the database described in this chapter we scale the C_2 line strengths in a certain wavelength region (see text). Not applying this correction results in notable differences in the Rosseland mean opacity of carbon-rich mixtures. ($X = 0.7$, $Z = 0.02$, no and maximum carbon enhancement in the top and bottom panel, respectively.)

apart from C, N, and O, are present in lower amounts than in the L03 case, and thus contribute a smaller fraction to the opacity at high and intermediate temperatures (beyond $\log T = 3.5$). At the lowest temperatures, more carbon-bearing molecules, such as C_3 and C_2H_2 , are likely to form and produce a higher value of κ_R , partially compensating for the lower atomic opacity contribution at intermediate temperatures. The sensitivity of our results to the adopted starting abundances is limited. The size of the differences with respect to the standard case is similar to other uncertainties discussed here. Hence, our data can be used to approximate the Rosseland opacity coefficients for a different set

of scaled solar abundances, as long as the CNO abundances do not deviate significantly from the values given in L03.

3.5.3.2 Uncertainties in molecular data

We first consider the molecular line data. For many molecules, there is more than one line list available. The Rosseland mean as a global quantity is insensitive to the precision of line positions so long as the overall opacity distribution is reproduced well. However, there are cases where data from different sources result in altered overall opacity coefficients. As an example, we consider the contribution of water, the major low-temperature opacity source in the oxygen-rich case, to κ_R . In this work we use the recently published BT2 water line list (Barber et al., 2006). An alternative would have been the SCAN database line list from Jørgensen et al. (2001). For the solar metallicity case, we calculated a table utilising this list and illustrate the results in the top panel of Fig. 3.11. The discrepancy in the resulting values are as high as 30 per cent. Pronounced differences between the two lists lie in the region where the weighting function in the definition of the Rosseland mean has its maximum, and we ascribe the deviating values of κ_R to this fact.

For the uncertain line data in the carbon-rich case, we mention the modifications to the C_2 line data from Querci et al. (1974). To reproduce carbon star spectra, Loidl et al. (2001) proposed a scaling of the gf values in the infrared region (suggested by Jørgensen, 1997a) based on a comparison with other line lists. More precisely, they scaled the line strengths by a factor of 0.1 beyond $1.5 \mu\text{m}$ and left them unchanged below $1.15 \mu\text{m}$. In-between, they assumed a linear transition. We adopt this method for the calculation of our opacity tables. By not applying this modification to the line strengths, we would have caused an increase of κ_R of roughly 25 per cent at $Z = 0.02$ with maximum enhanced carbon (Fig. 3.11, bottom panel). The error in these data will have a more significant effect at low metallicities, where one expects a higher enrichment in carbon. From the calculation of mean opacities, we observe a clear need for new and improved C_2 line data.

Beside the problems with existing data there are also molecules so far unconsidered that are suspected of providing non-negligible contributions to the opacity. The prime example is C_2H , which could be an important opacity source in carbon stars, although to date no line data have existed for this molecule (we refer to Gustafsson, 1995 for an overview).

Another decisive set of input parameters are the chemical equilibrium constants usually depicted by K_p . Each constant is in fact a temperature-dependent function setting the partial pressure of a molecule in relation to the product of the partial pressures of the molecule's constituents (cf. e.g. Tsuji, 1973). Helling et al. (2000) pointed out that the literature values for equilibrium constants from different sources could differ strongly at

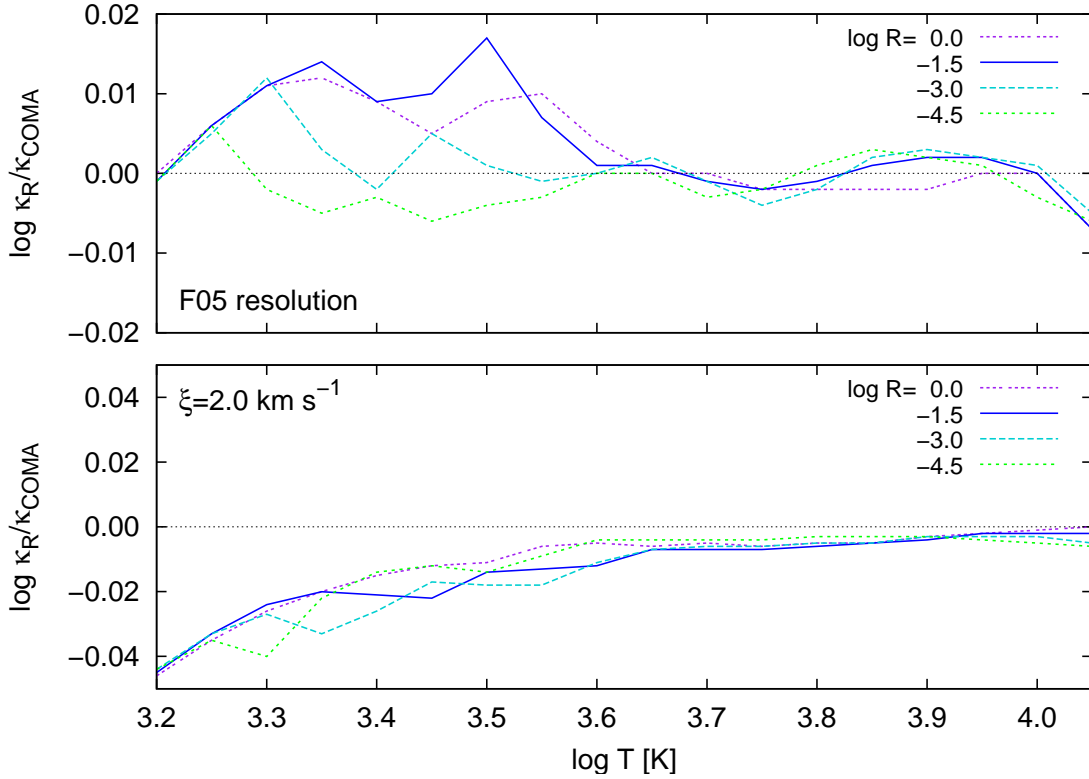


Figure 3.12 Influence of variations in resolution or microturbulence on the mean opacity. Top panel: The calculation of κ_R requires to know the monochromatic opacity at a large number of wavelength points. A high spectral resolution assures convergence but induces high computational costs. We use a lower resolution than F05 but the changes in the opacity coefficients are rather moderate especially when compared to other sources of uncertainty. Bottom panel: We adopted a microturbulent velocity of $\xi = 2.5 \text{ km s}^{-1}$ throughout this work. Changing this value to $\xi = 2.0 \text{ km s}^{-1}$ like in F05 causes κ_R to drop. ($X = 0.7$, $Z = 0.02$, no carbon enhancement.)

low temperatures. The critical point here is that one has not only to pay attention to the main opacity carriers but also to less abundant molecules competing with them for the same atomic species. Helling et al. (2000) referred to TiO and TiO₂ as examples but also reported other molecules for which order-of-magnitude differences in the partial pressures were found using different sets of K_p data. The data that we use are documented in Sect. 3.3.

The above examples underline that accurate molecular line data are not only desirable for high resolution applications but also of importance to the calculation of mean opacities. In general, all data used in calculating the Rosseland mean, whether line data or other accompanying data like partition functions or equilibrium constants and continuum sources, must always undergo critical evaluation.

3.5.3.3 Numerics and parameters

Apart from the imprecision due to the physical input data, there are other factors influencing the emerging opacity coefficients. For instance, an error source exists in the wavelength grid for which the opacities are calculated and the integration completed in deriving the opacity mean. Compared to F05, we use a considerably lower spectral resolution. To assess the uncertainties due to this difference, we simulated the resolution of F05, recalculated one of our tables, and compared our results to those for the original case. The differences found were relatively small as shown in Fig. 3.12 (upper panel). Since the error is low compared to other effects described above, we propose that use of a lower resolution is justifiable because it would reduce considerably the amount of CPU time.

On the other hand, additional physical parameters enter the calculation of κ_R , such as the microturbulent velocity ξ , which influences the width of the line profiles. The spectral lines are broadened according to the adopted value for ξ , which is somewhat arbitrary. Throughout this work, we used a value of $\xi = 2.5 \text{ km s}^{-1}$ for the generation of our data. Results from previous works on spectra of late-type stars (e.g. Aringer et al., 2002, Gautschy-Loidl et al., 2004 and Lebzelter et al., 2008a) have shown that this is a reasonable assumption. In the work of F05, however, ξ was set to equal 2.0 km s^{-1} . Both options are well within the range of values found for AGB star atmospheres (e.g. Smith and Lambert, 1990). In Fig. 3.12 (lower panel), we show the results of a test using the F05 value. Since the spectral lines possess a smaller equivalent width at a reduced value of ξ , the mean opacity is lower than for the COMA default case.

3.5.3.4 Application of the Rosseland opacity data

Beyond generating tables, there is further possibilities for introducing uncertainties while applying the data. First, there is the technical problem of interpolating the tabulated values. Compared to previously available data, the situation is worse because there are two more dimensions along which to interpolate, that is the varying amount of carbon and nitrogen. However, on the basis of the above discussion, it is unlikely that too sophisticated interpolation algorithms produce improved accuracy. This is, however, a problem that can in principle be solved by increasing the amount of computer power.

Far more worrying and the largest error source of all is potential misapplication of the data. Strictly speaking, the scope of the tables containing Rosseland mean opacity coefficients are regions where the diffusion approximation for the radiative transfer is fulfilled. In terms of the optical depth, this means $\tau \gg 1$ for all wavelengths. One of the main applications of our data will be the outermost parts of an AGB star evolution model. The outer boundary condition is usually set somewhere in the atmosphere ($\log T \leq 3.6$), where by definition $\tau \leq 1$. In some situations, the Rosseland mean might still be a good approximation for evaluating the radiative energy transport. However, in

general it is necessary to use a non-grey radiative transfer method because, due to the molecular absorbers, the spectral energy distribution is strongly wavelength-dependent. We refer to the work of Höfner et al. (2003), who demonstrated the shortcomings of a grey treatment of the radiative transfer for dynamical model atmospheres. Harris and Lynas-Grey (2007) investigated the effect of non-grey surface boundary conditions on the evolution of low mass stars and reported noticeable changes to RGB evolution tracks. We thus want to emphasise that our mean opacity tables are meant to provide an interim solution until modelling of non-grey radiative transfer in stellar evolution calculations becomes feasible.

3.6 Conclusions

We have presented a grid of low-temperature Rosseland mean opacity tables that take into account variations in the single element abundances of carbon and nitrogen. By gradually enhancing the carbon content of a metal mixture, the molecular contribution to opacity changes significantly due to the altered chemistry. Already within a certain regime (i. e. oxygen-rich or carbon-rich), the relative amount of carbon to oxygen has pronounced effects on κ_R . More distinctive, however, is the comparison between oxygen-rich and carbon-rich regimes. Different molecules serve as opacity sources in either case and thus result in a qualitatively and quantitatively different Rosseland mean opacity as a function of temperature and density. Changes in the nitrogen abundance also alter the opacity coefficients via certain nitrogen-bearing molecules.

The tables are designed such that an incorporation into existing codes that utilised AF94 or F05 data should be straightforward. Our data cover a wide metallicity range, and the overabundances of carbon and nitrogen are adjusted in each case. We are confident that with these data we provide a tool to simulate the giant branch phases in the evolution of low or intermediate mass stars in more detail. Our data include the effects of the ongoing nucleosynthesis and mixing events in AGB stars in terms of the opacity. As shown in previous papers (e. g. Cristallo et al., 2007), the incorporation of our tables into stellar evolution codes alters the physical properties of the stellar models. Once the star becomes carbon-rich, molecules form that are more opaque than those in an oxygen-rich regime. This in turn results in a steeper temperature gradient. A consequence is, for instance, a decrease in the effective temperature in stellar evolution models. The stellar radius increases, and the average mass-loss rate increases and erodes the envelope mass at a faster rate. Straniero et al. (2003) showed that a change in the envelope mass (as well as a change in the core mass) affect fundamental properties of AGB stars, e. g. the strength of the thermal pulses and the total amount of the mass dredged up. It will also be interesting to see how different mass-loss prescriptions interact with the newly calculated opacity coefficients, since these issues are physically closely coupled. See also the application examples of the data presented here in Chap. 4.

In the future, we plan to extend our tables to contain data about the enrichment in alpha elements. We must emphasise, however, that the data provided in the course of the current and future work must be seen as a transitional solution to the treatment of molecular opacity in AGB star envelopes and atmospheres. Due to the band structure of molecular absorption, mean opacities will yield inaccurate results. The past results from static and dynamical model atmosphere calculations demonstrate the importance of a frequency-dependent radiative transfer. Our data promise to bridge the gap until these methods are employed in stellar evolution models.

Finally, we emphasise that for forthcoming extensions of this database, it would be desirable to obtain extensive response from the community. Comments and criticisms that can lead to an improvement in the quality of the data are highly welcome.

4 Summary and future directions

This chapter contains a compact summary of the thesis results. Moreover, I give an outlook on potential improvements that may help to answer questions that remained unanswered or have been raised in the course of this work. The inevitable conclusion is that, fortunately, there is still plenty of work to accomplish in the field of AGB star research.

4.1 Third dredge-up and extra-mixing in cluster stars

The main outcomes of the investigation of LMC cluster stars can be summarised as follows.

- Analysing a sample of stars, each of which is located within the same cluster, is a viable approach to infer information about the onset and efficiency of TDU. In this way constraints for stellar evolution models can be derived.
- We found clear indications of TDU in the sample of oxygen-rich stars of NGC 1846. The carbon stars show $^{12}\text{C}/^{13}\text{C}$ ratios that are compatible with moderate extra-mixing. We found a good agreement with stellar evolution models.
- The picture for the AGB stars in the cluster NGC 1978 is not as clear. The oxygen-rich stars do not show conclusive signs of TDU, and the C stars display carbon isotopic ratios that cannot be explained with standard scenarios.
- The last two points show that clusters with similar parameters (mass and metallicity) apparently do not always show similar abundance patterns. Thus we need to advance our understanding of TDU and extra-mixing further in order to reproduce the observations with numerical models.
- We confirm that AGB stars are sites of fluorine production.

To obtain a more complete picture of the late stages of evolution of low-mass stars, in particular with regard to the nucleosynthesis and mixing mechanisms, it is crucial to collect further data and to increase the sample size. Thereby it is important to cover a range of metallicities and masses. There is a number of clusters in the Magellanic Clouds (see e.g. Lloyd Evans, 1980) that lend themselves to an investigation such as the one outlined in Chap. 2. We are in the progress of acquiring further data.

It will also be interesting to perform a similar analysis of AGB stars in nearby dwarf spheroidal galaxies. The next generation of telescopes (the *European Extremely Large Telescope* or the *Thirty Meter Telescope*, cf. Gilmozzi and Spyromilio, 2008 and Nelson and Sanders, 2008, respectively) will supposedly be equipped with capable infrared

spectrographs (e. g. Oliva and Origlia, 2008) allowing to obtain high signal-to-noise spectra for broad wavelength ranges of more distant targets.

With the help of such instruments it will also be possible to contribute to the improvement of molecular line data. There is a clear need for it from the modelling point of view. This issue has been discussed in Chaps. 2 and 3, however, it cannot be stressed enough. Especially for the analysis of high-resolution carbon star spectra, the line lists are often too inaccurate to reliably measure abundances. Representative examples are the molecules C_2 , CN, but also CO. Wahlin and Plez (2005) announced a new list for C_2 to replace the inexact data from Querci et al. (1974), but to date this list has not been published. Also in the case of CN, it is important to get better line data. There is a large amount of laboratory data available (Davis et al., 2005) that would help to refine line positions from *ab initio* calculations. As a last example, I want to mention the CO line data from Goorvitch and Chackerian (1994). It turned out during the analysis of the spectra discussed in Chap. 2 that some line positions in the K band needed revision. I therefore tested CO data generated by Chandra et al. (1996), which indeed match the observations in the K band far better. However, utilising the same list for the calculation of H-band spectra makes the CO band head at approximately 6418 cm^{-1} disappear, which conflicts with our observations—the calculated line intensities in this region are too low by orders of magnitude. For some molecules such as C_3 and C_2H_2 one is restricted to the use of opacity sampling data, while for others, namely C_2H , comprehensive line data are not available (see Sect. 3.5.3.2). Although in our case the synthetic spectra might not be affected (see e. g. Keady and Hinkle, 1988 for a detection of C_2H in carbon star spectra), it could, depending on the global behaviour of the absorption coefficient, influence the atmospheric structure of carbon stars though. This is because the abundance of C_2H is in general large compared with other species (cf. e. g. Fig. 5.4 in Habing and Olofsson, 2003). In the same way, this molecule could change the mean opacities described in Chap. 3.

Concerning stellar evolution models, the full exploration of mixing mechanisms will probably require to include physical mechanisms such as rotation or magnetic fields in the calculations in greater detail (see Chap. 1 for references). It also appears that for an improvement of the theory it will be necessary to resort to simulations in which the number of spatial dimensions is > 1 .

4.2 Low-temperature opacities

As for the mean opacity coefficients, there is only one major conclusion.

- Due to the special role of the CO molecule, the transition from a scaled solar (i. e. oxygen-rich) mixture to a carbon-rich regime results in opacities that can, at low temperatures, differ by orders of magnitude from the initial situation. The reason is that the mean opacity in either case is due to different molecular absorbers. Even within a

certain chemistry regime an alteration to the carbon abundance causes considerable changes in the Rosseland opacity. Variations in the abundance of nitrogen have less pronounced effects but, nevertheless, cannot be neglected.

This was discussed at length in Chap. 3 and the conclusions have been drawn in Sect. 3.6 from the molecular data point of view. At this point, I want to illustrate that in typical astrophysical applications it is indispensable to take into account opacity variations due to chemistry changes. The implications of the use of low-temperature Rosseland opacities were thoroughly discussed by Marigo (2002). Two important results of this work were the significant shortening of the carbon-star phase due to the earlier onset of an efficient stellar wind, and a consequent reduction of the carbon yields. To bolster these statements and to point out the improvements in comparison to earlier simulations, in the following I give some application examples of the data presented in Chap. 3 in different stellar evolution codes.

4.2.1 FRANEC

The carbon- and nitrogen-enhanced opacities were first used by Cristallo et al. (2007) in stellar evolution calculations for a low-mass metal-poor star undergoing TDU. The dredge-up of carbon is of great importance for the AGB evolution in many respects. First, the amount of carbon present influences the efficiency of the CNO cycle thus affecting the growth in mass of the helium-exhausted core. Second, the change in opacity due to the carbon enhancement is a relevant point, since the temperature gradient in a star is coupled to the opacity of stellar matter, and thus the physical properties and chemical yields are altered when the chemistry of the mantle and atmosphere changes.

The model presented by Cristallo et al. (2007) was calculated with the FRANEC code for a star with $M = 2 M_{\odot}$ and $Z = 0.0001$. To assess the effects of opacities with varied abundances of carbon and nitrogen, a key point was the comparison of three different models described below.

- *Z-fix* — this model considers variations of He and H only, the metallicity Z is always maintained equal to the initial value.
- *Z-int* — variations of He, H, and Z are considered, but the elemental distribution of heavy elements is always maintained scaled to solar.
- *CN-int* — properly takes into account variations of He, H, C, and eventually N caused by the TDU (i. e. using the opacity data described here). All other elements are maintained at their initial solar values.

Figure 4.1 shows the implications of the different opacity prescriptions for the stellar models in terms of physical parameters of the star and element abundances. Apart from

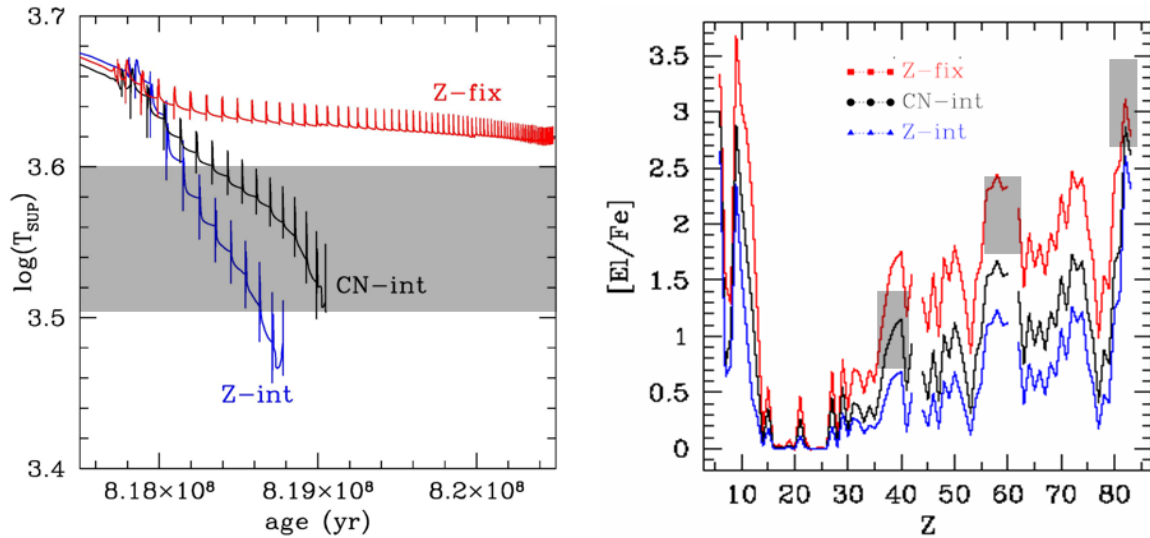


Figure 4.1 FRANEC models for a star with $M = 2 M_{\odot}$ and $Z = 0.0001$ using different opacity prescriptions. Left panel: Effective temperature versus age during the TP-AGB phase for the three cases *Z-fix* (red line), *Z-int* (blue line), and *CN-int* (black line) described in the text. The shaded area indicates the range of observed values of T_{eff} from Aaronson and Mould (1985). From Cristallo et al. (2007). Right panel: Resultant abundances of stellar evolution models using different opacity prescriptions (here the axis label Z depicts the atomic number). The observed abundances for the *ls*-, *hs*- and lead peak elements (shaded areas from left to right) are from Domínguez et al. (2004). Only the *CN-int* case delivers consistent results for both the observed stellar parameters and the element abundances. Figure courtesy of Cristallo (private communication). See text for details.

the change in the opacity coefficients, the three models have been calculated with identical input physics. The emerging differences in the AGB evolution are remarkable as can be inferred from Fig. 4.1. Although it is evident that the *Z-fix* and *Z-int* models do not represent physical reality, they provide nevertheless valuable insight into the problem of inappropriate opacity data. Not following the alterations in opacity at all (*Z-fix*) results in an effective temperature too high compared with observations (shaded areas in the left panel of Fig. 4.1, Aaronson and Mould, 1985). The test case *Z-int* where the changes in the chemical composition are mimicked by scaling up all metals leads to a lower value of T_{eff} . A correct opacity treatment (*CN-int*) results also in lowered surface temperatures, which is due to an increased opacity in the outer stellar layers. At a given luminosity this causes an increase in radius and leads to a larger mass-loss rate. With respect to a *Z-fix* model, the TP-AGB phase is significantly shortened, however, this effect is overestimated in a *Z-int* model. While the *Z-int* model cannot reproduce the observed

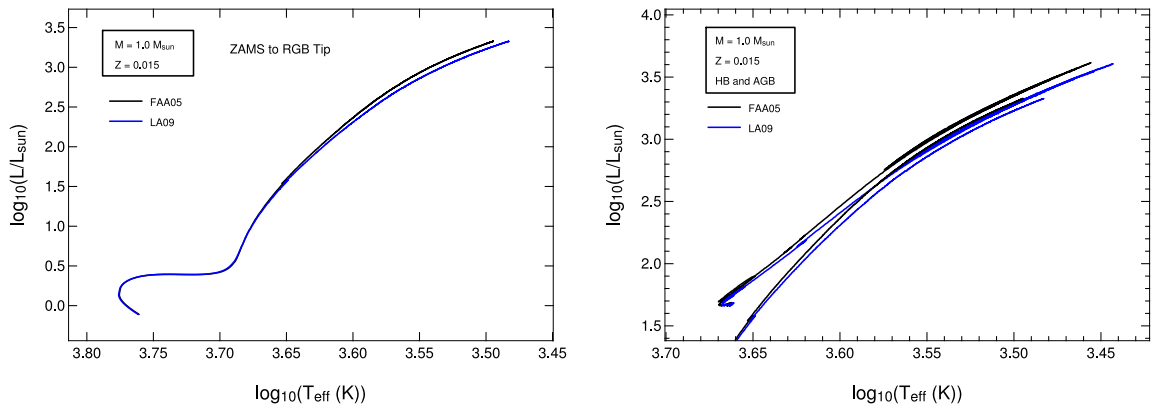


Figure 4.2 Stellar evolution tracks calculated with MONSTAR. These test calculations for a model with $M = 1 M_{\odot}$ and $Z = 0.015$ are based on the opacities from Ferguson et al. (2005, FAA05, black line) and the data presented in this thesis (LA09, blue line). The left panel shows the tracks from the ZAMS to the RGB tip, in the right panel also the HB and AGB phases are plotted. Figure courtesy of Campbell & Karakas (private communication). See text for details.

abundances for the *ls*-, *hs*- and lead peak elements (shaded areas from left to right in the right panel of Fig. 4.1, Domínguez et al., 2004), the *Z-fix* and the *CN-int* case fit the observed values reasonably well. Thus only the *CN-int* case delivers results consistent in terms of the observed stellar parameters.

The results described have been published in the paper by Cristallo et al. (2007), where additionally the effect of extra-mixing acting during the AGB was investigated using the ^{14}N dimension of the tables. Subsequent work was presented by Cristallo et al. (2009), in which models with $M = 2 M_{\odot}$ and $Z = 0.0138, 0.006, 0.003, 0.001, \text{ and } 0.0001$ are presented. All models make use of opacity data with varied abundances of carbon and nitrogen. Following our expectations, the effects caused by the use of different opacities get less pronounced as the metallicity increases. This is because the third dredge-up is less efficient for higher metallicities.

4.2.2 MONSTAR

As of the submission of this thesis, the opacities described in Chap. 3 are also being integrated in the Monash version of the Monash/Mount Stromlo stellar evolution code (MONSTAR, see e. g. Wood and Zarro, 1981 and Frost and Lattanzio, 1996). In Fig. 4.2, kindly provided by Campbell & Karakas (private communication), I show some test calculations for a model with $M = 1 M_{\odot}$ and $Z = 0.015$. The effects of different low-temperature opacity data, i. e. the ones from Ferguson et al. (2005, labelled FAA05 in this section) and the data presented in this thesis (LA09), are compared. In the case of the

LA09 tables, only data without element enhancements, i. e. $X(^{12}\text{C}) \times 1$, $X(^{14}\text{N}) \times 1$, are used to allow for a direct comparison. There is a small temperature difference between the two tracks that becomes more prominent when the star evolves on the giant branches. Towards the end of the AGB the discrepancy amounts to $\Delta(\log T_{\text{eff}}) \sim 0.015$. This can be explained by the slightly higher opacities of LA09 at lower temperatures in comparison to FAA05 (compare Fig. 3.5 and the associated discussion in Sect. 3.5.1). At any rate, the difference between the evolution tracks is small from a stellar modelling point of view. Nevertheless, as in the case of the FRANEC models, the evolution will change drastically when TDU is incorporated in the models and thus the opacity tables with carbon enhancements are used. Slightly lower temperatures at the end of the AGB may lead to a reduced number of TDU episodes, and thus less chemically enriched matter is ejected from the star. This is still to be checked by further test calculations. The goal is then to calculate models similar to the ones described in Campbell and Lattanzio (2008), but for a variety of metallicities.

4.2.3 MESA

The interplay of the opacities with different mass-loss prescriptions, as mentioned in Chap. 3, is investigated by the time this thesis is written. Mass-loss rates that emerged from a continuation of the work by Mattsson et al. (2008) and that were derived from dynamical model atmospheres developed by Höfner et al. (2003) are tested with the MESA code²⁹. The new mass-loss rates, like the opacities, depend on the relative abundance of carbon and oxygen. This is a fundamental difference to the formula from Bloeker (1995) which serves as reference. The opacities were calculated with the same methods as described here, but a few adaptations have been made to suit the stellar model specifications. The most important changes are as follows. We used a different set of solar element abundances, namely Grevesse and Noels (1993). We did not alter the nitrogen abundance but varied the mass fraction of oxygen instead. Of course, the carbon abundance is still varied, too. The step size in C/O is smaller compared with the original database, and the grid is dense around C/O = 1. In Fig. 4.3 I show some preliminary results for a $Z = 0.01$ and $M = 2 M_{\odot}$ model (Herwig, private communication). Like in the above examples the new opacity data cause a reduction of the effective temperature and, together with the theoretical mass-loss rates that give rise to the occurrence of a superwind (Fig. 4.3, bottom panel), influence the efficiency of the third dredge-up. Details will be given in a forthcoming paper by Mattsson et al. (in preparation).

4.2.4 Outlook

The extension of the opacity database with respect to alpha-element enhancements is straightforward and shall be set about before long. Furthermore, the inclusion of tables

²⁹ Developed by Bill Paxton, <http://mesa.sourceforge.net>.

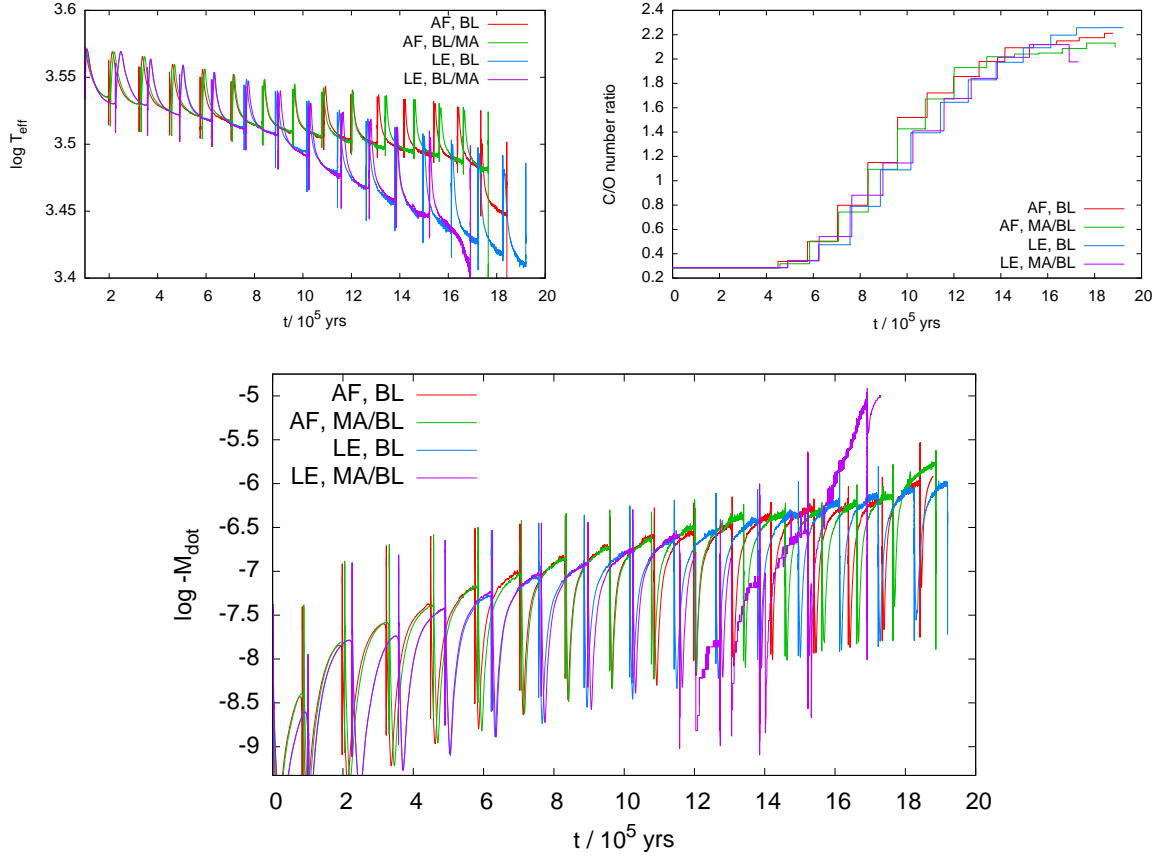


Figure 4.3 Preliminary MESA model results based on new opacities and mass-loss rates. LE refers to the opacities described in this work, AF depicts data from Alexander and Ferguson (1994). The mass-loss prescription from Bloeker (1995) is labelled BL. For the carbon-rich regime, new data from Mattsson et al. (in preparation) are adopted (MA). Like in the above examples, the effective temperature drops with respect to earlier calculations due to the new opacity data (top left panel). These influence, together with the mass-loss rate, also the efficiency of the third dredge-up as can be seen from the evolution of the C/O ratio (top right panel). Only when using LE opacities the model enters a regime where the MA mass-loss is switched on, which then results in a superwind phase at the end of the AGB phase (bottom panel). These are preliminary results for a $Z = 0.01$ and $M = 2 M_{\odot}$ model, an in-depth analysis will be given by Mattsson et al. (in preparation).

with an initial metallicity $Z = 0$ would be useful for researchers dealing with the evolution of the first stars. Other changes or improvements will require the feedback from the stellar evolution community.

It remains to be seen whether tabulated opacities will be the preferred choice for a long time. An alternative approach is to calculate opacities just-in-time during stellar evolution calculations from opacity sampling data for the individual molecules and chemical equilibrium routines. The feasibility of this method needs to be tested first (Marigo, private communication and Plez, private communication).

The usage of mean opacities will eventually be superseded by non-grey boundary conditions. First efforts in this direction were made for example by Harris and Lynas-Grey (2007), who included the MARCS code into stellar evolutionary calculations (see also VandenBerg et al., 2008). During a synthetic evolution sequence, atmospheric models are calculated alongside with the stellar structure. However, this approach is at the present time computationally costly. This problem, like many others, requires a smart solution or an increasing amount of computer power.

A The Hardy interpolation method

A.1 Problem description

The atmospheric model structures mentioned in Chap. 2 were calculated with the COMARCS code (e. g. Aringer et al., 2009). This code is a modified version of the MARCS code (Gustafsson et al., 1975, 2008 and Jørgensen et al., 1992). The modifications include the update of the opacity sources utilised in the calculation of the atmospheric structure (see Sect. 2.3.2 and also Fig. 2.5). Rather than changing the opacity routines in the MARCS code, we took advantage of the COMA code³⁰, which was deliberately developed for the purpose of calculating opacity and scattering coefficients for model atmosphere codes (Aringer, 2000 and Aringer et al., 2009). We thus pre-calculated opacity tables with COMA and adapted the MARCS code so that it can make use of these data.

While MARCS expects monochromatic opacity coefficients κ_ν as a function of temperature T and electron pressure P_e , the COMA code by design calculates the opacities as a function of T and the gas pressure P_g . Since the electron pressure is also a part of the COMA output, the data can be rearranged in order to provide tables that list $\kappa_\nu(T, P_e)$. However, when we start from a rectangular T - P_g grid as an input for COMA, the problem arises that the resulting T - P_e grid is in general non-rectangular. We therefore needed to implement an interpolation algorithm that is able to handle an irregular set of grid points.

A.2 Interpolation on arbitrary grids

A solution of our interpolation problem can be achieved with the multiquadric method of Hardy (1971) which is described in detail in the book of Späth (1991), who also presents an implementation of the corresponding interpolation algorithm. I sketch the method briefly and follow the nomenclature of Späth (1991).

The Hardy method is an interpolation in two dimensions on a grid of arbitrary distributed points, i. e. it is in particular applicable to non-rectangular grids. It is a global method that takes all grid points into account for the calculation of an interpolation value, irrespectively of the location of the desired point in the grid. The method is therefore in contrast to local methods such as C^1 splines or triangulation.

For the described method the grid points

$$P_i = (x_i, y_i) \quad i = 1, \dots, n \quad (\text{A.1})$$

³⁰ This is also the reason why MARCS is now called [CO(MA)RCS].

need to be pairwise different and must not be collinear, which requires $n \geq 3$. Based on this grid, we are looking for a smooth interpolation function that fulfils

$$F(x_i, y_i) = z_i \quad i = 1, \dots, n. \quad (\text{A.2})$$

In the case of the Hardy method, we start from an ansatz for this function.

$$H(x, y) = \sum_{k=1}^n a_k B_k(x, y) \quad (\text{A.3})$$

Here the B_k are basis functions that need to be explicitly defined (see below). The coefficients a_k ($k = 1, \dots, n$) are to be determined from the interpolation condition

$$\sum_{k=1}^n a_k B_k(x_i, y_i) = z_i \quad i = 1, \dots, n. \quad (\text{A.4})$$

We use radial basis functions (see Eqs. 6.20 and 6.21 in Späth, 1991)

$$B_k(x, y) = B(r_k), \quad r_k = \sqrt{(x - x_k)^2 + (y - y_k)^2}, \quad (\text{A.5})$$

more precisely in the form

$$B(r_k) = (r_k^2 + R^2)^q, \quad q \in \mathbb{R}. \quad (\text{A.6})$$

The quantity R is an arbitrary but not too big constant.

For numerical details of the method such as the condition number of the coefficient matrix we refer to Späth (1991). This book contains also a number of test cases and general comments about the method of Hardy, some of which shall be reproduced here, namely:

- a. Adequate choices for R and q depend on the grid, whereby it is possibly advisable to choose a value for q that is slightly smaller than $1/2$.
- b. Large values of n ($\gg 100$) could cause numerical problems, because the conditioning of the matrix may become problematic.
- c. Although the Hardy method is promising, because it is easy to implement and yields visually pleasing results, there are some open questions. For instance, how can R be set in a suitable manner in dependence on n and z_i ? Shall R be made dependent on the grid points, i. e. R_k ?

In the next section, we discuss the special case of the opacity interpolation and present our choice of the parameters.

A.3 Opacity interpolation

To provide opacities for the COMARCS code, we start from a grid of monochromatic opacity coefficients κ_ν as a function of temperature T and electron pressure P_e . This grid is calculated with COMA and contains $n = 918$ points, i. e. pairs (T, P_e) that are chosen such that a wide range of atmospheric model structures is covered.

Then we calculate the interpolation coefficients a_k by solving the linear system of equations in Eq. A.4 for the common logarithm of the involved quantities, so that we can write the monochromatic opacity at an arbitrary point (\bar{T}, \bar{P}_e) within the grid as (see Eqs. A.5 and A.6)

$$\log \kappa_\nu(\bar{T}, \bar{P}_e) = \sum_{k=1}^n a_k \left((\log \bar{T} - \log T_k)^2 + (\log \bar{P}_e - \log P_{e,k})^2 + R^2 \right)^q. \quad (\text{A.7})$$

After extensive tests, the parameters R and q were set to 0.3 and 0.45, respectively. Note that q is thus close to the suggestion of Späth (1991, see also previous section). We point out that it was not feasible to tune R and q for each wavelength point (see below) individually. Nevertheless, with our choice of parameters the opacities emerging from the interpolation routine are sufficiently accurate for the model calculation. The effects of small uncertainties vanish in the calculation of pressure–temperature structures of model atmospheres due to self-regulation effects (Aringer, private communication). The number of points is in our case much larger than 100, however, we did not encounter numerical problems in the interpolation routine.

For each combination of chemical composition and microturbulent velocity, the procedure described above is repeated for a number of 5364 wavelength points. The wavelength grid originates from Aringer et al. (1997). Using the COMA code, we save the (T, P_e) grid as well as the interpolation coefficients at each wavelength point into a file together with associated header data. This file is subsequently used in the COMARCS code for the calculation of model atmospheres. The subroutines involved in the interpolation procedure are based on the code listings in Späth (1991, Figs. U.34 and U.35).

B The Rosseland mean

The set of equations that describe the stellar structure consists of expressions for mass conservation (i. e. the continuity equation), energy conservation, hydrostatic equilibrium, and for the energy transport. These equations are completed by relations that characterise the material properties (the equation of state, as well as the opacity and the energy production of the medium). Depending on the physical circumstances, a large fraction of the energy is transported by means of the radiation field. In the sun, for example, energy transport by conduction is negligible and convection plays a role in the outer regions only. Therefore, astrophysical problems such as the treatment of the solar interior require to solve the radiation transport equation (RTE), which is in general not easy to accomplish. However, the conditions in the stellar interior allow considerable simplifications for the description of the radiative energy transport. I start with some order-of-magnitude estimates that can in greater detail be found in the books of Kippenhahn and Weigert (1990) and Shu (1991), for instance. Then I derive the mathematical expression for the Rosseland mean opacity which is utilised in Chap. 3.

B.1 Radiative transfer in the stellar interior

To assess the conditions under which radiative energy transport takes place, we start from the mean free path l_ν of a photon with frequency ν , which is given by

$$l_\nu \equiv \frac{1}{\kappa_\nu \rho}. \quad (\text{B.1})$$

We use typical solar values to estimate the value of l_ν in the stellar interior. The matter density ρ is calculated by dividing the solar mass by its volume, which yields $\rho \sim 1 \text{ g cm}^{-3}$.³¹ The absorption coefficient κ_ν varies with frequency, a lower limit is given by electron scattering (Kippenhahn and Weigert, 1990), for which $\kappa \sim 1 \text{ cm}^2 \text{ g}^{-1}$. With these values we obtain a typical mean free path of $l \sim 1 \text{ cm}$. This is obviously much smaller than the stellar radius, but the relevant reference length is the temperature scale height. A crude estimate for this quantity can be obtained by taking the temperature difference between the solar centre and the atmosphere divided by the solar radius. This leads to the conclusion that between two scattering events the temperature change is on the order of mK. Therefore, over the small mean free path l the medium is quasi isothermal, and thus the conditions can be excellently described by local thermodynamic equilibrium (LTE). Similar considerations concerning the isotropy of the radiation field under such conditions lead to the conclusion that the radiation field in the stellar interior is indeed almost isotropic (Kippenhahn and Weigert, 1990). The word "almost" is in this case

³¹ The values given here are accurate within an order of magnitude only.

essential, since the small deviation from isotropy guarantees a non-vanishing energy flux to the stellar surface which accounts for the stellar luminosity. By any means, these order-of-magnitude estimates allow significant simplifications of the RTE and justify the treatment of the radiation transport as a diffusion process (see next section). Moreover, the time-dependence of the RTE can be neglected, because the radiative transfer is a fast process compared with stellar evolution which happens on a nuclear time scale.

B.2 Derivation of the Rosseland mean

With the estimates from the last section it is straightforward to find the mathematical expression for the Rosseland mean. I follow the derivation given by Dorfi (2003). We start from the stationary radiation transport equation (RTE) for a spherically symmetric medium (see e. g. Mihalas and Weibel Mihalas, 1984).

$$\mu \frac{\partial I_\nu}{\partial r} + \frac{1 - \mu^2}{r} \frac{\partial I_\nu}{\partial \mu} + \kappa_\nu \rho (I_\nu - S_\nu) = 0 \quad (\text{B.2})$$

The quantities occurring in this equation are defined as follows.

Definitions

I_ν = specific intensity	erg cm ⁻² s ⁻¹ Hz ⁻¹ sr ⁻¹
μ = cos θ	1
θ = angle between radial direction and line of sight	rad
r = radial distance	cm
ν = frequency	Hz
κ_ν = absorption coefficient	cm ² g ⁻¹
S_ν = source function	erg cm ⁻² s ⁻¹ Hz ⁻¹ sr ⁻¹
ρ = mass density	g cm ⁻³

The specific intensity I_ν is the energy dE that passes through an area dA , radiating into a space angle $d\Omega$ per time interval dt and frequency interval $d\nu$, and we write $dE = I_\nu dA d\Omega dt d\nu$. The central axis of the cone into which the radiation is emitted encloses the angle θ with the radial direction. The source function is defined as the ratio of the emissivity to the absorptivity of the material through which the radiation passes.

To obtain an equation for the monochromatic radiative flux, we evaluate the first moment of the RTE.

$$\frac{\partial}{\partial r} \int \mu^2 I_\nu d\mu + \frac{1}{r} \int (\mu - \mu^3) \frac{\partial I_\nu}{\partial \mu} d\mu + \int \kappa_\nu \rho (I_\nu - S_\nu) \mu d\mu = 0 \quad (\text{B.3})$$

We assume an isotropic source function, perform a (partial) integration, and make use of the Eddington moments that are defined as

$$\{J_\nu, H_\nu, K_\nu\} \equiv \frac{1}{2} \int_{-1}^{-1} I_\nu \mu^{0,1,2} d\mu. \quad (\text{B.4})$$

This leads to

$$\frac{dK_\nu}{dr} - \frac{3K_\nu - J_\nu}{r} = -\kappa_\nu \rho H_\nu. \quad (\text{B.5})$$

The moments of the radiation field J_ν and K_ν , which correspond to the physical quantities radiation energy density and radiative pressure, respectively, are related to each other by the Eddington factor $f_\nu \equiv K_\nu/J_\nu$ (Mihalas and Weibel Mihalas, 1984). This factor is a measure for the geometry of the radiation field. For isotropic or marginally anisotropic radiation fields (to the first order of μ) f_ν becomes $1/3$. In the case of local thermodynamic equilibrium the mean intensity of the radiation field J_ν is given by the Planck function $B_\nu(T)$. The first moment of the radiation field is related to the physical flux by $F_\nu = 4\pi H_\nu$. Thus, Eq. B.5 becomes

$$\frac{dB_\nu(T)}{dr} = -\frac{3\kappa_\nu \rho}{4\pi} F_\nu. \quad (\text{B.6})$$

The total flux results from the integration of Eq. B.6 over all frequencies

$$F_{\text{rad}} = \int_0^\infty F_\nu d\nu = -\frac{4\pi}{3\rho} \int_0^\infty \frac{1}{\kappa_\nu} \frac{dB_\nu(T)}{dr} d\nu \quad (\text{B.7})$$

The dependence of the Planck function on spatial coordinates is introduced via the temperature structure of the medium under consideration. We utilise the chain rule and that way decouple the temperature gradient from quantities that can be evaluated independently of the stellar structure.

$$F_{\text{rad}} = -\frac{4\pi}{3\rho} \int_0^\infty \frac{1}{\kappa_\nu} \frac{\partial B_\nu(T)}{\partial T} \frac{\partial T}{\partial r} d\nu = -\frac{4\pi}{3\rho} \frac{\partial T}{\partial r} \int_0^\infty \frac{1}{\kappa_\nu} \frac{\partial B_\nu(T)}{\partial T} d\nu \quad (\text{B.8})$$

At this point we define the *Rosseland mean* κ_R using the integral term from the above equation and by introducing a normalisation factor.

$$\frac{1}{\kappa_R} = \frac{\int_0^\infty \frac{1}{\kappa_\nu} \frac{\partial B_\nu(T)}{\partial T} d\nu}{\int_0^\infty \frac{\partial B_\nu(T)}{\partial T} d\nu} \quad (\text{B.9})$$

According to the above equation, the Rosseland mean is a harmonic mean of the absorption coefficient κ_ν . Due to the structure of the integrand in the numerator of Eq. B.9, the Rosseland mean emphasises transparent wavelength regions, why it is occasionally referred to as representing the *transparency* of the medium rather than the *opacity*. The non-linear nature of κ_R causes that the Rosseland opacity of an element mixture cannot be calculated from the mean opacities of the individual species. For each chemical composition, one has to calculate the aggregate monochromatic opacities first and then

perform the integration over all frequencies, as it was carried out to obtain the results described in Chap. 3.

With the definition in Eq. B.9 we can write the radiative flux

$$F_{\text{rad}} = -\frac{4a_{\text{RC}}c}{3\kappa_{\text{R}}\rho} T^3 \frac{dT}{dr}. \quad (\text{B.10})$$

Here we used the analytical result of the integration of the denominator in Eq. B.9, which is $a_{\text{RC}}T^3/\pi^{32}$. Equation B.10 has the form of a diffusion equation, whereas the energy density of the radiation field ($\propto T^4$) is the quantity being diffused. By introducing the radiative luminosity $L_r = 4\pi r^2 F_{\text{rad}}$ and solving for the temperature gradient, one arrives at the energy transport equation being part of the equation set that describes the stellar structure in Eulerian coordinates.

$$\frac{dT}{dr} = -\frac{3\kappa_{\text{R}}\rho}{16\pi a_{\text{RC}}} \frac{1}{r^2 T^3} L_r \quad (\text{B.11})$$

³² The radiation-density constant is $a_{\text{R}} = 7.5657 \times 10^{-15} \text{ erg cm}^{-3} \text{ K}^{-4}$.

C Element abundances

The amount of a chemical element present in a mixture (the *abundance*) can be quantified in different ways. The choice of the abundance scale depends on the context in which it is used. In stellar evolution calculations, for example, the element (or isotope) abundances are measured in terms of a mass fraction, which is normalised such that the sum of all mass fractions amounts to 1. In the simplest form of this approach, the mass fractions of hydrogen, helium, and all elements with an atomic number greater than 2 (the "metals") are assigned the symbols X , Y , and Z , respectively.

These quantities (beside the C/O ratio) also characterise the Rosseland opacity tables described in Chap. 3. For the calculation of the opacity data, we started from a set of solar element abundances. These are usually tabulated in spectroscopic notation (the scale in which the abundance of hydrogen corresponds to a value of 12, see Sect. C.1). The abundances in this scale are based on the particle number rather than mass. The conversion from one scale to the other is straightforward, and it might appear that it is not necessary to elaborate on the mathematical background. However, the verification of our abundance transformations by a comparison to literature values was hampered by the fact that most authors do not provide details about their approach (one exception is Piersanti et al., 2007). Moreover, it turned out that there is a dissent in the literature about the nomenclature of quantities related to element abundances. Remarkably often one reads the phrase "*we adopt the usual spectroscopic notation*", and although the meaning is clear from the context and the numerical values of the quoted abundances, the lack of proper definitions can cause some confusion. I give a number of examples in Sect. C.1.2.

For the sake of clarity, I document the method of abundance transformations used in this work in Sect. C.2. In this appendix, \log depicts the common logarithm.

C.1 Spectroscopic notation

C.1.1 Preferred definition

In spectroscopic notation, the abundances of the elements are given by

$$A(\text{El}) = \log \varepsilon(\text{El}) + 12 = \log \frac{n(\text{El})}{n(\text{H})} + 12, \quad (\text{C.1})$$

with n designating the number (or number density, i. e. number of particles divided by volume) of the element El. Here we also implicitly define $\varepsilon(\text{El}) \equiv n(\text{El})/n(\text{H})$ as the particle number (or density) of an element relative to the one of hydrogen. Without any further assumptions about the actual value of $n(\text{H})$, it directly follows that $A(\text{H}) = 12$.

The name of the abundance scale indicates its relation to the chemical analysis of stellar atmospheres. The equivalent width of a weak spectral line in the linear part of the curve of growth (i. e. the relation between the abundance of an element to the equivalent width of a spectral line of that species) is proportional to the fraction $n(\text{El})/n(\text{H})$ (Goldberg et al., 1960 and Gray, 1992). The abundance of the element El influences the appearance of a spectral line while the amount of hydrogen determines to a large extent the continuum level against which the equivalent width is measured. Apart from helium, the abundances of the other elements are by orders of magnitude lower than the one of hydrogen. It is thus natural to adopt a logarithmic scale to obtain a compact measure of the abundances.

The intention behind the addition of 12 to the logarithm of number ratios is somewhat obscure. Goldberg et al. (1960) wrote:

“The abundance of each element is derived relative to hydrogen, e. g. $N_{\text{El}}/N_{\text{H}}$. Following Claas (1951), we have added 12 to the logarithm of the abundance ratios.”

The PhD thesis of Claas (1951) is unfortunately not available to me, so I can only speculate about whether Claas was the first to add 12 to the abundances ratios and why he possibly did so. Perhaps it was for aesthetic reasons, since in the work of Goldberg et al. (1960) all quoted abundances are positive numbers between 0 and 12. Thus, by the addition of 12 one avoids to express the amount of particles by negative numbers, and also one does not have to assign a value of 0 to the most abundant element, hydrogen. However, recent solar chemical composition tables list the abundances of uranium and other elements such as tantalum or the noble gases (when determined from meteoritic sources) with a negative A -value. In conclusion, since the addition of 12 to the abundance ratios is not physically motivated, it should be dropped from the definition of the abundance scale. It only causes confusion and inconsistencies in the definition of the quantities A and ε , as will be shown in the next section.

The abundance ratios of two chemical elements are often compared to the respective solar values, which serve as a reference. This is also performed on a logarithmic scale, and in shorthand notation the element symbols under consideration are put in a fraction and enclosed by square brackets.

$$[\text{El}_1/\text{El}_2] \equiv \log \left(\frac{n(\text{El}_1)}{n(\text{El}_2)} \right)_{\star} - \log \left(\frac{n(\text{El}_1)}{n(\text{El}_2)} \right)_{\odot} \quad (\text{C.2})$$

El_1 and El_2 are two chemical elements. In the case that $\text{El}_2 = \text{H}$, we find from Eq. C.1

$$[\text{El}/\text{H}] = A(\text{El})_{\star} - A(\text{El})_{\odot}. \quad (\text{C.3})$$

This notation is frequently used to indicate the metallicity of a star relative to the sun ($[\text{Fe}/\text{H}]$). Another example is to specify the content of alpha elements relative to iron in comparison to the solar value ($[\alpha/\text{Fe}]$).

The method of quoting element abundances relative to the number of hydrogen atoms breaks down for hydrogen-deficient carbon (HdC) stars or R CrB stars (e. g. Asplund et al., 2000). It might also not be the most adequate choice for investigating the evolution of initially zero-metallicity stars.

C.1.2 Literature tour (de force)

This section contains a number of selected examples to illustrate the diverging nomenclature referring to element abundances in the literature. In some cases, I reproduce whole paragraphs that contain remarks about the definition of quantities. The styles of the formulae were adopted from the cited papers.

The nomenclature in Eq. C.1 agrees with the one of Grevesse and Sauval (1998), Grevesse et al. (2007) and Caffau et al. (2008), for instance, although they skipped the definition of ε . The definitions in Sect. C.1.1 are also consistent with Asplund et al. (2005), but they did not define A :

“The chemical composition of the Sun is one of the most important yardsticks in astronomy with implications for basically all fields from planetary science to the high-redshift Universe. Standard practise is to compare the element content in a cosmic object with the corresponding value for the Sun using the normal logarithmic abundance scale $[X/H] \equiv \log(N_X/N_H)_\star - \log(N_X/N_H)_\odot \equiv \log \varepsilon_{X,\star} - \log \varepsilon_{X,\odot}$. Abundance ratios such as $[C/Fe]$ are defined correspondingly. Hydrogen is the chosen reference element since it is the most common element in the Universe as a whole and that it normally dominates the continuous opacity in the formation of the stellar spectra. The solar abundances are, however, not only of interest as a reference point in astronomy but are also of profound importance for the understanding of our own solar system and the solar interior.”

Lambert et al. (1986) used ε inconsistently. They defined $\varepsilon \equiv n_X/n_H$, but later in the paper they wrote $\log \varepsilon_{O,\odot} = 8.92$, for instance. Definition and application of the quantity ε differ by 12 in this case (see previous section). Other opinions on how ε should be defined were contributed by Piersanti et al. (2007) and Przybilla et al. (2008) who claimed

$$\varepsilon(\text{El}) = \log \left(\frac{n(\text{El})}{n(\text{H})} \right) + 12. \quad (\text{C.4})$$

McWilliam (1997) provided an additional alternative:

“ $[A/B]$ refers to an abundance ratio in \log_{10} solar units, where A and B represent the number densities of two elements: $[A/B] = \log_{10}(A/B)_\star - \log_{10}(A/B)_\odot$. Note that $\varepsilon(M) = \log_{10}(M/H)$.”

The disorder of A and ε is completed by Durrant (1988) who suggested $A_X = N_X/N_H$.

In some cases, the addition of 12 is incorporated in the definition of ε , which can for example be found in Lodders (2003)

$$A(\text{El}) = \log \varepsilon_{\text{El}} = \log \left(\frac{n_{\text{El}}}{n_{\text{H}}} \right) + 12, \quad (\text{C.5})$$

or in Beers and Christlieb (2005)

“Elemental abundances can also be referred to as an “absolute” scale, relative to the number of hydrogen atoms, defined by $\log \varepsilon(A) \equiv \log_{10}(N_A/N_H) + 12.0$, where A can be taken to represent any element. Astronomers often refer to an element as either “under-” or “overabundant” when its logarithmic ratio, compared with the same ratio in the Sun, is lower or higher, hence negative or positive, respectively. For the sake of clarity, unless otherwise stated, the observed elemental abundances in stars are assumed to pertain to their outer atmospheres, where the absorption lines under study are formed, not to a volume average over their interiors.”

The reason to adopt this definition is unclear, because it is not obvious what purpose the quantity $\varepsilon_X = n_X/(n_H/10^{12})$ should serve for.

Lugaro et al. (2008) defined

$$A(\text{Element}) = \log N(\text{Element}) + 12. \quad (\text{C.6})$$

The quantity N appears to denote the element number (density). Judging from the quoted A -values for the element fluorine, it cannot be the absolute number of particles. To interpret N as a number density we lack the knowledge of the respective volume.

It is also common practice to introduce the abundance scale by fixing the abundance of hydrogen to 12. Unfortunately, rather than specifying $A(\text{H}) = 12$ (in the notation of Eq. C.1), it is claimed that $\log n(\text{H}) = 12$ (Lodders, 2003 and Gratton et al., 2003), or $\log \text{H} = 12$ (Abia, 2008 and Mucciarelli et al., 2008b). The two versions are consistent insofar as the element symbol often stands in place of the number density (as in the case of the C/O ratio). However, the quantity $n(\text{H}) = 10^{12}$ is not meaningful, neither when it is interpreted as an absolute number nor as a number density, because no reference volume is given. Moreover, I recall that the definition of the A -scale does not require to set $n(\text{H})$ to a certain value.

The next example can cause some difficulties in the interpretation of its meaning, since it introduces a derived quantity based on the spectroscopic notation. This is the *carbon excess*, which is denoted $\varepsilon_C - \varepsilon_O$ by Abia et al. (2008) and $\tilde{\varepsilon}$ by Mattsson et al. (2008). ε_C stands for the quantity that I call $A(\text{C})$ here (Eq. C.1), the same is true for the abundance of oxygen. From the numerical values of “ $\varepsilon_C - \varepsilon_O$ ” and $\tilde{\varepsilon}$, for which “ $\varepsilon_C - \varepsilon_O$ ” = $\tilde{\varepsilon} \approx \varepsilon_C \approx \varepsilon_O$ holds, it is obvious that the minus sign has to be regarded as a symbolic notation. After a close inspection it arises that “ $\varepsilon_C - \varepsilon_O$ ” actually stands for—in the notation of Eq. C.1— $\log(\varepsilon_C - \varepsilon_O) + 12 = \log\left(\frac{n_C - n_O}{n_H}\right) + 12$.

Centeno and Socas-Navarro (2008a) specify their abundances as *ppm* (part per million)³³. One is tempted to interpret that as “in a sample of 1 million particles, there are x

particles of flavour X ". The authors, however, mean "for every 1 million hydrogen atoms, there are x particles of flavour X ". The analysed sample indeed contains more particles than 1 million, namely $n_{\text{H}} + n_{\text{X}} + n_{\text{rest}}$. More remarkable is the equation they give in their footnote 2 when commenting on the correspondence of *their* ε to the *astrophysical* ε , between which is not discriminated in terms of notation. They write

$$\log \varepsilon = 12 + \log_{10}(\varepsilon \times 10^{-6}). \quad (\text{C.7})$$

The left-hand side corresponds to the quantity A in Eq. C.1. The above equation reads in a slightly reduced form

$$\log \varepsilon = \log \varepsilon + 6. \quad (\text{C.8})$$

This "equation" is well suited to mark the end of this section.

C.2 Formulae

C.2.1 Conversion from A values to isotopic mass fractions

We start from Eq. C.1 and solve for the number (density or fraction) $n(\text{El})$ of the element El under consideration.

$$n(\text{El}) = n(\text{H}) 10^{A(\text{El})-12} \quad (\text{C.9})$$

The number abundance of an isotope i of the element El then is

$$n_i(\text{El}) = f_i n(\text{El}) = f_i n(\text{H}) 10^{A(\text{El})-12}. \quad (\text{C.10})$$

The f_i are isotopic fractions and fulfil $\sum_i f_i = 1$. Values for the solar system are tabulated e.g. by Anders and Grevesse (1989) and Lodders (2003). To migrate to mass units, we multiply by the relative atomic mass \mathcal{A}_i of the isotope and get

$$m_i(\text{El}) \equiv n_i(\text{El}) \mathcal{A}_i = f_i \mathcal{A}_i n(\text{H}) 10^{A(\text{El})-12}. \quad (\text{C.11})$$

To obtain the mass fraction X_i of the isotope in a mixture, we have to set the above quantity in relation to the total mass of the mixture that can be calculated by summing over all isotopes. The summation index i is always an $i(\text{El})$.

$$M = \sum_{\text{El}} \sum_i m_i(\text{El}) = \sum_{\text{El}} \sum_i f_i \mathcal{A}_i n(\text{H}) 10^{A(\text{El})-12} \quad (\text{C.12})$$

³³ The units *ppm* and *ppb* are actually deprecated by NIST in the guidelines about the correct usage of the SI units. <http://physics.nist.gov/cuu/Units/checklist.html> (March 10, 2009).

With this result we write

$$X_i(\text{El}) = \frac{m_i(\text{El})}{M} = \frac{f_i \mathcal{A}_i 10^{A(\text{El})-12}}{\sum_{\text{El}} \sum_i f_i \mathcal{A}_i 10^{A(\text{El})-12}}, \quad (\text{C.13})$$

whereby the unknown or unspecified $n(\text{H})$ cancelled out. The mass fraction of an element is obtained by summing over the mass fractions of its isotopes.

$$X(\text{El}) = \sum_i X_i(\text{El}) = \frac{10^{A(\text{El})-12} \sum_i f_i \mathcal{A}_i}{\sum_{\text{El}} 10^{A(\text{El})-12} \sum_i f_i \mathcal{A}_i} \quad (\text{C.14})$$

Note in particular the appearance of

$$\alpha(\text{El}) \equiv \sum_i f_i \mathcal{A}_i \quad (\text{C.15})$$

which is the mean relative atomic mass of an element. The terminology for the quantities \mathcal{A}_i and α are not unique. The National Institute of Standards and Technology (NIST) uses the same symbol, namely $\mathcal{A}_r(X)$, for the relative atomic mass (formerly called *atomic weight*) of an isotope and the standard atomic weight (more appropriately called *relative atomic mass*) of an element.³⁴ I refer also to the section about terminology in Holden (1980) and the adjacent comments about the definition of the relative atomic mass. There it can be read that, amongst other things, (a) atomic weights can be defined for any sample, and (b) the data refer to natural terrestrial sources. Complementary information from the NIST web pages reads as follows:

“In the opinion of the Subcommittee for Isotopic Abundance Measurements (SIAM), these values [Representative Isotopic Composition (%): Mole fraction of the various isotopes] represent the isotopic composition of the chemicals and/or materials most commonly encountered in the laboratory. They may not, therefore, correspond to the most abundant natural material. [...]”

Since the isotope abundances in the atmosphere of a late-type star change in the course of stellar evolution, it is in my opinion correct to calculate mean relative atomic masses from astrophysical isotopic fractions rather than to adopt literature values of the *standard atomic weight* (such as completed for example by Piersanti et al., 2007), which in general refer to terrestrial sources.

With the definition of α and resorting to Eq. C.9 we write the mass fraction of an element in compact form as

$$X(\text{El}) = \frac{n(\text{El}) \alpha(\text{El})}{\sum_{\text{El}} n(\text{El}) \alpha(\text{El})}. \quad (\text{C.16})$$

Here it is also evident that $\sum_{\text{El}} X(\text{El}) = 1$ as desired.

³⁴ <http://physics.nist.gov/PhysRefData/Compositions/notes.html> (March 10, 2009)

C.2.2 Conversion from isotopic mass fractions to A values

To infer abundances in spectroscopic notation (Sect. C.1) we need to calculate the ratio $n(\text{El})/n(\text{H})$ from mass fractions. For this purpose we utilise Eq. C.16 and find

$$\frac{X(\text{El})}{X(\text{H})} = \frac{n(\text{El}) \alpha(\text{El})}{n(\text{H}) \alpha(\text{H})}, \quad (\text{C.17})$$

and thus

$$\frac{n(\text{El})}{n(\text{H})} = \frac{\frac{X(\text{El})}{\alpha(\text{El})}}{\frac{X(\text{H})}{\alpha(\text{H})}}. \quad (\text{C.18})$$

The total mass fraction of an element is simply the sum of the corresponding isotopic mass fractions (Eq. C.14). Before we can insert this ratio into Eq. C.1, we need to calculate α from the isotopic mass fractions of hydrogen and the respective element, which requires to know the isotopic number fractions f_i (Eq. C.15). The f_i can be calculated using Eqs. C.10, C.11, and C.13.

$$f_i = \frac{\frac{m_i(\text{El})}{\mathcal{A}_i}}{\sum_i \frac{m_i(\text{El})}{\mathcal{A}_i}} = \frac{\frac{M X_i(\text{El})}{\mathcal{A}_i}}{\sum_i \frac{M X_i(\text{El})}{\mathcal{A}_i}} = \frac{\frac{X_i(\text{El})}{\mathcal{A}_i}}{\sum_i \frac{X_i(\text{El})}{\mathcal{A}_i}} \quad (\text{C.19})$$

Then α is (Eq. C.15)

$$\alpha(\text{El}) = \frac{X(\text{El})}{\sum_i \frac{X_i(\text{El})}{\mathcal{A}_i}}. \quad (\text{C.20})$$

Inserting this expression into Eq. C.18 we find

$$\frac{n(\text{El})}{n(\text{H})} = \frac{\sum_i \frac{X_i(\text{El})}{\mathcal{A}_i(\text{El})}}{\sum_i \frac{X_i(\text{H})}{\mathcal{A}_i(\text{H})}}, \quad (\text{C.21})$$

and finally

$$A(\text{El}) = \log \frac{\sum_i \frac{X_i(\text{El})}{\mathcal{A}_i(\text{El})}}{\sum_i \frac{X_i(\text{H})}{\mathcal{A}_i(\text{H})}} + 12. \quad (\text{C.22})$$

C.2.3 Setting the mass fraction of ^{12}C to match a certain C/O ratio

As discussed in Chap. 3, a crucial quantity for molecular opacities is the carbon-to-oxygen ratio, C/O. For the calculation of the opacity tables, I altered the mass fraction of ^{12}C only. The question now is how to set $X(^{12}\text{C})$ in order to arrive at a given C/O ratio γ .

A particular case of interest is $\gamma = 1$. In the notation utilised hitherto, C/O corresponds to $n(\text{C})/n(\text{O})$. We start from Eq. C.18 which leads to

$$\frac{n(\text{C})}{n(\text{O})} = \frac{\frac{X(\text{C})}{\alpha(\text{C})}}{\frac{X(\text{O})}{\alpha(\text{O})}} = \gamma. \quad (\text{C.23})$$

From Eq. C.20 it follows that

$$\gamma \frac{X(\text{O})}{\alpha(\text{O})} = \frac{X(\text{C})}{\frac{\sum_i \frac{X_i(\text{C})}{\mathcal{A}_i(\text{C})}}{\sum_i \frac{X_i(\text{C})}{\mathcal{A}_i(\text{C})}}} = \sum_i \frac{X_i(\text{C})}{\mathcal{A}_i(\text{C})} = \frac{\tilde{X}({}^{12}\text{C})}{\mathcal{A}({}^{12}\text{C})} + \sum_{i \setminus 12} \frac{X_i(\text{C})}{\mathcal{A}_i(\text{C})}. \quad (\text{C.24})$$

In the last step I split the summation that includes all carbon isotopes into the desired contribution of the new mass fraction $\tilde{X}({}^{12}\text{C})$ and a sum over the remaining isotopes. Trivial algebraic transformations result in

$$\tilde{X}({}^{12}\text{C}) = \mathcal{A}({}^{12}\text{C}) \left(\gamma \frac{X(\text{O})}{\alpha(\text{O})} - \sum_{i \setminus 12} \frac{X_i(\text{C})}{\mathcal{A}_i(\text{C})} \right). \quad (\text{C.25})$$

To retain $\sum_{\text{El}} X(\text{El}) = 1$ in the element mixture under consideration, one possible approach is to subtract the difference between the new and the old ${}^{12}\text{C}$ mass fraction

$$\Delta X({}^{12}\text{C}) = \tilde{X}({}^{12}\text{C}) - X({}^{12}\text{C}) \quad (\text{C.26})$$

from the mass fraction of the main helium isotope, i. e.

$$\tilde{X}({}^4\text{He}) = X({}^4\text{He}) - \Delta X({}^{12}\text{C}), \quad (\text{C.27})$$

as was outlined in Chap. 3. Analogous expressions can be derived for a certain carbon excess C–O.

References

- Aaronson, M. and Mould, J. 1985, *ApJ*, 290, 191-210
- Abia, C. 2008, *AJ*, 136, 250-258
- Abia, C., Busso, M., Gallino, R., Domínguez, I., Straniero, O. and Isern, J. 2001, *ApJ*, 559, 1117-1134
- Abia, C., de Laverny, P. and Wahlin, R. 2008, *A&A*, 481, 161-168
- Abia, C., Domínguez, I., Gallino, R., Busso, M., Straniero, O., de Laverny, P. and Wallerstein, G. 2003, *Publications of the Astronomical Society of Australia*, 20, 314-323
- Abia, C., Recio-Blanco, A., de Laverny, P., Cristallo, S., Domínguez, I. and Straniero, O. 2008, *ArXiv e-prints* 0812.3103
- Adams, F. C., Graves, G. J. M. and Laughlin, G. 2004. Red Dwarfs and the End of the Main Sequence. In Garcia-Segura, G., Tenorio-Tagle, G., Franco, J. and Yorke, H. W., editors, *Revista Mexicana de Astronomía y Astrofísica Conference Series*, number 22 in *Revista Mexicana de Astronomía y Astrofísica Conference Series*, pages 46-49.
- Alcaíno, G., Liller, W., Alvarado, F., Kravtsov, V., Ipatov, A., Samus, N. and Smirnov, O. 1999, *A&AS*, 135, 103-109
- Alexander, D. R. and Ferguson, J. W. 1994, *ApJ*, 437, 879-891
- Alexander, D. R., Rypma, R. L. and Johnson, H. R. 1983, *ApJ*, 272, 773-780
- Alvarez, R. and Plez, B. 1998, *A&A*, 330, 1109-1119
- Anders, E. and Grevesse, N. 1989, *Geochim. Cosmochim. Acta*, 53, 197-214
- Aringer, B. 2000. *The SiO Molecule in the Atmospheres and Circumstellar Envelopes of AGB Stars*. PhD thesis, University of Vienna.
- Aringer, B. 2005. Infrared Spectra of Red Giants: Molecular and Atomic Lines. In Käufl, H. U., Siebenmorgen, R. and Moorwood, A., editors, *High Resolution Infrared Spectroscopy in Astronomy*, pages 303-308.
- Aringer, B., Girardi, L., Nowotny, W., Marigo, P. and Lederer, M. T. 2009. Synthetic photometry for carbon-rich giants. I. Hydrostatic dust-free models. *A&A*, accepted.
- Aringer, B., Jørgensen, U. G. and Langhoff, S. R. 1997, *A&A*, 323, 202-210
- Aringer, B., Kerschbaum, F. and Jørgensen, U. G. 2002, *A&A*, 395, 915-927
- Arlandini, C., Käppeler, F., Wisshak, K., Gallino, R., Lugaro, M., Busso, M. and Straniero, O. 1999, *ApJ*, 525, 886-900
- Asplund, M., Grevesse, N. and Sauval, A. J. 2005, , 336, 25
- Asplund, M., Gustafsson, B., Lambert, D. L. and Rao, N. K. 2000, *A&A*, 353, 287-310
- Balick, B. and Frank, A. 2002, *ARA&A*, 40, 439-486
- Barber, R. J., Harris, G. J. and Tennyson, J. 2002, *J. Chem. Phys.*, 117, 11239-11243
- Barber, R. J., Tennyson, J., Harris, G. J. and Tolchenov, R. N. 2006, *MNRAS*, 368, 1087-1094
- Basu, S. and Antia, H. M. 2008, *Phys. Rep.*, 457, 217-283
- Bauschlicher C. W., J., Ram, R. S., Bernath, P. F., Parsons, C. G. and Galehouse, D. 2001, *J. Chem. Phys.*, 115, 1312-1318

References

- Beasley, M. A., Hoyle, F. and Sharples, R. M. 2002, *MNRAS*, 336, 168-188
- Beers, T. C. and Christlieb, N. 2005, *ARA&A*, 43, 531-580
- Bernath, P. F. 2005. *Spectra of Atoms and Molecules*. Oxford University Press, 2nd edition.
- Bessell, M. S., Wood, P. R. and Evans, T. L. 1983, *MNRAS*, 202, 59-76
- Bica, E., Dottori, H. and Pastoriza, M. 1986, *A&A*, 156, 261-267
- Bloeker, T. 1995, *A&A*, 297, 727
- Bonnarel, F., Fernique, P., Bienaymé, O., Egret, D., Genova, F., Louys, M., Ochsenbein, F., Wenger, M. and Bartlett, J. G. 2000, *A&AS*, 143, 33-40
- Burbidge, E. M., Burbidge, G. R., Fowler, W. A. and Hoyle, F. 1957, *Reviews of Modern Physics*, 29, 547-650
- Busso, M. 2007. Nuclear Processes in AGB Stars. In Kerschbaum, F., Charbonnel, C. and Wing, R. F., editors, *Why Galaxies Care About AGB Stars: Their Importance as Actors and Probes*, number 378 in *Astronomical Society of the Pacific Conference Series*, pages 26.
- Busso, M., Gallino, R., Lambert, D. L., Travaglio, C. and Smith, V. V. 2001, *ApJ*, 557, 802-821
- Busso, M., Gallino, R. and Wasserburg, G. J. 1999, *ARA&A*, 37, 239-309
- Busso, M., Wasserburg, G. J., Nollett, K. M. and Calandra, A. 2007, *ApJ*, 671, 802-810
- Caffau, E., Ludwig, H.-G., Steffen, M., Ayres, T. R., Bonifacio, P., Cayrel, R., Freytag, B. and Plez, B. 2008, *A&A*, 488, 1031-1046
- Campbell, S. W. and Lattanzio, J. C. 2008, *A&A*, 490, 769-776
- Cantiello, M., Hoekstra, H., Langer, N. and Poelarends, A. J. T. 2007. Thermohaline Mixing in Low-mass Giants: RGB and Beyond. In Stancliffe, R. J., Dewi, J., Houdek, G. and Martin Tout, C. A. R. G., editors, *Unsolved Problems in Stellar Physics: A Conference in Honor of Douglas Gough*, number 948 in *American Institute of Physics Conference Series*, pages 73-77.
- Carpenter, J. M. 2001, *AJ*, 121, 2851-2871
- Carrera, R., Gallart, C., Hardy, E., Aparicio, A. and Zinn, R. 2008, *AJ*, 135, 836-849
- Cassisi, S., Potekhin, A. Y., Pietrinferni, A., Catelan, M. and Salaris, M. 2007, *ApJ*, 661, 1094-1104
- Castellani, V., Degl'Innocenti, S., Marconi, M., Prada Moroni, P. G. and Sestito, P. 2003, *A&A*, 404, 645-653
- Catelan, M. 2007. Structure and Evolution of Low-Mass Stars: An Overview and Some Open Problems. In Roig, F., Alcaniz, J., de La Reza, R. and Lopes, D., editors, *Graduate School in Astronomy: XI Special Courses at the National Observatory of Rio de Janeiro (XI CCE)*, number 930 in *American Institute of Physics Conference Series*, pages 39-90.
- Centeno, R. and Socas-Navarro, H. 2008a, *ApJ*, 682, L61-L64
- Chabrier, G. 2005. The Initial Mass Function: from Salpeter 1955 to 2005. In Corbelli, E., Palla, F. and Zinnecker, H., editors, *The Initial Mass Function 50 Years Later*, number 327 in *Astrophysics and Space Science Library*, pages 41.

-
- Chabrier, G. and Baraffe, I. 2000, *ARA&A*, 38, 337-377
- Chandra, S., Maheshwari, V. U. and Sharma, A. K. 1996, *A&AS*, 117, 557-559
- Charbonnel, C. and Zahn, J.-P. 2007, *A&A*, 467, L15-L18
- Chieffi, A., Limongi, M. and Straniero, O. 1998, *ApJ*, 502, 737
- Chiosi, E. and Vallenari, A. 2007, *A&A*, 466, 165-179
- Cioni, M.-R. L., van der Marel, R. P., Loup, C. and Habing, H. J. 2000, *A&A*, 359, 601-614
- Claas, W. J. 1951. *The composition of the solar atmosphere*. Haarlem, J. Enschede, 1951.
- Cohen, J. G. 1982, *ApJ*, 258, 143-153
- Cole, A. A., Tolstoy, E., Gallagher III, J. S. and Smecker-Hane, T. A. 2005, *AJ*, 129, 1465-1482
- Cook, C. W., Fowler, W. A., Lauritsen, C. C. and Lauritsen, T. 1957, *Physical Review*, 107, 508-515
- Cristallo, S., Gallino, R., Straniero, O., Piersanti, L. and Dominguez, I. 2006, *Memorie della Societa Astronomica Italiana*, 77, 774
- Cristallo, S., Straniero, O., Gallino, R., Lederer, M. T., Piersanti, L. and Domínguez, I. 2008. Progresses in AGB Modelling. In *Evolution and Nucleosynthesis in AGB Stars*, number 1001 in American Institute of Physics Conference Series, pages 3-10.
- Cristallo, S., Straniero, O., Gallino, R., Piersanti, L., Domínguez, I. and Lederer, M. T. 2008a. Why galaxies care about asymptotic giant branch stars. To appear in the *MemSAIt*, Vol. 80.
- Cristallo, S., Straniero, O., Gallino, R., Piersanti, L., Dominguez, I. and Lederer, M. T. 2009, *ArXiv e-prints 0902.0243 ApJ*, accepted
- Cristallo, S., Straniero, O. and Lederer, M. T. 2008b. Evolution and Nucleosynthesis of Low-Mass Metal-Poor AGB Models with C- and N-Enhanced Molecular Opacities. In O'Shea, B. W. and Heger, A., editors, *First Stars III*, number 990 in American Institute of Physics Conference Series, pages 320-324.
- Cristallo, S., Straniero, O., Lederer, M. T. and Aringer, B. 2007, *ApJ*, 667, 489-496
- Cunha, K., Smith, V. V., Lambert, D. L. and Hinkle, K. H. 2003, *AJ*, 126, 1305-1311
- Dalgarno, A. and Williams, D. A. 1962, *ApJ*, 136, 690
- Davis, S., Wallace, L., Brault, J. and Engleman, R. 2005. *The CN spectrum from the infrared to the ultraviolet*. NSO Technical Report.
- de Laverny, P., Abia, C., Domínguez, I., Plez, B., Straniero, O., Wahlin, R., Eriksson, K. and Jørgensen, U. G. 2006, *A&A*, 446, 1107-1118
- Dejonghe, H. and van Caelenberg, K. 1999. AGB stars and galactic dynamics. In Le Bertre, T., Lebre, A. and Waelkens, C., editors, *Asymptotic Giant Branch Stars*, number 191 in *IAU Symposium*, pages 501.
- Denissenkov, P. A., Pinsonneault, M. and MacGregor, K. B. 2008, *ArXiv e-prints 0806.4346*
- Denissenkov, P. A., Pinsonneault, M. and Terndrup, D. M. 2006, *ApJ*, 651, 438-443
- Domínguez, I., Abia, C., Straniero, O., Cristallo, S. and Pavlenko, Y. V. 2004, *A&A*, 422, 1045-1052

References

- Dorfi, E. A. 2003. *Astrophysik 1, Skriptum zur Vorlesung*. Version WS2002/2003.
- Dotter, A., Chaboyer, B., Ferguson, J. W., Lee, H.-c., Worthey, G., Jevremović, D. and Baron, E. 2007, *ApJ*, 666, 403-412
- Dottori, H. A., Pastoriza, M. G. and Bica, E. L. D. 1983, *Ap&SS*, 91, 79-91
- Doughty, N. A. and Fraser, P. A. 1966, *MNRAS*, 132, 267
- Doughty, N. A., Fraser, P. A. and McEachran, R. P. 1966, *MNRAS*, 132, 255
- Doyle, R. O. 1968, *ApJ*, 153, 987
- Dray, L. M., Tout, C. A., Karakas, A. I. and Lattanzio, J. C. 2003, *MNRAS*, 338, 973-989
- Dulick, M., Bauschlicher Jr., C. W., Burrows, A., Sharp, C. M., Ram, R. S. and Bernath, P. 2003, *ApJ*, 594, 651-663
- Durrant, C. J. 1988. *The atmosphere of the sun*. Bristol: Hilger, 1988.
- Eggleton, P. P., Dearborn, D. S. P. and Lattanzio, J. C. 2008, *ApJ*, 677, 581-592
- Feast, M. 2004. AGB variables as distance indicators. In Kurtz, D. W. and Pollard, K. R., editors, *IAU Colloq. 193: Variable Stars in the Local Group*, number 310 in *Astronomical Society of the Pacific Conference Series*, pages 304.
- Ferguson, J. W., Alexander, D. R., Allard, F., Barman, T., Bodnarik, J. G., Hauschildt, P. H., Heffner-Wong, A. and Tamanai, A. 2005, *ApJ*, 623, 585-596
- Ferraro, F. R., Mucciarelli, A., Carretta, E. and Origlia, L. 2006, *ApJ*, 645, L33-L36
- Fischer, P., Welch, D. L. and Mateo, M. 1992, *AJ*, 104, 1086-1099
- Fox, M. W. and Wood, P. R. 1982, *ApJ*, 259, 198-212
- Frantsman, I. L. 1988, *Ap&SS*, 145, 251-261
- Freedman, R. S., Marley, M. S. and Lodders, K. 2008, *ApJS*, 174, 504-513
- Freeman, K. C., Illingworth, G. and Oemler Jr., A. 1983, *ApJ*, 272, 488-508
- Frémat, Y., Antonova, A., Damerdjji, Y., Hansen, C. J., Lederer, M. T., Tüysüz, M., Lampens, P. and van Cauteren, P. 2006, *Communications in Asteroseismology*, 148, 77-81
- Frogel, J. A., Mould, J. and Blanco, V. M. 1990, *ApJ*, 352, 96-122
- Frost, C. A. and Lattanzio, J. C. 1996, *ApJ*, 473, 383
- Gail, H.-P. and Sedlmayr, E. 1988, *A&A*, 206, 153-168
- Gallart, C., Stetson, P. B., Meschin, I. P., Pont, F. and Hardy, E. 2008, *ApJ*, 682, L89-L92
- Gautschy, A. and Saio, H. 1995, *ARA&A*, 33, 75-114
- Gautschy-Loidl, R., Höfner, S., Jørgensen, U. G. and Hron, J. 2004, *A&A*, 422, 289-306
- Gilmozzi, R. and Spyromilio, J. 2008. The 42m European ELT: status. In *Society of Photo-Optical Instrumentation Engineers (SPIE) Conference Series*, number 7012 in Presented at the Society of Photo-Optical Instrumentation Engineers (SPIE) Conference.
- Gingerich, O. 1964, *SAO Special Report*, 167, 17
- Girardi, L., Chiosi, C., Bertelli, G. and Bressan, A. 1995, *A&A*, 298, 87
- Goldberg, L., Muller, E. A. and Aller, L. H. 1960, *ApJS*, 5, 1
- Goorvitch, D. and Chackerian Jr., C. 1994, *ApJS*, 91, 483-489
- Gorfer, M. 2005. Metal lines in cool stars. Master's thesis, University of Vienna.
- Gratton, R. G., Carretta, E., Claudi, R., Lucatello, S. and Barbieri, M. 2003, *A&A*, 404, 187-210

-
- Gratton, R. G., Carretta, E., Matteucci, F. and Sneden, C. 2000a, *A&A*, 358, 671-681
- Gratton, R. G., Sneden, C., Carretta, E. and Bragaglia, A. 2000b, *A&A*, 354, 169-187
- Gray, D. F. 1992. *The observation and analysis of stellar photospheres*. Camb. Astrophys. Ser., Vol. 20.
- Grebel, E. K. 2007. Star Formation Histories as Probed by AGB Stars. In Kerschbaum, F., Charbonnel, C. and Wing, R. F., editors, *Why Galaxies Care About AGB Stars: Their Importance as Actors and Probes*, number 378 in Astronomical Society of the Pacific Conference Series, pages 375.
- Grevesse, N., Asplund, M. and Sauval, A. J. 2007, *Space Science Reviews*, 130, 105-114
- Grevesse, N. and Noels, A. 1993, *Physica Scripta Volume T*, 47, 133-138
- Grevesse, N. and Sauval, A. J. 1998, *Space Science Reviews*, 85, 161-174
- Grocholski, A. J., Cole, A. A., Sarajedini, A., Geisler, D. and Smith, V. V. 2006, *AJ*, 132, 1630-1644
- Grocholski, A. J., Sarajedini, A., Olsen, K. A. G., Tiede, G. P. and Mancone, C. L. 2007, *AJ*, 134, 680-693
- Gustafsson, B. 1995. Opacity Incompleteness and Atmospheres of Cool Stars. In Adelman, S. J. and Wiese, W. L., editors, *ASP Conf. Ser. 78: Astrophysical Applications of Powerful New Databases*, pages 347.
- Gustafsson, B. 2007. Towards a Satisfactory Understanding of AGB-Star Atmospheres?. In Kerschbaum, F., Charbonnel, C. and Wing, R. F., editors, *Why Galaxies Care About AGB Stars: Their Importance as Actors and Probes*, number 378 in Astronomical Society of the Pacific Conference Series, pages 60.
- Gustafsson, B., Bell, R. A., Eriksson, K. and Nordlund, A. 1975, *A&A*, 42, 407-432
- Gustafsson, B., Edvardsson, B., Eriksson, K., Jørgensen, U. G., Nordlund, Å. and Plez, B. 2008, *A&A*, 486, 951-970
- Habing, H. J. 1993. OH/JR stars as tracers of Galactic populations. In Dejonghe, H. and Habing, H. J., editors, *Galactic Bulges*, number 153 in IAU Symposium, pages 57.
- Habing, H. J. and Olofsson, H., editors 2003. *Asymptotic giant branch stars*
- Hardy, R. L. 1971, *J. Geophys. Res.*, 76, 1905-1915
- Harris, G. J. and Lynas-Grey, A. E. 2007. The Effect of a Non-grey Surface Boundary Condition on the Evolution of Low-mass Stars. In Stancliffe, R. J., Dewi, J., Houdek, G., Martin, R. G. and Tout, C. A., editors, *Unsolved Problems in Stellar Physics: A Conference in Honor of Douglas Gough*, number 948 in American Institute of Physics Conference Series, pages 195-199.
- Harris, G. J., Tennyson, J., Kaminsky, B. M., Pavlenko, Y. V. and Jones, H. R. A. 2006, *MNRAS*, 367, 400-406
- Harris, M. J., Lambert, D. L., Hinkle, K. H., Gustafsson, B. and Eriksson, K. 1987, *ApJ*, 316, 294-304
- Helling, C. and Jørgensen, U. G. 1998, *A&A*, 337, 477-486
- Helling, C., Jørgensen, U. G., Plez, B. and Johnson, H. R. 1996, *A&A*, 315, 194-203
- Helling, C., Winters, J. M. and Sedlmayr, E. 2000, *A&A*, 358, 651-664

References

- Herwig, F. 2000, *A&A*, 360, 952-968
- Herwig, F. 2005, *ARA&A*, 43, 435-479
- Herwig, F. and Austin, S. M. 2004, *ApJ*, 613, L73-L76
- Herwig, F., Blöcker, T. and Driebe, T. 2000, *Memorie della Societa Astronomica Italiana*, 71, 745
- Herwig, F., Freytag, B., Hueckstaedt, R. M. and Timmes, F. X. 2006, *ApJ*, 642, 1057-1074
- Herzberg, G. 1950. *Molecular spectra and molecular structure. I. Spectra of diatomic molecules.* Van Nostrand Reinhold, New York.
- Hill, V., François, P., Spite, M., Primas, F. and Spite, F. 2000, *A&A*, 364, L19-L25
- Hinkle, K., Wallace, L. and Livingston, W. C. 1995. *Infrared atlas of the Arcturus spectrum, 0.9-5.3 microns.* San Francisco, Calif. : Astronomical Society of the Pacific.
- Hinkle, K. H., Blum, R. D., Joyce, R. R., Sharp, N., Ridgway, S. T., Bouchet, P., van der Bliik, N. S., Najita, J. and Winge, C. 2003. The Phoenix Spectrograph at Gemini South. In Guhathakurta, P., editor, *Society of Photo-Optical Instrumentation Engineers (SPIE) Conference Series*, number 4834 in Society of Photo-Optical Instrumentation Engineers (SPIE) Conference Series, pages 353-363.
- Hinkle, K. H., Cuberly, R. W., Gaughan, N. A., Heynssens, J. B., Joyce, R. R., Ridgway, S. T., Schmitt, P. and Simmons, J. E. 1998. Phoenix: a cryogenic high-resolution 1- to 5-um infrared spectrograph. In Fowler, A. M., editor, *Proc. SPIE Vol. 3354, p. 810-821, Infrared Astronomical Instrumentation, Albert M. Fowler; Ed.*, number 3354 in Presented at the Society of Photo-Optical Instrumentation Engineers (SPIE) Conference, pages 810-821.
- Hinkle, K. H., Hall, D. N. B. and Ridgway, S. T. 1982, *ApJ*, 252, 697-714
- Hodge, P. W. 1960, *ApJ*, 132, 341
- Höfner, S. 2008, *A&A*, 491, L1-L4
- Höfner, S., Gautschy-Loidl, R., Aringer, B. and Jørgensen, U. G. 2003, *A&A*, 399, 589-601
- Höfner, S., Gautschy-Loidl, R., Aringer, B., Nowotny, W., Hron, J. and Freytag, B. 2005. Dynamic Model Atmospheres of Cool Giants. In Käufl, H. U., Siebenmorgen, R. and Moorwood, A., editors, *High Resolution Infrared Spectroscopy in Astronomy*, pages 269-280.
- Holden, N. E. 1980, *Pure & Appl. Chem.*, 52, 2349-2384 [International Union of Pure and Applied Chemistry (IUPAC), Inorganic Chemistry Division, Commission on atomic weights and isotopic abundances; Pergamon Press Ltd., 1980]
- Houdashelt, M. L., Bell, R. A. and Sweigart, A. V. 2000a, *AJ*, 119, 1448-1469
- Houdashelt, M. L., Bell, R. A., Sweigart, A. V. and Wing, R. F. 2000b, *AJ*, 119, 1424-1447
- Hoyle, F., Dunbar, D. N. F., Wenzel, W. A. and Whaling, W. 1953, *Phys. Rev.*, 92, 1095
- Hron, J., Aringer, B., Kerschbaum, F., Lebzelter, T., Nowotny, W., Posch, T., Lederer, M., Richter, H., Galsterer, W., Höfner, S., Gautschy-Loidl, R. and Verhoelst, T. 2006. The Many Faces of Red Giants. In Coudé Du Foresto, V., Rouan, D. and Rousset, G., editors, *Visions for Infrared Astronomy, Instrumentation, Measure, Métrologie*, pages 107-110.

-
- Iben Jr., I. and Renzini, A. 1983, *ARA&A*, 21, 271-342
- Iben, I. J. 1973, *ApJ*, 185, 209-212
- Iglesias, C. A. and Rogers, F. J. 1996, *ApJ*, 464, 943
- Irwin, A. W. 1981, *ApJS*, 45, 621-633
- Irwin, A. W. 1988, *A&AS*, 74, 145-160
- Jeans, J. H. 1928. *Astronomy and cosmogony*. Cambridge [Eng.] The University press, 1928.
- Johnson, H. B. 1994. Effects of Non-Local Thermodynamic Equilibrium (NLTE) on Molecular Opacities. In Jørgensen, U. G., editor, *IAU Colloq. 146: Molecules in the Stellar Environment*, number 428 in Lecture Notes in Physics, Berlin Springer Verlag, pages 234.
- Jørgensen, U. G., editor (1994). *Molecules in the Stellar Environment*, number 428 in Lecture Notes in Physics, Berlin Springer Verlag.
- Jørgensen, U. G. 1995. Molecular databases. In Adelman, S. J. and Wiese, W. L., editors, *Astrophysical Applications of Powerful New Databases*, number 78 in Astronomical Society of the Pacific Conference Series, pages 179-203.
- Jørgensen, U. G. 1997a. Cool star models. In van Dishoeck, E. F., editor, *IAU Symposium*, number 178 in IAU Symposium, pages 441-456.
- Jørgensen, U. G., Almlof, J. and Siegbahn, P. E. M. 1989, *ApJ*, 343, 554-561
- Jørgensen, U. G., Jensen, P., Sørensen, G. O. and Aringer, B. 2001, *A&A*, 372, 249-259
- Jørgensen, U. G., Johnson, H. R. and Nordlund, A. 1992, *A&A*, 261, 263-273
- Jorissen, A., Frayer, D. T., Johnson, H. R., Mayor, M. and Smith, V. V. 1993, *A&A*, 271, 463
- Jorissen, A., Smith, V. V. and Lambert, D. L. 1992, *A&A*, 261, 164-187
- Kaehler, H. 1978. The Vogt-Russell theorem, and new results on an old problem. In Philip, A. G. D. and Hayes, D. S., editors, *The HR Diagram - The 100th Anniversary of Henry Norris Russell*, number 80 in IAU Symposium, pages 303-311.
- Karakas, A. and Lattanzio, J. C. 2007, *Publications of the Astronomical Society of Australia*, 24, 103-117
- Karzas, W. J. and Latter, R. 1961, *ApJS*, 6, 167
- Keady, J. J. and Hinkle, K. H. 1988, *ApJ*, 331, 539-546
- Keenan, P. C. and Boeshaar, P. C. 1980, *ApJS*, 43, 379-391
- Kippenhahn, R. and Weigert, A. 1990. *Stellar Structure and Evolution* Stellar Structure and Evolution, XVI, 468 pp. 192 figs. Springer-Verlag Berlin Heidelberg New York. Also Astronomy and Astrophysics Library.
- Kupka, F. G., Ryabchikova, T. A., Piskunov, N. E., Stempels, H. C. and Weiss, W. W. 2000, *BaltA*, 9, 590-594
- Kwok, S. 2000. *The Origin and Evolution of Planetary Nebulae*. The origin and evolution of planetary nebulae / Sun Kwok. Cambridge ; New York : Cambridge University Press, 2000. (Cambridge astrophysics series ; 33).
- Lagadec, E. and Zijlstra, A. A. 2008, *MNRAS*, 390, L59-L63
- Lambert, D. L., Gustafsson, B., Eriksson, K. and Hinkle, K. H. 1986, *ApJS*, 62, 373-425
- Lambert, D. L., Smith, V. V., Busso, M., Gallino, R. and Straniero, O. 1995, *ApJ*, 450, 302

References

- Langhoff, S. R. and Bauschlicher, C. W. 1993, *Chem. Phys. Lett.*, 211, 305-311
- Lebzelter, T., Hinkle, K., Lederer, M. T., Posch, T. and Wood, P. 2007. AGB Stars in Globular Clusters. In Kerschbaum, F., Charbonnel, C. and Wing, R. F., editors, *Why Galaxies Care About AGB Stars: Their Importance as Actors and Probes*, number 378 in *Astronomical Society of the Pacific Conference Series*, pages 105-110.
- Lebzelter, T., Hinkle, K. H., Lederer, M. T., Cristallo, S., Straniero, O., Nowotny, W. and Wood, P. 2008. Observing Third Dredge Up in NGC 1846. In Guandalini, R., Palmerini, S. and Busso, M., editors, *Evolution and Nucleosynthesis in AGB Stars*, number 1001 in *American Institute of Physics Conference Series*, pages 56-62.
- Lebzelter, T. and Hron, J. 2003, *A&A*, 411, 533-542
- Lebzelter, T., Lederer, M. T., Cristallo, S., Hinkle, K. H., Straniero, O. and Aringer, B. 2008a, *A&A*, 486, 511-521
- Lebzelter, T., Lederer, M. T., Cristallo, S., Straniero, O. and Hinkle, K. H. 2008d. A study of AGB stars in LMC clusters. To appear in the proceedings of the IAU Symposium No. 256.
- Lebzelter, T. and Obbrugger, M. 2009, ArXiv e-prints 0902.4096
- Lebzelter, T. and Wood, P. R. 2007, *A&A*, 475, 643-650
- Lederer, M. T. and Aringer, B. 2008a. Low Temperature Mean Opacities for the Carbon-rich Regime. In Guandalini, R., Palmerini, S. and Busso, M., editors, *Evolution and Nucleosynthesis in AGB Stars*, number 1001 in *American Institute of Physics Conference Series*, pages 11-18.
- Lederer, M. T. and Aringer, B. 2009, *A&A*, 494, 403-416
- Lederer, M. T., Aringer, B., Höfner, S. and Kerschbaum, F. 2007. Water Opacity in M Stars. In Kerschbaum, F., Charbonnel, C. and Wing, R. F., editors, *Why Galaxies Care About AGB Stars: Their Importance as Actors and Probes*, number 378 in *Astronomical Society of the Pacific Conference Series*, pages 127-128.
- Lederer, M. T., Lebzelter, T., Aringer, B., Nowotny, W., Hron, J., Uttenthaler, S. and Höfner, S. 2006, *Memorie della Societa Astronomica Italiana*, 77, 1008-1013
- Lederer, M. T., Lebzelter, T., Cristallo, S., Straniero, O., Aringer, B. and Hinkle, K. 2007. Third Dredge-up in Globular Cluster AGB Stars: Observation Versus Theory. In *American Institute of Physics Conference Series*, number 948 in *American Institute of Physics Conference Series*, pages 43-50.
- Lederer, M. T., Lebzelter, T., Cristallo, S., Straniero, O., Hinkle, K. H. and Aringer, B. 2009. The puzzling dredge-up pattern in NGC 1978. *A&A*, submitted.
- Leonardi, A. J. and Rose, J. A. 2003, *AJ*, 126, 1811-1835
- Littleton, J. E. 2007.
- Lloyd Evans, T. 1980, *MNRAS*, 193, 87-96
- Lloyd Evans, T. 1983, *MNRAS*, 204, 985-996
- Lodders, K. 2003, *ApJ*, 591, 1220-1247
- Loidl, R., Lançon, A. and Jørgensen, U. G. 2001, *A&A*, 371, 1065-1077
- Luck, R. E. and Bond, H. E. 1991, *ApJS*, 77, 515-540

-
- Lugaro, M., Davis, A. M., Gallino, R., Pellin, M. J., Straniero, O. and Käppeler, F. 2003, ApJ, 593, 486-508
- Lugaro, M., de Mink, S. E., Izzard, R. G., Campbell, S. W., Karakas, A. I., Cristallo, S., Pols, O. R., Lattanzio, J. C., Straniero, O., Gallino, R. and Beers, T. C. 2008, A&A, 484, L27-L30
- Lugaro, M., Herwig, F., Lattanzio, J. C., Gallino, R. and Straniero, O. 2003, ApJ, 586, 1305-1319
- Mackey, A. D. and Broby Nielsen, P. 2007, MNRAS, 379, 151-158
- Maeder, A. and Zahn, J.-P. 1998, A&A, 334, 1000-1006
- Maraston, C. 1998, MNRAS, 300, 872-892
- Maraston, C. 2005, MNRAS, 362, 799-825
- Marigo, P. 2002, A&A, 387, 507-519
- Marigo, P. 2007. Population Synthesis Models including AGB Stars and their Ingredients. In Kerschbaum, F., Charbonnel, C. and Wing, R. F., editors, *Why Galaxies Care About AGB Stars: Their Importance as Actors and Probes*, number 378 in Astronomical Society of the Pacific Conference Series, pages 392.
- Marigo, P. and Girardi, L. 2007, A&A, 469, 239-263
- Marigo, P., Girardi, L. and Bressan, A. 1999, A&A, 344, 123-142
- Matsuura, M., Wood, P. R., Sloan, G. C., Zijlstra, A. A., van Loon, J. T., Groenewegen, M. A. T., Blommaert, J. A. D. L., Cioni, M.-R. L., Feast, M. W., Habing, H. J., Hony, S., Lagadec, E., Loup, C., Menzies, J. W., Waters, L. B. F. M. and Whitelock, P. A. 2006, MNRAS, 371, 415-420
- Matsuura, M., Zijlstra, A. A., van Loon, J. T., Yamamura, I., Markwick, A. J., Whitelock, P. A., Woods, P. M., Marshall, J. R., Feast, M. W. and Waters, L. B. F. M. 2005, A&A, 434, 691-706
- Mattsson, L., Wahlin, R., Höfner, S. and Eriksson, K. 2008, A&A, 484, L5-L8
- Mayer, M. and Duschl, W. J. 2005, MNRAS, 358, 614-631
- McSaveney, J. A., Wood, P. R., Scholz, M., Lattanzio, J. C. and Hinkle, K. H. 2007, MNRAS, 378, 1089-1100
- McWilliam, A. 1997, ARA&A, 35, 503-556
- Menut, J.-L., Gendron, E., Scharmann, M., Tuthill, P., Lopez, B., Danchi, W. C., Wolf, S., Lagrange, A.-M., Flament, S., Rouan, D., Clénet, Y. and Berruyer, N. 2007, MNRAS, 376, L6-L10
- Merrill, S. P. W. 1952, ApJ, 116, 21
- Mihalas, D. 1965, ApJS, 9, 321
- Mihalas, D. 1978. *Stellar atmospheres /2nd edition/*. San Francisco, W. H. Freeman and Co., 1978. 650 p.
- Mihalas, D. and Weibel Mihalas, B. 1984. *Foundations of radiation hydrodynamics*. New York: Oxford University Press, 1984.
- Mucciarelli, A., Carretta, E., Origlia, L. and Ferraro, F. R. 2008a, AJ, 136, 375-388

References

- Mucciarelli, A., Ferraro, F. R., Origlia, L., Carretta, E. and Fusi Pecci, F. 2008b, *Memorie della Societa Astronomica Italiana*, 79, 529
- Mucciarelli, A., Ferraro, F. R., Origlia, L. and Fusi Pecci, F. 2007a, *AJ*, 133, 2053-2060
- Mucciarelli, A., Origlia, L. and Ferraro, F. R. 2007b, *AJ*, 134, 1813
- Nelson, J. and Sanders, G. H. 2008. The status of the Thirty Meter Telescope project. In *Society of Photo-Optical Instrumentation Engineers (SPIE) Conference Series*, number 7012 in Presented at the Society of Photo-Optical Instrumentation Engineers (SPIE) Conference.
- Neuforge, C. 1993, *A&A*, 274, 818
- Nollett, K. M., Busso, M. and Wasserburg, G. J. 2003, *ApJ*, 582, 1036-1058
- Nordhaus, J., Busso, M., Wasserburg, G. J., Blackman, E. G. and Palmerini, S. 2008, *ApJ*, 684, L29-L32
- Nowotny, W., Aringer, B., Höfner, S., Gautschy-Loidl, R. and Windsteig, W. 2005, *A&A*, 437, 273-284
- Oberhummer, H. 1993. *Kerne und Sterne. Einführung in die nukleare Astrophysik*. Barth, Leipzig (Germany).
- Oliva, E. and Origlia, L. 2008. High-resolution near-IR spectroscopy: from 4m to 40m class telescopes. In *Society of Photo-Optical Instrumentation Engineers (SPIE) Conference Series*, number 7014 in Presented at the Society of Photo-Optical Instrumentation Engineers (SPIE) Conference.
- Olofsson, H., Lindqvist, M., Nyman, L.-A. and Winnberg, A. 1998, *A&A*, 329, 1059-1074
- Olszewski, E. W., Schommer, R. A., Suntzeff, N. B. and Harris, H. C. 1991, *AJ*, 101, 515-537
- Palacios, A., Charbonnel, C., Talon, S. and Siess, L. 2006, *A&A*, 453, 261-278
- Peach, G. 1970, *MmRAS*, 73, 1
- Piccirillo, J. 1980, *MNRAS*, 190, 441-457
- Piersanti, L., Straniero, O. and Cristallo, S. 2007, *A&A*, 462, 1051-1062
- Piotto, G., Bedin, L. R., Anderson, J., King, I. R., Cassisi, S., Milone, A. P., Villanova, S., Pietrinferni, A. and Renzini, A. 2007, *ApJ*, 661, L53-L56
- Plez, B. 2007.
- Przybilla, N., Nieva, M.-F. and Butler, K. 2008, *ApJ*, 688, L103-L106
- Querci, F., Querci, M. and Tsuji, T. 1974, *A&A*, 31, 265
- Renzini, A. 2008, *MNRAS*, 391, 354-362
- Rey, S.-C., Yoon, S.-J., Lee, Y.-W., Chaboyer, B. and Sarajedini, A. 2001, *AJ*, 122, 3219-3230
- Reyniers, M., Abia, C., van Winckel, H., Lloyd Evans, T., Decin, L., Eriksson, K. and Pollard, K. R. 2007, *A&A*, 461, 641-650
- Rosseland, S. 1925, *ApJ*, 61, 424
- Rossi, S. C. F., Maciel, W. J. and Benevides-Soares, P. 1985, *A&A*, 148, 93-96

-
- Rothman, L. S., Jacquemart, D., Barbe, A., Chris Berner, D., Birk, M., Brown, L. R., Carleer, M. R., Chackerian, C., Chance, K., Coudert, L. H., Dana, V., Devi, V. M., Flaud, J.-M., Gamache, R. R., Goldman, A., Hartmann, J.-M., Jucks, K. W., Maki, A. G., Mandin, J.-Y., Massie, S. T., Orphal, J., Perrin, A., Rinsland, C. P., Smith, M. A. H., Tennyson, J., Tolchenov, R. N., Toth, R. A., Vander Auwera, J., Varanasi, P. and Wagner, G. 2005, *Journal of Quantitative Spectroscopy and Radiative Transfer*, 96, 139-204
- Rothman, L. S., Wattson, R. B., Gamache, R., Schroeder, J. W. and McCann, A. 1995, *SPIE*, 2471, 105-111
- Russell, H. N. 1934, *ApJ*, 79, 317
- Russell, H. N., Dugan, R. S., Stewart, J. Q. and Young, C. A. 1926. *Astronomy; a revision of Young's Manual of astronomy*. Boston, New York [etc.] Ginn and company [c1926-27].
- Salpeter, E. E. 1952, *ApJ*, 115, 326-328
- Sauval, A. J. and Tatum, J. B. 1984, *ApJS*, 56, 193-209
- Schommer, R. A., Suntzeff, N. B., Olszewski, E. W. and Harris, H. C. 1992, *AJ*, 103, 447-459
- Schönberg, M. and Chandrasekhar, S. 1942, *ApJ*, 96, 161
- Schröder, K.-P. and Connors Smith, R. 2008, *MNRAS*, 386, 155-163
- Schuler, S. C., Cunha, K., Smith, V. V., Sivarani, T., Beers, T. C. and Lee, Y. S. 2007, *ApJ*, 667, L81-L84
- Schwarzschild, M. 1958. *Structure and evolution of the stars*. Princeton, Princeton University Press, 1958.
- Schwarzschild, M. and Härm, R. 1965, *ApJ*, 142, 855
- Schwenke, D. W. 1997.
- Schwenke, D. W. 1998. Opacity of TiO from a coupled electronic state calculation parametrized by AB initio and experimental data. In *Chemistry and Physics of Molecules and Grains in Space. Faraday Discussions No. 109*, pages 321.
- Seaton, M. J. 1993, *MNRAS*, 265, L25
- Seaton, M. J. 1996, *MNRAS*, 279, 95-100
- Seaton, M. J. 2005, *MNRAS*, 362, L1-L3
- Seaton, M. J. and Badnell, N. R. 2004, *MNRAS*, 354, 457-465
- Semenov, D., Henning, T., Helling, C., Ilgner, M. and Sedlmayr, E. 2003, *A&A*, 410, 611-621
- Sharp, C. M. and Burrows, A. 2007, *ApJS*, 168, 140-166
- Shu, F. H. 1991. *Physics of Astrophysics, Vol. I*. Physics of Astrophysics, Vol. I, by Frank H. Shu. Published by University Science Books, ISBN 0-935702-64-4, 429pp, 1991.
- Siess, L. 2007. The Chemical Imprint of Super-AGB Stars. In Kerschbaum, F., Charbonnel, C. and Wing, R. F., editors, *Why Galaxies Care About AGB Stars: Their Importance as Actors and Probes*, number 378 in *Astronomical Society of the Pacific Conference Series*, pages 9-19.

References

- Skrutskie, M. F., Cutri, R. M., Stiening, R., Weinberg, M. D., Schneider, S., Carpenter, J. M., Beichman, C., Capps, R., Chester, T., Elias, J., Huchra, J., Liebert, J., Lonsdale, C., Monet, D. G., Price, S., Seitzer, P., Jarrett, T., Kirkpatrick, J. D., Gizis, J. E., Howard, E., Evans, T., Fowler, J., Fullmer, L., Hurt, R., Light, R., Kopan, E. L., Marsh, K. A., McCallon, H. L., Tam, R., Van Dyk, S. and Wheelock, S. 2006, *AJ*, 131, 1163-1183
- Smith, V. V., Hinkle, K. H., Cunha, K., Plez, B., Lambert, D. L., Pilachowski, C. A., Barbuy, B., Meléndez, J., Balachandran, S., Bessell, M. S., Geisler, D. P., Hesser, J. E. and Winge, C. 2002, *AJ*, 124, 3241-3254
- Smith, V. V. and Lambert, D. L. 1990, *ApJS*, 72, 387-416
- Snedden, C. 1991. CNO Abundances of Stars Undergoing First Dredge up Mixing. In Michaud, G. and Tutukov, A. V., editors, *Evolution of Stars: the Photospheric Abundance Connection*, number 145 in IAU Symposium, pages 235.
- Somerville, W. B. 1964, *ApJ*, 139, 192
- Somerville, W. B. 1965, *ApJ*, 141, 811
- Soria-Ruiz, R., Alcolea, J., Colomer, F., Bujarrabal, V. and Desmurs, J.-F. 2007, *A&A*, 468, L1-L4
- Späth, H. 1991. *Zweidimensionale Spline-Interpolations-Algorithmen*. R. Oldenburg-Verlag, München.
- Stancliffe, R. J. 2006, *MNRAS*, 370, 1817-1822
- Stancliffe, R. J. and Glebbeek, E. 2008, *MNRAS*, 389, 1828-1838
- Stancliffe, R. J., Lugaro, M., Karakas, A. I. and Tout, C. A. 2005, *Nuclear Physics A*, 758, 569-572
- Stancliffe, R. J., Tout, C. A. and Pols, O. R. 2004, *MNRAS*, 352, 984-992
- Stanghellini, L., Shaw, R. A. and Gilmore, D. 2005, *ApJ*, 622, 294-318
- Stehle, C. 1995, *VizieR Online Data Catalog*, 6082, 0
- Stift, M. J. 2000, *A Peculiar Newsletter*, 33, 27
- Straniero, O., Chieffi, A., Limongi, M., Busso, M., Gallino, R. and Arlandini, C. 1997b, *ApJ*, 478, 332
- Straniero, O., Domínguez, I., Cristallo, R. and Gallino, R. 2003, *Publications of the Astronomical Society of Australia*, 20, 389-392
- Straniero, O., Gallino, R. and Cristallo, S. 2006, *Nuclear Physics A*, 777, 311-339
- Sweigart, A. V. and Mengel, J. G. 1979, *ApJ*, 229, 624-641
- Talon, S. and Charbonnel, C. 2008, *A&A*, 482, 597-605
- Tanabé, T., Nishida, S., Nakada, Y., Onaka, T., Glass, I. S. and Sauvage, M. 1998, *Ap&SS*, 255, 407-413
- Tipping, R. H. 2007.
- Tosi, M. 2007. AGB Stars and the Chemical Evolution of Galaxies. In Kerschbaum, F., Charbonnel, C. and Wing, R. F., editors, *Why Galaxies Care About AGB Stars: Their Importance as Actors and Probes*, number 378 in Astronomical Society of the Pacific Conference Series, pages 353.
- Tsuji, T. 1966, *PASJ*, 18, 127

-
- Tsuji, T. 1973, *A&A*, 23, 411-431
- Ugalde, C., Azuma, R. E., Couture, A., Görres, J., Lee, H. Y., Stech, E., Strandberg, E., Tan, W. and Wiescher, M. 2008, *Phys. Rev. C*, 77(3), 035801
- Uttenthaler, S., Aringer, B., Höfner, S., Hron, J., Käufl, H. U., Lebzelter, T. and Nowotny, W. 2004, *Memorie della Societa Astronomica Italiana*, 75, 590
- Uttenthaler, S., Hron, J., Lebzelter, T., Busso, M., Schultheis, M. and Käufl, H. U. 2007, *A&A*, 463, 251-259
- Uttenthaler, S., Lebzelter, T., Hron, J., Aringer, B., Lederer, M. T., Palmerini, S., Busso, M. and Käufl, H. U. 2008. Testing Evolutionary Models with Observations of Galactic Bulge AGB Stars. In Guandalini, R., Palmerini, S. and Busso, M., editors, *Evolution and Nucleosynthesis in AGB Stars*, number 1001 in American Institute of Physics Conference Series, pages 313-320.
- Uttenthaler, S., Lebzelter, T., Palmerini, S., Busso, M., Aringer, B. and Lederer, M. T. 2007, *A&A*, 471, L41-L45
- van den Bergh, S. 2000a. *The Galaxies of the Local Group*. The galaxies of the Local Group, by Sidney Van den Bergh. Published by Cambridge, UK: Cambridge University Press, 2000 Cambridge Astrophysics Series Series, vol no: 35, ISBN: 0521651816.
- van den Bergh, S. 2000b, *PASP*, 112, 529-536
- van den Bergh, S. 2008, *AJ*, 135, 1731-1737
- Van Eck, S., Goriely, S., Jorissen, A. and Plez, B. 2001, *Nature*, 412, 793-795
- van Winckel, H. 2003, *ARA&A*, 41, 391-427
- VandenBerg, D. A., Edvardsson, B., Eriksson, K. and Gustafsson, B. 2008, *ApJ*, 675, 746-763
- Vidler, M. and Tennyson, J. 2000, *J. Chem. Phys.*, 113, 9766-9771
- Vogt, H. 1926, *Astronomische Nachrichten*, 226, 301
- Wahlin, R., Eriksson, K., Gustafsson, B., Hinkle, K. H., Lambert, D. L., Ryde, N. and Westerlund, B. 2006, *Memorie della Societa Astronomica Italiana*, 77, 955
- Wahlin, R. and Plez, B. 2005. A new linelist for the C₂ molecule. In Favata, F., Hus-sain, G. A. J. and Battrick, B., editors, *13th Cambridge Workshop on Cool Stars, Stellar Systems and the Sun*, number 560 in ESA Special Publication, pages 1013.
- Wasserburg, G. J., Boothroyd, A. I. and Sackmann, I.-J. 1995, *ApJ*, 447, L37
- Weigert, A. 1966, *Zeitschrift fur Astrophysik*, 64, 395
- Weiss, A., Salaris, M., Ferguson, J. W. and Alexander, D. R. 2006, *ArXiv astro-ph/0605666*
- Wilson, R. E. 1953. *General catalogue of stellar radial velocities*. Washington, [Carnegie Institution of Washington] 1953.
- Wood, P. R., Bessell, M. S. and Fox, M. W. 1983, *ApJ*, 272, 99-115
- Wood, P. R., Olivier, E. A. and Kawaler, S. D. 2004, *ApJ*, 604, 800-816
- Wood, P. R. and Zarro, D. M. 1981, *ApJ*, 247, 247-256
- Woosley, S. E., Heger, A. and Weaver, T. A. 2002, *Reviews of Modern Physics*, 74, 1015-1071

References

- Yong, D., Meléndez, J., Cunha, K., Karakas, A. I., Norris, J. E. and Smith, V. V. 2008, *ApJ*, 689, 1020-1030
- Zahn, J.-P. 1992, *A&A*, 265, 115-132
- Zhang, Y. and Liu, X.-W. 2005, *ApJ*, 631, L61-L64

Figures

1.1	Schematic view of an AGB star	4
1.2	Example colour-magnitude diagram and Hertzsprung-Russell diagram.	6
1.3	Reactions of the triple-alpha process.	10
1.4	Thermal pulses (or <i>He-shell flashes</i>) and third dredge-up in a Kippenhahn diagram.	13
1.5	Schematic illustration of extra-mixing.	15
1.6	Sample spectra showing molecular bands of CO.	18
2.1	Distribution of observed targets in the cluster NGC 1846.	26
2.2	Distribution of observed targets in the cluster NGC 1978.	27
2.3	Overview about observations of NGC 1846 targets.	30
2.4	Overview about observations of NGC 1978 targets.	31
2.5	Changes in the atmospheric structure due to changed opacity data.	32
2.6	Observation and fit of the oxygen-rich star LE8 in NGC 1846.	39
2.7	Observation and fit of the carbon star B in NGC 1978.	40
2.8	Part of the K-band spectrum of LE8 in NGC 1846.	43
2.9	Fit of the H-band spectrum of the target LE5 in NGC 1978 adopting different oxygen abundances.	47
2.10	Measured abundances ratios for the targets in NGC 1978.	48
2.11	Colour-magnitude diagram based on 2MASS data for NGC 1978.	50
2.12	Colour-magnitude diagram of the oxygen-rich stars in the NGC 1846 sample.	52
2.13	C/O versus $^{12}\text{C}/^{13}\text{C}$ for the oxygen-rich stars in the NGC 1846 sample.	53
2.14	Fluorine abundances of the oxygen-rich sub-sample of NGC 1846 as a function of the C/O ratio.	55
2.15	H-band spectrum of LE13 in NGC 1846.	56
2.16	C/O versus $^{12}\text{C}/^{13}\text{C}$ for the full sample of NGC 1846.	59
2.17	Simplistic picture of the third dredge-up.	63
2.18	Comparison between observational data and theoretical models.	64
2.19	Comparison between observational data and theoretical models.	66
2.20	C/O ratio for a series of models including an overshoot at the base of convective zone generated by the TPs.	68
3.1	Contents of the opacity database in some showcases.	85
3.2	Rosseland opacity changing with the carbon content in the metal mixture as a function of temperature.	86
3.3	Effects of an increased nitrogen abundance on the Rosseland mean opacity at various log R values relative to the case without any nitrogen enhancement.	87

3.4	Graphical representation of two opacity tables that belong to the set with initial metallicity $Z = 0.02$	91
3.5	Comparison of COMA and F05 values at a metallicity of $Z = 0.02$	92
3.6	Comparison of COMA values with OP and OPAL for $Z = 0.02$	93
3.7	Comparison of COMA values with OP and OPAL.	94
3.8	Comparison of COMA with OP at a low metallicity ($Z = 0.00001$) with scaled solar abundances of carbon and nitrogen, and with C and N enhanced to the maximum values.	95
3.9	Evolution of the Rosseland mean as a function of the C/O ratio for different metallicities ($Z = 0.02$ and $Z = 0.00001$) and a representative value of $\log R = -1.5$	96
3.10	Changes in the Rosseland opacity when using different sets of solar element abundances, for instance Grevesse and Sauval (1998, GS98) and Grevesse et al. (2007, GAS07).	98
3.11	Uncertainties in the molecular data that affect the mean opacity.	99
3.12	Influence of variations in resolution or microturbulence on the mean opacity.	101
4.1	FRANEC models for a star with $M = 2 M_{\odot}$ and $Z = 0.0001$ using different opacity prescriptions.	108
4.2	Stellar evolution tracks calculated with MONSTAR.	109
4.3	Preliminary MESA model results based on new opacities and mass-loss rates.	111

Tables

2.1	NGC 1978 additional targets beyond LE.	27
2.2	Radial velocities and cluster membership of NGC 1846 targets.	41
2.3	Data and fit results for oxygen-rich (first group) and carbon-rich (second group) targets in NGC 1846.	42
2.4	Radial velocities and cluster membership of NGC 1978 targets.	46
2.5	Data and fit results for oxygen-rich (first group) and carbon-rich (second group) targets in NGC 1978.	46
3.1	Wavenumber grid	76
3.2	Continuous opacity sources	78
3.3	Molecular line data	80
3.4	Metallicities and enhancement factors	81

Showcases

3.1	Table header of the file 103.Z.02.karo.	89
3.2	Example data block from the file 103.Z.02.karo with $Z = 0.02$, $X = 0.7$, and scaled solar carbon and nitrogen abundances.	90
3.3	Example data block from the file 103.Z.02.karo for an initial metallicity $Z = 0.02$, $X = 0.7$, and with $X(^{12}\text{C}) \times 5.0$ and $X(^{14}\text{N}) \times 1.5$	90

Acronyms

AGB	asymptotic giant branch
BHB	blue horizontal branch
CMD	colour-magnitude diagram
CSE	circumstellar envelope
FDU	first dredge-up
GC	globular cluster
HB	horizontal branch
HBB	hot bottom burning
HRD	Hertzsprung-Russell diagram
ISM	interstellar medium
LMC	Large Magellanic Cloud
LPV	long period variable
LTE	local thermodynamic equilibrium
MS	main sequence
PDCZ	pulse-driven convection zone
PN	planetary nebula
PNN	planetary nebula nucleus
RGB	red giant branch
RHB	red horizontal branch
RTE	radiation transport equation
SGB	sub-giant branch
SMC	Small Magellanic Cloud
SRV	semi-regular variable
TDU	third dredge-up
TP	thermal pulse
WD	white dwarf
ZAMS	zero-age main sequence



Danksagungen/Acknowledgements

Allen voran gilt mein Dank meinem Betreuer Thomas Lebzelter. Dadurch, dass er mich ohne überwältigende Vorkenntnisse über AGB-Sterne in sein Projekt geholt hat, erhielt ich die Möglichkeit in der Forschung zu arbeiten und meine Dissertation zu verfassen. Seine Betreuung war ein stimmiges Paket aus Rat, wenn er nötig war, Freiheit, wenn sie möglich war, und Weitergabe von Wissen sowie Vertrauen in meine Arbeit die ganze Zeit über. Neben all diesen Dingen danke ich ihm für das Verständnis für meine Anliegen und für den einen oder anderen Schubs in die richtige Richtung zum gegebenen Zeitpunkt, etwa wenn es um den ersten Vortrag auf einer Konferenz oder den ersten Beobachtungsaufenthalt ging.

Bernhard Aringer danke ich für die zahllosen Lektionen über Opazitäten, Molekülchemie, Sternatmosphären und Astrophysik im Allgemeinen, sowie für einige Insiderinformationen darüber, wie der Hase in der lokalen, nationalen und internationalen Astronomengemeinschaft läuft. Ich habe im Laufe dieser Arbeit ständigen Gebrauch von den Programmen COMA und MARCS gemacht, die entweder von ihm geschrieben oder (teilweise nach meinen Vorstellungen) weiterentwickelt wurden. Auch dafür danke ich ihm. Zuletzt danke ich meinem Sitznachbarn für sein bereitwilliges Teilen von Süßigkeiten, wodurch bei mir ein substantieller Massenverlust abgewendet werden konnte.

Dem Leiter der AGB-Arbeitsgruppe Josef Hron danke ich für seinen Rat und seine Kritik jeweils zur rechten Zeit, für seine Führungsqualität und für das Bemühen um eine gute Atmosphäre innerhalb der Gruppe, welches wiederum durch Verteilen von Süßigkeiten und das Zurverfügungstellen einer von mir weidlich genutzten Espressomaschine unterstützt wurde.

Meinem Kollegen Walter Nowotny möchte ich für die Hilfe bei der Handhabung von dynamischen Modellen danken.

Allen weiteren Kollegen der AGB-Arbeitsgruppe danke ich für ein entspanntes, angenehmes Arbeitsklima und für die Hilfsbereitschaft bei aufgetretenen Problemen.

Für finanzielle Unterstützungen bin ich folgenden Institutionen zu Dank verpflichtet: dem Fonds zur Förderung der wissenschaftlichen Forschung (FWF) für Mittel aus dem Projekt P-18171, der Österreichische Akademie der Wissenschaften (ÖAW) für die Zuerkennung eines DOC-Stipendiums, der Österreichische Forschungsgemeinschaft (ÖFG) für die Gewährung von Förderungen im Rahmen des Programms "Internationale Kommunikation", der Österreichischen Gesellschaft für Astronomie und Astrophysik (ÖGAA) für einen Reisekostenzuschuss, dem Österreichischen Austauschdienst (OeAD) für ein Erasmus-Stipendium, dem OPTICON und der European Astronomical Society (EAS) für die Ermöglichung der Teilnahme an der NEON-Sommerschule, der ESO für die Gewährung und Finanzierung eines Beobachtungsaufenthalts. Dem Institut für Astronomie der Universität Wien danke ich für die Zurverfügungstellung eines Arbeitsplatzes.

Special thanks goes to Sergio Cristallo for asking me whether I can calculate opacities for him. I turned out that I could, and although this was not part of my original plan, the work on Rosseland opacities makes up half of my thesis now. I thank him and Oscar Straniero for a fruitful collaboration. Ken Hinkle is thanked for the operation of the Phoenix spectrograph and his assistance during my stay at the Gemini South telescope.

Susanne Höfner danke ich für ihre Gastfreundschaft und ihre Betreuung während meiner Zeit in Uppsala. Ich hoffe, dass, nun da diese Dissertation abgeschlossen ist, unsere gemeinsame Arbeit schlussendlich Früchte tragen wird.

I thank the referees of this thesis, Paola Marigo and Peter Wood, for agreeing to write their reports on short notice.

Allen meinen Freunden möchte ich aufrichtig Dank aussprechen dafür, dass sie für die Aufrechterhaltung des Gleichgewichts zwischen Arbeit und Freizeit gesorgt haben, rechtzeitig bevor es zu Ungunsten der Freizeit gekippt ist. Zumindest hat das meistens so funktioniert, wenn auch nicht immer.

Meiner Familie danke ich für die vielen gemeinsamen, schönen Stunden und für ihr Interesse an meiner Arbeit. Ich durfte immer auf ihre Unterstützung in allen Belangen zählen. Insbesondere danke ich auch meinen Eltern, durch die es mir überhaupt erst möglich wurde, mich dem Studium der Physik und später der Astronomie zu widmen.

Liebe Tamara, viele Dinge haben zum Gelingen dieser Dissertation beigetragen, aber nichts so sehr wie deine Liebe und Unterstützung. Auch in Zeiten, in denen ich meiner Arbeit zu viel und dir zu wenig Aufmerksamkeit geschenkt habe, hast du nicht an mir gezweifelt. Ich danke dir für dein Verständnis für meine Interessen, für die Geduld die du dabei aufbringen musstest, und für den Humor, mit dem du das Zusammenleben mit einem Wissenschaftler bewältigst. Danke, dass du bei mir bist.

Curriculum vitae

Personal details

Michael T. Lederer
Manker Straße 5
A-3200 Ober-Grafendorf
Austria

Born 8th October, 1977 in St. Pölten (Austria)
Austrian citizen

michael.lederer@gmx.at

Education

2005 – 2009	PhD studies of Astronomy at the University of Vienna
2001 – 2005	Studies of Astronomy at the University of Vienna Graduation ("Magister der Naturwissenschaften") with distinction
1997 – 2005	Studies of Technical Physics at the Vienna University of Technology Graduation ("Diplom-Ingenieur") with distinction
1991 – 1996	Bundeshandelsakademie St. Pölten (high school) Final examination ("Matura") with distinction
1987 – 1991	Bundesrealgymnasium St. Pölten (junior high school)
1983 – 1987	Volksschule Ober-Grafendorf (elementary school)

Scientific Activities

03/2009	Expected defense of the PhD thesis
12/2008	Observing run at the Very Large Telescope, Cerro Paranal, Chile
03/2008 – 05/2008	Research stay at the Department of Physics and Astronomy, Uppsala University, Sweden
02/2008 – 03/2009	Scientific co-worker at the Department of Astronomy, University of Vienna, Austria
12/2006	Observing run at the Gemini South Observatory, Cerro Pachon, Chile
07/2006	Attendance of the 5 th NEON Observing School, Observatoire de Haute-Provence (OHP), France
02/2006 – 01/2008	DOC scholarship of the Austrian Academy of Sciences
08/2005 – 01/2006	Scientific co-worker at the Department of Astronomy, University of Vienna, Austria

Talks

- Invited to give a talk at the workshop "The Giant Branches", Lorentz Center, Leiden, May 2009
- Seminar talk, Department of Physics and Astronomy, Uppsala University, May 2008
- Seminar talk, Department of Astronomy, University of Padova, November 2007
- IX Torino Workshop on Nucleosynthesis in AGB stars, Perugia, October 2007
- Unsolved Problems in Stellar Physics, Cambridge, June 2007
- Scientific Annual Meeting of the Austrian Society for Astronomy and Astrophysics (ÖGA²), Innsbruck, April 2006
- VIII Torino Workshop on Nucleosynthesis in AGB Stars, Granada, February 2006

